The Drying of Inkjet Printed Drops on Patterned Substrates

BETHANY KATE KAZMIERSKI

Durham University

The Drying of Inkjet Printed Drops on Patterned Substrates

A thesis submitted in partial fulfilment of the requirements for the degree of Doctor of Philosophy in the University of Durham by,

Bethany Kate Kazmierski

Department of Chemistry

Durham University

January 2018

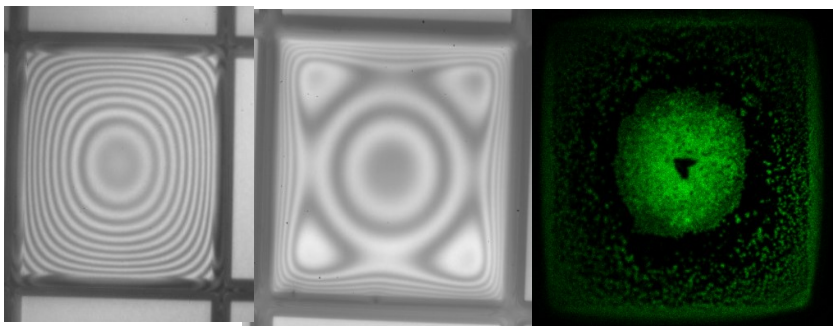

Abstract

Inkjet printing provides a promising method for the fabrication of OLED displays but currently, inkjet printed displays are not commercially viable. This thesis focuses on understanding the drying processes that occur once drops have been delivered to the patterned substrates necessary for OLED devices. To this end, internal flows in drops evaporating within wells were investigated and the changing drop profiles during drying were imaged. A method was suggested for successful fabrication of OLED devices.

Particle tracking was carried out on both pure solvents and binary solvent mixtures within square wells. Due to the large particle size in comparison to the depth of fluid these experiments were not very informative, though they did confirm evaporation was faster at the contact line than in the centre of the drops. Evaporation was also slightly faster in the corners of the wells relative to the straight edges.

Studies on pure solvents identified the influence of evaporation rate on profile development in drying drops. Two main drying regimes were identified and the main influence on drop profile development was found to be the evaporation rate of the solvent. Slow drying drops gave U-shaped profiles and fast drying drops gave W-shaped profiles.

The influence of thermal effects on drop profiles was also considered. Thermal Marangoni flows were found to have a profound influence on profile development, with drops giving M-shaped profiles. Thermal effects could not always be reliably reproduced and it was concluded that further experimentation in this area was necessary. The lack of repeatability in the results was assumed to be due to the sensitivity of the drop profile to its initial behaviour.

Binary solvent mixtures were also found to have an impact on profile progression during drying. Solutal Marangoni flows gave M-shaped profiles in the case where the more volatile solvent had a lower surface tension and enhanced drainage from the corners of the wells towards the centre in the case where the more volatile solvent had a higher surface tension.

The thesis then moved on to investigate the effect of active materials on drop profiles. The active materials used were found to increase the surface tension of the solvents, giving M-shaped profiles when dissolved in single solvents. In some slow drying solvents, diffusion of the material evened out concentration gradients during drying and U-shaped profiles were seen. When solvent mixtures which had shown flows in opposition to those caused by active materials were used to print the actives, the profile development showed enhanced drainage from the corners of the wells suggesting solvent driven Marangoni flows were dominant over

active material driven Marangoni flows. Crystallisation of the active material in this case showed re-circulatory flows were present with the active materials following the flows. This suggested particle tracking should be possible in these systems.

A proposed method for obtaining flat deposits from printed drops was then presented, along with some initial results towards that goal. The initial results were promising but more investigation is needed in this area.

Acknowledgements

This PhD would not have been possible without a number of people, all of whom have helped me in different ways. Thanks must go to my supervisor Prof. Colin Bain for the many interesting and rewarding scientific discussions we have had, as well as the many opportunities he has provided me with over the last 5 years. Thank you also to Merck Chemicals Ltd and The EPSRC for financially supporting the project. To my supervisors at Merck, past and present, thank you for all of your guidance throughout the project. Without Phil May, Pawel Miskiewicz, Dan Walker and Li Wei Tan this project would not have progressed as far as it did.

Thanks must also go to the Bain group for their enjoyable company and friendship during my time here. Special thanks go to Lisong Yang who has answered many a stupid question and provided me with an unbelievable amount of practical help in the lab. Always with a smile on her face, she has also been a good friend and provided much fun and laughter over my time in the group.

A great number of friends have helped me through the last four years (and more) and it is impossible to name them all. But to Abigail, who has always been there, thank you for everything. Becca, Anna, Jas, Ben, LiLi, Becky, Flora and Hannah, thank you for providing me with a source of sanity when everything got too much. To Jacquie, thank you for giving me the opportunity to do something I have grown to really love and thank you also for your friendship and support over the last few years.

To my family who have always encouraged me in everything I decide to do, no matter how big or small, thank you for your support and love throughout my life. Popa you were always my biggest fan when it came to my Masters and I know you would have been the same with my PhD, this one is for you.

Finally to Laurie, who has the patience of a saint! Thank you for everything you do and have done for me. I certainly would not have got through this without your support, and I pretty much owe this thesis to you.

Publications List

The following publications were made during the course of this thesis:

- B. Kazmierski, L. Yang, E. Talbot, L. W. Tan, D. Walker, C. D. Bain, Inkjet Printing onto Patterned Substrates, *Printing for Fabrication: 32nd International Conference on Digital Printing Technologies, and Digital Fabrication (NIP), 2016, September 2016, The Society for Imaging Science and Technology,* (2016), 170-174.

Declaration

MATLAB post processing routines for particle tracking were developed by Lisong Yang, Emma Talbot and Arganthaël Berson at the University of Durham. MATLAB post processing routines for interferometry measurements were developed by Lisong Yang and Jing Shi at the University of Durham.

All substrates used throughout the thesis were provided by Merck Chemicals Ltd. The circular wells were made in house by them.

Epifluorescence measurements of active material deposits were carried out in conjunction with Dr Robert Pal at the University of Durham.

Copyright Notice

List of Symbols

E_f	Fermi level
E_g	Band gap
Re	Reynold's number
ρ_f	Fluid density
v_d	Drop velocity
D_0	Drop diameter in flight
η	Fluid viscosity
We	Weber number
σ	Surface tension
Oh	Ohnesorge number
We^*	Reduced Weber number
E_{kin}	Kinetic energy of drop on impact
E_{surf}	Surface energy of drop
R_c	Contact radius
t	Time
N	Tanner's law constant
l_c	Capillary length
g	Gravitational constant
B_0	Bond number
Ca	Capillary number
u	Internal flow velocity
σ_{sv}	Solid-vapour interfacial tension
σ_{sl}	Solid-liquid interfacial tension
σ_{lv}	Liquid-vapour interfacial tension
θ	Equilibrium contact angle
p	Pressure
r_1, r_2	Principal radii of curvature
H_c	Mean curvature
p_1, p_2	Vapour pressures of components 1 and 2
ΔH	Enthalpy of vapourisation
R	Ideal gas constant
T	Temperature
x_A, x_B	Mole fractions of components A and B

p_A, p_B	Partial vapour pressures of components A and B
p_A^*, p_B^*	Vapour pressures of pure A and B
p_t	Total vapour pressure
H_B	Henry's constant
γ_A	Activity coefficient of component A
a_A	Activity of component A
μ	Chemical potential
μ^{θ}	Chemical potential under standard conditions
β	Interaction parameter
δD	Dispersion forces
δP	Polar forces
δH	Hydrogen bonding forces
E_c	Cohesive energy density
V	Molar volume
E_D	Dispersion forces contribution to E_c
E_P	Polar forces contribution to E_c
E_H	Hydrogen bonding forces contribution to E_c
Ra	Distance in Hansen space
R_0	Radius of sphere
p_v	Vapour pressure
A, B, C	Antoine constants
D	Diffusion coefficient of vapour under ambient conditions
c	Concentration
Kn	Knudsen number
λ_p	Mean free path
x	Tangential co-ordinate
n	Normal co-ordinate
Ma	Marangoni number
h	Fluid height
u_{cap}	Velocity of capillary flows
κ	Thermal conductivity
θ_r	Receding contact angle
θ_a	Advancing contact angle
Pe	Peclet number for mass transfer
L	Length scale of droplet

k_B	Boltzmann constant
a	Particle radius
t_{diff}	Diffusion time
λ	Wavelength
n_a	Refractive index of air
θ_{in}	Angle of incidence
θ_{re}	Angle of refraction
n_s	Refractive index of solvent
θ_c	Cone angle
d_f	Depth of focus
D_f	Distance between interference fringes
L_c	Coherence length
$\Delta\lambda$	Full-width half-maximum
t_{dry}	Drying time
$\bar{x}_B$	Mean Brownian displacement
h_{max}	Maximum dimple height
κ_s	Thermal conductivity of substrate
κ_l	Thermal conductivity of liquid
Pe_h	Peclet number for heat transfer
α	Thermal diffusivity
M	Mass of droplet
$J(r)$	Mass flux
n_s	Saturation vapour density
n_∞	Ambient vapour density
θ_i	Initial contact angle
γ	Latent heat of vapourisation
r	Radial position
p_s	Vapour pressure at drop surface
p_∞	Vapour pressure at infinite distances
u_r	Velocity od radial flows
z	Direction normal to surface
u_M	Velocity of Marangoni flows
C_T	Thermal constant
d_{max}	Maximum depth of drained region
Y	Proportion of solvent in the vapour phase

X	Proportion of solvent in the liquid phase

Abbreviations

OLED	Organic light emitting diode
LC	Liquid crystal
VB	Valence band
CB	Conduction band
ETL	Electron transport layer
HTL	Hole transport layer
HIL	Hole injection layer
LUMO	Lowest unoccupied molecular orbital
HOMO	Highest occupied molecular orbital
QE	Quantum efficiency
ISC	Intersystem crossing
CIJ	Continuous inkjet
DOD	Drop on demand
TIJ	Thermal inkjet
piezo	Piezoelectric
ITO	Indium tin oxide
SAM	Self-assembled monolayer
HSPs	Hansen solubility parameters
HSPiP	Hansen Solubility Parameters in Practice
RED	Relative energy difference
VLE	Vapour-liquid equilibria
CAH	Contact angle hysteresis
PTFE	Polytetrafluoroethylene
ELWD	Extra-long working distance
NA	Numerical aperture
LED	Light emitting diode
FWHM	Full-width half-maximum
CWL	Central wavelength
RH	Relative humidity
ROI	Region of interest
PTV	Particle tracking velocimetry
LSPR	Localised surface plasmon resonance

SPR	Surface plasmon resonance
IPA	Isopropyl alcohol

Contents

1. Introduction

1.1 Motivation

Organic light emitting diodes (OLEDs) have the theoretical capability to offer low-cost, high resolution displays which require little energy to drive them compared to current display screen technologies such as liquid crystals (LCs).[1] With the identification of OLEDs as the potential future of display screen technology, many studies have been performed to develop the necessary materials for use in such displays.[1,2,11,12,3–10] The materials required to manufacture OLED screens have now been developed to a point whereby they are commercially viable and long lasting enough to be sold on a large scale.[2,13,14] However the manufacturing costs of OLED displays far outweigh those for LCs. [6,15] In order to make OLED screens more widely accessible, the manufacturing methods used to create them need to be reviewed and developed to reduce costs.[15] Inkjet printing provides an opportunity to reduce manufacturing costs for OLED displays; though devices manufactured in this way are not currently commercially viable.[1,16,17]

In order for ink-jet printing to become viable for the production of display screens, problems with the performance and lifetime of the devices need to be rectified. In order to improve performance and device lifetime, control over the deposit morphology from printed OLED materials is essential. OLED deposits for display screens must be level across their entire area to ensure even light output across devices; if light output is not even, the devices are not commercially viable. Uneven deposits from printed drops cause problems with short lifetimes, thin regions give higher currents which leads to rapid aging. When printing OLED materials, drops are deposited into wells and surrounded by walls on all sides; understanding how the presence of walls surrounding drying drops has an impact on deposit morphology is necessary for control of the deposits. Much is understood about the driving mechanisms behind deposit morphology for drops drying on flat substrates and how the drying can be controlled to give even deposits;[18–25] very little on the other hand is understood about drops drying within wells. The research which has been carried out into deposits from drops printed into wells generally focuses on the final deposit morphology or stills from the drying process[1,26] rather than looking at the entire drying process in real time which is necessary to understand fully the mechanisms driving the process and to develop strategies to control deposits from printed drops.

This thesis aims to understand the fundamental processes behind the drying of drops printed into wells and what drives deposit morphology. The investigation focuses on the relevant flows and transport mechanisms present in drying drops, along with how the profile of drops

changes during drying. Once an understanding of the drying process and relevant driving forces behind deposit morphology has been established, it can be used to suggest ways in which deposit morphology can be controlled to give commercially viable ink-jet printed OLED devices.

In order to understand the processes behind drying, a number of different experimental techniques were used to look at a range of different organic solvents. Initially a range of single solvents was investigated before looking at the effect binary solvent mixtures had on the drying process. Once the driving mechanisms behind the drying of pure and mixed solvents were understood, the effect of the presence of active materials on drying was also investigated. The influence of changes in the ambient temperature surrounding evaporating drops was considered and the consequences of temperature on drop profiles were identified. Knowledge of the physical processes and transport mechanisms important during drying were then used to suggest ways in which morphology could be controlled to ensure deposits are even across their entire area. The work in this thesis is important for the development of industrial processes to manufacture OLED displays that are commercially viable, as well as furthering the academic understanding of droplet evaporation. Whilst there are many different processes involved in inkjet printing, this thesis focuses on the drying behaviour of the drop after impact and spreading.

In this chapter, the motivation behind the work undertaken in this thesis is reviewed and the main theoretical concepts relating to the work are discussed. The main literature contributions relating to the evaporation of single solvents and solvent mixtures along with deposit formation are discussed along with their relevance to printed OLED systems.

Chapter 2 explains the main experimental techniques used for data collection and image analysis.

Chapter 3 investigates the internal flows present within drops drying in wells. The main driving mechanisms behind particle transport are considered and the role of walls surrounding the drops is discussed. Both single solvents and solvent mixtures are considered and the influence of the presence of co-solvents (if any) on the drying is identified.

Chapter 4 focuses on the changing drop profile during drying and its relationship to particle transport processes. Profile development is found to be dependent on the speed of evaporation of the drops and two main drying regimes are identified.

Chapter 5 concentrates on the effect of substrate temperature on the drying of single solvent drops. Some solvents showing thermal surface tension gradients are identified and the effect

of temperature on drop profile development is discussed. The influence of changing the temperature of drying drops not showing thermal effects at room temperature is also investigated.

Chapter 6 considers the effect of binary solvent mixtures on drop profile development during drying. Some flows due to solutal surface tension gradients are identified and the potential influence on the drying of OLED materials is discussed.

Chapter 7 investigates the effect the presence of active materials has on drop profiles during drying and final deposit morphologies. Active materials are printed from both single solvents and binary mixtures, and found to have a profound influence on profile development. Deposits dried under ambient conditions are compared to those dried in a vacuum.

Chapter 8 gives concluding remarks and identifies areas to be investigated further in the future. A method for obtaining level deposits from drops printed into wells is proposed and some preliminary experiments to determine its feasibility are presented.

1.2 OLEDs

An organic light emitting diode is a solid-state semiconductor, formed of a series of thin films, which emits light on application of a voltage. OLEDs have the capability to provide low energy, high resolution displays. Much research has been carried out in recent years to improve the materials and manufacturing methods used to create OLED displays so they can be produced on a commercial scale at a competitive price.[15] The materials used have now been developed to a point whereby the lifetimes of light emitting materials are what would be necessary to give commercially viable devices.[2,13,14,27] The manufacturing methods used to produce commercial OLED devices do give even light output across the entire area but are costly and time consuming,[15] as such commercially produced OLED screens are too expensive to be accessible to the majority of consumers.

1.2.1 Working Principle

In order for a material to be conductive it must contain mobile holes or electrons. The Fermi level of a material (E_f) is defined as the energy at which there would be a 50 % chance of an electron occupying an electronic state at a given temperature. In pure conductors, such as metals, there are a number of different energy levels available for electrons to occupy. These energy levels form a continuous band of levels of filled and empty states (figure 1.1). Due to the continuous band of energy levels in a metal the Fermi level lies somewhere within a band, allowing for easy transport of electrons through the metals and so easy conduction. Insulating materials have a series of filled states, referred to as the valence band (VB), and empty states, referred to as the conduction band (CB). The gap between the VB and CB is referred to as the band gap (E_g). In a pure insulator E_f lies within the band gap, and E_g is large enough that thermal excitation from the VB to the CB is not possible (figure 1.1). In semiconductors, E_g is small enough that thermal excitation from the VB to the CB is possible (figures 1.1 and 1.2).[28–30]

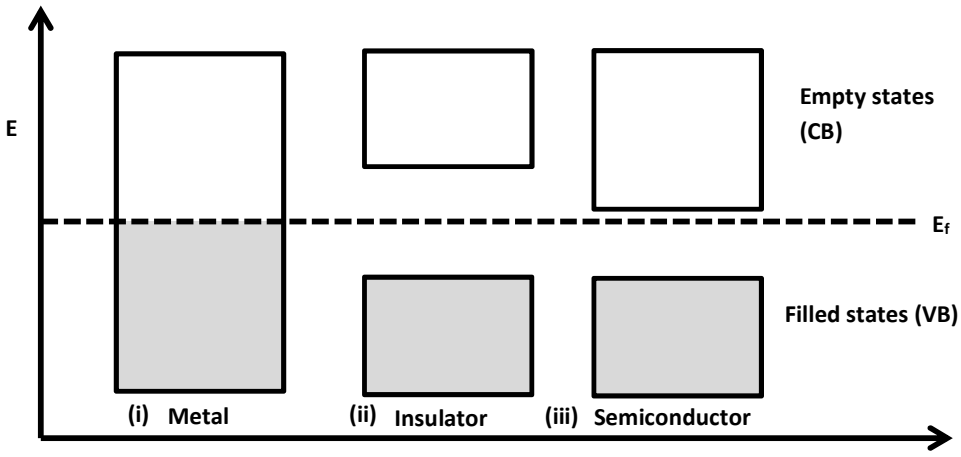

Figure 1.1: A schematic diagram showing the relevant energy levels in metals (i), insulators (ii) and semiconductors (iii). Grey areas show the filled states and white areas show the empty states.

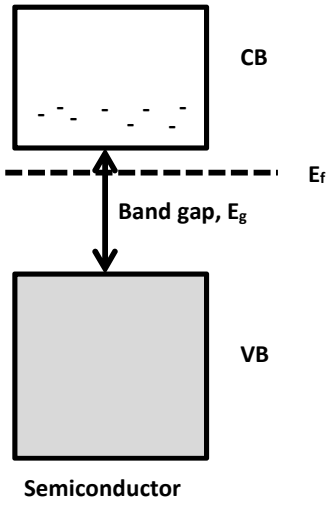

Figure 1.2: A schematic diagram showing the presence of electrons (-) in the CB and E_g for a semiconductor material.

In OLED devices layers of organic material are sandwiched between two electrodes. A schematic of a typical OLED device is shown in figure 1.3. The substrate is used to support the device and provides a base onto which the remaining layers can be deposited. The backplane contains all of the electronic circuitry used to drive the device. The device also contains a number of organic layers, including a few different host materials and an emissive material. Host materials can be constructed from either small molecules or polymers, and the emissive layer is usually formed of a heavy metal complex (eg. Iridium). In some cases dopants are introduced into the host layers to improve efficiency and output as well as reducing operating

voltages. A barrier layer, or encapsulation of the device, is also necessary as host materials are sensitive to both oxygen and water.[2,6]

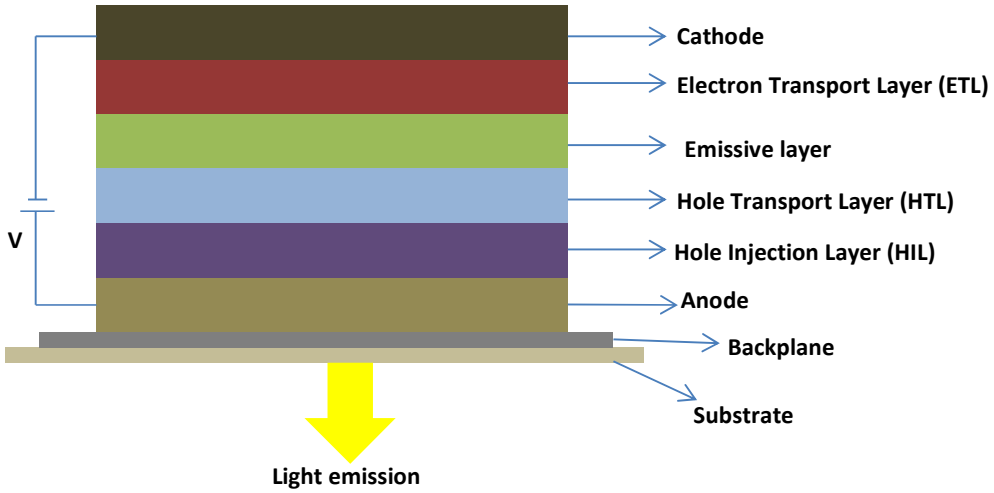

Figure 1.3: A schematic diagram showing the necessary layers in an OLED device.

The layers of organic materials in OLED devices act as a semiconductor. When a voltage is applied electrons flow from the cathode to the anode (figure 1.4). As the electrons move through the device, they are injected from the cathode into the electron transport layer (ETL) where they act as charge carriers. The ETL has a lowest unoccupied molecular orbital (LUMO) close in energy to the work function of the cathode so injection of the electrons into the ETL is trivial.[5,6,11,31] As electrons are being injected into the ETL the anode is removing electrons from the hole transport layer (HTL) via the hole injection layer (HIL) to form holes. The energy of the highest occupied molecular orbital (HOMO) of the HTL is close to the work function of the anode, making the removal of electrons from the HTL facile.[5,6,11,31] Collectively the ETL, HTL and HIL are known as the host materials of the device. The materials in the host layers contain a network of extended conjugation and delocalisation, allowing the holes and electrons created to move towards one another through the device. Eventually the holes and electrons meet in the emissive layer and combine to form an exciton. Excitons are an excited bound state of holes and electrons which then decay back to a ground state by emitting a photon and causing luminescence from the device.[5,8] The energy of the photon produced and the resulting wavelength of light depends on the HOMO-LUMO gap of the organic materials present in the HTL and ETL respectively. Therefore the wavelength of light emitted on decay of the exciton can be tuned by altering the organic materials used.[6,8,11,31]

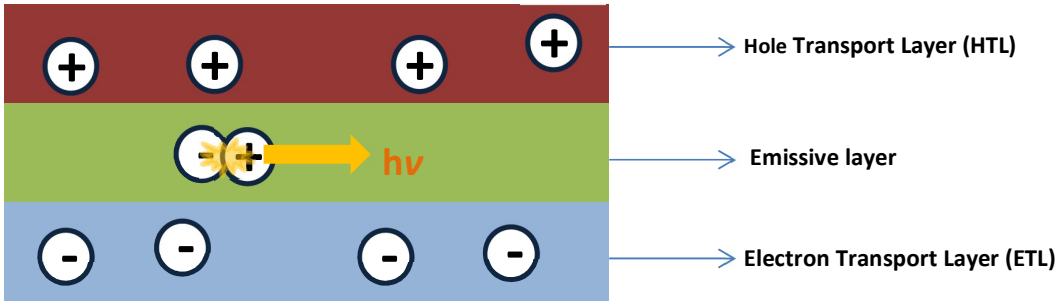

Figure 1.4: A schematic diagram showing the working principle of an OLED device.

The luminescence from OLED devices can be either fluorescence or phosphorescence depending on the organic materials used. Fluorescence is emission from an excited singlet state whereas phosphorescence is emission from an excited triplet state. Fluorescence is a spin-allowed process and so is very fast when compared to phosphorescence, which is a spin-forbidden process (the order of nanoseconds as opposed to microseconds–seconds). When two half-integer spin materials are combined in an excited state, three triplet states are formed for every singlet state. Therefore the maximum quantum efficiency (QE) of fluorescence is 25 % as opposed to the 75 % for phosphorescence.[7,9,10,14,31,32] When a heavy metal atom like iridium is present the spin selection rule is relaxed allowing crossing from a singlet excited state to a triplet excited state, a process known as intersystem crossing (ISC). ISC increases the maximum QE of phosphorescence from 75 % to 100 %. Electrons and holes both have half-integer spin meaning OLED devices can form both singlet and triplet excited states to give either fluorescence or phosphorescence. The increased maximum QE of phosphorescence makes it more desirable than fluorescence, though phosphorescent blue emitter materials are difficult to synthesise with appropriate lifetimes so often a combination of fluorescent (blue) and phosphorescent (red and green) materials are used.[7,8,10,31]

1.2.2 Benefits and Limitations

OLEDs have a number of benefits when compared to current commercially available display screen technologies. Most display screens on the market today are constructed from LCs. Liquid crystal devices, like OLEDs, are made from a number of different layers[4] (figure 1.5). The light source in LC displays is a white backlight behind the screen; the rest of the layers comprise crossed polarising filters, electrodes and a liquid crystal layer. Each pixel is switched on or off on application of a voltage which shifts the orientation of the molecules within the liquid crystal layer. The shift in orientation of the molecules either prevents light from passing through the layer or allows it through. In the “on” state, light is able to pass through the LC layer, as the orientation of the molecules allows the rotation of the polarisation of plane

polarised light. Rotation allows light to pass through a polarising filter angled at 90° to the polarisation of the original light source and the pixel is lit up. In the "off" state no rotation occurs so light is not able to pass through the LC layer and the pixel remains dark.[4]

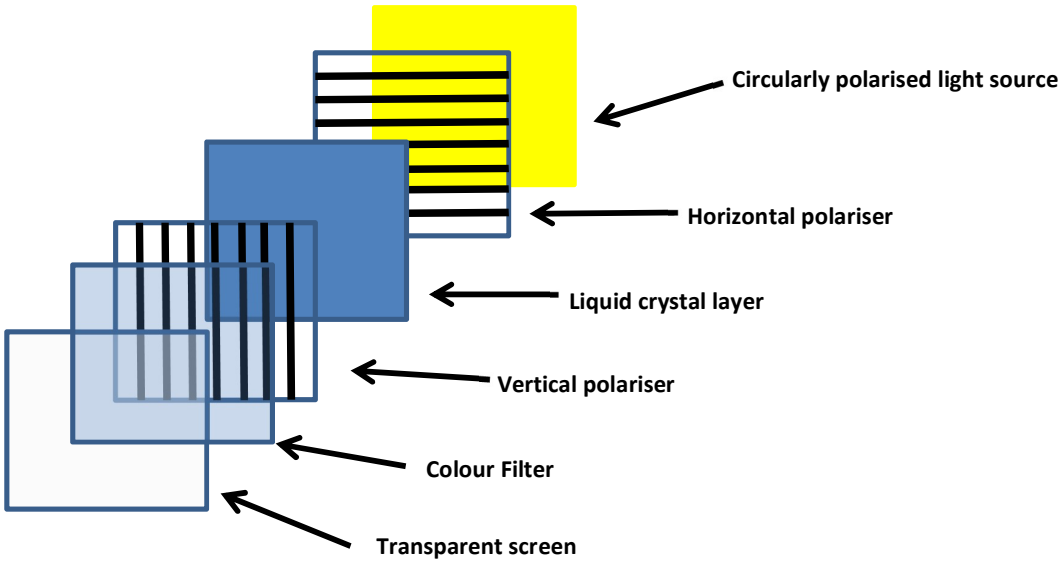

Figure 1.5: A schematic diagram showing the structure of a liquid crystal device.

LC devices use a single backlight which is always on, even when the pixels are not in use. In OLED devices by contrast, only the pixels which are in use are lit. Therefore the energy consumption in OLED devices is dependent on the image displayed on screen but in LCs the energy consumption is constant regardless of the image displayed. The energy efficiency of OLED devices therefore has the potential to be greater than that of LCs. The absence of a backlight in OLEDs also improves the contrast and resolution of screens and increases viewing angles. The requirement for a backlight in LCs means all layers above the light source, apart from the liquid crystals themselves, must be transparent in order for light to pass through. As the pixels themselves are emissive in OLED devices there is no need for all of the layers to be transparent and the range of uses for OLEDs compared to LCs is greatly increased. The low number of layers in OLED devices compared to LCs ensures they are relatively lightweight and low in bulk and are easier to transport. The relative lack of bulk in OLED devices also opens the possibility of manufacturing screens onto flexible substrates.[1,4–6,15]

Whilst OLED devices offer many benefits compared to the display screens currently available commercially, there are also limitations to their use. The light output of OLED devices decreases over time, a problem known as burn in. Areas of the screen lit more often than others fade more quickly to give light and dark patches across the device screen. Different lifetimes of the different emissive colours further enhance the problem of burn in. However compounds with long enough lifetimes for devices to be commercially viable are now

available. It is also possible to compensate for burn in using a variety of methods, including differing pixel sizes.[5,6,15]

The major problem with OLED devices when compared to LCs is the relatively high cost of fabrication. The technology behind the fabrication of LC devices is very advanced compared to the technology behind OLED devices and LCs are much cheaper to manufacture than OLEDs.[6,15]

1.2.3 Fabrication

There are two main factors which need to be considered when fabricating OLED devices: patterning of the pixels and deposition of the active materials. OLED devices consist of pixels of red, green and blue emitter materials. The pixels within devices must be well defined and the patterning must be distinct. As the active materials in OLED devices are emissive themselves they need to be deposited evenly both within and across pixels to prevent images on the screen from appearing patchy.

OLED devices currently available commercially are manufactured using vacuum evaporation.[1] In vacuum evaporation the materials are cooled and condensed onto the substrate (figure 1.6), patterning of the pixels is done using a shadow mask. A shadow mask is a thin layer of metal with the patterning of the pixels cut into it, which is placed over the substrate in the chamber. The active materials are deposited individually and the shadow mask is moved between each deposition. Vacuum evaporation gives devices a very even layer coating but it is not a very efficient process: a lot of the active material is deposited on the mask and walls of the chamber so material wastage is high. As each emitter material has to be deposited individually it is also a time consuming process.[2]

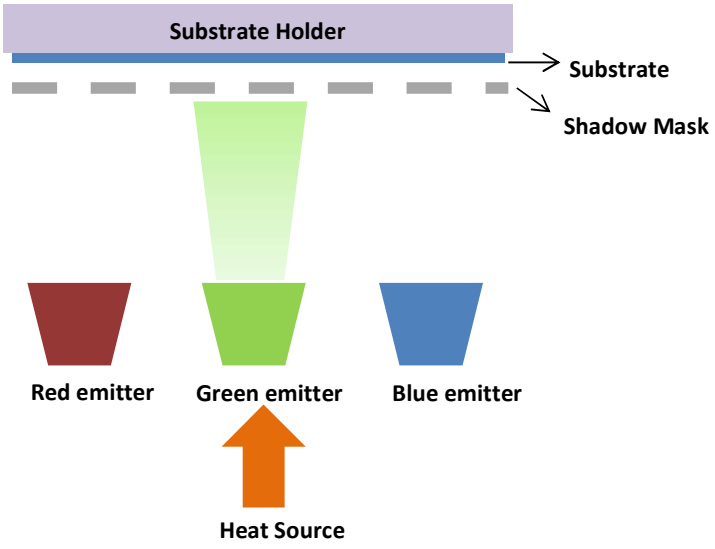

Figure 1.6: A schematic diagram showing the vacuum evaporation process.

Vacuum evaporation also presents problems due to the shadow mask. Using an external mask for the patterning of pixels limits the resolution of devices as the holes within the mask are limited to a certain size. At large areas the shadow masks also start to sag in the centre, reducing the accuracy of the patterning of the pixels. The problem of sagging in the centre of shadow masks makes scaling up to large device areas difficult. The problems associated with scaling up to large areas, limits on the resolution and the cost of vacuum evaporation could be addressed by using inkjet printing as a manufacturing method instead.

1.3 Inkjet Printing

Inkjet printers are well established in the printing of both text and graphics onto paper and other porous substrates. Alongside the well-established uses for inkjet printing, in recent years, a variety of new uses have been developed including the printing of three-dimensional parts, arrays of proteins and nucleic acids and printed electronics.[33–35] Inkjet printing is an attractive method for the production of OLED displays as deposition and patterning can happen at the same time and all emitter materials can be deposited together. The manufacturing of OLED devices using inkjet printing has the potential to be a fast, scalable and efficient process which could make OLED displays commercially viable and low-cost in comparison to LC displays.

Inkjet printing is a non-contact, material-conserving deposition technique which is used to deposit liquid-phase materials onto a substrate. A variety of different materials can be printed, usually in the form of a solid which is either dissolved or dispersed in a solvent. Inkjet printing allows a pre-determined quantity of material to be deposited to a high degree of precision and accuracy. Inkjet printing technologies were reviewed by Hoath *et.al* in 2016.[36] In general, a fixed quantity of ink is ejected from a chamber due to a sudden reduction in the chamber volume, the drop then falls to a substrate where it spreads and dries.

1.3.1 Types of Inkjet Printing

The term inkjet printing covers any technology which involves the digitally controlled ejection of fluid drops from a print-head onto a substrate. There are a number of ways in which ejection of the fluid can be controlled; most ways are covered by the headings continuous inkjet (CIJ) or drop on demand (DOD).[37,38] CIJ printing (figure 1.7a) is mainly used for coding and marking of products and packaging. In CIJ fluid is forced through the nozzle in the form of a jet which is then broken-up into droplets due to a perturbation caused by a vibrating piezoelectric crystal. The perturbation of the jet induces a Plateau- Rayleigh instability[39] and bulges and necks form as a result. Bulges have a lower curvature than the neck regions and so have a lower Laplace pressure; pressure-driven flow is therefore from the neck towards the bulges. Pinch off of the jet occurs once the neck radius reaches zero (figure 1.7b). After pinch-off, spherical droplets are formed in order to minimise the surface energy of the fluid. Control of the jet perturbation using a piezoelectric crystal forms droplets with a controlled size at a known frequency. Once formed, droplets pass through a set of electrodes that place a charge on each drop. The charged drops then pass a deflection plate (electrostatic field) which either deflects the drop towards either the substrate or the collection reservoir.

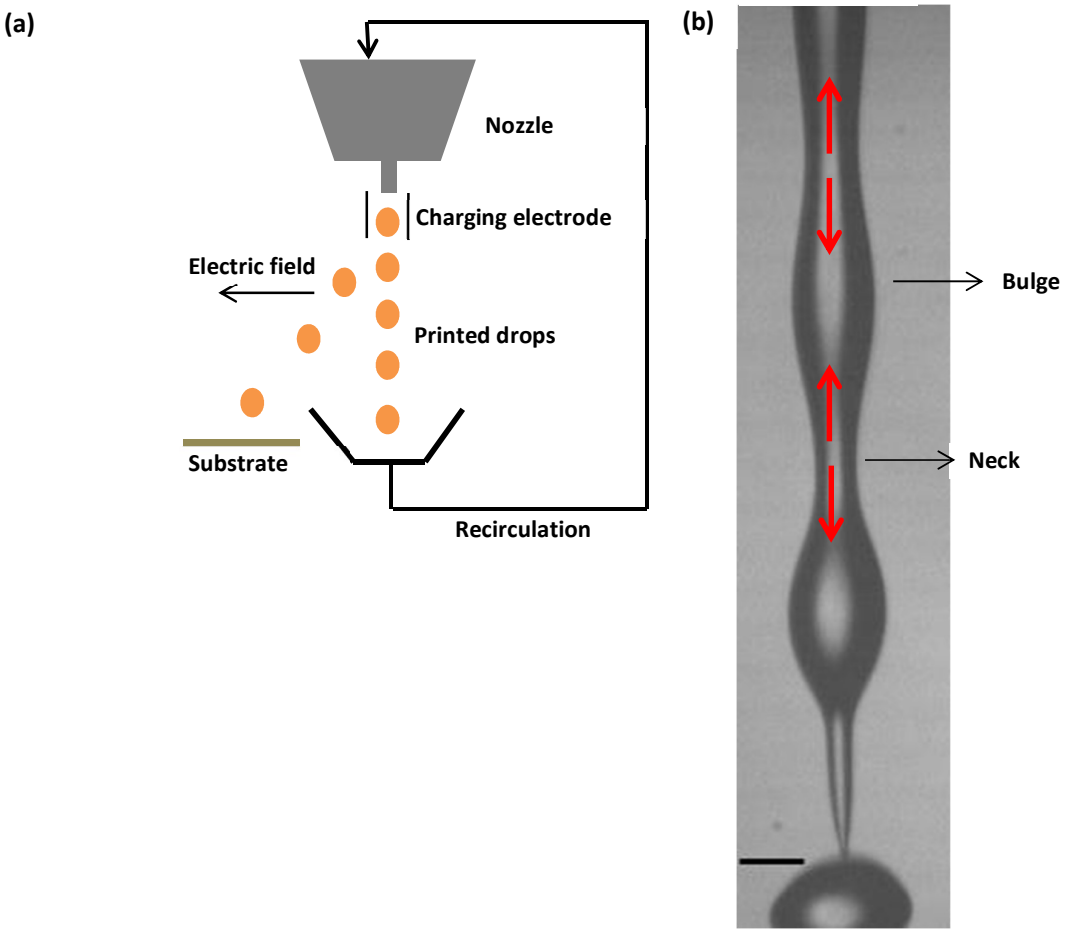

Figure 1.7: Schematic diagram showing the CIJ printing process (a) and an image of the presence of bulges and necks in the printed jet[40] (b) the red arrows show the direction of pressure driven flow.

The high ejection frequency of drops in CIJ gives high-speed printing and the high velocity of falling drops allows for relatively large distances between the print-head and the substrate. Typical drop sizes in CIJ are 40–70 µm with viscosities of approximately 1 mPa s. Printing frequencies are of the order of hundreds of kHz with printing speeds of up to 10 m s^{-1}. CIJ gives low print resolution compared to DOD, and the equipment requires a lot of maintenance due to high workloads. Inks for use in CIJ are limited as they must have the potential to be charged electrically.[36–38]

In drop on demand inkjet printing, drops are only ejected from the print-head when required. Drop formation is a result of a pressure pulse in the print-head. Typical drop sizes in DOD are between 10 and 100 µm with viscosities between 2 and 50 mPa s. Typical printing frequencies are of the order of tens of kHz with drop velocities of 5-8 m s^{-1}. There are two main subdivisions of DOD printing: thermal and piezo. Thermal inkjet printing (TIJ) is often used in commercial desktop printers, a resistive element is heated rapidly within the ink chamber to

temperatures as high as 400 ^{o}C. Heating causes a thin film of ink around the element to evaporate, giving a rapidly expanding bubble which forces a drop through the nozzle (figure 1.8). As the drop is ejected it leaves a void which is replaced with fluid from a reservoir in preparation for the next drop.[37,41,42] TIJ gives the potential for small drop sizes and high resolution. A higher nozzle density is possible compared to CIJ so devices are more compact and cheaper to produce. Limitations exist on the fluids used in TIJ; they must be vaporisable and capable of withstanding high temperatures.[36,37]

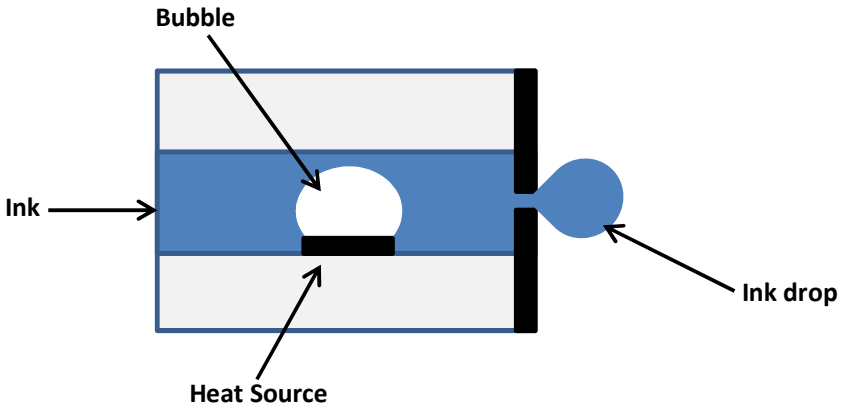

Figure 1.8: A schematic diagram showing the processes involved in thermal inkjet printing.

Piezoelectric (piezo) DOD printing is common in industrial inkjet applications. In such devices, a piezo crystal is distorted on application of an electric field, causing a pressure pulse in the chamber which forces a drop from the nozzle[37,38,43–45] (figure 1.9). Advantages of piezo DOD include the ability to print a wide range of fluids to a good degree of reliability and control. The print-heads used in piezo DOD printers do have a high cost however, limiting their application for low cost, home and office printers.[36–38]

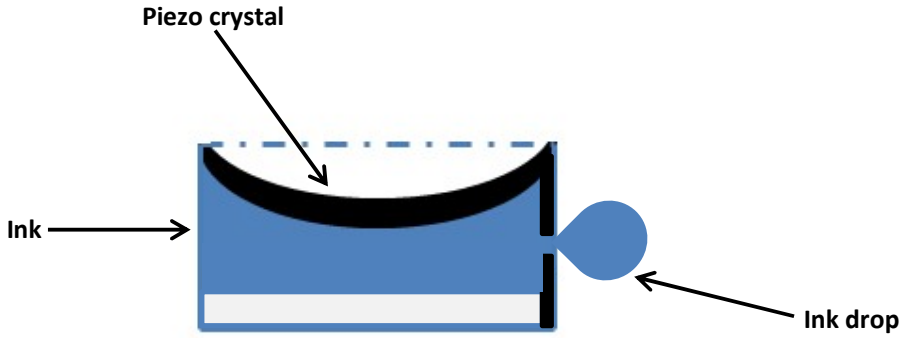

Figure 1.9: A schematic diagram showing the processes involved in piezoelectric DOD printing.

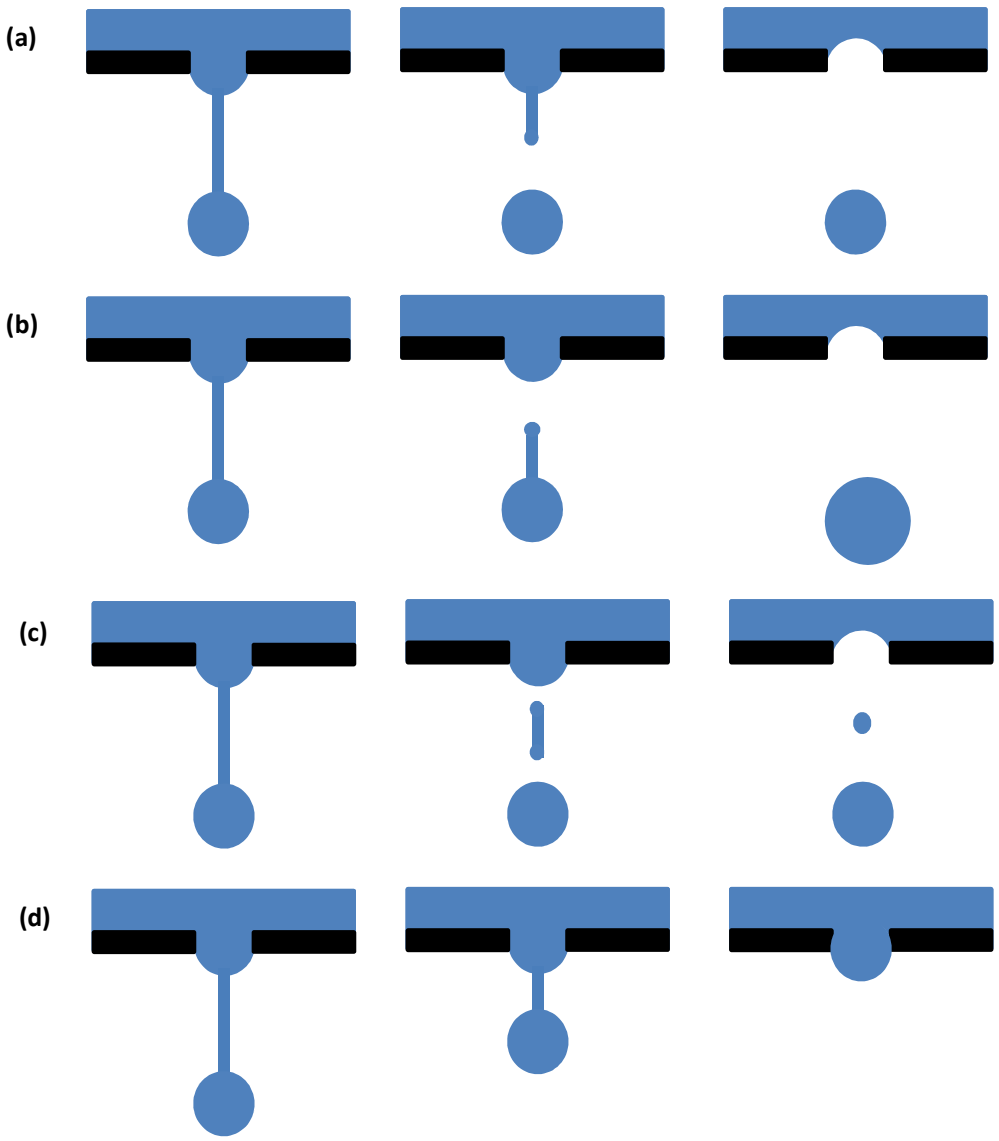

Figure 1.10: A schematic diagram showing the different drop break-off modes in DOD printing (a) shows ideal drop formation where pinch-off occurs at the droplet, (b) shows pinch-off at the top of the ligament, (c) shows satellite formation and (d) shows a misfiring droplet.

Once droplets formed in a DOD process have been actuated, their behaviour is similar regardless of how they were formed. [46,47] In all cases the fluid forms a droplet connected to the nozzle via a ligament, if the conditions are correct the ligament then pinches-off and retracts back into the nozzle to leave a spherical droplet. However if pinch-off occurs at the nozzle rather than the droplet the ligament joins the drop rather than retracting into the nozzle to give a droplet of a larger volume. It is also possible for the ligament to break off at both the nozzle and the droplet, or for it to break up into multiple fragments to give satellite droplets; satellite droplets are smaller, secondary drops. Satellites are undesirable in inkjet printing as they can degrade the quality of the printed product and can be deposited within the printer itself. Figure 1.10 shows the possible break-up regimes from DOD droplets. In

some cases the printed drop fails to break away from the ligament, if pinch off fails the droplet remains attached to the printing nozzle and may be pulled back into it. If a drop is pulled back into the nozzle it can cause the next drop to misfire (as well as the retracted drop) due to a disturbance of the meniscus.

1.3.2 Benefits and Limitations

There are a few common problems associated with inkjet-printed droplets: namely print failure, whereby no drop is ejected from the nozzle, and misdirected droplets whereby drops are not deposited in the correct place. The most common causes of print failure are misfiring[48,49] (due to retracted droplets,[47] air bubbles[50,51] or use of the wrong perturbation[52]), nozzle obstruction[53,54] and flooding of the nozzle plate.[55] One form of obstruction is clogging whereby a thin particulate film is formed across the nozzle. Clogging occurs when fluid is left at the nozzle for long enough periods that particles build up at the orifice. Clogging is less of a problem for CIJ than DOD printing as there is constant flow in CIJ. However both CIJ and DOD are susceptible to blockage due to particles larger than the orifice diameter or aggregations of particles.

Misdirection of printed drops usually occurs due to either satellites or tail-hooking.[47] Tail-hooking occurs when the drop ligament does not form in the centre of the orifice but to one side of it; as break off occurs the ligament then hooks to one side and prevents the droplet from falling straight. Misdirection of droplets can be problematic for DOD printed products which usually require high precision and print quality but is less of a problem for CIJ which is a high-throughput, lower quality technique.

The formulation of inks to be used in inkjet printing is a complicated process. The ink must last from when it is made up until the final deposit has been printed, so the lifetime of the ink needs to be considered. Inks consist of many different components aside from the solvents and pigments; surfactants and polymers are often used as wetting agents, dispersants or binders. The presence of many components can induce complicated flows in drying drops which have an impact on deposit morphology. The many components within an ink also affect the surface tension, viscosity and elasticity of the fluid, all of which must be carefully controlled for a fluid to be printable.[56,57]

There are a variety of other printing methods which could be used to manufacture OLEDs: flexographic printing, offset lithography and screen printing are some examples. Flexographic printing comprises a four-roller system whereby one of the rollers contains an engraved pattern. The engraved roller is covered in ink by another roller and the inked pattern is

transferred onto a third roller. The third roller comes into contact with the substrate and the ink is transferred on contact. Offset lithography is similar to flexographic printing though instead of an engraved roller the pattern is formed from hydrophobic areas, which are not wetted by the ink, and hydrophilic areas which are. The patterned roller is covered in ink by another roller and the pattern is then transferred onto the substrate on contact. Screen printing uses a screen of woven material glued to a frame under tension. The pattern is formed by coating areas of the screen with an emulsion that is impervious to the coating ink in areas of the screen where the image should not appear. The screen is then filled with the coating ink and brought close to the substrate where pressure is applied from one side to the other to transfer the image.

Despite its limitations, inkjet printing offers some benefits over other printing techniques, the main benefit being that it is a non-contact technique. There are also many other benefits relating to its flexibility and wide ranging applications. The range of fluids which can be deposited through inkjet printing is wide and as such it is accessible for numerous applications, many more than other printing methods, though the lower viscosity required of ink-jet printed drops does limit the solid content of the inks. Some examples of applications more accessible to inkjet printing than other printing techniques include: pharmaceutical compounds for use in dosing tablets, OLED materials, metallic nanoparticles for use in conducting wires, biological samples for high-throughput assays and ceramics for 3D printing and prototyping.[58–62] Alongside the wide range of inks available to inkjet printing, the lack of contact between print-head and substrate means the range of substrates which can be printed onto is equally wide ranging. All substrate types from rigid to flexible and flat to 3D are accessible to inkjet printing.

Alongside the wider range of fluids and substrates available to inkjet-printed products, there are other benefits associated with the technique. It allows layers of material to be built up using multiple passes of the print-head, reducing printing times and material wastage. Compared to lithographic methods inkjet printing is more efficient for short runs as no mask is required, though for longer runs the extra time spent preparing masters pays off for offset lithography and flexographic printing where the run speed is higher. Ink-jet inks are more expensive and more ink is required for the same colour density compared to other printing methods.

In most cases the desired deposit morphology from inkjet-printed drops is flat with a uniform distribution of particles and optical density. A pinned contact line during drying is also desired in order for deposits to have a well-defined, neat edge. The properties of the ink and substrate

need to be carefully controlled in order for the desired deposit morphology to be gained from inkjet-printed drops.

1.3.3 Inkjet Printing of OLEDs

In the inkjet printing of OLEDs, picolitre sized droplets containing active materials are deposited onto a pixelated substrate containing a series of wells surrounded by walls (figure 1.11). Typically the base of the wells are formed from glass topped with an indium tin oxide (ITO) film and the walls separating wells are made from a polymer resist material. Typical pixel dimensions are 60 × 180 µm for the well size with walls 1-2 µm high (figure 1.12).

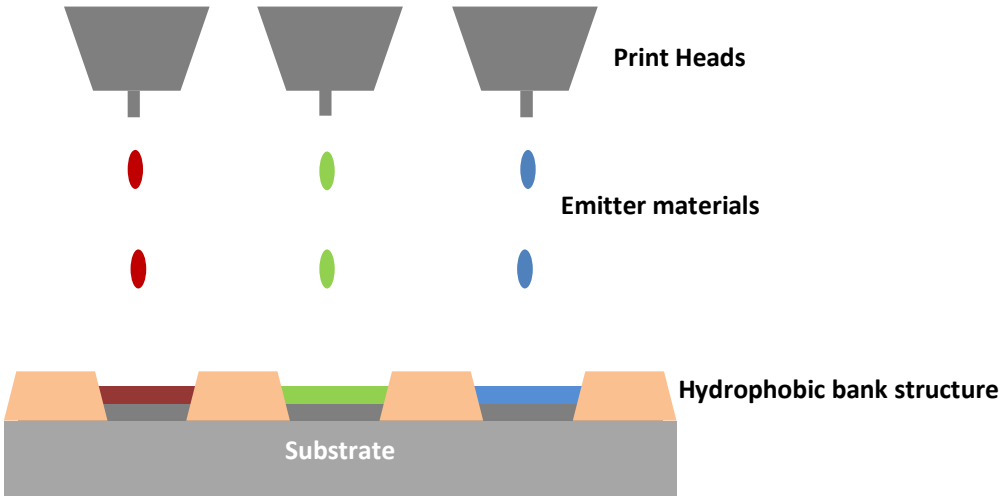

Figure 1.11: A schematic diagram showing inkjet printing as a fabrication method for OLED devices.

The inkjet printing of OLEDs was first reported in the literature in 1998 by Hebner et al,[63] who reported the successful fabrication of a polymer-based OLED display. The printed device had a large variation in drop height and diameter and a low efficiency compared to a spin-coated device made from the same materials. Early devices such as this suffered from poor reproducibility in the positioning of printed drops and uneven distribution of active materials in deposits.[35] As printing technology improved over subsequent years the accurate positioning of drops ceased to be a problem,[64,65] though even distribution of active materials was still lacking.

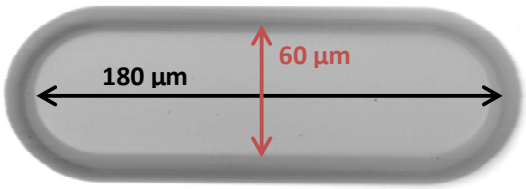

Figure 1.12: An image showing the typical pixel dimensions of a pixel for use in the inkjet printing of OLEDs.

Polymer-based OLEDs are generally easier to process in solution than small molecule OLEDs and have the advantage of being easier to tailor in terms of their surface tension and viscosity. Solutions of small molecules also have a tendency to de-wet from the substrate during drying to leave pin-holes in the dried film due to lower viscosities forming more unstable films than in the case of polymers. Pin-holes can be mitigated by controlling the chemical and physical properties of the substrate, as reported by Ding *et al.* in 2011.[66] Whilst it is now possible to produce pin-hole free devices, gaining even light output across devices is still problematic.[64,66–68] The problem of uneven active material distribution in deposits is common to both small-molecule and polymer-based OLED devices.

1.4 Deposition

As the drop reaches the substrate it deforms due to the resulting change in pressure; the level of deformation on impact depends on the kinetic energy of the drop and the angle at which it strikes the substrate.[36] The drop then spreads and dries on the substrate. Impact and spreading regimes of micrometre drops are characterised by the Reynolds and Weber numbers.[69] The Reynolds number, Re, is the ratio of inertial to viscous forces and is given by

$$Re = \frac{\rho_f v_d D_0}{\eta} \quad (1.1)$$

where ρ_f is the fluid density (kg m^{-3}), v_d is the drop velocity (m s^{-1}), D_0 is the drop diameter in flight (m) and η is the fluid viscosity (Pa s). The Weber number, We, is the ratio of inertial forces to the surface tension, σ, and is given by

$$We = \frac{\rho_f v_d^2 D_0}{\sigma} \quad (1.2).$$

Average impact speeds in DOD printing are > 5 m s^{-1}, [36] though for the systems considered in this thesis 1–2 m s^{-1} is more common. For the aromatic organic solvents discussed in this thesis, anisole has been identified as a typical representative. For anisole, ρ_f is 990 kg m^{-3}, η is 1.001 mPa s and σ is 34.96 mN m^{-1}. [70] Using an impact velocity of 2 m s^{-1} the Reynolds and Weber numbers for anisole are 99 and 6 respectively, for a drop diameter of 50 µm.

Another value important in identifying impact and spreading regimes of printed drops is the Ohnesorge number, Oh, which describes the ratio of viscous and inertial forces to surface tension effects. In the case of Oh there is no dependence on drop velocity, only the material properties and drop size are important. For anisole,

$$Oh = \frac{\sqrt{We}}{Re} \approx 0.02 \quad (1.3).$$

In order for a fluid to print without any satellites or splashing, the Ohnesorge number must fall between 0.1 and 1[57,71] and in order for the kinetic energy to dominate over surface tension forces (so detachment can occur) the Weber number must be greater than 4.[72] In the case of anisole above, kinetic forces dominate surface tension forces so detachment will occur. The Ohnesorge number for anisole does suggest some splashing or satellites may be present however. If $Re > 1$, as in the case of anisole, the drop has enough kinetic energy to dominate viscous forces within the drop and as such the ligament will detach during printing.[56] The Weber number also defines the level of deformation drops will undergo on impact; if $We < 12$ (as in the case of anisole), the drop will only undergo small deformations on impact. The reduced Weber number, We^*, explains why $We < 12$ is required for small deformations

(equation 1.4). The level of deformation then increases along with We.[56] The reduced Weber number is given by

$$We^* = \frac{We}{12} = \frac{E_{kin}}{E_{surf}} \qquad (1.4)$$

where $\frac{E_{kin}}{E_{surf}}$ is the ratio of kinetic energy on impact to surface energy of the drop. If $We^* > 1$ i.e. $We > 12$ then kinetic energy is dominant over surface energy on impact, and the drop will undergo large deformation.[56]

When a drop impacts the substrate its shape is altered from a spherical drop to a spherical cap, the drop then spreads giving a reduction in contact angle to its equilibrium value. In the case of small, viscous drops (where small implies the capillary length ,l_c, is smaller than the radius of the drop) the spreading of the contact radius, R_c, with time, t, for wetting fluids is given by Tanner's law[73]

$$R_c(t) \; \alpha \; t^N \qquad (1.5)$$

where $N = 0.1$ for small viscous drops. N is a constant and depends on the rate of energy dissipation near the contact line. The capillary length, l_c , is given by

$$l_c = \sqrt{\sigma / \rho_f g} \quad (1.6)$$

where g is acceleration under gravity. A sessile drop whose largest dimension is much smaller than l_c will take the shape of a spherical cap.

After impact and spreading of drops onto a substrate, the shape of the drop is determined by the balance of surface tension and gravitational forces. Surface tension acts to minimise the surface area of the drop, so tries to maintain a spherical cap shape, whereas gravity acts to flatten the drop shape. The Bond number, B_0, characterises the ratio of surface tension to gravitational effects

$$B_0 = \frac{\rho_f g R_c^2}{\sigma} \qquad (1.7).$$

For an anisole drop of diameter 200 µm as typical for this thesis, the Bond number is of the order 1×10^{-2}. Comparing equations 1.6 and 1.7 tells us that if $R_c \ll l_c$, gravity can be neglected. Gravity is not the only deforming influence on sessile drops however; viscous forces can also cause deformation. The relative importance of viscous and surface tension forces is characterised by the capillary number, Ca; approximately 6×10^{-7} for anisole,

assuming the internal flow velocity, u, is approximately 20×10^{-6} m s^{-1} as evidenced in chapter 3 of this thesis.

$$Ca = \frac{\eta u}{\sigma} \qquad (1.8)$$

The numbers for anisole suggest surface tension forces are dominant in determining the shape of sessile drops; as $B_0 \ll 1$ and $Ca \ll 1$. As such, sessile drops should take the shape of a spherical cap.[56,57] However the fluid properties are not the only factors which determine the shape of the drop on the substrate, the properties of the substrate also have an impact.

If the substrate is perfectly smooth and chemically homogeneous, the balance of surface tension forces is given by the Young-Laplace equation

$$\frac{\sigma_{sv} - \sigma_{sl}}{\sigma_{lv}} = \cos\theta \qquad (1.9)$$

where σ_{sv} is the solid-vapour interfacial tension, σ_{sl} is the solid-liquid interfacial tension, σ_{lv} is the liquid-vapour interfacial tension and θ is the equilibrium contact angle of the fluid on the substrate. The capillary pressure within the drop is then estimated by the Laplace pressure

$$p = \sigma\left(\frac{1}{r_1} + \frac{1}{r_2}\right) \qquad (1.10)$$

where r_1 and r_2 are the principal radii of curvature of the drop. The maximum Laplace pressure for the drops in the systems investigated in this thesis is approximately 10 Pa where the minimum radius of curvature is approximately 5×10^{-3} m.

In OLED systems the pixelated substrate is not perfectly smooth, as drops lie within wells surrounded by banks. As the bank material is different to that of the base, the substrates are also chemically inhomogeneous, equations 1.9 and 1.10 still hold however. If drops printed into wells pin at the bank tops the shape of the well will define the shape of the drops, the drop will still have constant mean curvature however as surface tension forces will still be dominant. The mean curvature across a drop surface, H_c, is given by

$$H_c = \frac{1}{2}\left(\frac{1}{r_1} + \frac{1}{r_2}\right) \qquad (1.11).$$

In the printing of OLED drops into wells, uneven particle distribution in final deposits is problematic. To improve light output across printed OLED devices, a number of groups began to tailor the wettability of the wells and walls of the pixels to control the shape of the drying drops, so controlling the structure of the final deposit.[66,67,74] Ely et al[74] used self-assembled monolayers (SAMs) and/or oxygen reactive plasma to control the wettability of polymer wells and identified three main scenarios, represented in figure 1.13. When the wettability of the

walls was much lower than that of the base of the wells, there was a build-up of material in the centre of the drop with very little at the edges (figure 1.13i). If the wettability of the walls was much higher than the base there was a large build-up of fluid at the edge of the wells with very little in the centre (figure 1.13iii). Finally when the wettability of the walls and base was approximately equal, the resulting drop was spread evenly across the pixel (figure 1.13ii). To give more even deposits from drops printed into wells the wettability of the walls and base must be roughly equal, usually requiring treatment of the substrate base before fabrication.

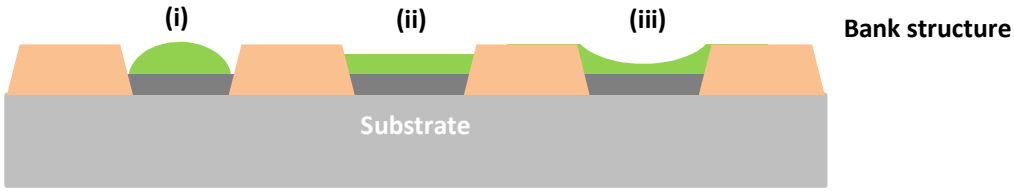

Figure 1.13: A schematic diagram showing how the wettability of the walls surrounding the drops impacts the shape of the drop within the wells (i) shows the case whereby the wettability of the walls is much lower than that of the base, (ii) the wettability of the walls and base are roughly equal and (iii) the wettability of the walls is greater than that of the base.

Tailoring the wettability of the walls and base of the wells to give drying as in figure 1.13ii improved uniformity in inkjet-printed OLEDs. However complete uniformity has still not been achieved, likely due to poorly understood evaporation of the drops.

1.5 Thermodynamics of fluids

The equilibrium vapour pressure of a fluid is the pressure exerted by the vapour on its surroundings. In the case of picolitre sized drops, like those considered in this thesis, the surface of the drop is usually in local equilibrium so the vapour pressure of the gas at the surface is equal to the equilibrium vapour pressure. A fluid with a high vapour pressure at standard temperature is often referred to as volatile whereas a fluid with a low vapour pressure at standard temperature is referred to as involatile. There is no defined cut-off vapour pressure at which a solvent becomes either volatile or involatile; usually the terms are used in relation to other systems being investigated.

The vapour pressure of a fluid depends on the temperature. For an ideal gas the change in vapour pressure with temperature for an ideal system obeys the Clausius-Clapeyron equation

$$ln\frac{p_2}{p_1} = \frac{-\Delta H}{R}\left(\frac{1}{T_2} - \frac{1}{T_1}\right) \quad (1.12)$$

where $p_1$and p_2 are the vapour pressures at temperatures T_1 and T_2 respectively, ΔH is the enthalpy of vapourisation and R is the ideal gas constant. The Clausius-Clapeyron equation shows that vapour pressures increase exponentially with temperature.

In the case of drops drying within wells, the fluid surface will be curved and this will lead to capillarity in the drying drop. The Kelvin equation (equation 1.13) tells us that the capillarity in the fluid surface will have an impact on the vapour pressure of the solvent

$$ln\left(\frac{p_v}{p_0}\right) = \frac{2\sigma V_m}{R_c RT} \quad (1.13)$$

where p_0 is the saturated vapour pressure of the solvent and V_m is the molar volume. Equation 1.13 tells us that the greater the curvature in a drop surface, the higher the vapour pressure and the more enhanced the evaporation of the solvent. Therefore in drops drying within wells the vapour pressure will increase as evaporation progresses and, in the late stages of drying, the vapour pressure will be higher at the edges of the wells than in the centre.

In binary mixtures in which the two solvents are chemically similar, the total vapour pressure of the system obeys Raoult's law

$$p_t = p_A + p_B = p_A^* x_A + p_B^* x_B \quad (1.14)$$

where p_t is the total vapour pressure of the system, p_A and p_B are the partial vapour pressures of components A and B, p_A^* and p_B^* are the vapour pressures of pure A and B and x_A and x_B are the mole fractions of A and B. Raoult's law assumes the mixture is ideal; meaning each

component within the mixture interacts with itself and the other component identically. In most real mixtures however the interactions are not identical and vapour pressures show deviations from Raoult's law (figure 1.14a). In cases where one component is dilute, the major component often follows Raoult's law and the dilute component follows Henry's law

$$p_B = H_B x_B \qquad (1.15)$$

where H_B is the Henry constant. Henry constants are determined experimentally and represent the slope of the tangent to the p_B curve as x_B tends to zero. A system in which the major component obeys Raoult's law and the dilute component obeys Henry's law is termed an ideal-dilute solution (figure 1.14b).

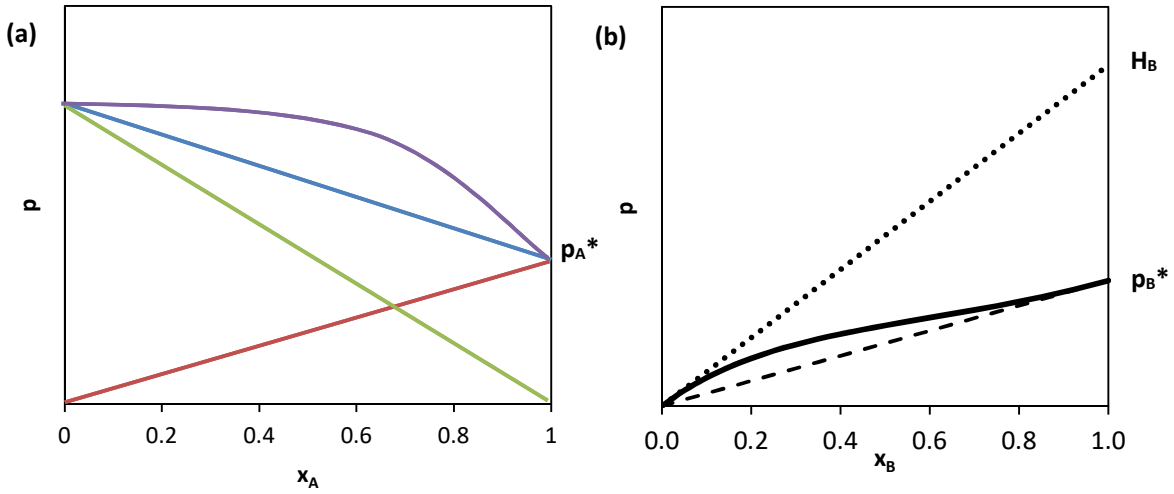

Figure 1.14: The variation of vapour pressure with mole fraction of A in an ideal mixture of A and B (a); the blue line shows the total vapour pressure of the ideal mixture, the red line shows the partial vapour pressure of A, green shows the partial vapour pressure of B and the purple line gives an example of non-ideal behaviour. The variation of vapour pressure with mole fraction of B in an ideal-dilute mixture (b).

In some cases, deviations from Raoult's law are significant enough that a minimum or maximum in the total vapour pressure of the system arises at a certain composition; such mixtures are termed azeotropes. If the deviation is positive, the mixture boiling point is lower than either of the pure solvents and if the deviation is negative the reverse is true. Deviations from ideal behaviour in a mixture are represented by the activity coefficient, γ, of each component

$$a_A = \gamma_A x_A = \frac{p_A}{p_A^*} \qquad (1.16)$$

where a_A is the activity of component A within the mixture and the vapour is assumed to be ideal. In an ideal solution, the activity coefficient is one. In all systems molecules aim to

minimise their chemical potential, μ. The chemical potential of a component within a mixture is given by

$$\mu_A = \mu_A^{\ominus} + RTln\, x_A + RTln\, \gamma_A \qquad (1.17)$$

where $\mu_A^{\ominus}$ is the chemical potential of component A in its standard state. The Margules equations describe the simplest non-ideal solution:

$$\ln \gamma_A = \beta x_B^2 \qquad \ln \gamma_B = \beta x_A^2 \qquad (1.18)$$

where β is an interaction parameter which measures the energy of same-species interactions with respect to cross-species interactions. If the mixture is ideal, β = 0. In mixtures which do not phase separate (those considered in this thesis), $\beta < 2RT$. When $\beta > 0$, homo-nuclear interactions are preferred over hetero-nuclear interactions. As most mixtures considered within this thesis contain one polar and one non-polar solvent, homo-nuclear interactions will always be favoured over hetero-nuclear interactions and as such $0 < \beta < 2RT$. Combining equations 1.17 and 1.18 gives us

$$\mu_A = \mu_A^{\ominus} + RTln\, x_A + \beta x_B^2 \qquad (1.19)$$

$$\mu_B = \mu_B^{\ominus} + RTln\, x_B + \beta x_A^2 \qquad (1.20).$$

Combining equations 1.16 and 1.19 then tells us

$$p_A = p_A^* x_A \exp\left(\frac{\beta x_B^2}{RT}\right) \qquad (1.21).$$

Equation 1.20 shows that in the case where $\beta > 0$, the vapour pressure is enhanced versus the ideal case. Therefore, for the mixtures considered in this thesis, vapour pressures of the solvents will be enhanced versus the ideal case.

1.5.1 Hansen Solubility Parameters

Hansen Solubility Parameters (HSPs) were developed by Charles Hansen and are a way of predicting the solubility of one material in another. The core assumption of the program Hansen Solubility Parameters in Practice (HSPiP) is that "like dissolves like", specifically that a solute is more soluble in a solvent if their intermolecular forces are similar. Each molecule in the program is defined by three solubility parameters: *δD*, *δP* and *δH*. *δD* is a measure of dispersion forces, *δP* a measure of polar forces and *δH* is a measure of hydrogen bonding interactions. The units of each solubility parameter are $MPa^{0.5}$.

The HSPs are calculated using the cohesive energy density, E_c/V, of a molecule

$$\frac{E_c}{V} = \frac{E_D}{V} + \frac{E_P}{V} + \frac{E_H}{V} \qquad (1.22)$$

where V is the molar volume of the solvent, E_D, E_P and E_H are the dispersive, polar and H-bonding contributions to the cohesive energy respectively and $\delta^2 = {}^{E}/_{V}$.

Once they have been calculated, *δD*, *δP* and *δH* are used as co-ordinates in 'Hansen space' and the closer molecules are in this space, the more likely they are to dissolve one another. The distance between two molecules in Hansen space, Ra, is given by

$$Ra^2 = 4(\delta D_2 - \delta D_1)^2 + (\delta P_2 - \delta P_1)^2 + (\delta H_2 - \delta H_1)^2 \qquad (1.23).$$

Measurement on "good" and "bad" solvents can then be used to define a sphere of radius R_0 which encompasses all of the "good" solvents. The relative energy difference, RED, can then be used to tell you where you are in solubility space

$$RED = Ra/R_0 \qquad (1.24).$$

HSPs can be used to predict more than the solubility of a solute in a solvent as the solubility parameters and RED provide some measure of the ideality of a mixture. As HSPs are defined by energies they can be used to calculate activity coefficients and Antoine constants for solvent mixtures, these can then be used to predict vapour-liquid equilibria (VLE) data for solvent mixtures. The Antoine constants are described by the Antoine equation which is a semi-empirical equation describing the relationship between vapour pressure and temperature for pure solvents

$$\log p_v = A - \frac{B}{T+C} \qquad (1.25)$$

where p_v is the vapour pressure, T is temperature and A, B and C are the Antoine constants. VLE data provides a measure of the ideality of the mixture and whether evaporation is enhanced or depressed compared to the ideal case.

1.6 Evaporation

Understanding evaporative processes in drying drops is important for a number of industrial applications including spray painting and crop spraying, along with numerous inkjet printing applications. A complete description of evaporative processes can involve a number of different considerations; the most important aspects in the inkjet printing of OLED materials are the deposit morphology and active material distribution. Deposition is usually controlled by the position and movement of the contact line during drying alongside internal flows. If evaporative processes are understood improvements can be made industrially, as such many investigations into drop evaporation have been carried out in recent years.[22–24,75–79]

1.6.1 Evaporation of Single Solvents

As previously described, inkjet-printed drops can be modelled as spherical caps and, whilst OLED materials printed into wells may be distorted by the well shape, in the case of circular and square wells they can still be assumed to have constant mean curvature across the drop surface. In the case of oval wells the two principal radii of curvature will be quite different, even at the apex, and as such the drop shape will deviate from having constant mean curvature, though the shape will still be determined by surface tension. The low capillary numbers associated with the solvents discussed in this thesis ensure the pressure required to drive internal flow is small compared to the Laplace pressure and in the early stages of drying the surface tension dominates drop shape, giving constant mean curvature across the drop surface. In the later stages of drying however the drop shape is no longer dominated by surface tension and there is no longer constant mean curvature across the drop surface.

Evaporation is an endothermic process and as such requires energy from the surroundings to take place. Molecules must have enough energy to overcome the barrier and transfer into the vapour phase. Molecules with a higher thermal energy are more likely to be transferred to the vapour phase and as such the droplet surface cools during evaporation, a process known as evaporative cooling.[80,81] In order for more liquid molecules to then be transferred into the vapour phase, heat transfer to the liquid-vapour interface is required. The rate of evaporation in drops has three main limiting factors: movement of vapour away from the interface, transfer of molecules across the interface and transfer of heat to the interface.[76,78] In the macroscale under ambient pressure, the movement of vapour away from the interface is normally the rate limiting factor in evaporation.

Transport of vapour away from the interface can either happen by diffusion[19,82] or ballistically.[83] For diffusion to occur there must be a concentration gradient in the vapour phase. If a droplet is in an atmosphere saturated with its own vapour there is no concentration gradient and so no evaporative flux. Macroscale drops evaporating under ambient pressure at standard temperature are evaporating in the diffusive regime. As a drop evaporates, the position of the liquid-vapour interface changes over time and the vapour concentration surrounding the drop also has a time dependence determined by

$$\frac{dc}{dt} = D\nabla^2 c \qquad (1.26)$$

where c is the vapour concentration and D is the diffusion coefficient of the vapour in the ambient atmosphere. If the movement of the liquid-vapour interface is slow compared to diffusion of the vapour, as in the case of the drops discussed in this thesis, the time dependent terms in equation 1.26 can be ignored and the vapour concentration profile is given by the Laplace equation

$$\nabla^2 c = 0 \qquad (1.27).$$

In this thesis only quasi-steady, diffusion-limited evaporation is considered where the vapour close to the drop is saturated and in equilibrium with the liquid. Far from the drop surface the vapour is at ambient concentration.

Ballistic evaporation occurs when the vapour molecules travel many times the size of the droplet before collisions occur, as such the likelihood of molecules re-entering the liquid phase is negligible. Ballistic movement of molecules away from the liquid-vapour interface on the macroscale requires reduced pressures. The presence of ballistic evaporation is identified when the Knudsen number, Kn, is greater than one

$$Kn = \frac{\lambda_p}{R_c} \qquad (1.28)$$

where λ_p is the mean free path of the vapour.

For drops drying in the diffusive regime, evaporation is enhanced near to the contact line relative to the apex when the contact angle is less than 90°.[18,84] Figure 1.15 shows an evaporating drop with diffusive transport of vapour normal to the interface. If θ = 90° each segment in figure 1.15a would be the same area and evaporation across the drop surface would be uniform. When θ < 90° the region near the contact line (7 in figure 1.15a) does not intersect the liquid-vapour interface and as such vapour diffuses into this region from the region adjacent to it (6). As diffusion is enhanced in region 6 the concentration gradient in this

region increases and evaporation from region 6 is enhanced. Diffusion from region 5 into region 6 goes some way to replenish the vapour lost to region 7 and so on; giving the highest evaporation rate at the contact line, decreasing towards the apex of the drop (figure 1.15b).

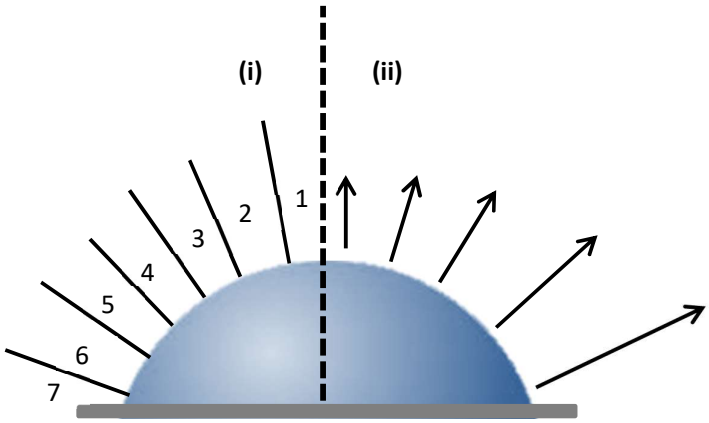

Figure 1.15: A schematic diagram showing the diffusive transport of vapour away from a sessile drop normal to the interface (i) and the resulting evaporative flux (ii) around a droplet with a contact angle less than 90°.

Whilst most of the evaporating drops discussed in this thesis are imaged in the diffusive regime; industrially, inkjet-printed OLEDs are dried in a vacuum chamber. As such it is possible OLED devices are drying in the ballistic regime rather than the diffusive regime, though this will depend on the pressure within the vacuum chamber and the profile used to pump the pressure down. λ_p is approximately 10^{-8} m at 1 bar and, for the drops considered in this thesis, R_c is approximately 10^{-4} m. Therefore in order for $Kn > 1$ we require $p < 10^{-4}$ bar to be drying in the ballistic regime. Whilst drops drying in the diffusive regime may not be directly applicable to industrial systems, understanding the processes behind drying in the diffusive regime will still provide information relevant to the ballistic regime. Some data from vacuum dried OLED devices is considered and compared to devices dried in the diffusive regime.

In the case of contact line motion in an evaporating drop on a flat surface, there are two limiting modes of evaporation, constant contact angle and constant contact area.[85] In the constant contact angle mode the contact line of the drop recedes during drying and the contact angle remains constant, whereas in the constant contact area mode the contact line remains pinned during drying and the contact angle reduces (figure 1.16). An intermediate stick-slip mode exists whereby the contact line recedes intermittently.[77] Drops which dry in the constant contact area mode often move into the constant contact angle mode once the

receding contact angle of the fluid is reached. In drops drying with a pinned contact line (constant contact area), the domination of surface tension over gravitational effects causes radial flows from the apex of the drop towards the contact line[85–87] (where evaporation is enhanced) to maintain the constant mean curvature of the drop surface (figure 1.17). In drops with a moving contact line (constant contact angle), flows are not solely radially outwards towards the contact line as an additional inward component complicates the flow profiles.[88]

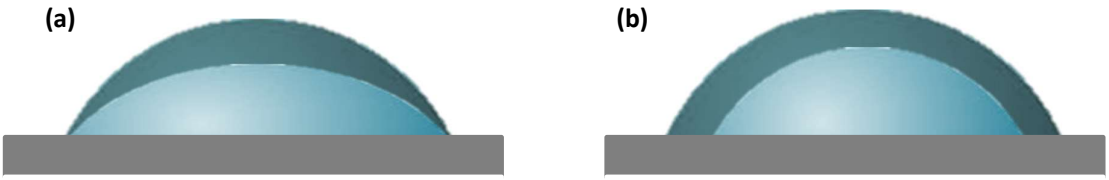

Figure 1.16: A schematic diagram showing the evaporative modes in a drying drop: (a) constant contact area mode and (b) constant contact angle mode. The dark green area shows the drop at the beginning of evaporation and the light green area shows the drop after time has passed.

.

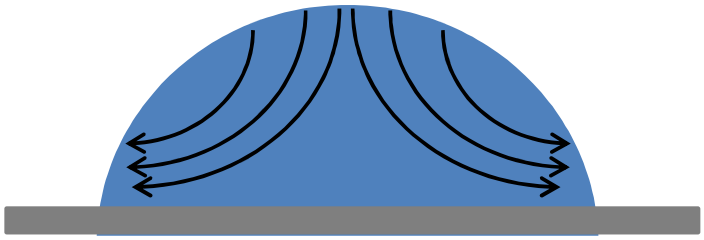

Figure 1.17: A schematic diagram showing the radial flows present when drops dry with a pinned contact line.

The thermal properties of the substrate can also have a significant impact on the evaporation rate in drying drops;[22,81,89,90] good thermal conductors maintain a constant substrate temperature and heat transfer within the drop determines evaporative cooling. In poor thermal conductors heat transfer in the substrate is also important and the substrate temperature in contact with the liquid falls, leading to lower temperatures of the liquid and slower evaporation. On substrates where the thermal properties change across the surface, different effects can be induced in drying drops.

1.6.2 Evaporation of Mixed Solvents

The introduction of co-solvents to form binary solvent mixtures can have a significant impact on evaporation when compared to single solvents.[24,91–95] In mixtures where the two components have significantly different volatilities, early evaporation rates tend to match those of the more volatile component and later evaporation rates match those of the less volatile component, as observed by Sefiane et al.[91] In cases where the contact line moves during drying, the contact angle of the drop can change as the relative proportions of the two solvents change. The diffusion coefficients, D, of components, and the vapour pressures are both important in determining the relative evaporation rates of the components in a mixture. In mixtures of components which have different surface tensions as well as volatilities, Marangoni flows can be induced.

Marangoni flows arise due to an imbalance of surface tension forces at the liquid-vapour interface and were first explained in the literature in 1855.[96] In the case of sessile droplets, the presence of surface tension gradients causes Marangoni recirculation cells to form within the drops (figure 1.18).[25,97] Areas of high surface tension pull more on the surrounding fluid than areas of low surface tension, leading to tangential stresses across the drop surface. Flows then occur from areas of low to high surface tension to balance the tangential stress:

$$\frac{d\sigma}{dx} = -\eta \frac{du}{dn} \qquad (1.29)$$

where x is the tangential co-ordinate, n is the normal co-ordinate and u is the tangential component of the fluid velocity at the liquid-vapour interface.

The Marangoni number, Ma, can be used to determine whether Marangoni flows will dominate particle transport during drying. Ma gives the ratio of surface tension to viscous forces

$$Ma = \frac{\Delta\sigma h}{u_{cap}\eta R_c} \qquad (1.30)$$

where u_{cap} is the fluid velocity due to capillary flows and h is the drop height. If $Ma \gg 1$, surface tension gradients across the drop surface will cause spontaneous, surface-tension-driven flows that compete with or dominate capillary flows. Marangoni flows can occur in both single solvent systems and systems with multiple solvents.

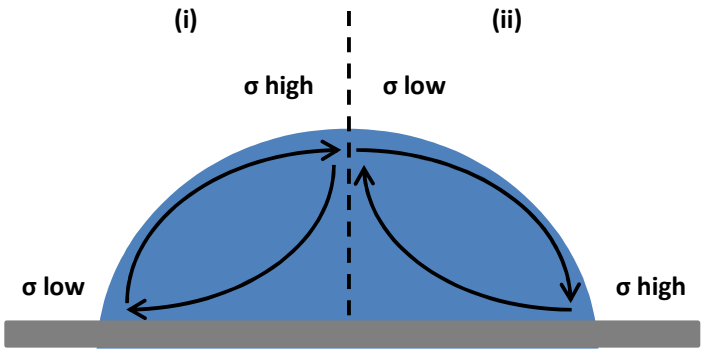

Figure 1.18: A schematic diagram showing the recirculatory flows present within drying drops on flat substrates due to the presence of Marangoni stresses across the drop surface. (i) shows the case of a higher surface tension at the apex than the contact line and (ii) shows a higher surface tension at the contact line than at the apex.

In the case of binary solvent mixtures, solutal Marangoni flows can arise due to compositional gradients along the liquid-vapour interface. Preferential evaporation of the more volatile component within a mixture, combined with enhanced evaporation at the contact line, causes a depletion of the more volatile component at the contact line relative to the apex. In the case where the more volatile component has a lower surface tension than the less volatile component, the contact line has a higher surface tension than the apex and Marangoni flows along the liquid-vapour interface are from the apex towards the contact line (figure 1.18ii). If the more volatile component has a higher surface tension than the less volatile component, surface tension gradients and Marangoni flows along the liquid-vapour interface are from the contact line towards the apex of the drop (figure 1.18i). The presence of surfactants or non-adsorbing solutes in a drying drop can also cause solutal Marangoni flows in either direction;[24,92,98–100] depending on whether materials increase or reduce the surface tension of the fluid.

1.6.3 Thermal Effects during Drying

Thermal Marangoni flows can arise due to temperature gradients within drying drops, as modelled by Hu and Larson in 2005[101] and backed up experimentally by Ristenpart et al in 2007.[102] Enhanced evaporation at the contact line of a drop causes more evaporative cooling at the contact line than at the apex, giving a temperature gradient across the drop surface. As a reduction in temperature increases the surface tension of a liquid, thermal gradients induce surface tension gradients across the liquid-vapour interface. As such thermal gradients can induce Marangoni flows. If heat transfer within the liquid is fast enough however, evaporative cooling can be negated.

The thermal conductivity of the substrate can have an impact on the relative direction of thermal gradients within drying drops.[102] If the thermal conductivity, κ, of the substrate is above a critical value (κ > 2 W m^{-1} K^{-1}), energy transfer to the droplet makes it warmest at the contact line and coldest at the apex, due to the relative length of conduction pathways. If the thermal conductivity of the substrate is low (κ < 1.45 W m^{-1} K^{-1}), heat transfer to the drop is poor and evaporative cooling causes the contact line of the drop to be cold relative to the apex.[103] The direction of thermal gradients across the drop surface determines the direction of surface tension gradients and resulting Marangoni flows.

When the thermal conductivity of the substrate takes an intermediate value (1.45 < κ < 2), the contact angle of the fluid on the substrate becomes important in determining the relative direction of thermal gradients in a drop. Some industrial applications include the heating or cooling of the substrate; which can also induce thermal gradients.[104,105] When the substrate is heated, transfer of heat to the drop causes a warmer contact line and a cooler apex, resulting in thermal gradients.

1.6.4 OLED Systems

The patterning of the substrates used in the printing of OLED devices will affect the mode of evaporation. Pixelated OLED devices are designed so drops evaporate in the constant contact area mode with a changing contact angle. The presence of banks causes pinning of drops at the bank tops in the early stages of drying, the angle of the bank and receding contact angle of the fluid then determine what happens later in the drying. The drop will remain pinned at the top of the banks until the receding contact of the fluid on the bank material is reached, at which point the fluid will recede down the banks.

It is not clear how the presence of surface tension gradients will affect flow profiles of drops drying within wells as the shape of the walls distorts the drop shape from a spherical cap. Re-circulatory flows may still occur but the drying of drops within wells has not yet been extensively investigated in the literature. The materials used for the patterning of OLED pixels complicate heat transfer. The base of the wells is made of glass topped with an ITO film whereas the walls are made from a polymer resist. The thermal conductivity of the glass/ITO base is higher than that of the polymer walls.

1.7 Deposit Formation

The presence of internal flows within drying drops causes material transport in the presence of a solute or other material dispersed throughout the solvent. Transport mechanisms during drying are the determining factor in deposit morphology. Most industrial processes require even material distribution across a deposit and as such transport mechanisms within drying drops need to be manipulated and controlled for industrial applications. Internal flows within drying drops generally depend on contact line motion, evaporative flux across the droplet and motion of the liquid-vapour interface. Though the main cases discussed in this thesis are evaporation driven radial flow and Marangoni flow.

1.7.1 The Coffee-Ring Effect

Ring stains are a well-known phenomenon in the evaporation of droplets containing either a solute or dispersion. Transport of solutes towards the contact line in an evaporating drop causes precipitation at the contact line as the concentration exceeds the saturation point of the solution.[106,107] Ring stains were first explained by Deegan et al in 1997[19] who also coined the phrase 'coffee-ring effect' as the phenomenon is evident when coffee dries on a flat surface (figure 1.19). Time-resolved microscopy experiments have shown internal radial flows within evaporating drops towards the contact line for a variety of solvents and substrates, causing a ring of concentrated deposit.[18,19,98,108–112]

Figure 1.19: An image showing the ring stain left behind when coffee dries on a flat surface.

For ring stains to form the contact line of the drop must be pinned. Strong attractive interactions between the solvent and the substrate mean the numerator in the Young-Laplace equation (equation 1.9) is large and the receding contact angle is small or zero. Contact angles on a substrate often depend on whether the drop is advancing or receding across the

substrate and the difference between contact angles is referred to as the contact angle hysteresis (CAH)[113] given by

$$CAH = \cos\theta_r - \cos\theta_a \qquad (1.31)$$

where θ_r is the receding contact angle and θ_a is the advancing contact angle. Higher values of CAH make it more likely the receding contact angle is zero and so more likely the contact line remains pinned. Strong attractive interactions between the solvent and the substrate therefore increase the likelihood of contact line pinning and hence ring stains.[114–116]

Coffee-rings do not form below a characteristic length[117] which corresponds to a critical droplet diameter. This characteristic length depends on the rate of evaporation of the drop relative to the speed of diffusive transport of the particles. Drops with a diameter below a critical point, usually on the nanoscale, do not show ring staining as particles collecting at the contact line are able to diffuse back to the centre on the timescale at which the drop evaporates; providing convective flow within the drop can be overcome.

The Peclet number, Pe, provides a measure of whether or not diffusion of a material will even out compositional gradients during the drying time of a drop and a measure of the critical length below which ring stains will not form

$$Pe = \frac{uL}{D} \qquad (1.32)$$

where L is the length scale associated with the drop. For a droplet drying in an OLED pixel, in the vertical direction $L \sim 1.5 \times 10^{-6}$ m and internal flow velocities are of the order of 20×10^{-6} m s^{-1} (as evidenced in chapter 3). Assuming Ir(ppy)$_3$ (figure 1.20) represents a typical emitter material and takes the shape of a sphere, the radius can be calculated to be 6×10^{-10} m assuming a density of 0.9 g cm^{-3}. The diffusion coefficient of a molecule is then given by

$$D = \frac{k_B T}{6\pi a} \approx 4 \times 10^{-10} \text{ m}^2 \text{ s}^{-1} \qquad (1.33)$$

where k_B is the Boltzmann constant (1.38×10^{-23} J K^{-1}), T is temperature (298 K), a is the particle radius ($\sim 6 \times 10^{-10}$ m) and η is the fluid viscosity ($\sim$1 mPa s). In the case of Ir(ppy)$_3$ $Pe \sim 0.08$ and as such diffusion averages concentration in the vertical direction quickly. Diffusion time, t_{diff}, is given by

$$t_{diff} = Pe\,\frac{L}{u} \approx 6 \times 10^{-3} \text{ s} \qquad (1.34).$$

In the horizontal direction, $L \sim 1 \times 10^{-4}$ m and as such $Pe \sim 5$ and $t_{diff} \approx 25$ s. The averaging of concentration in the horizontal direction will therefore depend on the drying time of the drop.

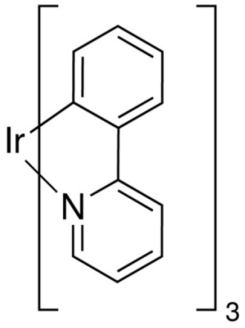

Figure 1.20: The structure of $Ir(ppy)_3$ identified as a typical emitter material.

As previously discussed, the banks in pixelated OLED substrates are designed to pin the fluid and therefore ring stains are likely.

1.7.2 Mitigation of Ring Stains

There are two main conditions which must be met in order for the coffee-ring effect to occur, pinning of the contact line and enhanced evaporation from the contact line. If the contact line of the drop is not pinned, fluid at the contact line does not need to be replaced in order to maintain a spherical cap. Therefore the flows inside an evaporating drop with a receding contact line are not solely radially outwards and ring stains do not necessarily form.[88] Prevention of contact line pinning can be achieved through electrowetting where the application of an alternating voltage to the drop to cause oscillation of the contact line.[118,119] Electrowetting can be a difficult technique to use on an industrial scale however.

Alternatively, reducing the evaporative flux of a drop at the contact line can change internal flows within an evaporating drop. One example of reducing evaporation at the contact line is to dry drops in a closed environment with a hole above the drop to increase evaporation rates at the apex relative to the contact line. Reducing evaporation rates at the contact line leads to less distinctive coffee rings or even a central deposit.[18,120,121]

Surface tension gradients along the liquid-vapour interface can also be used to mitigate ring staining.[24,25,93,97,122] The introduction of surface tension gradients and resulting recirculatory flows does not require the contact line to be mobile or the evaporative flux to be reduced at the contact line. In some cases it actually requires evaporative flux at the contact line to be enhanced relative to the apex, as discussed in section 1.6. However if Marangoni flows end

during evaporation, or if capillary flows become dominant over Marangoni driven flows, radial flows will transport particles to the contact line and a ring stain will reform.

In the case of OLED devices, the pinning of the contact line around the wall tops is necessary for defined pixel patterning so cannot be prevented. It is possible the relative evaporative flux across the drop surface can be manipulated in OLED systems and it is also possible that surface tension gradients could be used to mitigate ring staining.

2. Experimental Method

2.1 The Experimental Setup

This section describes the experimental set-ups used for the high speed imaging of droplet drying. Printed solutions were ejected from a piezo-electric single-nozzle print head (Microfab, MJ-ABP-01) with an orifice diameter of 50 µm, to give sub-nanolitre sized droplets. The nozzle was resistant to both aqueous and organic solvent-based fluids at temperatures up to 50 °C. The print head was connected to a fluid reservoir which was pressurised using a syringe such that the meniscus of the fluid was pushed to the tip of the orifice without pushing the fluid through. For most solutions (due to low surface tensions) a slight negative pressure was required to hold the fluid in the nozzle and prevent any dripping. To prevent any leaks PTFE tape was used to seal the vials holding solutions. Any bubbles present in the nozzle or tubing prevented jetting and so had to be eliminated. The print head was actuated with a symmetrical bipolar waveform (figure 2.1) to give drop-on-demand printing and a single drop per pulse. An electronic pulse was sent to the piezoelectric device contained within the print head; controlled using a Microfab driver unit (Microfab JetDrive III Controller CT-M3-02). The voltage of the pulse was varied according to factors such as the viscosity and surface tension of the fluid to give a single drop per pulse with no satellites. The typical voltage range used was 12-30 V and typical separation between the nozzle and substrate was 2-3 mm. The substrate was held on a motorised stage (Laser2000, T-XYZ-LS13) with a travel range of 13 mm to an accuracy of ± 15 microns. The stage was moved after each measurement in order to give a clean section of substrate to be printed on. The use of a motorised stage also allowed arrays of drops to be printed for later analysis of the deposits. Before each measurement, a small number of drops were ejected from the nozzle in order to replenish the fluid at the orifice.

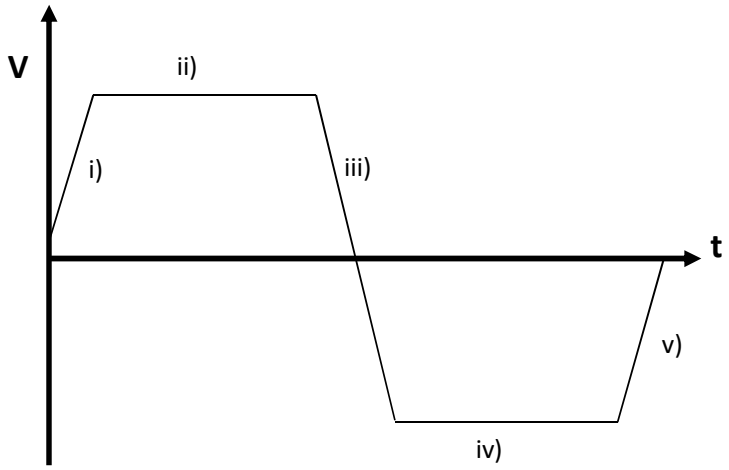

Figure 2.1: An example waveform used to actuate the nozzle for drop emission. Typical time periods for all solvents were (i) a rise time of 10 μs, (ii) a dwell time of 100 μs, (iii) a fall time of 20 μs, (iv) an echo time of 100 μs and (v) another rise time of 10 μs

All imaging of droplet drying was done on an inverted microscope, as shown in figure 2.2. The inverted microscope allowed imaging of internal flows along with the imaging of interferometric profiles of the drying drops. Both setups had the same basic optical arrangement but differed in their illumination.

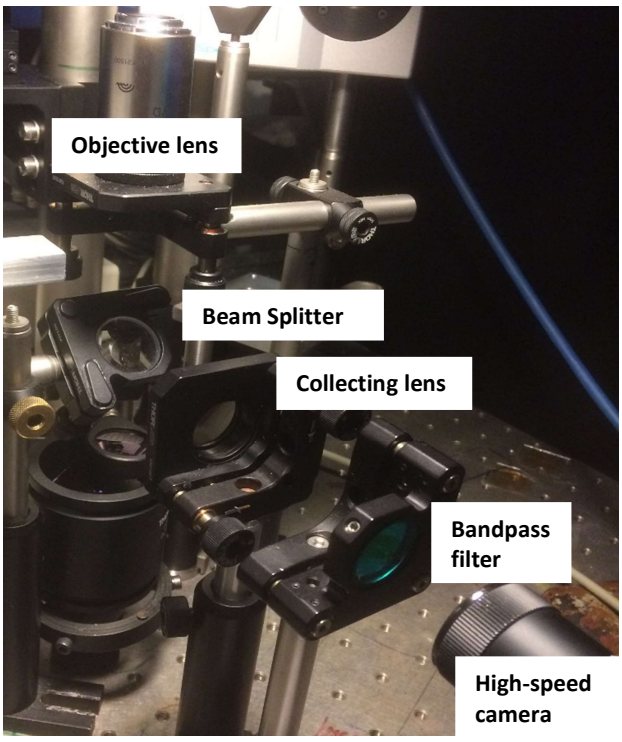

Figure 2.2: A labelled image of the experimental rig; illumination sources, the substrate and the nozzle are excluded for clarity.

The inverted microscope used a high-speed camera (Photron, fastcam SA4) and a 50x magnification objective (Nikon, TU Plan ELWD, NA 0.6) mounted directly below the substrate to capture images. For the imaging of internal flows, the fluid was seeded with silica tracer particles (Kisker Bioteck, fluo-green beads, 500 nm) or gold particles (Nanopartz, gold particles in toluene, 50 nm) and particle movement was imaged using dark-field microscopy. A cold LED (Thorlabs, 1000 mA, 470 nm), labelled LED 1 in figure 2.3, was mounted above and focused on the substrate from an oblique angle. The angle of the LED was chosen to ensure illumination light missed the nozzle and made the particles visible without flooding the camera with light. The particles appeared as bright spots (of forward scattered light) against a dark background. Shutter times between 1000 and 1250 µs were used depending on the fluid, ensuring enough forward scattered light reached the camera to image flows but particles were still distinct. Frame rates were varied between 125 and 1000 fps depending on the solvents and particle velocities. More volatile solvents were imaged using higher frame rates and shutter speeds. Particle movement was imaged from below the substrate so both the substrate and fluid needed to be transparent. The smallest resolvable particle size using a light source at 470 nm is given by the diffraction limit

$$\frac{\lambda}{2NA} = 391\ nm \qquad (2.1)$$

where λ is the wavelength of the light source and NA is the numerical aperture of the objective (0.6). However the dimensions represented by one pixel in the images were approximately 0.43 × 0.43 µm, giving a smallest resolvable particle size limit of approximately 430 nm.

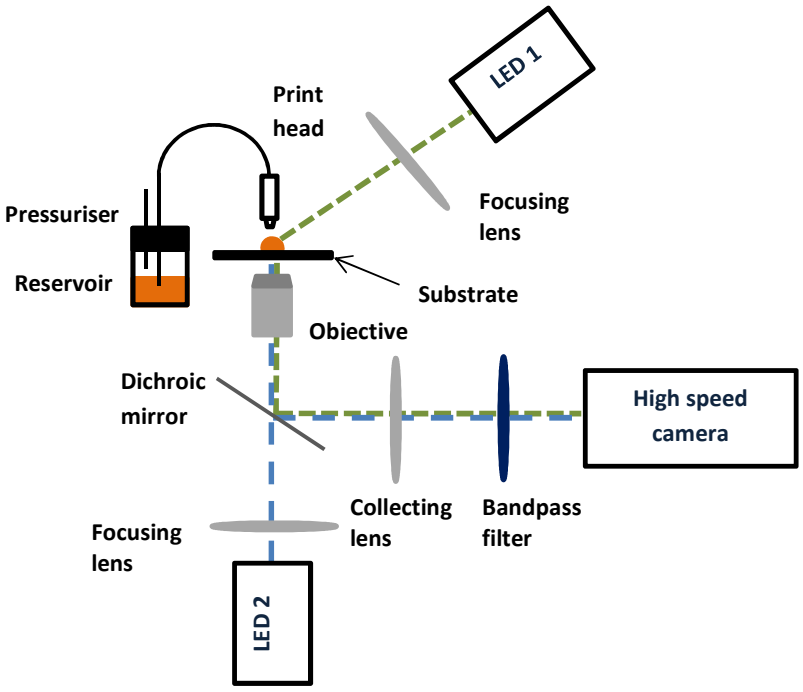

Figure 2.3: A schematic diagram of the experimental rig used for particle tracking and capture of interferometric fringes. LED 1 and the green light track represents particle tracking experiments, LED 2 and the blue light tracks represent interferometry measurements. The bandpass filter was only present for interferometry measurements.

One of the limitations associated with the tracking of internal flows is the presence of a bright region in the drying images. The bright region arises from refraction of light by the curved drop surface. The size of the bright region is a function of the angle of the LED, the contact angle of the drop, refractive index of the fluid and the numerical aperture of the objective lens. Light which encountered the drop on the side of the drop closest to the LED had a larger angle of refraction than light on the far side of the drop. The refracted angles were calculated according to Snell's law[123];

$$n_a \sin\theta_{in} = n_s \sin\theta_{re} \qquad (2.2)$$

where n_a is the refractive index of air (1.00), θ_{in} is the angle of incidence of light (°), n_s is the refractive index of the solvent (1.516) and θ_{re} is the angle of refraction.

The objective had numerical aperture 0.6 which corresponded to a half-cone angle of 37° in air (equation 2.3)[124]

$$NA = \sin\theta_c \qquad (2.3)$$

where θ_c is the half-cone angle in the solvent. So any light which deviated from the optical axis (normal to the substrate rather than the drop surface) by less than 37° was collected by the objective to give a bright region in the collected images.

In the bright region, the intensity of light scattered by particles was less than the intensity of the LED so particles could not be seen or tracked in this region. In general, the lower the angle of the LED with respect to the optical axis, the larger the area of the bright region. In the systems investigated in this project, the refractive index of the solvents (1.516) was close to the refractive index of the particles (1.457) so a low angle between the LED and the optical axis had to be used in order to distinguish the particles from the solvent. However, the drops used were all relatively flat and had a low contact angle (<10°) which meant the angle of the light relative to the optical axis and the angle of the light normal to the drop surface were the same across the drop surface. As such the area of the bright region was reduced and a low angle of the LED relative to the optical axis was possible without the bright region being too large to gain any useful information (figure 2.4).

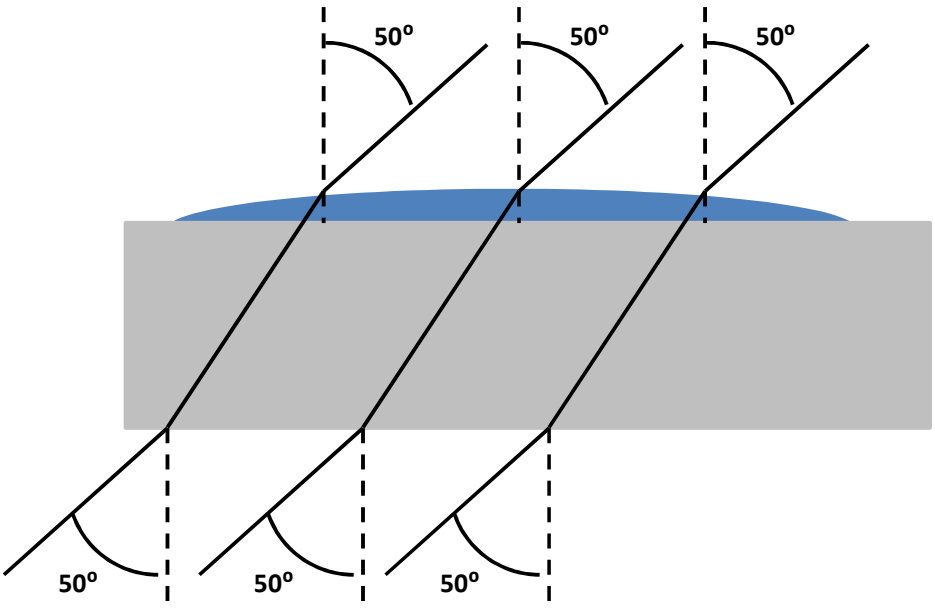

Figure 2.4: A schematic diagram showing example refracted light angles across the surface of a drop. The contact angle of the drops was too low to measure (<10°) and the drops were much wider than they were high; the width of drops was 200 µm whereas the height was approximately 5 µm. As a result of this the refracted angle of the light as it travelled through the drop was close to the angle of the LED relative to the optical axis.

The objective lens used had a finite depth of focus given by[125]

$$d_F = \frac{\lambda n_a}{NA^2} \qquad (2.4)$$

giving a depth of focus of approximately ±1.5 μm. As the analysis program could detect particles not sharply in focus, particles outside of this 3 μm range will have been detected. The initial height of drops imaged was of the order of 5 μm and so particles throughout the entire drop height were imaged during drying. It was not easy to determine the vertical position of the particles in the drops.

It would also have been possible to image particle moving using bright-field illumination (from above) whereby particles would have appeared black against a bright background. However, this option was discounted due to the presence of interference fringes during drying which made the particles difficult to track. The use of interference fringes and illumination from below was however useful in determining the changing profile of the drying drop. Illumination from below would have given the appearance of bright field illumination due to reflections from the substrate and would also allow for particle tracking whereby particles appear bright against dark fringes and dark against bright fringes. Illumination from below was also discounted due to problems with interference fringes making particles difficult to track.

Interferometry measurements used the same high-speed camera and objective lens mounted below the substrate for image capture but illumination came from directly below the drying droplets through a dichroic mirror. A cold LED (Thorlabs, 1000 mA, 470 nm), labelled LED 2 in figure 2.3, was mounted below and focused on the substrate. The substrate/drop and drop/air interface provided two different reflective surfaces; giving two reflected beams from the illumination light which recombined before reaching the camera to give an interference pattern in the final images. As reflections from the substrate were constant, any changes in the interferometry images during drying could be attributed to changes in the drop profile. Images were recorded at shutter times between 333 and 1000 μs depending on the solvent; speeds were chosen to maximise the number of fringes that could be seen. Frame rates were set between 50 and 3000 fps to ensure no fringes were skipped in the analysis. The distance from bright fringe to bright fringe is given by[126]

$$D_f = \frac{\lambda}{2n_s} \qquad (2.5)$$

where D_f is the distance between fringes (nm). As the wavelength of light used was 470 nm and the refractive index of the solvents was of the order of 1.5 the distance from bright fringe to bright fringe (change in height) was 155 nm.

The coherence length, L_c (nm), of the light source is given by[127]

$$L_c = \sqrt{\frac{2ln2}{\pi}} \frac{\lambda^2}{\Delta\lambda} \qquad (2.6)$$

where $\Delta\lambda$ is the full width half maximum (FWHM) of the light source assuming a Gaussian emission profile. The FWHM of the LED was 20 nm, as can be seen in figure 2.5, giving a coherence length of approximately 7 µm. Some drop profiles appeared to show noise in the early stages of drying, due to miscounting of fringes as the drop height reached the coherence limit of the light source. For later measurements, a narrow-width bandpass filter (Thorlabs, CWL 470 nm, FWHM 10 nm) was mounted between the collecting lens and camera in order to increase the coherence length of the light reaching the camera. The presence of the bandpass filter reduced the FWHM of the light to 10 nm (figure 2.5) so doubling the coherence length of light to approximately 15 µm and improving the appearance of early film profiles.

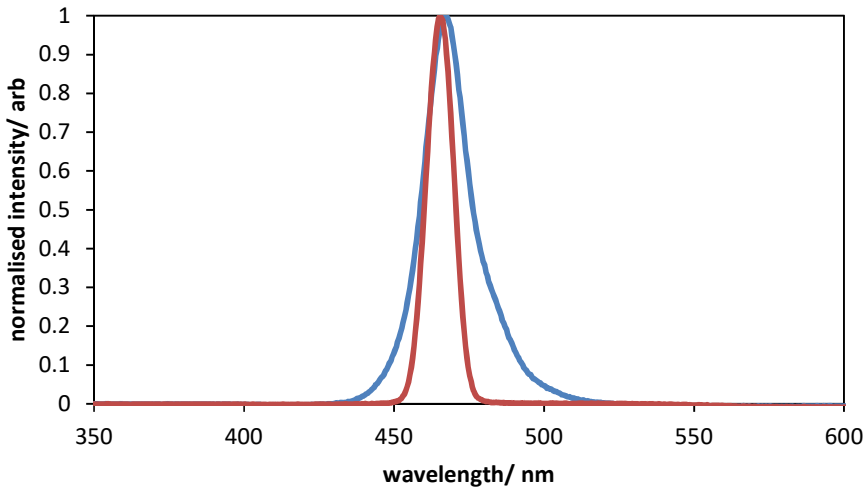

Figure 2.5: Plots showing the emission profiles of the illumination LED in the absence of (blue line) and presence of (red line) the narrow-width bandpass filter. The presence of the filter reduced the FWHM of the light from 20 nm to 10 nm.

It is important to note there were actually three reflective surfaces present in the drying drops (figure 2.6): the substrate/air interface, the substrate/drop interface and the drop/air interface. However, the depth of the substrate was approximately 2 mm and as the coherence length of the light was 7-15 µm, reflections from the substrate/air interface were incoherent with the other reflections and so did not have an impact on the interference patterns seen.

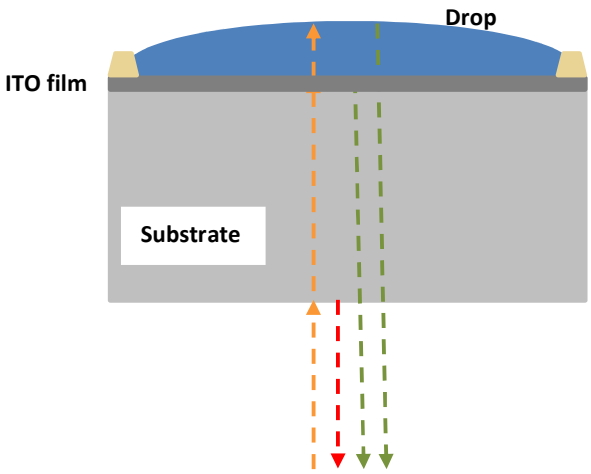

Figure 2.6: A schematic diagram showing the different reflective surfaces in a drop; reflections from the substrate air interface (red) were incoherent with reflections from the substrate/drop and drop/air interfaces (green). The incoming beam is orange.

As evaporation and fluid flows are sensitive to temperature, cold light sources were used to prevent uneven heating across the drop surface. The relative humidity (RH) and ambient temperature in the laboratory were controlled and recorded using a thermohygrometer (Extech) before each experiment. The temperature was generally kept between 20 and 23 °C, recorded to an accuracy of ±1 ^{o}C. The RH generally varied between 40 and 50 %, recorded to an accuracy of ±4 %. As all systems investigated in this project were based on organic solvents, the RH should not have had an impact on evaporation or fluid flows. The rig was surrounded by walls or curtains on all sides to prevent any drafts which may have had an impact on the drying. As the solvents used in experiments were organic and volatile an extraction system was set up in the lab to avoid inhalation of vapours. The extract was set up directly above the drying drops with a plenum to ensure it pulled evenly across the surface of the drop (figure 2.7).

Figure 2.7: An image of the extraction system (left) used with a plenum (right) to ensure even extraction across the surface of the drop.

For some experiments a heated stage was used to control the temperature of the drying drop used (figure 2.8). The temperature of the stage was controlled using a pair of peltier elements mounted between an aluminium plate and a heat sink. The peltier elements were controlled using a microprocessor employing a PID algorithm. A high precision digital temperature sensor (absolute accuracy of ±0.13 °C between 20 and 70 °C and of ±0.25 °C between -40 and 125 °C) was used to give real time information on the temperature of the stage. The temperature could be varied between 15.0 and 45.0 °C with a long term stability of ±0.02 °C (figure 2.9). When heating up, the stage would overshoot the set temperature and then quickly return before stabilising (figure 2.10). The substrate was left at the set temperature for 5 minutes before any measurements were taken.

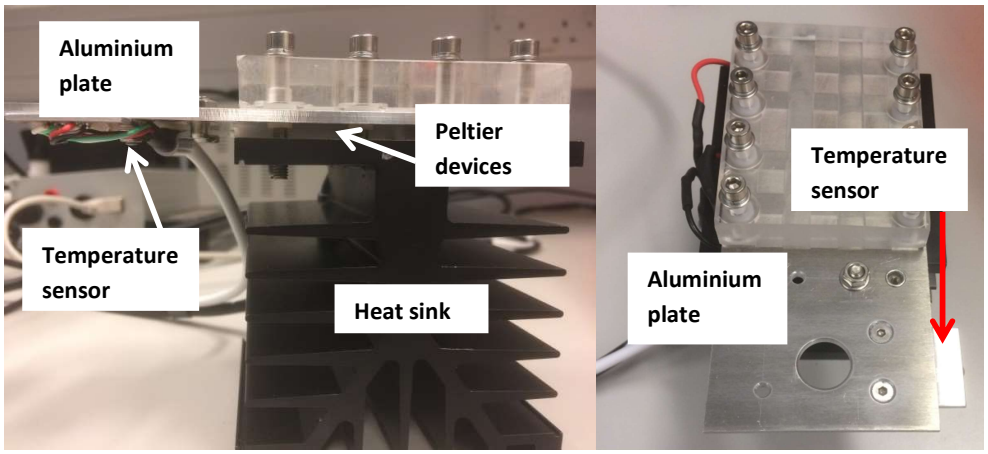

Figure 2.8: A labelled image of the heated stage used in some experiments from the side (left) and above (right).

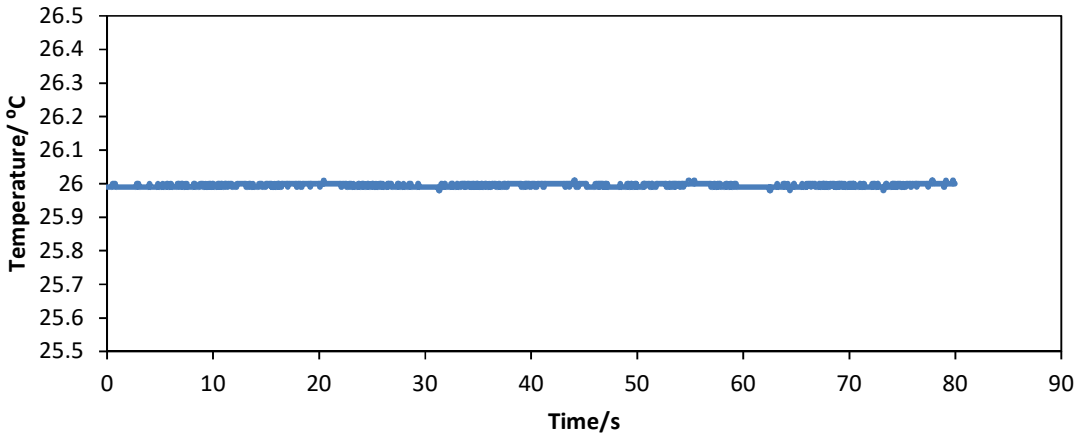

Figure 2.9: Plot showing the long term temperature stability of the heated stage.

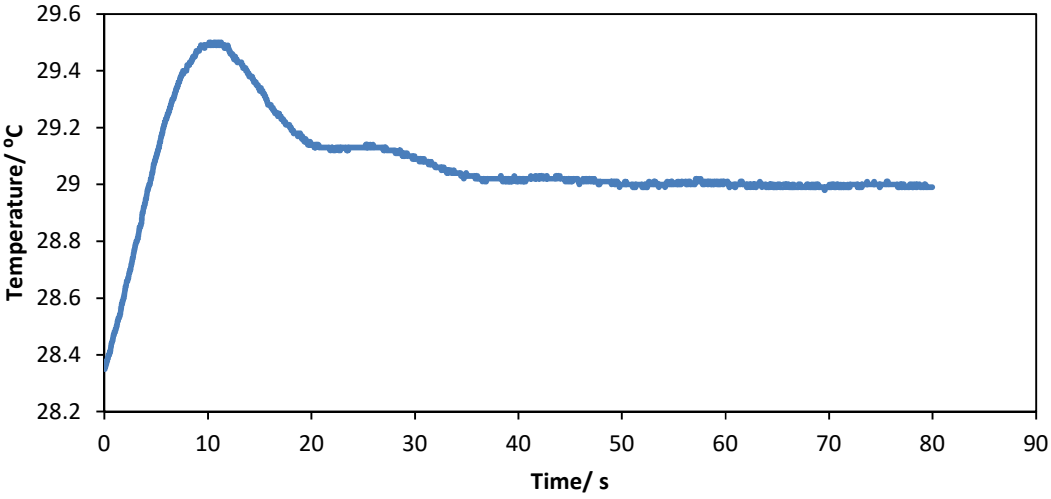

Figure 2.10: Plot showing the temperature profile of the heated stages as it reached a new set temperature of 29 °C. The stage overshot the temperature initially but quickly settled onto its set value.

To measure the distance between the substrate and the nozzle a mid-speed camera (Optronis, CR450×3) was mounted to the side of the nozzle and substrate, and a cold LED (Thorlabs, 1000 mA, 470 nm) was mounted opposite so shadow images of the nozzle/substrate gap could be taken (figure 2.11). The distance between the nozzle and substrate was determined using the known pixel spacing of the camera (3 µm). Side images were also used to ensure the nozzle was directly above any printed drops during drying as light scattered off the nozzle when the LED was placed directly below it, and the tip of the nozzle appeared bright in the images. The nozzle was held on a manual translation stage (Thorlabs, MT3- ½" XYZ Translation Stage) with a travel range of 13 mm.

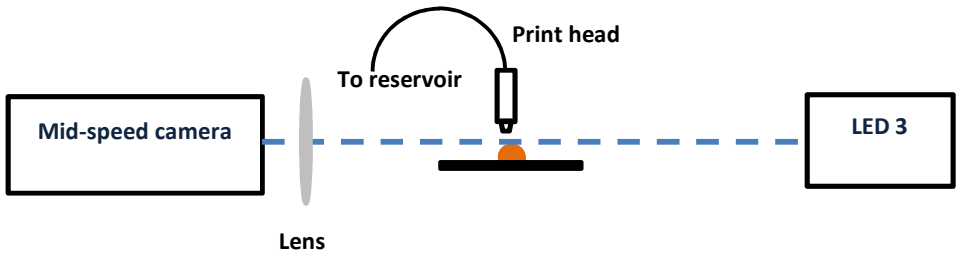

Figure 2.11: A schematic diagram showing the experimental setup used to determine the relative distance between the nozzle and the substrate.

2.2 Preparation of Solutions

Six organic solvents were investigated for use in the printing of OLED materials; anisole (ReagentPlus, 99 %), methyl anisole (99 %), dimethyl anisole (99 %), methyl benzoate (99 %), o-xylene (99 %) and mesitylene (98 %). All six solvents were purchased from Sigma Aldrich. Later on some model solvents were used: ethanol (Sigma Aldrich, 99.5 %), butyl actetate (Sigma Aldrich, 99 %), butanol (Fisher Scientific, 99 %), toluene (Fisher Scientific, 99 %) and methoxy propanol (Sigma Aldrich, 99.5 %). All solvents throughout were used as supplied. Densities of mixtures were measured by adding 1.000 cm^3 of solution from a pipette (± 0.001 cm^3) to a vial weighed using a high precision balance (±0.00005 g) and calculating the difference in mass. A table summarising the properties of all fluids is shown below.

Table 2.1: Showing the properties of all fluids investigated, all values are quoted at 25 ^oC.

Solvent	Surface Tension/ mN m^{-1}	Density/ g cm^{-3}	Viscosity/ mPa s	Vapour Pressure/ kPa
Anisole	34.96[70]	0.990[70]	1.001[70]	0.477[70]
4-Methyl anisole	32.88	0.971	n/a	n/a
3,4-Dimethyl anisole	32.41	0.962	n/a	n/a
Methyl benzoate	37.27[70]	1.085[70]	1.958[70]	0.051[70]
o-xylene	29.60[70]	0.876[70]	0.747[70]	0.876[70]
Mesitylene	28.05[70]	0.861[70]	0.916[70]	0.327[70]
Ethanol	23.39[70]	0.787[70]	1.057[70]	7.83[70]
n-Butyl acetate	24.78[70]	0.876[70]	0.677[70]	1.52[70]
1-Butanol	25.67[70]	0.806[70]	2.599[70]	0.931[70]
Toluene	27.93[70]	0.865[70]	0.548[70]	3.76[70]
1-Methoxy 2-propanol	27.7[128]	0.916[128]	1.7[128]	1.2[129]

For particle tracking experiments the fluids were seeded with tracer particles; either silica (Kisker Bioteck, fluo-green beads, 500 nm) or gold (Nanopartz, gold particles in toluene, 50 nm). The silica particles were supplied as a dry powder which was added to solvents up to a concentration of 0.05 % by weight and placed in an ultrasonic bath for 30-60 minutes until evenly dispersed. Gold particles came dispersed in toluene and were added to solvents up to a concentration of 0.05 % by volume, then placed in an ultrasonic bath for 30-60 minutes before use. Solvents were measured out using a micropipette (Eppendorf, 1-5 ml, ±0.012 ml).

For interferometry measurements the solvents were measured out using a glass syringe (Hamilton, 5 ml, ±0.1 ml) and passed through a 0.45 µm Teflon filter before use to eliminate any dust particles which may influence the measurements. For measurements in the presence

of active OLED materials (Livilux TH-123, host material, Merck Chemicals), solutions were made up to concentrations between 5 and 40 mg cm^{-3}, the material was added to the filtered solvent and placed in an ultrasonic bath for 15 minutes or until evenly dispersed.

2.3 Preparation of Substrates

All substrates used were provided by Merck and consisted of wells with a glass base topped with an indium tin oxide (ITO) film, surrounded by walls of polymer resist (figure 2.12). Drops sat within the wells and were surrounded by walls during the drying process. Three different geometries were used: square, oval and circular.

Figure 2.12: A schematic diagram showing the different layers present in the substrates. Not to scale.

Square substrates consisted of wells of size 200 × 200 µm separated by walls which were 1.5 µm high and 20 µm wide (figure 2.13). The majority of experiments were carried out in the square wells as they were by far the most abundantly available for experimentation and drying effects were most exaggerated in the square geometry. Whilst the square systems were not axisymmetric, the same drying patterns existed in all geometries (including the axisymmetric circular systems) so the same mechanisms could be applied to all geometries.

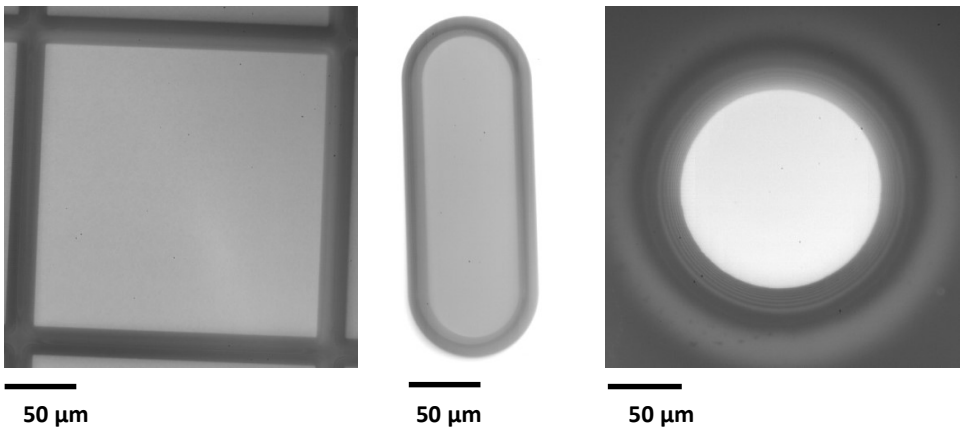

Figure 2.13: Images of the substrates used for experimentation showing the square (left), oval (middle) and circular (right) geometries.

The oval wells were the closest to bank structures which might be used industrially; they consisted of wells which were 64 × 212 µm in size, separated by walls which were 2 µm high (figure 2.13). In the case of the oval wells, the walls were treated to make them hold fluid in more easily (so drops did not spill over into adjacent wells). The circular wells had a diameter

of 134 µm and a wall height of approximately 1.3 µm (figure 2.13); there were some inconsistencies in the wall heights of the circular and square wells.

Close up images of the square wells (figure 2.14a) show they are not flat-topped but look more like an inverted "V" with a rounded apex. The banks are also not of uniform height, the intersection between banks are 200-250 nm lower than the bank tops. Non-uniformity of the bank height will influence the shape of the free liquid surface and may introduce some complexity into the interference patterns. Close up images of the oval wells (figure 2.14b) did not clarify whether the bank tops were flat or not but it is likely they are rounded as in the square wells. Close up images of the circular wells showed gently sloping walls (figure 2.14c) which may encourage de-pinning down the walls during drying, though the bank tops in the circular wells were flat. There were no intersections between wells in the case of the oval or circular wells so the banks would be of uniform height.

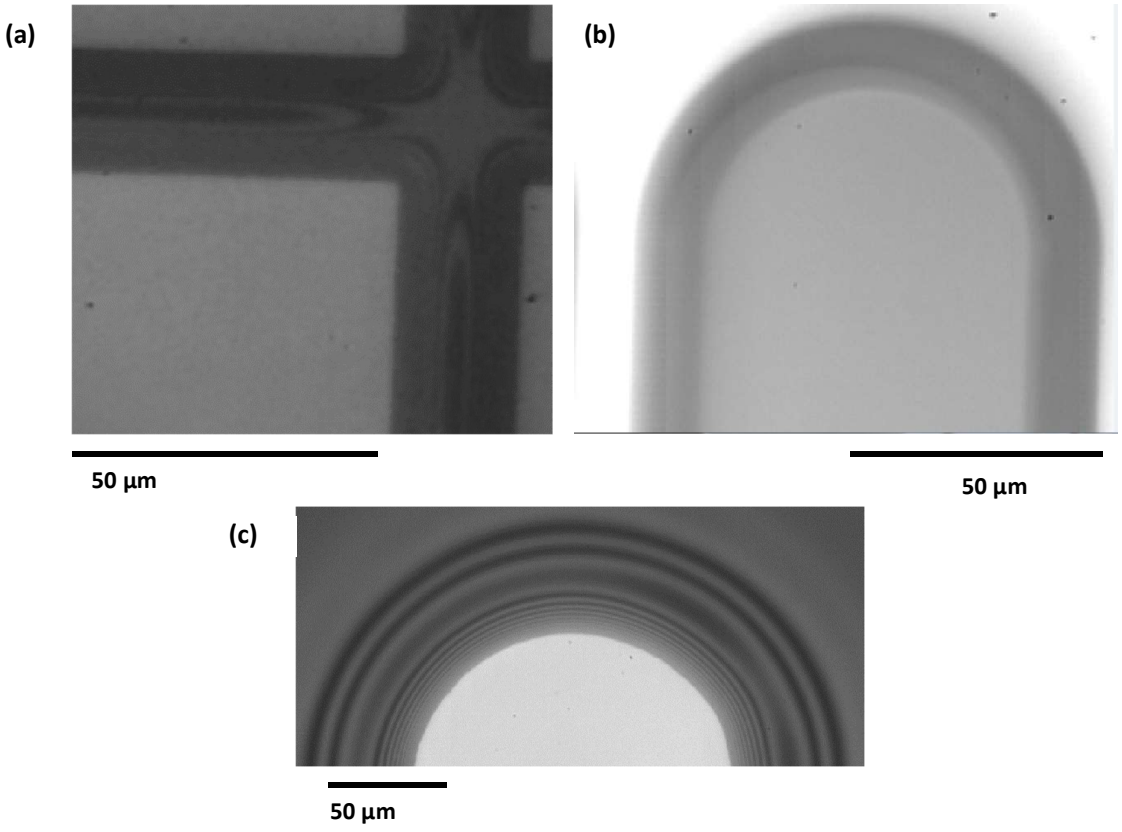

Figure 2.14: Close up images of the banks in the square (a), oval (b) and circular (c) wells.

All substrates were cleaned and prepared in the same way; they were placed in IPA in an ultrasonic bath for 2 × 15 minutes with a change of IPA in between. They were then placed back in the ultrasonic bath in ultra-high purity water (Milli-Q A-10, Millipore) for 15 minutes. Substrates were blown dry with argon or nitrogen before being placed in an oven at 230 °C for 2 hours. If they were then used again at a later date they were placed back in the oven at 180 °C for 10 minutes. For all experiments only one drop was imaged at any one time, in the absence of any other drops drying around it. Therefore there were no vapour effects from adjacent drops at any time.

In some cases it was necessary to use glass cover slips for preliminary experiments; cover slips were cleaned as outlined above. Some substrates were then treated with trichloro(octadecyl)silane (Sigma Aldrich) prior to use. Throughout the cleaning and coating process slides were held separated in a Teflon slide holder. Once the slides were clean and dry they were dip coated in trichloro(octadecyl)silane to silanise the surface and increase its hydrophobicity. A 2% trichloro(octadecyl)silane solution in toluene (Sigma Aldrich) was prepared and the cleaned glass slides were soaked in this solution for 60 minutes. They were then soaked for 2 $\times$ 1 minute in toluene with a change of toluene between each minute long soak. Each slide was then rinsed once again with the high-purity water, blown dry with nitrogen gas and dried in an oven at 37-45 ^{0}C overnight. Slides were then stored in the slide holder at room temperature.

Silanisation of square bank structures was also necessary on occasion and was carried out in both the liquid phase and the gas phase. Substrates were cleaned as described above and then left in a vacuum dessicator with a small vial of the silane solution overnight. Once removed from the dessicator slides were soaked in IPA for 2 $\times$ 1 minute with a change of IPA in between. Each slide was then rinsed once again with high purity water, blown dry with nitrogen gas and dried in an oven at 37-45 ^{0}C overnight.

2.4 Characterisation of Materials

Static surface tensions were measured using a tensiometer (First Ten Ångstroms, FTA200). Drop shape analysis was carried out on a pendant drop which had been ejected from a syringe (Hamilton, 250 µl) to the point just before break off. The shape of the drop was fitted to the Young-Laplace equation (equation 2.7) to give the equilibrated surface tension of the solution[130,131]:

$$\Delta p = \sigma\left(\frac{1}{r_1} + \frac{1}{r_2}\right) \qquad (2.7)$$

where Δp is the pressure difference across the air/fluid interface. The Young-Laplace equation assumes the shape of the drop is entirely determined by gravity and surface tension.

Advancing and receding contact angles were also measured on the tensiometer. Fluid was dispensed from the syringe using a syringe pump driven by a stepper motor. To measure advancing and receding contact angles a series of images was taken as the fluid was either dispensed from or drawn into the syringe, respectively. The syringe tip remained in the drop throughout measurement (figure 2.15). Images were analysed to show how the contact angle of the fluid changed as the drop was either dispensed or drawn in and the static angle reached was defined as the advancing/receding contact angle of the fluid. Contact angles were determined by manually selecting the intersection of the baseline with the drop profile where the program used tangents to determine the gradients of the slopes. Arctangents of the slopes were then taken to obtain angles and the difference between the baseline angle (in this case zero) and the drop profile angle gave the contact angle.

Figure 2.15: Schematic diagrams showing the measurement of advancing (left) and receding (right) contact angles. The darkest blue shade represents the earliest time in measurement with the lightest blue representing the latest time in measurement.

Before all surface tension and contact angle measurements the dispensing syringe was cleaned by placing in an ultrasonic bath in decon solution for 30 minutes and rinsing with high purity

water 40 times. The tensiometer was calibrated using the known external diameter of the needle tip and ultra-high purity water was used to ensure calibration was correct and everything was clean. Static surface tensions were measured for each solution until three readings within ±0.1 mN m^{-1} had been recorded. Generally the three readings within ±0.1 mN m^{-1} were successive; if the measurements were not successive they were only recorded if the measurement which broke them up was a clear anomaly (≥ 0.5 mN m^{-1} away from all other readings). All measurements were carried out in a quartz cuvette (Sigma Aldrich) at saturated vapour pressure.

Printed deposits of active OLED materials (Livilux TH-123, host material, Merck Chemicals) were imaged using epifluorescence. Samples were excited using a 355 nm laser (Leica SP5 II Laser scanning confocal microscope) and fluorescence or phosphorescence was collected using a high-gain, red-sensitive, hybrid-detector. An air immersion objective was used with a working distance of 1 mm.

2.5 Image Analysis

Images taken of the particle motion due to internal flows in drying drops were analysed in MATLAB and particle tracking velocimetry (PTV) was carried out in order to find flow velocities. The particle tracking code was originally taken from Georgetown University[132] and was adapted for use in these systems by Emma Talbot and Lisong Yang (Durham University).

The program began by applying a spatial bandpass filter to the images in order to suppress pixel noise and long wavelength image variations. The lower limit of the filter was one pixel and the upper limit 5 pixels. Particles in the images were then located by finding local maxima in the images to calculate the centroids of the particles; which were then tracked through frame by frame. Any particles moving fewer than three pixels in the total time tracked were considered to be stationary by the program. All particles were issued an identification number to aid with the tracking through frame by frame; particles which disappeared for 4 frames or more were then issued a new identification number if they reappeared. A threshold was set for the maximum expected distance a particle would move in a single frame (5 pixels) to ensure the same particles were being followed throughout. The contact line of the drop was selected manually for each analysis as the top and bottom walls of the square banks appeared bright on the images (figure 2.16), complicating automatic detection of the contact line. Particle tracking was only carried out in the square geometry.

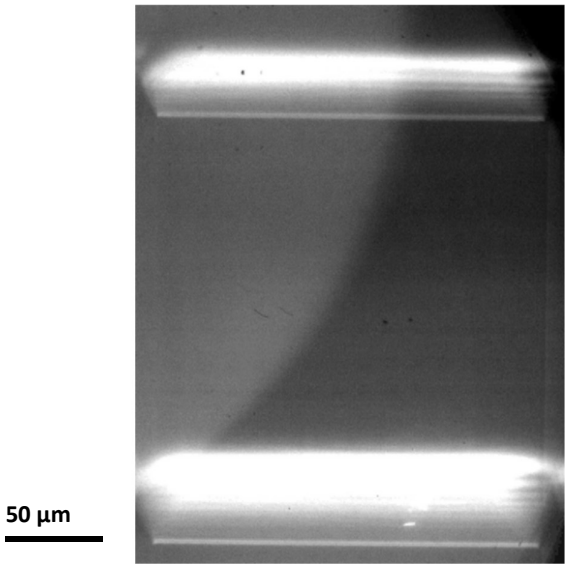

Figure 2.16: An image showing the square substrates under the particle tracking illumination. The top and bottom walls are visible in the image whereas the side walls are not. The bright areas of the walls complicated automatic contact line detection so all contact lines were selected manually for analysis. Illumination across the bank was not even due to the high angle of the LED.

When calculating particle velocities, the tracked particles were binned spatially in a grid array of n × m squares using Cartesian co-ordinates. Temporal binning was by $0.1t_{dry}$ where t_{dry} was the total drying time of a drop. Mean particle velocities were then found for each bin.

Interferometry images were also processed in MATLAB to build up a picture of the changing drop profile during drying. The region of interest (ROI) was selected manually in all geometries as a square area; in oval and circular geometries, where the selected ROI included areas of wall, the program then discounted areas which showed no change in fringe intensity from the analysis. To track fringes, analysis began at the end of drying where there was no fluid in the wells. It then tracked frames through drying for each pixel from the end to the beginning, building up a picture of the drying drop. The intensity of each pixel was plotted against the time in frames (figure 2.17) and the resulting plot was used to determine the height of the pixel at different points in the drying; peaks in the curve were bright fringes and troughs were dark fringes. A linear interpolation was then used to determine the film height between fringes (figure 2.18). An extrapolation for the elements of $t/$ frame outside the interval spanned by the height was performed in case the first fringe was not located within the first frame. To plot the profile of the drying drop at different times during drying a cross section across the drop was selected to give a plot of the height of the drop across a line of pixels at different times during drying.

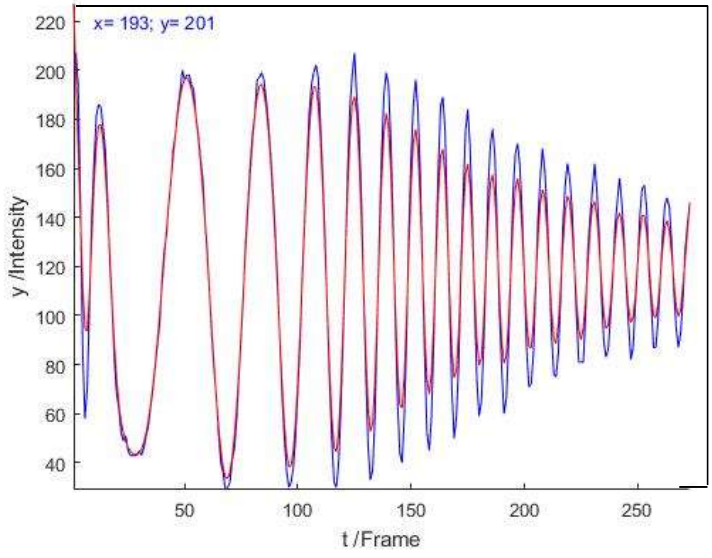

Figure 2.17: An example plot of pixel intensity against time used to find the position of bright and dark fringes in the drying drop. The blue line shows the raw data and the red line shows a smoothed curve employed to ensure any noise is averaged.

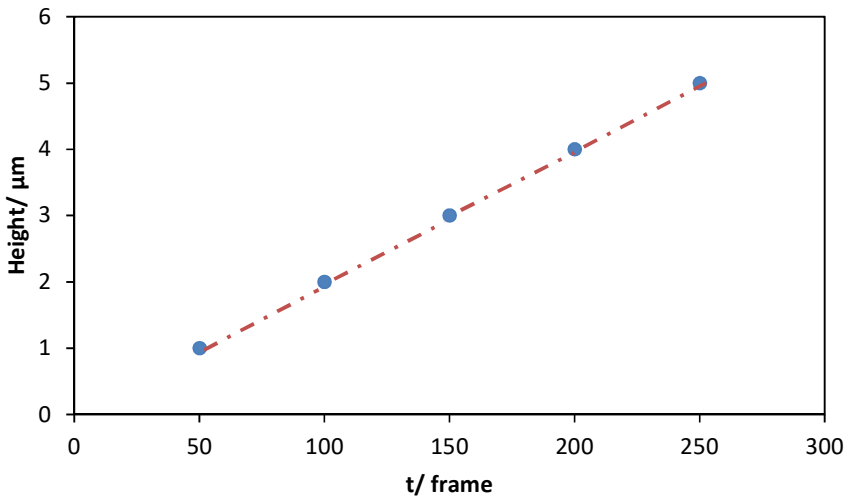

Figure 2.18: An example plot film height against time and the linear interpolation between points used to determine the film height between fringes. The above plot is not based on real data; it has been constructed to show how extrapolation was done. Blue points show the drop height based on the fringe data and the red line shows the linear extrapolation to determine the height between fringes.

Close to the bank walls the fringes were very close together and not distinguishable by the program. In certain cases therefore the plots had to be extrapolated back to the walls; though as drops could be seen to be pinning at the wall tops during drying, extrapolation was not difficult. In certain cases some data correction had to be implemented after image processing; there were cases where the miscounting of some fringes in a certain region would occur. Miscounted fringes were corrected by manually altering the data points to bring them in line with other data points (figure 2.19), the same correction was made for each time profile in a single drop. Data points were only ever altered by an exact number of fringes to ensure data was not being manipulated unnecessarily.

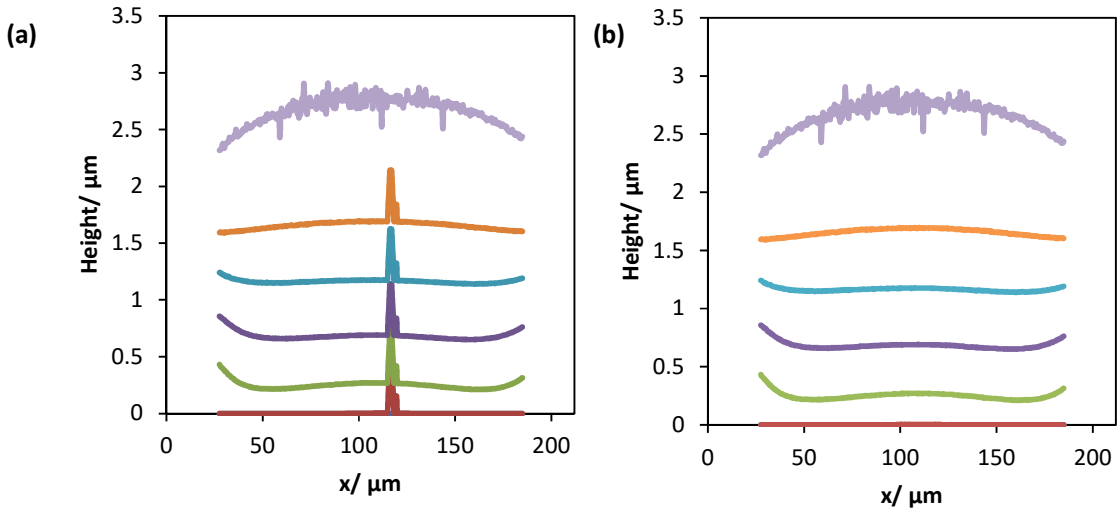

Figure 2.19: Plots showing example data correction (a) shows the uncorrected data with miscounting of fringes and (b) shows the data after correction. Any points moved were only altered by an exact number of fringes (a multiple of 0.15 µm).

Images of the fluorescent deposits of active materials were also analysed in MATLAB; analysis identified the intensity of green light emitted across the surface of the deposits, giving a plot of intensity against pixel distance. Whilst this did not give an absolute measure of the thickness of a film it gave information on the relative light emission, and so film thickness, across a well.

3. Internal Flows Inside Drops Evaporating in Banked Structures

3.1 Introduction

In inkjet printed OLED devices it is essential that deposits are of an even thickness across their entire area to optimise device performance. To predict and control deposit morphology from printed drops, an understanding of material transport during drying is necessary. Many studies have looked at particle transport during the drying of drops on flat substrates, both for single component drops and binary solvent mixtures.[18,19,23,93,97,133] However there are very few reports in the literature of drying mechanisms in banked structures; where drops sit in wells and are surrounded by walls on all sides. Studies which have looked at drops drying within banked structures have tended to look at the final deposit morphology or stills from the drying, rather than imaging particle motion throughout the drying process.[17,26,68,134,135] Looking at deposits alone is not useful in understanding drying as you gain no information on the mechanisms behind transport or the way in which a deposit is formed. If the transport mechanisms are not understood it is difficult to develop and implement strategies to control deposit morphology. For inkjet printing to become a viable method for the production of OLED devices it is necessary to understand the driving forces behind particle transport and deposit morphology and so imaging particle transport throughout the drying process is important.

This chapter focuses on particle tracking velocimetry (PTV) which allows calculation of average particle velocities in different areas of the wells as well as giving qualitative information on the direction of particle flows.[136–139] There are limitations on PTV and the systems it can be used to investigate: the substrate and the solvent must be transparent as particles are viewed through them (when imaged from below). For very thin droplets (as imaged here) the transparency of the solvent is not as much of an issue as for thicker droplets. Particles should be spherical in order to follow the flow streamlines,[136,137,139] and small enough to have no impact on the drying process and remain suspended throughout drying. Particles also need to be small in comparison to the depth of the liquid so that there are not large velocity gradients across particles, but should be large enough that the intensity of forward scattered light is sufficient for particles to be seen. Brownian motion cannot dominate convection over internal fluid flows.[136,137,139] In picolitre sized drops, internal flows can be very rapid so high frame rates and shutter speeds are required to track particles accurately. In the systems investigated in this thesis, once the fluid dries below the level of the wall tops the 500 nm silica particles represent a significant proportion of the fluid height. As the velocity within the fluid film will be different at different film heights, once the fluid is below the level of the walls, particles will give at best

a qualitative measurement of the average velocity across the height of the film (figure 3.1). Velocity gradients across particles cause them to spin and introduce other forces.

The aromatic organic solvents discussed in this thesis presented some challenges in finding suitable tracer particles: the solvents dissolved most polymer materials and had a similar refractive index to most polymers (a difference in refractive index is essential for particles to be visible through scattered light). The likelihood of Brownian motion being a factor in particle movement also had to be considered. The diffusion coefficient of a particle (D) is given by the Stokes-Einstein equation (chapter 1 equation 1.32).

Assuming a particle radius of 500 nm and fluid viscosity of 1 mPa s, $D = 4 \times 10^{-3}$ m^2 s^{-1}. The mean Brownian displacement ($\bar{x}_B$) for a particle during one time bin $0.1t_{dry}$ (approximately 2.5 s for methyl benzoate which is the slowest drying solvent) is then given by

$$\bar{x}_B = \sqrt{2Dt} \approx 1.4\ \mu m \qquad (3.1).$$

The estimated mean Brownian displacement above is the maximum possible value as it has been calculated for the slowest drying solvent. The value of 1.4 µm is significantly less than the distance travelled by particles in the radial direction in $0.1t_{dry}$ for all solvents; so Brownian motion can be assumed to have a negligible impact on particle transport in the radial direction. Brownian motion is not negligible over the height of the drop and, for slower drying solvents, particles will diffuse across the height of the well during drying. The average velocity represented by a time bin will be an average over different fluid heights, fluid velocities therefore need to be averaged across many tracks at each radial position. If the particles have a non-uniform flow profile over the z direction they may diffuse into regions at different speeds. Experiments have all been carried out under ambient laboratory conditions (approximately 295 K and 1 atm pressure) and as such evaporation of the drops is assumed to be diffusion limited.

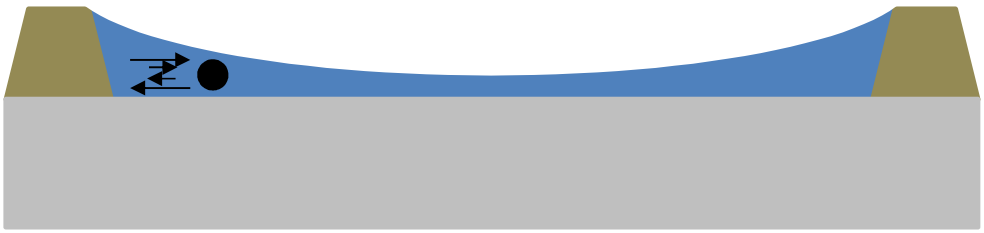

Figure 3.1: A schematic diagram showing the different velocities experienced across a tracer particle once the particle becomes a significant size compared to the film thickness. The length of the arrows is proportional to the velocity of the flows.

There can be a large difference in the drying behaviour and particle transport mechanisms on flat substrates between pure solvents and binary solvent mixtures.[18,19,23,93,97,133] Single solvents drying on flat substrates tend to exhibit radial flows towards the contact line, driven by capillary forces. Capillary flows compensate for evaporation of fluid from a drop with a pinned contact line to maintain the spherical cap shape of the sessile drop.[19] When a co-solvent is introduced to form a binary mixture, the mechanisms for particle movement switch to being surface-tension driven.[97] In a drop containing two solvents with differing surface tensions and volatilities the more volatile solvent is depleted at the contact line (due to enhanced evaporation there). When the solvents have different surface tensions, a depletion of one of the solvents at the contact line causes a surface tension gradient across the drop surface and flows are induced from areas of low to high surface tension. Induced flows then rapidly re-circulate to maintain the spherical cap shape of the drop. Rapid re-circulation of flows has been shown to combat ring stains in drying drops.[97] In the case of OLED systems, experiments will determine relative evaporation rates across drops and the effect of Marangoni forces during drying. Marangoni forces on drops drying within wells have not yet been investigated in the literature.

In this chapter, internal flows in picolitre sized droplets drying in banked structures are studied. High-speed imaging of tracer particles in drops of five different solvents (anisole, methyl anisole, methyl benzoate, mesitylene and o-xylene) has been attempted in order to determine the driving forces behind particle transport in single solvent systems. Alongside single solvents, particle flows present in binary solvent mixtures have also been investigated to determine the effect co-solvents have on drying. The complete drying process was recorded to give information about the driving mechanisms behind particle transport in banked substrates, though imaging was not possible for all solvents in the end.

3.2 Evaporation of Single Solvent Drops

This section reports the internal flows within single solvent, picolitre-sized droplets drying in square wells. Anisole, methyl anisole, methyl benzoate, mesitylene and o-xylene were suggested by Merck Chemicals as representative of solvents used to dissolve active OLED materials in an industrial setting. Drops were printed and imaged as described in chapter 2 section 2.1. The properties of the solvents are shown in table 3.1. Silica particles aggregated in o-xylene and mesitylene and could not be used to image flows in the pure solvents.

Table 3.1: Properties of solvents at 25 ^{o}C.

Solvent	**Surface Tension/ mN m^{-1}**	**Density/ g cm^{-3}**	**Viscosity/ mPa s**	**Vapour Pressure/ kPa**	**Diffusion Coefficient of vapour in air/ m^2 s^{-1} × 10^{-6}**
Anisole	34.96[70]	0.990[70]	1.001[70]	0.477[70]	n/a
Methyl anisole	32.84	0.971	n/a	n/a	n/a
Methyl benzoate	37.27[70]	1.085[70]	1.958[70]	0.051[70]	n/a
Mesitylene	28.05[70]	0.861[70]	0.916[70]	0.327[70]	6.63[140]
o-Xylene	29.60[70]	0.876[70]	0.747[70]	0.876[70]	7.27[140]

Particle tracks for the first half of drying for each solvent are shown in figure 3.2; from the tracks the contact line of the drop appeared to remain pinned throughout the drying process, though it was not clear where on the bank the drops were pinned. It is likely the drops remain pinned close to the top of the banks and this will be assumed for the discussion of results in this chapter. Initial particle flows were radially outwards towards the contact line, similar to the flows seen in single solvent drops drying on flat substrates. Due to the high density of silica (2.65 g cm^{-3}) relative to the solvents ($\sim$ 1 g cm^{-3}), a large number of tracer particles settled out on impact of the drop. With a calculated sedimentation rate of approximately 0.1 µm s^{-1}, sedimentation was not fast enough for particles to settle out during the drying period. In order for inertial forces to be important Re must be >1. In the general case of aromatic organic solvents and silica particles, $Re \approx 1 - 5$ and as such inertial forces could drive silica particles to the substrate. Particles appeared to adhere to the substrate and remain there for the rest of the drying period. The concentration of particles in the drop was high enough that there was still particle movement until the end of drying in all solvents. The initial stages of drying in single solvent drops did not show any particle recirculation and flows were consistent with evaporation-driven convection towards the banks.[19]

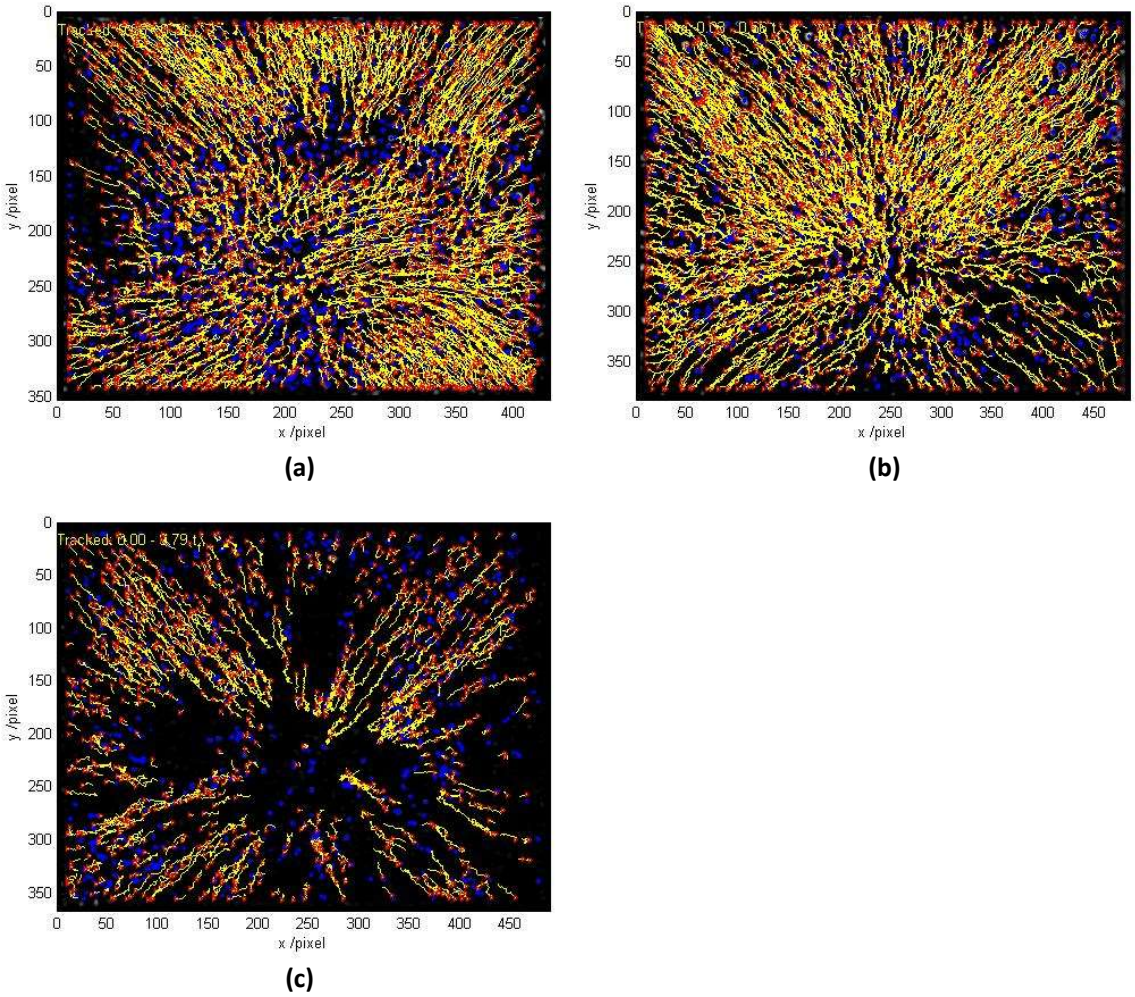

Figure 3.2: Particle tracks for the early stages of drying (roughly the first half) in anisole (a), methyl anisole (b) and methyl benzoate (c). Images were recorded at 1000 fps with a shutter speed of 1 ms for anisole and methyl anisole and at a frame rate of 125 fps and shutter speed of 1.11 ms for methyl benzoate. Blue spots represent particles which were stationary throughout the drying process, red

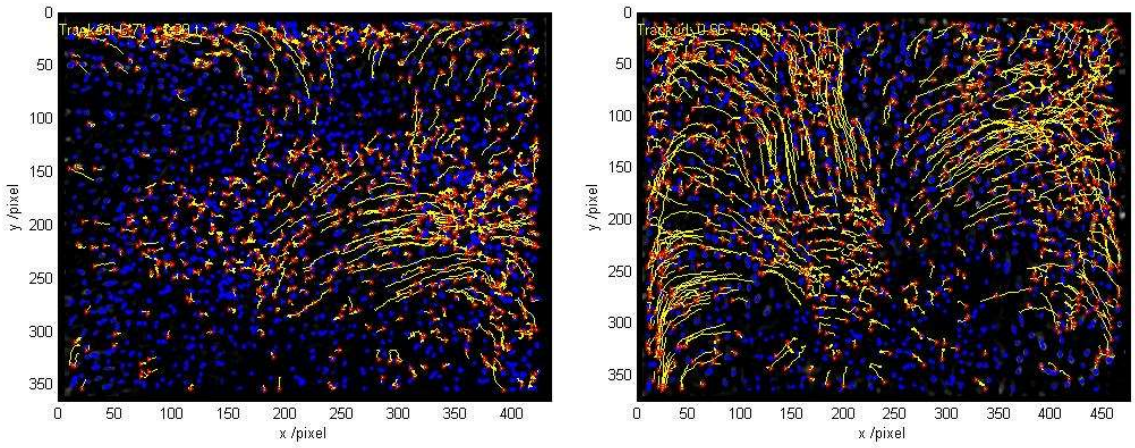

(a) **(b)**

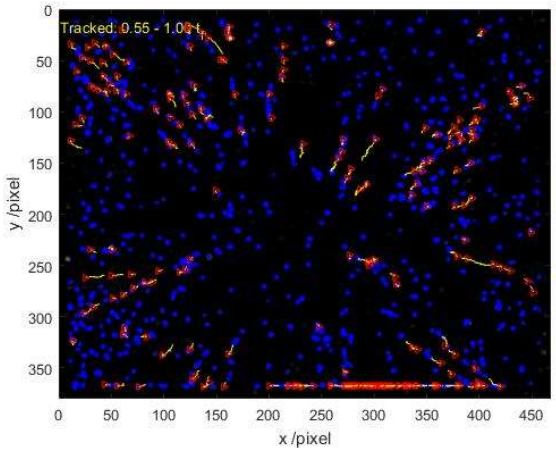

(c)

Figure 3.3: Particle tracks for the late stages of drying (roughly the last third) in anisole (a), methyl anisole (b) and methyl benzoate (c). Images were recorded at 1000 fps with a shutter speed of 1 ms for anisole and methyl anisole and a frame rate of 125 fps and shutter speed of 1.11 ms for methyl benzoate. Blue spots represent particles which were stationary throughout the drying process, red spots represent the end of particle travel and yellow lines represent the direction of particle travel.

In the last third of drying, particle movement became concentrated towards the corners of the wells (along the walls) in all three of the solvents (figure 3.3). There was not much particle movement in the late stages of drying for the methyl benzoate drop as most particles had stopped moving; methyl benzoate generally took 25–45 seconds to dry and was the slowest evaporating solvent. With an approximate sedimentation rate of 0.1 µm s^{-1} the particles would settle over a distance of approximately 2.5 µm in the drying time of a methyl benzoate drop. With an initial drop height of 2 – 5 µm, some sedimentation of particles is possible in the case of methyl benzoate drops. Videos relating to figures 3.2 and 3.3 are videos 1-3 on the attached disk.

The velocity profiles for the initial stages of drying (0.3-0.4 t_{dry}) are shown in figure 3.4, demonstrating radial flow towards the contact line. Faster particle movement at the contact

line of the drop suggests evaporation was enhanced here. Measured velocities were generally highest in the corners of the wells; evaporation was enhanced at the corners compared to the straight edges as there was more free space for vapour to diffuse into. Particle velocities were slower for the less volatile methyl benzoate drop than for the more volatile anisole and methyl anisole drops.

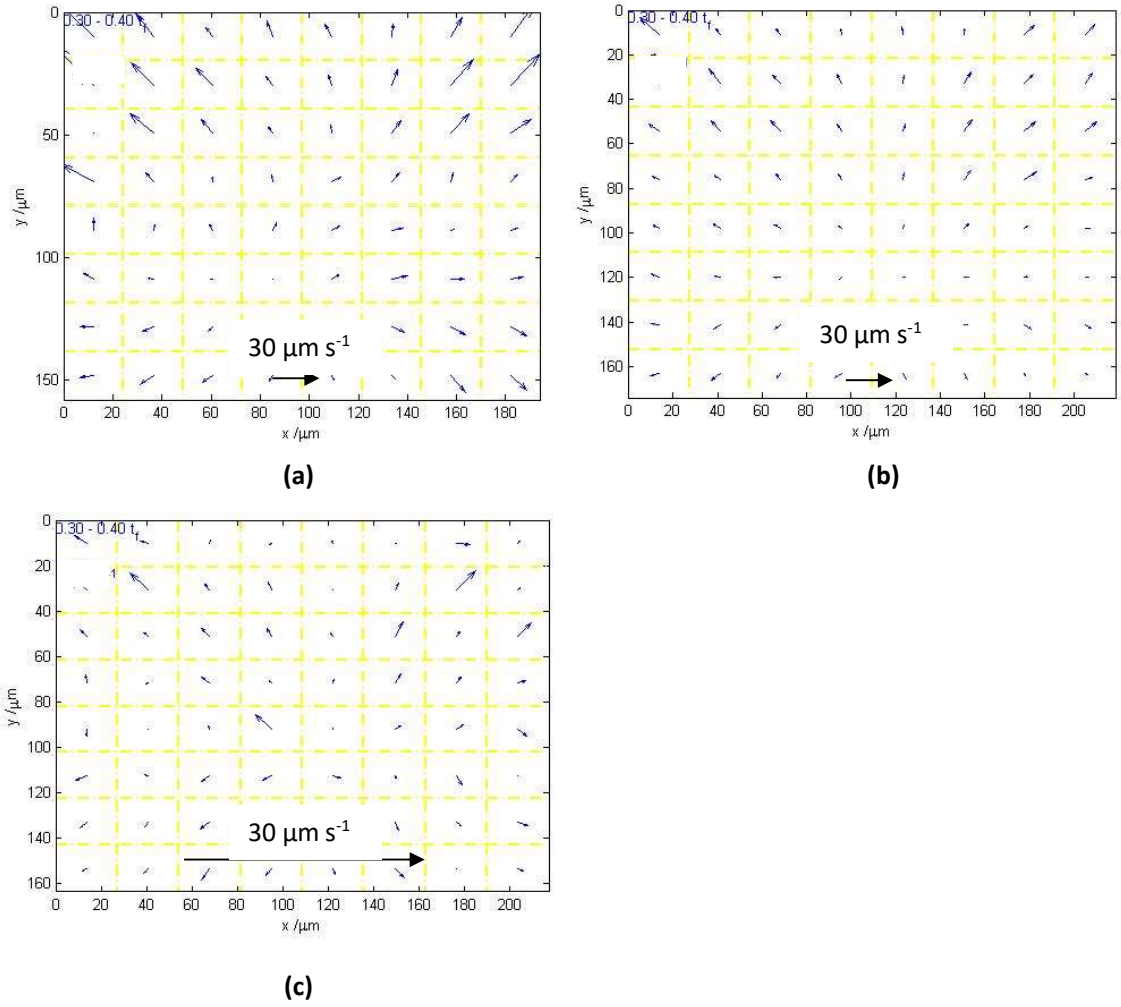

Figure 3.4: Velocity profiles between 0.3 – 0.4 t_{dry} in anisole (a), methyl anisole (b) and methyl benzoate (c). Images were recorded at 1000 fps with a shutter speed of 1 ms for anisole and methyl anisole and at a frame rate of 125 fps and shutter speed of 1.11 ms for methyl benzoate.

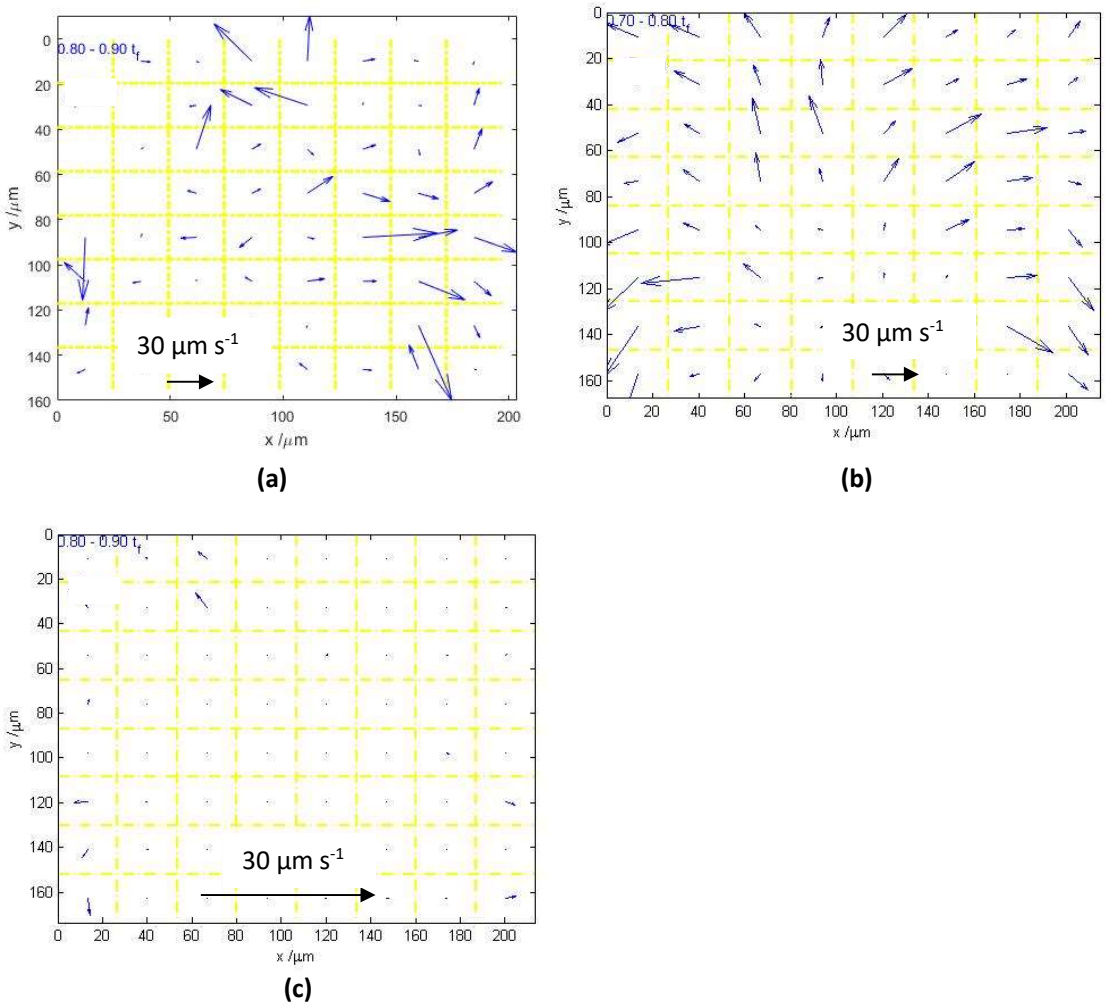

Figure 3.5: Velocity profiles between 0.7 – 0.8 t_{dry} for (b) methyl anisole and between 0.8 – 0.9 t_{dry} for (a) anisole and (c) methyl benzoate. Images were recorded at 1000 fps with a shutter speed of 1 ms for anisole and methyl anisole and a frame rate of 125 fps and shutter speed of 1.11 ms for methyl benzoate.

The velocity profiles for the later stages of droplet drying (0.7-0.8 t_{dry} or 0.8-0.9 t_{dry}) are shown in figure 3.5. Particle speeds generally increased as the liquid film thinned and particle movement was concentrated towards the corners of the wells. Once again, particle velocities were slower in the methyl benzoate drop than in the anisole or methyl anisole drops. Faster particle movement towards the end of drying suggested flows were capillary driven as capillary forces are strengthened in thin films. The strength of capillary forces within a film is determined by the Laplace pressure; as the film thins the radius of curvature decreases due to the pinning of the drop at the wall tops (figure 3.6) and the strength of capillary pressure increases (equation 1.10). If constant mean curvature was maintained across the drop surface after the drop dried past flat it would soon cut the base of the wells, it is evident from drying images that this did not happen. Therefore the centre of the fluid must flatten out in the later

stages of drying before curving up to the bank tops (figure 3.6). As the curvature in the corners of the wells was greater than that along the straight edges, the increased capillary pressure towards the corners of the wells that would result also explains the concentrated movement towards the corners in the later stages of drying.

The particle tracks and velocity profiles showed the same pattern of movement for all three solvents, the only real difference being the speed of particle movement. The faster drying solvents gave faster particle movement during the drying. The particle tracks from single solvents are consistent with enhanced evaporation near a pinned contact line and in the corners of the drop, compared to the apex. To determine the full mechanisms behind particle transport however it is necessary to have information on the drop profile during drying.

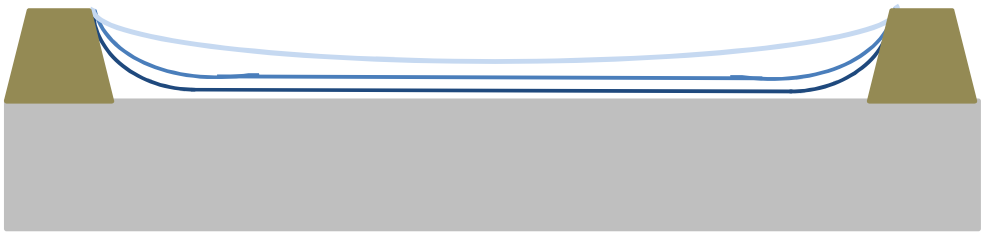

Figure 3.6: A schematic diagram showing the changing radius of curvature as the drying film thins. Darker blue lines represent later stages in the drying process.

3.3 Evaporation of Binary Solvent Systems

In this section the internal flows within binary solvent droplets of anisole + methyl benzoate and anisole + mesitylene drying in square wells are reported and the results are compared to the single solvent data. The drops were printed and imaged as described in chapter 2 section 2.1. When mixed with anisole the silica particles did not aggregate in the presence of mesitylene so particle tracking was possible.

Figures 3.7 and 3.8 show the surface tension and density as a function of composition for the two mixtures. Figure 3.7a does not show a smooth change in surface tension with increasing proportions of methyl benzoate, indicating non-ideal behaviour. The dip in surface tension and density at a proportion of 0.6 of methyl benzoate is not physically plausible and as such cannot be accurate. Repeats of this data set were taken both with the same sample and a different sample; all showed this dip. It is therefore likely the dip was a result of an error beyond the readings taken on one particular sample. The data in figure 3.7b show a smooth change in surface tension with increasing proportions of mesitylene, so not discounting ideal behaviour of the solution.

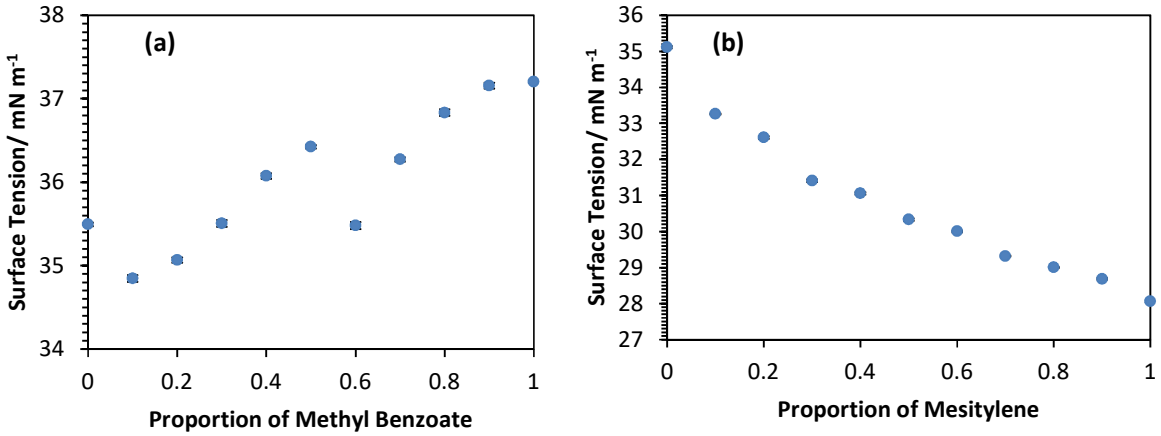

Figure 3.7: The relationship between surface tension and composition for the anisole + methyl benzoate (a) and anisole + mesitylene (b) mixtures. Proportions are quoted as a volume %. Error bars show the standard deviation in measurements. If error bars are not visible they are smaller than the size of the data points.

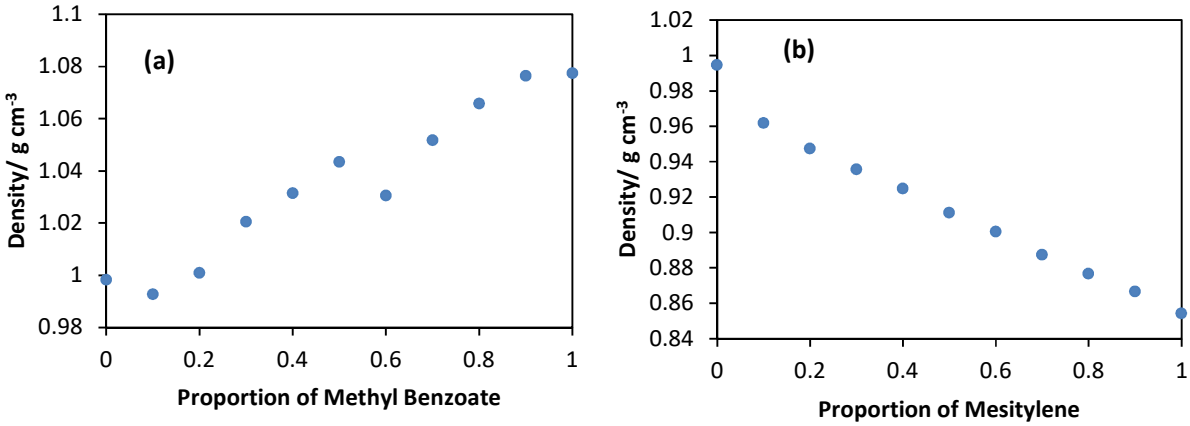

Figure 3.8: The relationship between density and composition for the anisole + methyl benzoate (a) and anisole + mesitylene (b) mixtures. Proportions are quoted as a volume %. The systematic error associated with density measurements was ± 0.001 g cm^{-3}.

The relationship between density and proportion of methyl benzoate in figure 3.8a should be smooth and as such the dip at 0.6 is unexpected. Density measurements on another anisole + methyl benzoate sample also showed this dip, though it was less severe. The presence of the dip is most likely due to errors outside the random errors associated with the measurements. To determine whether an error in density measurement had caused the dip at 0.6 in figure 3.7a the measured densities were plotted against the measured surface tensions. As density was used to determine the surface tension of the solutions, errors in density measurement would give errors in surface tension measurement. If an error in density was the cause of the dip at 0.6 in figure 3.7a the relationship between density and surface tension would be smooth. Figure 3.9 shows a linear relationship, though there was some spread in the data. Therefore the dip in surface tension at 0.6 in figure 3.7a is a consequence of an error in density measurement for that solution.

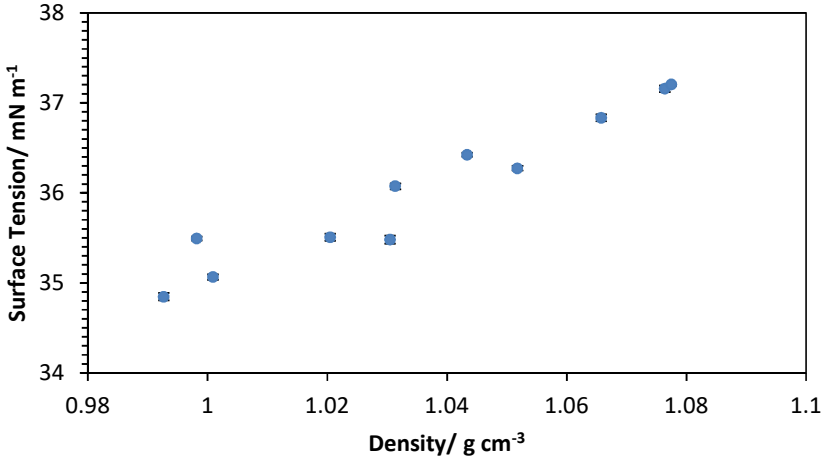

Figure 3.9: Plot showing the measured densities against the measured surface tensions for the anisole + methyl benzoate mixture. Error bars show the standard deviation in measurements. If error bars are not visible they are smaller than the size of the data points.

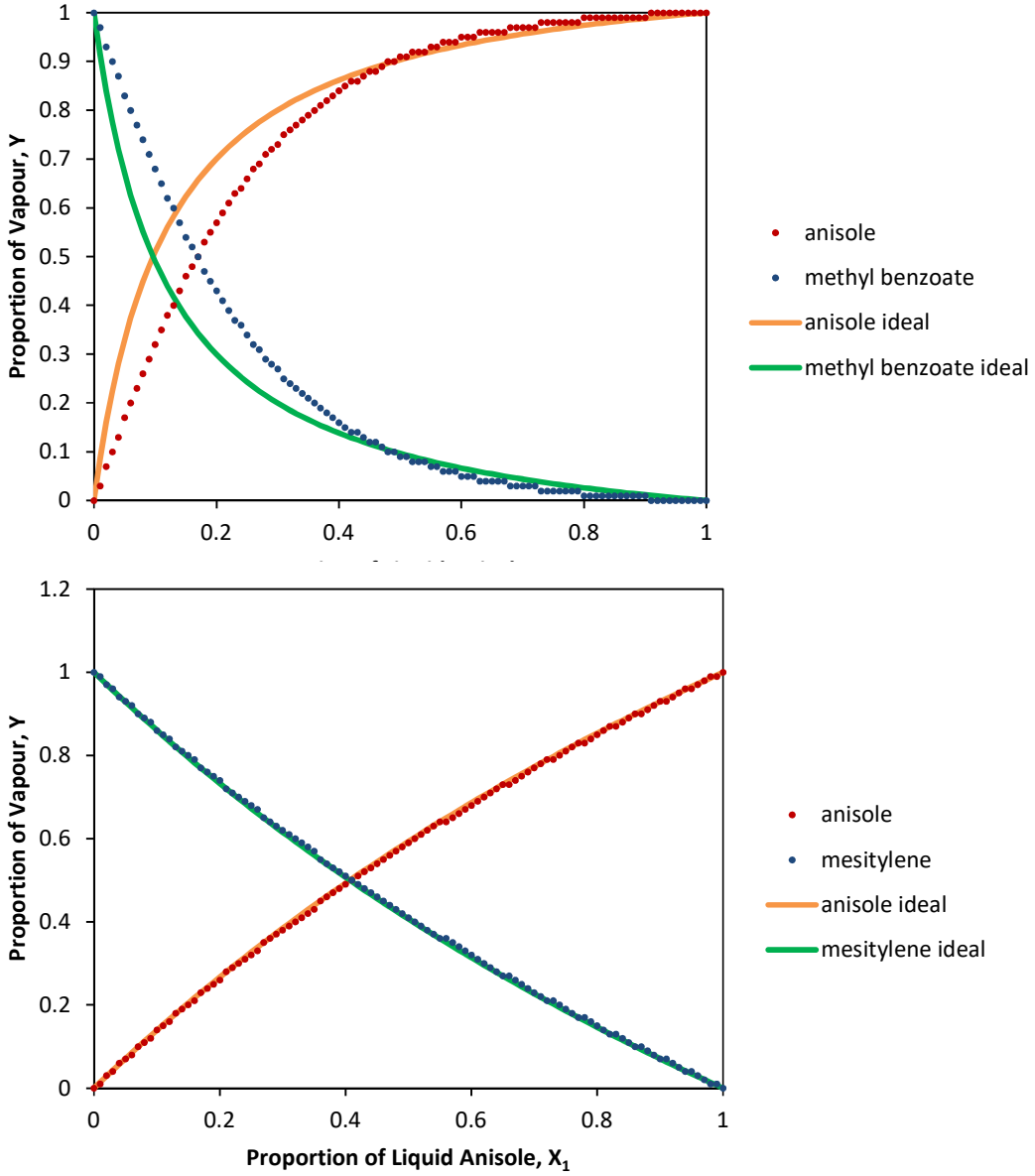

Figure 3.10: VLE curves[141] for the anisole + methyl benzoate (a) and anisole + mesitylene (b) mixtures. The apparent steps in the data are the result of numerical limitations in the computations.

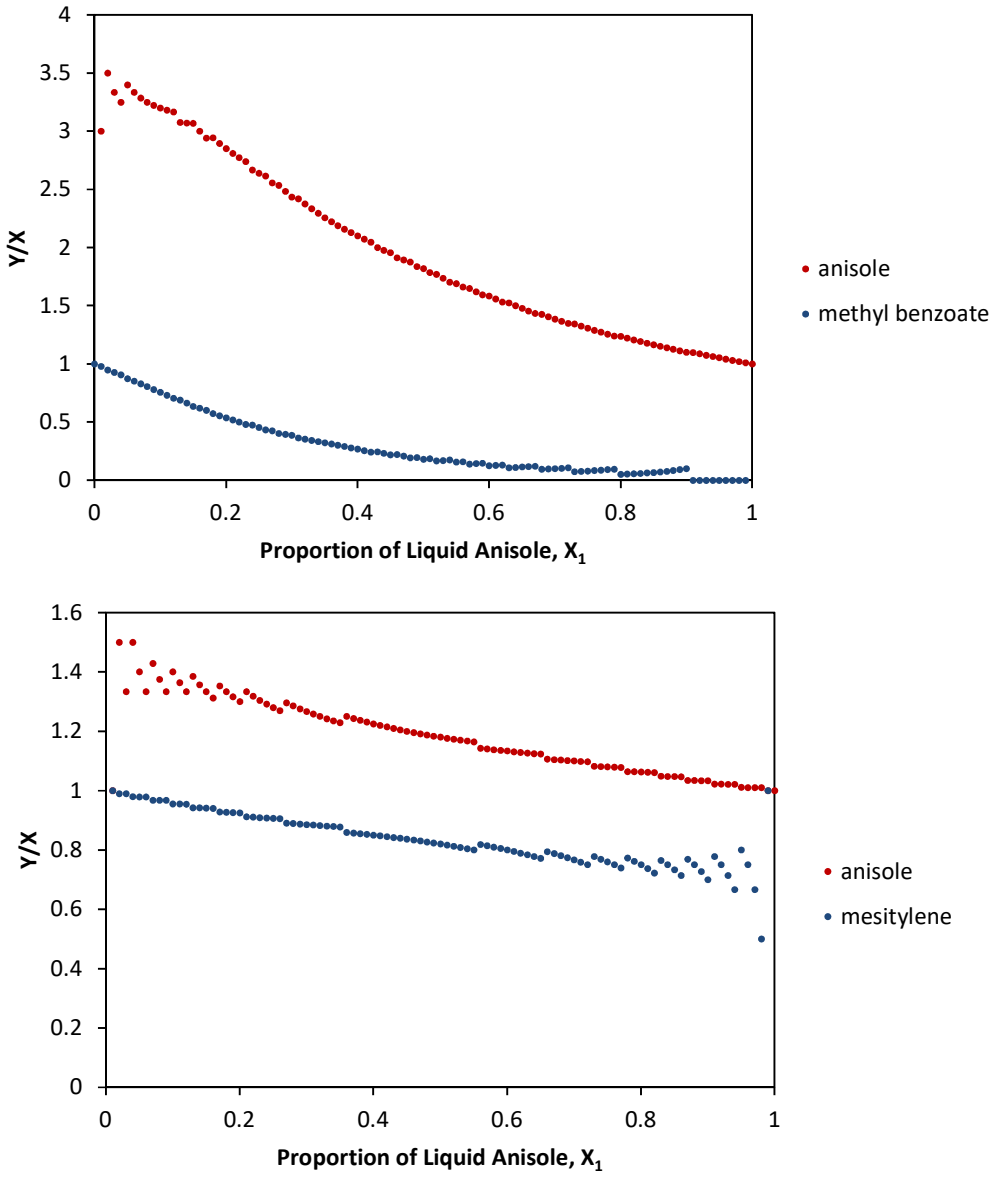

Figure 3.11: Proportion of each solvent in the vapour phase relative to the liquid phase for the anisole + methyl benzoate (a) and anisole + mesitylene (b) mixtures. The apparent steps and divergence in the data are a result of numerical limitations in the computations[141].

The vapour-liquid equilibrium (VLE) curves for anisole + methyl benzoate and anisole + mesitylene mixtures are shown in figure 3.10. These curves are calculated from Hansen Solubility Parameters (HSPs) and compared with the ideal behaviour. Apparent steps and divergence in the data are a result of numerical limitations in the computations. The anisole + methyl benzoate mixture shows deviations from ideal behaviour whereas the anisole + mesitylene mixture shows ideal behaviour. Figure 3.11 shows the ratio of solvents in the vapour phase to the liquid phase, $^{Y}/_{X}$, where Y is the proportion of the solvent in the vapour phase and X is the proportion of the solvent in the liquid phase for the two mixtures at all

compositions. Assuming the vapours are ideal, which is reasonable as we are a long way from the boiling points of the solvents and the vapour density is low, the larger Y/X value tells us which of the solvents is evaporating more quickly relative to the bulk concentration. In the case of both anisole + methyl benzoate and anisole + mesitylene, the calculations confirm the anisole is evaporating more quickly relative to the bulk at all proportions. However, in the case of anisole + mesitylene, as the vapour pressures of anisole and mesitylene are similar the difference in evaporation rates is not likely to be large.

The mixtures were chosen to give surface tension gradients, and so Marangoni stresses, in opposite directions. Anisole is the more volatile component in both mixtures so will be depleted at the contact line relative to the apex. Anisole has a lower surface tension than methyl benzoate so the highest surface tension in this mixture should be at the contact line with a lower surface tension at the apex, giving potential Marangoni recirculations as shown in figure 3.12a. In the case of anisole + mesitylene, anisole has the higher surface tension, so giving a higher surface tension at the apex of the drop relative to the contact line. Therefore anisole + mesitylene mixtures would be expected to give Marangoni recirculations as shown in figure 3.12b.

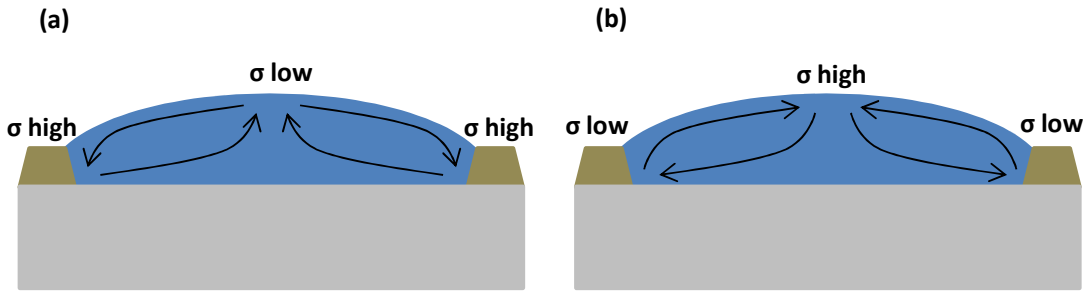

Figure 3.12: Schematic diagrams showing the potential direction of Marangoni flows in the anisole and methyl benzoate (a) and anisole and mesitylene (b) mixtures.

Particle tracking experiments for both solvent mixtures appeared to show the same pattern of particle movement during drying as the single solvents, there was no evidence of Marangoni driven flows in either case (figures 3.13 and 3.14). Both the particle tracks and velocity profiles suggested evaporation rate was enhanced at the contact line (and especially in the corners) relative to the apex of the drop and radial flow was apparent in the initial stages of drying. The pattern seen in single solvents of concentrated particle movement along the edges of the wells towards the corners was apparent in the later stages of drying. Videos relating to figure 3.13 are videos 4 and 5 on the attached disk.

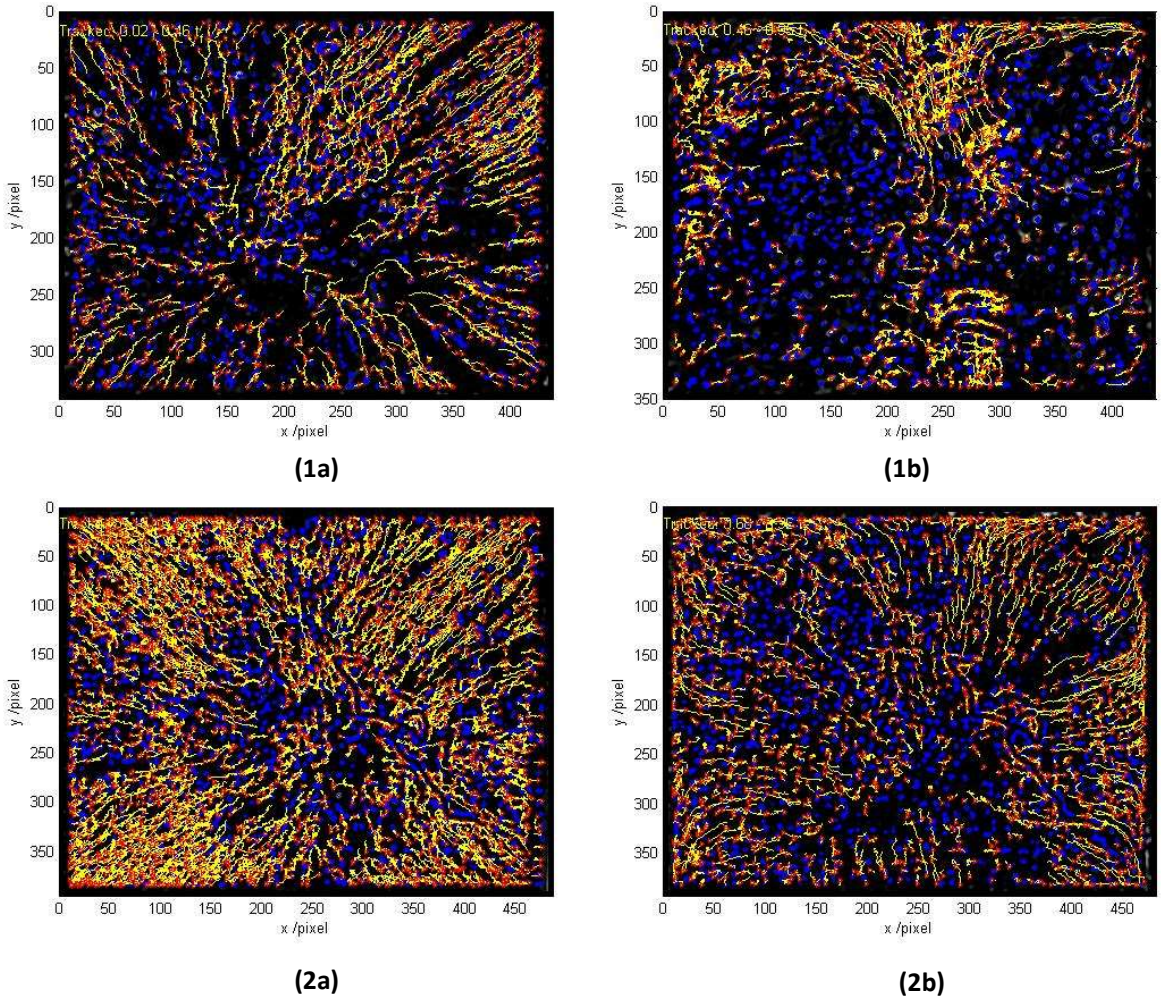

Figure 3.13: Particle tracks for the early (a) and late (b) stages of drying (early is first half of drying, late is last third of drying) in the anisole + methyl benzoate mixture (1) and the anisole + mesitylene mixture (2). Images were recorded at 750 fps with a shutter speed of 1.25 ms for the anisole + methyl benzoate mixture and at a frame rate of 1000 fps and shutter speed of 1 ms for anisole + mesitylene mixture. Blue spots represent particles which were stationary throughout the drying process, red spots represent the end of particle travel and yellow lines represent the direction of particle travel.

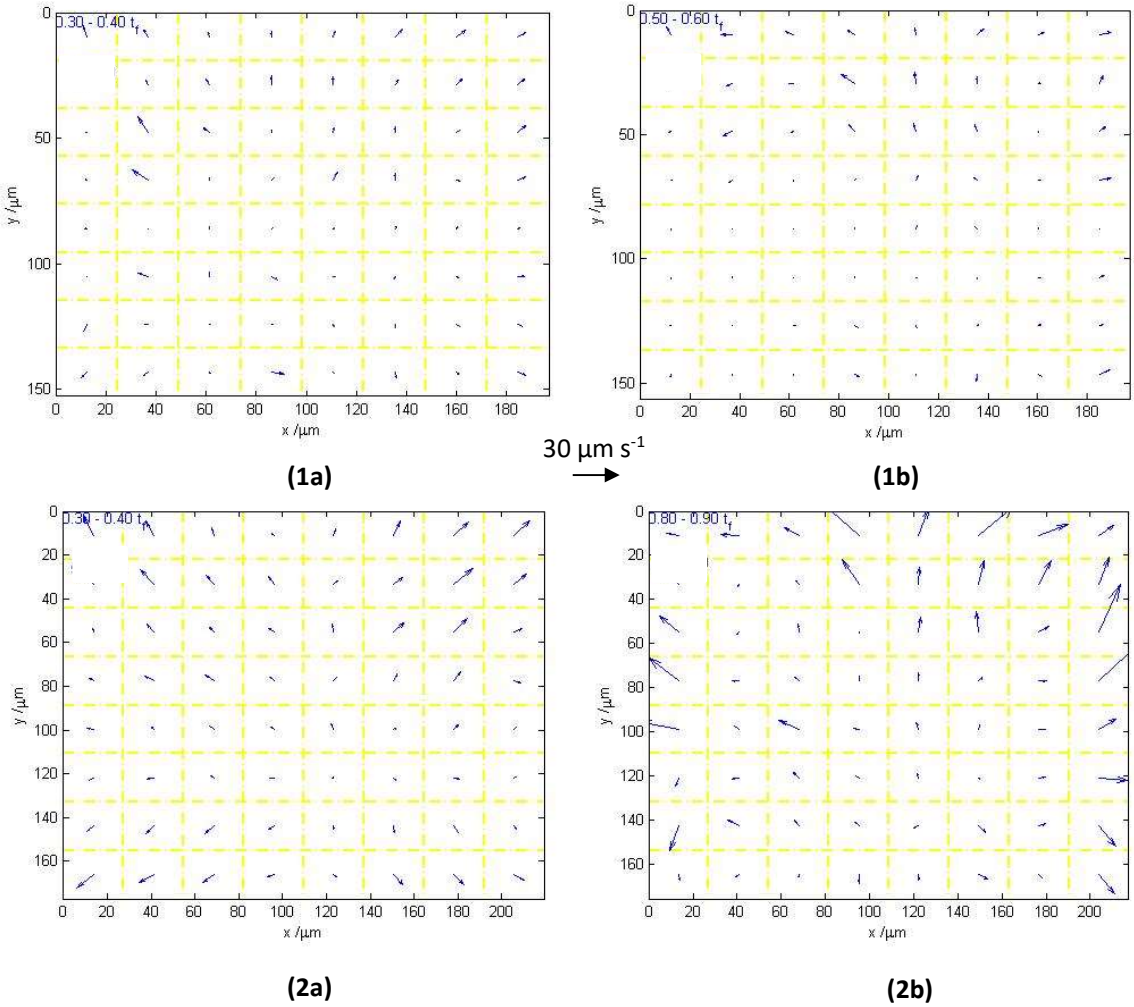

Figure 3.14: Velocity profiles for the anisole + methyl benzoate mixture (1) and the anisole + mesitylene mixture (2) in the early stages of drying (0.3 – 0.4 t_{dry}) (a) and the lates stages of drying (0.5 – 0.6 t_{dry} for anisole + methyl benzoate and 0.8 – 0.9 t_{dry} for anisole + mesitylene) (b). Images were recorded at 750 fps with a shutter speed of 1.25 ms for the anisole + methyl benzoate mixture and at a frame rate of 1000 fps and shutter speed of 1 ms for anisole + mesitylene. The central arrow shows the velocity scale for all four profiles.

The absence of recirculatory flows in drying binary mixtures was not necessarily indicative of the absence of surface tension gradients (though this is one possibility); a number of factors could have had an influence on the drying behaviour. It is possible Marangoni flows were not dominant over capillary flows, even if surface tension gradients were present. We could be observing Marangoni flows superimposed on larger capillary flows. In the case of methyl benzoate, $Pe \ll 1$ so diffusion will average out compositional gradients.

One factor which is likely to have had an impact on the formation of recirculatory flows was the relatively small amount of fluid each well could hold. The banks on the square substrates were untreated and so, due to the low surface tension of the solvents, did not retain fluid

within the well. Poor retention of the fluid meant the drop did not extend very high above the bank walls (5 µm at most). Viscous drag in a liquid film goes as $\left(\frac{du}{dh}\right)^2$, at the low Reynold's numbers relevant to the systems imaged here, Marangoni stresses and viscous drag forces are balanced. So at small film thicknesses (low drop heights) the velocity of Marangoni flows is also low; however the velocity of capillary flows accelerates as a film thins in the case of a pinned contact line. Therefore at low drop heights the velocity of capillary flows is likely to be competitive with the velocity of Marangoni flows and either could dominate particle transport.

One also needs to consider the size of the silica tracer particles relative to the film thickness. Once the drop reaches the level of the banks (1.5 µm) the 500 nm silica particles represent a significant proportion of the film thickness and they no longer represent the flow profiles correctly. As the silica particles show an average over different heights within the fluid film any flows present cause the particles to rotate, giving extra forces.

3.4 Gold Particles

The 500-nm silica particles used in tracking experiments do not accurately represent flow profiles once the fluid film dries below the level of the banks, as they become a significant size compared to the thickness of the film. Silica particles smaller than 500 nm in radius are not visible with the current illumination source as silica is not very strongly scattering and the intensity of forward scattered light reaching the camera is insufficient to be seen. To use smaller silica particles a more intense light source would be necessary. Gold on the other hand is strongly scattering and easier to view under a microscope due to localised surface plasmon resonance (LSPR).[142–144] Surface plasmon resonance (SPR) is the coherent oscillation of electrons within the conduction band of some materials such as gold.[142–144] Oscillations occur on excitation with electromagnetic radiation (visible light in this case). When the light source is interacting with particles much smaller than its wavelength (as is the case here) plasmon oscillations occur locally around the particles in question, known as localised surface plasmon resonance (LSPR).[142–144] The presence of LSPR in gold nanoparticles enhances the amount of light seen as forward scattered light in particle-tracking measurements, and so it is possible to see gold particles of a smaller radius than particles from most other materials.

In order for particles to accurately follow fluid flows once the drop dries below the bank walls, they need to be a size of the order of tens of nm. Gold represented the only realistic option for particles which would still be visible with the current experimental set-up; 50 nm gold particles were investigated as possible tracer particles, however, as the lowest resolvable particle size (due to the pixel size on the camera) was of the order of 400 nm the gold particles would appear to be approximately 400 nm in diameter. The limit on pixel resolution also meant it was not possible to tell whether one particle was being tracked or whether aggregates of particles were present within that pixel space. In these experiments, 50-nm gold particles were dispersed in anisole as described in chapter 2 section 2.2 and particle tracking was attempted.

Initial experiments used flat substrates (glass cover slips) to determine whether the particles were visible under the inverted microscope. A Pasteur pipette was used to place a large drop (the order of millimetres) of anisole containing 50-nm gold nanoparticles on the glass surface. Cover slips were cleaned before use as described in chapter 2 section 2.3. No particles could be seen in the bulk of the fluid, however once the plane of focus was altered to the substrate rather than the drop it became apparent the gold particles were adhering to the glass (figure 3.15). On observing the glass vial the particles were provided in, it was obvious the particles

had also been sticking to the glass in the vial. Adhesion between the particles and the glass was occurring and no tracking experiments could take place. However the particles could be seen which was encouraging. As the banked substrates (square) were coated in an ITO film over the glass base, some drops were printed onto the square substrates to determine whether the gold nanoparticles would also adhere to the ITO. On printing the drops it was apparent all particles were adhering to the ITO base as they had been on the glass cover slips. The sedimentation rate of the gold particles in the anisole was approximately 25 nm s^{-1} and as such it is not likely they were settling out during the drying time. However, $D \sim 1 \times 10^{-11}$ m^2 s^{-1} for the gold nanoparticles and as such they will diffuse ~4 µm in 1 s. The particles will therefore diffuse along the depth of a printed drop in ~1 s and adhere to the substrate.

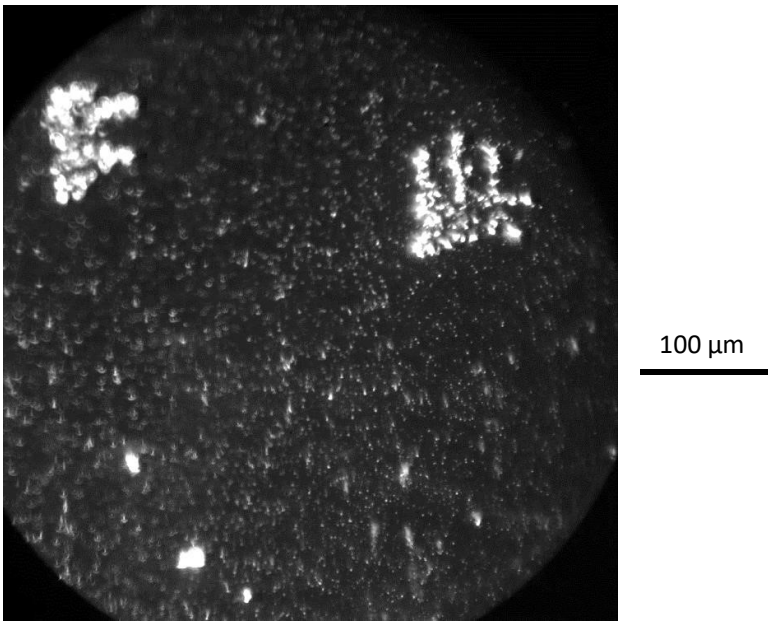

Figure 3.15: Image showing the gold nanoparticles adhered to the glass cover slip after a large drop had been pipetted onto the surface. The fluid was still present when the images were taken but no particles were suspended in the fluid. The large bright areas were a result of scratches on the glass.

To prevent nanoparticles from adhering to the glass, the cover slips were treated to make them hydrophobic (as described in chapter 2 section 2.3). Once again large drops were deposited onto the cover slips using a Pasteur pipette. The treatment of the substrates did prevent the particles from adhering to the surface and they could be seen moving through the fluid. However the intensity of forward scattered light was too low to track the particles at sensible frame rates. Particles could be seen well enough to track at a frame rate of 50 fps with as long a shutter time as possible (20 ms) but the frame rates necessary for particle tracking were up to 2000 fps depending on the solvent used. When the frame rate of the camera was increased past 50 fps and consequently the shutter time was reduced the particles

were no longer visible in the images. To make particles visible at higher frame rates a more intense light source is necessary.

Silanisation of the square wells was attempted as described in chapter 2 section 2.3 to prevent particles from adhering to the ITO. A number of different timescales for treatments were tested and coating was attempted both in solution and in the gas phase. Unfortunately all of the methods for silanisation were unsuccessful; in all cases the polymer from the bank walls appeared to have dissolved and been re-deposited in clumps on the base of the wells (figure 3.16). Therefore we have not been able to treat bank structures sufficiently to make them hydrophobic and as such the gold nanoparticles continued to adhere to the base of the wells. Even with a more intense illumination source, particle tracking within the bank structures will not be possible until the adhesion between the ITO and the particles is prevented.

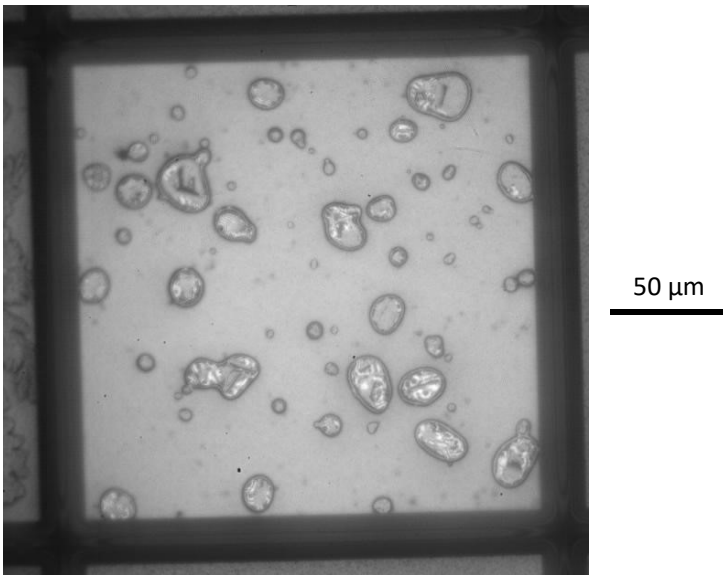

Figure 3.16: Image showing the deposits of bank wall material left on the base of the square substrates after silanisation of the surface had been attempted.

3.5 Summary

Particle tracks for all single solvents within square wells exhibited the same behaviour: initial radial flow followed by concentrated particle movement towards the corners of the wells in the later stages of drying. The initial radial flow in all solvents was due to the pinning of the contact line and akin to the evaporation of drops on flat substrates. The reason for concentrated particle movement towards the corners of the wells at the end of drying was likely due to the two dimensional curvature in the corners relative to the one dimensional curvature along the straight edges.

Particle tracks for two solvent mixtures were investigated: anisole + methyl benzoate and anisole + mesitylene. Both mixtures showed the same pattern of particle movement during drying as the single solvents, with initial radial flow followed by concentrated movement towards the corners of the wells. The ideality of the mixtures was considered: anisole + methyl benzoate exhibited non-ideal behaviour whereas anisole + mesitylene showed ideal behaviour.

The use of 50-nm gold particles as tracer particles was considered as silica particles were no longer following flows once $a < h$ (ie. once the fluid dried below the level of the banks). Gold particles were visible but not at frame rates high enough to enable particle tracking and adhered to the bare glass and ITO substrates. Treatment of the substrates was necessary to prevent adhesion; the banks did not survive the silanisation treatment.

None of the data collected for this chapter was particularly surprising; thus far drops drying in banked structures appear to behave in a manner similar to those on flat substrates. The contact line is pinned and flows are mainly radially outwards towards the contact line with enhanced flow towards the corners of the wells.

4. Drop Profile Development During Drying

4.1 Introduction

Predicting the final deposit morphology of inkjet printed drops is essential for most applications. When printing active materials for OLED devices, a knowledge of the mechanisms behind drying is necessary to produce commercially viable devices. The PTV carried out in chapter 3 was not very informative about the way drops dry within wells. An understanding of the drop profile, *h(x,y)*, during drying and where the contact line is pinned (or not) is helpful in determining the mechanisms behind particle transport and final deposit morphology. Studies of drops drying on flat substrates have shown the pinning of the drop as it dries is an important factor in deposit morphology; more specifically the drying mode determines whether or not a ring stain forms.[18,19] Therefore it is important to know whether or not the contact line recedes across the ITO base during drying , which is undesirable in the case of OLEDs, but also whether the contact line moves up and down the banks during drying (determines the sign of curvature at the interface).

This chapter reports the use of interferometry to provide real-time information on the changing drop profile during drying. Interferometry allows the height of the drop to be mapped across the majority of its surface at all times during the drying, so giving a three-dimensional picture of the profile.[126] Solvents are compared and differences related to solvent properties. The LED used for interferometry has a finite coherence length, which limits the drop height that can be resolved.[127] As the coherence limit of the light source is approached the miscounting of fringes in the analysis can occur and the data appears to be noisy for early drop profiles. Measurements taken early on in this investigation used light with a coherence length of approximately 7 μm and consequently early profiles for these measurements appear quite noisy. Later, a narrow-width bandpass filter was used to double the coherence length to approximately 15 μm and early drop profiles became much smoother. Fringes close to the walls cannot be resolved late in the drying because they are too closely spaced. However, if the film height in the centre of the wells is known, extrapolation back to the walls can be performed by manually counting the fringes outwards in individual frames. Extrapolation back to the walls has been carried out for selected data throughout this thesis.

In this chapter the drying of six organic solvents in wells is discussed. The complete drying process was recorded in each case to build up a three-dimensional drop profile with time. Drying was recorded in all three substrate geometries (square, oval and circular) though the majority of the measurements were in the square wells.

4.2 The Effect of Drying Speed on Drop Profile in Square Wells

Drops were printed and imaged as described in Chapter 2 section 2.1 and analysis of the images was carried out as described in section 2.5. Square substrates were used as described in section 2.3. The solvents investigated were anisole, methyl anisole, dimethyl anisole, methyl benzoate, mesitylene and o-xylene. The properties of the solvents are shown in table 4.1.

Table 4.1: Properties of aromatic solvents at 25 ^{o}C.

Solvent	Surface Tension/ mN m^{-1}	Density/ g cm^{-3}	Viscosity/ mPa s	Vapour Pressure/ kPa
Anisole	34.96[70]	0.990[70]	1.001[70]	0.477[70]
4-methyl anisole	32.88 ± 0.05	0.971	n/a	n/a
3,4-dimethyl anisole	32.41 ± 0.05	0.962	n/a	n/a
Methyl benzoate	37.27[70]	1.085[70]	1.958[70]	0.051[70]
o-xylene	29.60[70]	0.876[70]	0.747[70]	0.876[70]
Mesitylene	28.05[70]	0.861[70]	0.916[70]	0.327[70]

The drop profile in the early stages of drying was the same for all solvents; the drop sat above the walls in the shape of a quasi-spherical cap with distortions near the walls to maintain constant mean curvature (figure 4.1a).

Data for the drying of all solvents is provided in appendix A though only data for the extremes of behaviour are shown here. The initial quasi-spherical cap shape of the drop, combined with the apparent pinning of the contact line to give a constant contact area, explains the presence of the radial flows seen in the particle tracks from the early stages of drying.[18,19] After the initial quasi-spherical cap was formed, drops for all solvents then dried down with a pinned contact line towards the level of the bank tops (figure 4.1b) as the corners of the banks were lower in height than the straight edges the fluid was never completely flat. For all solvents the contact line then remained pinned at or near the top of the banks until the final stages of drying, when the fringes can no longer be resolved.

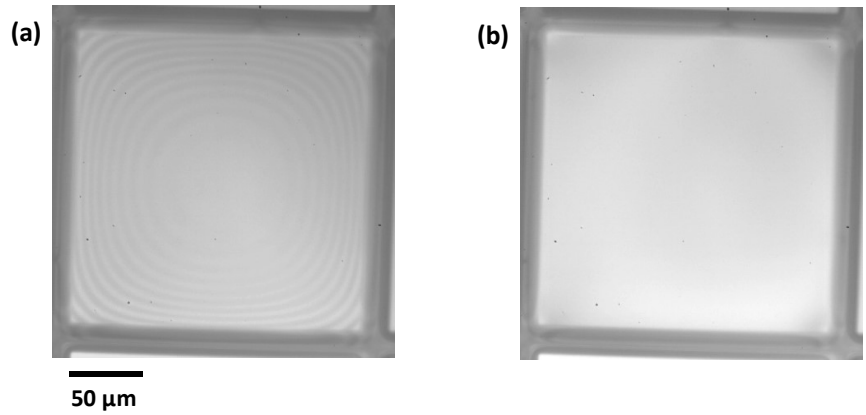

Figure 4.1: Images showing a dimethyl anisole drop sitting above the walls in the form of a quasi-spherical cap (a) and the same drop then at the same level as the bank tops (b).

The pinning of the drops at the bank tops makes the later stages of evaporation within wells, which are many times wider than they are tall, analogous to the drainage of thin liquid foam films which have planar lamellae between tightly curved Plateau borders. Drainage of the thin film is driven by the negative capillary pressure in the curved region. In a foam the liquid then drains, through the network of plateau borders, by gravity. Here it is lost by evaporation.

Many researchers have developed models which describe transport processes within draining thin films. Reynolds[145] developed a solution for Newtonian fluids flowing between two parallel-plane disks that were being forced towards one another. Reynolds' theory has been applied by a number of researchers.[146,147] Experimental observations of draining thin liquid films have shown they are often of non-uniform thickness, a thick region or "dimple" forms in the centre separated from the Plateau border by a thinner "barrier ring".[148–150]

In 1962 Frank and Mysels[148] presented a hydrodynamic theory for the profile and evolution of a dimple. They found the rate of thinning in the barrier ring was similar to that predicted by Reynolds but the rate of thinning in the centre was much slower. The model presented by Frank and Mysels was in reasonable agreement with the experiments carried out by Platikanov in 1964.[149]

In 1992, Joye et al[150] developed a model to describe the entire process of dimple formation and drainage which was in agreement with experiments by Scheludko.[151] Joye et al used a dimensionless parameter, C_R, to represent the ratio of the modulus of the maximum curvature in the dimple to the modulus of the curvature in the meniscus, analogous to the radius of curvature of the drop as a whole. As C_R was proportional to the half-thickness in the centre it did not remain constant during the draining process. The radius of curvature in the dimple represents the driving force for flows from the centre to the periphery of the drop whereas the curvature in the meniscus represents the driving force for flows from the periphery to the meniscus of the film (figure 4.2). If the radius of curvature in the dimple is bigger than the

curvature in the meniscus, more liquid is pushed out of the periphery into the meniscus than can be compensated for by the amount drained from the centre due to capillary suction and a dimple forms. The argument by Joye at al does however suggest a dimple should always form as if there is no dimple the radius of curvature in the dimple is 0.

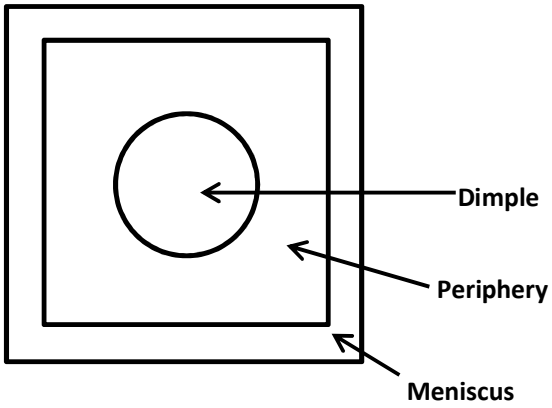

Figure 4.2: A schematic showing the location of the dimple, periphery and meniscus of the film according to Joye et al.

Once the drop dried below the level of the wall tops the profile of the film became highly dependent on the evaporation rate of the fluid. For the slower drying solvents (dimethyl anisole, methyl benzoate and mesitylene) the drop remained pinned at the wall tops and took the shape of an inverted quasi-spherical cap. In the last quarter of drying the centre of the drop then flattened out to give a flat central region which curved steeply upwards at the edges to the wall tops. This flattening was likely because as the film thins the resistance to flow increases and a larger Laplace pressure difference is needed to drive capillary flow to the edges. Consequently the mean curvature in the centre of the well decreases. Images from drying and the profile of a dimethyl anisole drop at different stages during drying are shown in figure 4.3; it showed a U-shaped final film profile. The video relating to figure 4.3 is video 6 on the attached disk. The profile in the later stages of drying provided an explanation for the particle movement seen in Chapter 3 as at the end of drying there was only fluid left around the edges of the wells. Concentration of particle movement towards the corners was a result of curvature in the drying film; the pinning of the drops at the wall tops resulted in a negative Laplace pressure across the drop surface which caused drainage from the centre of the wells towards the edges. In the corners the curvature was two-dimensional compared to the one-dimensional curvature along the straight edges and so movement became concentrated towards the corners.

To determine where the drop is pinning on the banks, extrapolation of the data can be performed. The image at 20 s in figure 4.3a is analogous to the curve at 20 s in figure 4.3b. The height of the film in the centre of the wells in this image is 0.39 µm. If we count the fringes in the image from the centre to the banks, the height can be extrapolated to the banks. There are seven bright fringes between the centre and the contact line, which equates to a change of 1.1 µm in height. As the film in the centre of the wells is 0.39 µm deep the film height at the contact line is therefore 1.49 µm, which is the height of the banks. Therefore the drop appears to be pinning at the wall tops. The same extrapolation for the image and plot at 30 s gives a film height at the walls of 1.4 µm; suggesting the fluid recedes slightly down the wall during drying but only in the late stages of drying.

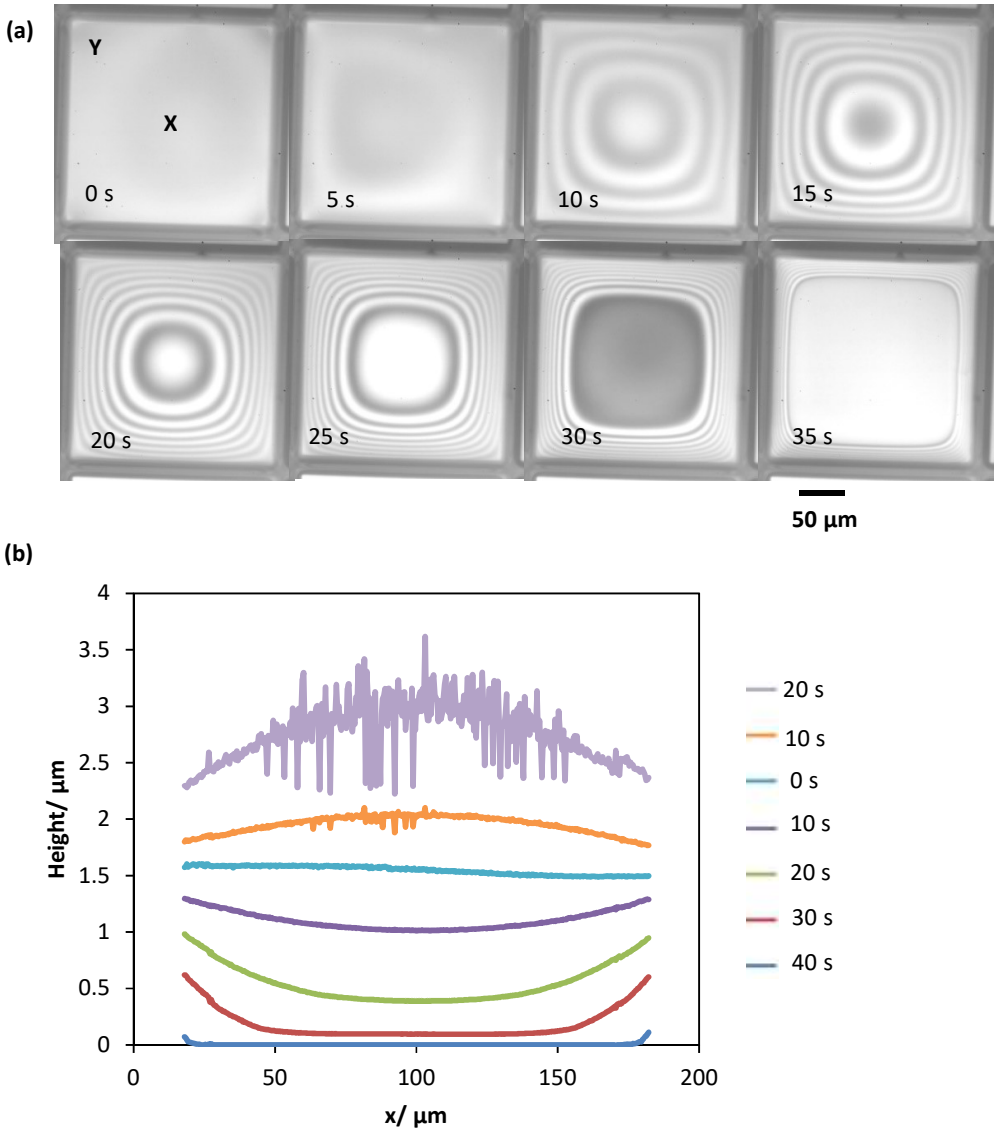

Figure 4.3: Images showing the progression of a drying dimethyl anisole drop (a) and a plot showing a cross section of the profile throughout the drying (b). Images were recorded at 50 fps with a shutter speed of 1 ms. In the image sequence zero time has been defined as when the fluid is on average level with the banks. Total drying time for the drop was 77 s. Cross sections were taken horizontally across the centre of the drop.

Figure 4.4 shows the change in height of the dimethyl anisole drop in the centre (X in figure 4.3a) compared with the top left intermediate region (Y in figure 4.3a). Figure 4.4 shows that the rates of thinning are almost constant until $t \sim 10$ s with the rate of thinning being faster in the centre than at the edge despite faster evaporation near the edge. Therefore there must be outward capillary flows present in the drying drop. At $t \approx 10$ s the thinning in the centre seems to accelerate before it slows down sharply at $t \approx 15$ s and hence the thinning at the edge accelerates (since the total evaporative flux is approximately constant).

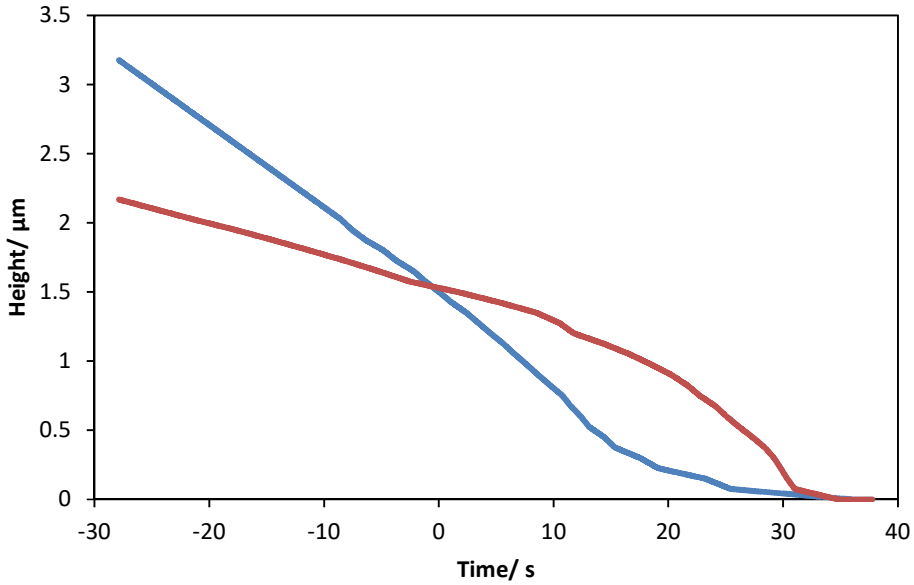

Figure 4.4: The relationship between drop height and time for the dimethyl anisole drop imaged in figure 4.3 in the centre (blue, location marked by X in figure 4.3a) and the top left intermediate region of the drop (red, location marked by Y in figure 4.3a).

The more volatile solvents (anisole, methyl anisole, o-xylene) dried in a different way. The drop still remained pinned at the wall tops but, as drying progressed, a dimple formed in the centre of the wells whereby thinning became fastest in the intermediate regions and slower in the centre (figure 4.5). The dimple often began to form before the drop had dried below the level of the banks. The plot in figure 4.5b shows the faster drying solvents had the thickest fluid region in the centre of the well and at the edges with the thinnest fluid region in the intermediate areas, giving a W-shaped final film profile. The video relating to figure 4.5 is video 7 on the attached disk. Extrapolation of the image and curve at 0.4 s in figure 4.5 gives a film height at the walls of 1.32 µm suggesting the fluid has receded down the banks slightly during drying though the banks may not all be identical, the 0 s image in figure 4.5a gives a height of $\sim$ 1.4 µm which suggests the bank height is slightly lower than the quoted 1.5 µm.

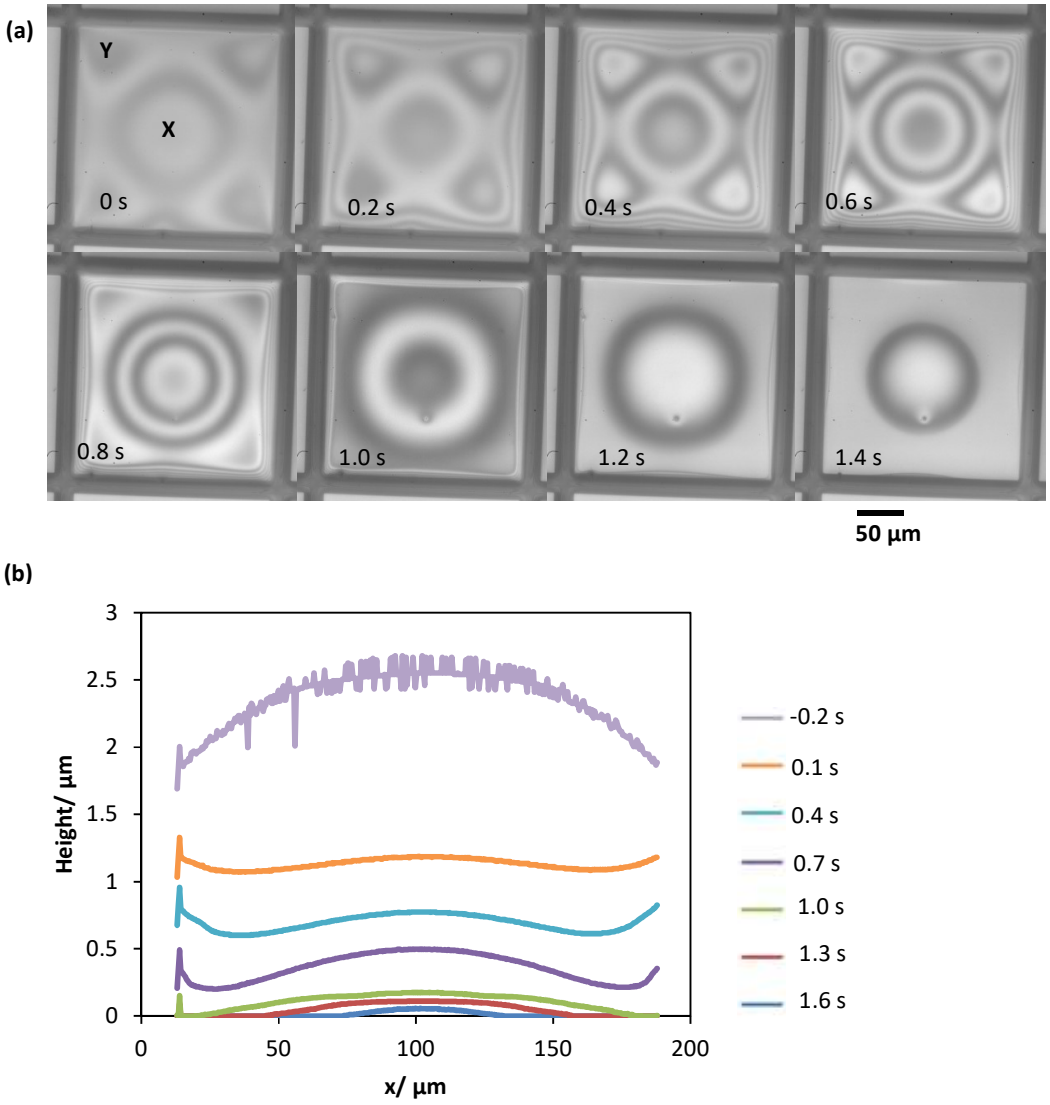

Figure 4.5: Images showing the progression of a drying anisole drop (a) and a plot showing a cross section of the profile throughout the drying (b). Images were recorded at 500 fps with a shutter speed of 1.11 ms. In the image sequence zero time has been defined as when the average height of the drop is equal to the average height of the bank. Total drying time for the drop was 4 s. Cross sections were taken horizontally across the centre of the drop.

Evaporation of a drop with a pinned contact line causes a Laplace pressure from the centre towards the edges to drive a flow of liquid, giving less negative curvature in the centre of the well than at the edges. This is true of all solvents and seen by the flattening of the centre of the film in slower drying solvents. The initial non-uniformity then appears to be amplified in the fast drying solvents as drying progresses to give dimple formation (figure 4.6). Dimple formation in fast evaporating drops within wells is analogous to the dimple formation reported by Joye et al[150] .

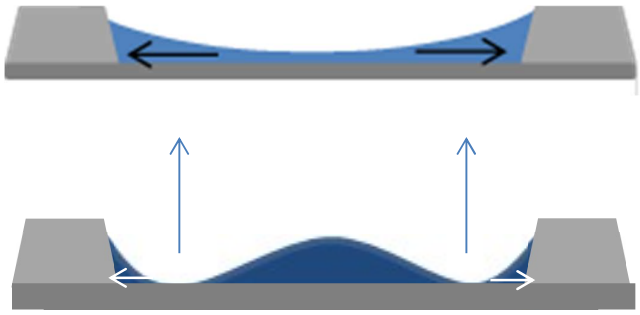

Figure 4.6: Schematic diagrams of capillary drainage from the centre of the wells (top) and consequent dimple formation in the faster drying drops (bottom).

Figure 4.7 shows the change in height of the anisole drop in the centre (X in figure 4.5a) compared with the top left intermediate region (Y in figure 4.5a). It shows that the centre of the drop is higher than the intermediate regions for the entire drying process, unlike the data in figure 4.4. The data in figure 4.7 is consistent with the pinning of the drop at the bank tops and W-shaped profile progression from there. The rate of thinning in the centre was initially faster than the intermediate regions until $t \approx -0.3$ s where the rate of thinning became equal. At $t \approx 0$ s the rate of thinning in the centre became slower than in the intermediate regions for most of the remainder of drying.

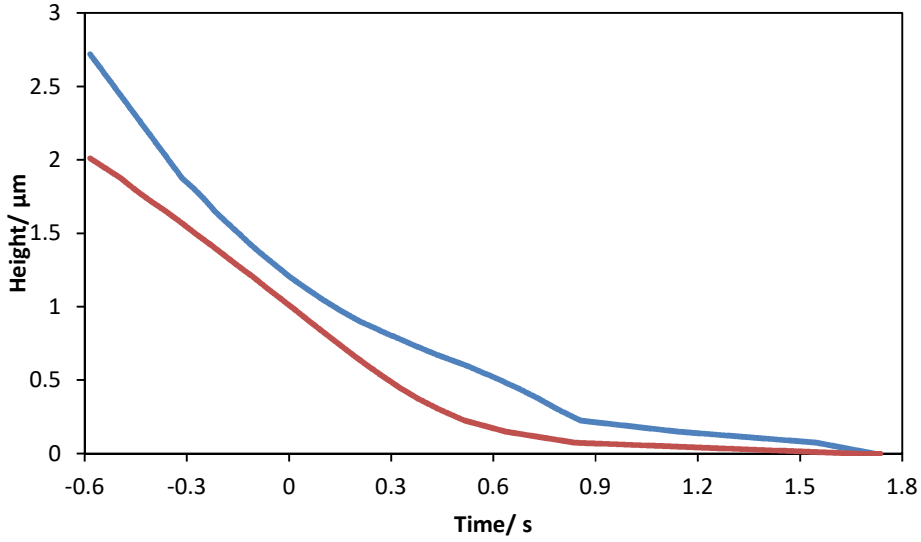

Figure 4.7: The relationship between drop height and time for the anisole drop imaged in figure 4.5 in the centre (blue, location marked by X in figure 4.5a) and the top left intermediate region of the drop (red, location marked by Y in figure 4.5a).

Thus far the solvents investigated have been separated into fast and slow drying solvents but in reality the distinction between 'fast' and 'slow' is gradual. The evaporation rate of the

printed drops was influenced by a number of factors including the ambient temperature and the distance between the printing nozzle and the drying drop (which affects the solvent vapour pressure around the drying drop). The most important factor in determining the shape of the film profile during drying was the speed at which the drop evaporated under experimental conditions and not the identity of the solvent. To determine the relationship between dimple formation and evaporation rate, the maximum dimple height (h_{max}) was measured for each drop. h_{max} was defined as the maximum difference between the highest and lowest points on the dimple during the drying process (figure 4.8). As there was some uncertainty in the initial drop volume due to variability in the volume of droplets delivered by the nozzle the mean evaporation rate was estimated by the difference in time from when the average height of the fluid was equal to the height of the bank to when the fluid was completely dry, divided by the wall height (1.5 µm in the square substrates). As the well size was constant, if the fluid just filled the wells the volume was also constant. h_{max} is plotted against evaporation rate in figure 4.9.

Figure 4.8: A schematic diagram showing the definition of h_{max} for solvents which dry to give a W-shaped film profile.

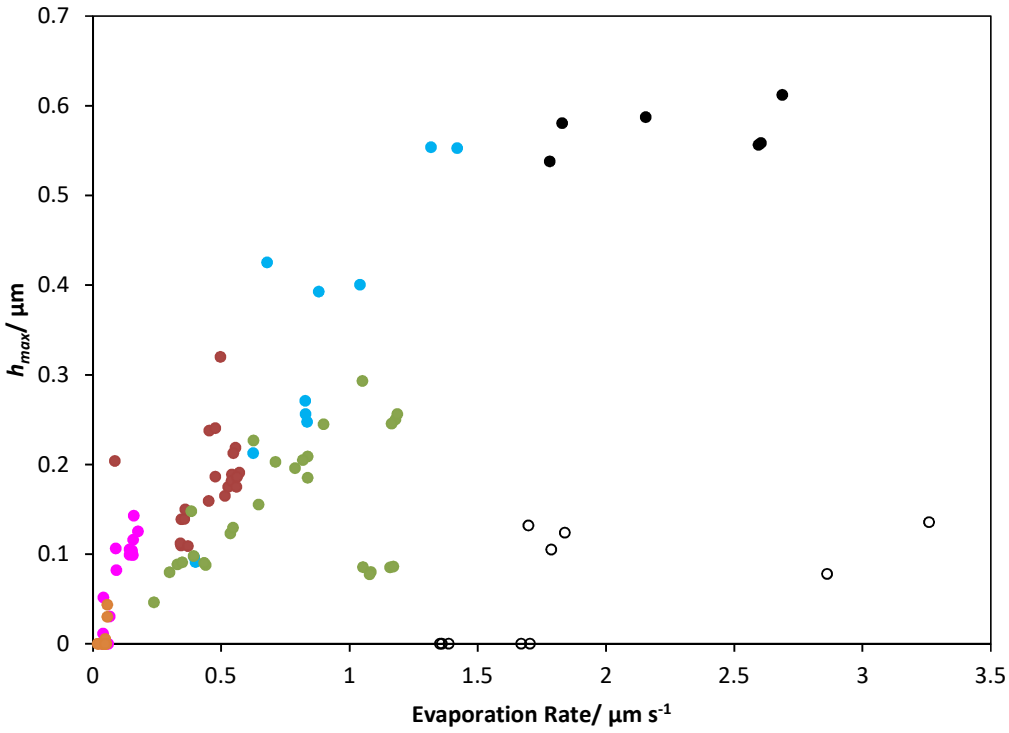

Figure 4.9: The relationship between h_{max} and evaporation rate for anisole (blue), methyl anisole (red), mesitylene (green), o-xylene (black), methyl benzoate (pink) and dimethyl anisole (orange) drying in square wells. Each point represents a single drop, open symbols showed qualitative differences in the drop profile during drying.

Figure 4.9 shows that h_{max} increases with increasing evaporation rate independent of the identity of the solvent. Each point on the plot in figure 4.9 represents a measurement on a single drop; each solvent was imaged over a minimum of 3 different days with 5 measurements per day. Some of the solvents gave both U- and W-shaped final film profiles depending on the drying speed on the day, suggesting the evaporation rate was the important factor in profile development and not the identity of the solvent. The open symbols for o-xylene in figure 4.9 fell outside of the overall trend and showed a qualitative difference in the drying profile; these drops drained from the centre of the wells to give an M-shaped profile (figure 4.10). The centre of the drops dipped below the level of the banks before the edges had reached that level, showing apparent enhanced drainage from the centre of the drop. The Laplace pressure in the drying drop opposes M-shaped profiles so another mechanism must be responsible for giving enhanced drainage from the centre of the well. Possible external factors that could have influenced the drying of o-xylene drops are discussed in section 4.4.

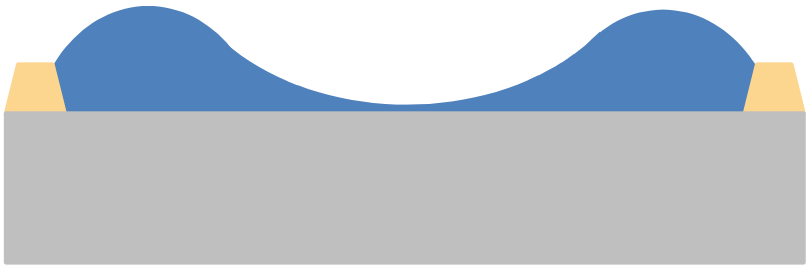

Figure 4.10: Schematic diagram showing the M-shaped profile progression observed in some of the drying o-xylene drops.

In summary, single solvents exhibit two drying profiles: U-shaped and W-shaped. The maximum height of the dimple in the W-profile increases with increasing evaporation rate. One of the key factors in profile development from drops printed into wells was the rate of evaporation combined with the pinning of the drop contact line. The behaviour in square wells contrasts with droplets on flat substrates, where the mode of drying is not controlled by the evaporation rate under isothermal conditions. The behaviour does however have analogies in the drainage of soap films.

4.3 Other Substrate Geometries

The data taken from the square substrates showed that the speed of evaporation determined whether or not a dimple formed during drying. However the square well geometry is not industrially relevant nor is it axisymmetric, which would be easier to model analytically or on a computer. This section describes the drying of single solvent drops within other well geometries. Drops were printed and imaged as described in Chapter 2 section 2.1 and analysis of the images was carried out as described in section 2.5. The substrates used were the oval and circular geometries described in section 2.3. Oval substrates had dimensions of 64 × 212 µm and circular substrates had a diameter of 134 µm. The oval shaped wells are industrially relevant so it is important to know whether the mechanisms behind drying are the same in oval wells and square wells. The circular wells are an axisymmetric system which provides data for comparison with axisymmetric models. The same solvents were investigated in all three geometries (section 4.2).

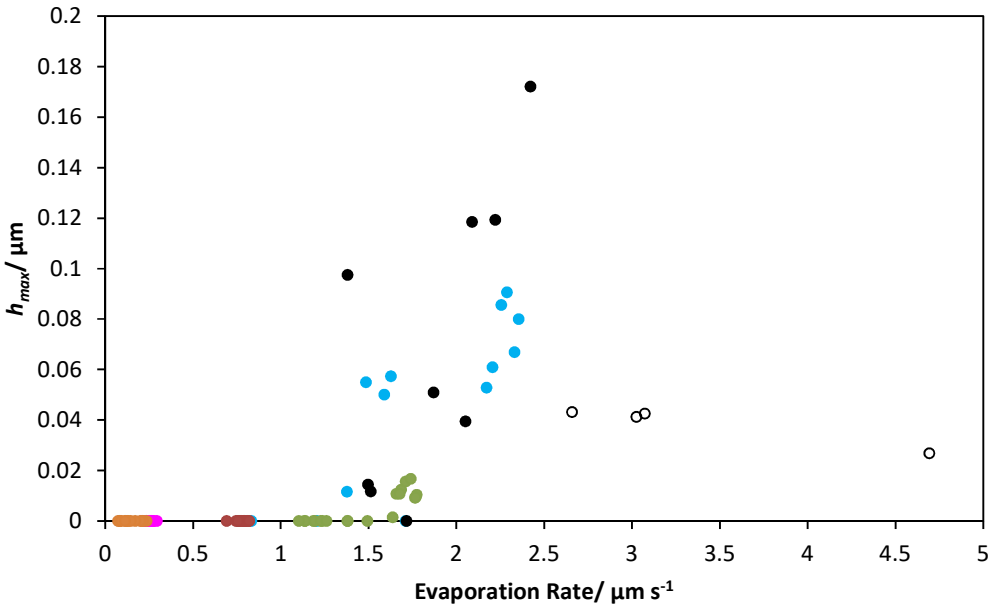

Figure 4.11: The relationship between h_{max} and evaporation rate for anisole (blue), methyl anisole (red), mesitylene (green), o-xylene (black), methyl benzoate (pink) and dimethyl anisole (orange) drying in oval wells. Each point represents a single drop, open symbols showed qualitative differences in the drop profile during drying.

Figure 4.11 shows the relationship between h_{max} and evaporation rate for the oval wells; overall they show a similar pattern of drying to the square substrates (figure 4.9) whereby slow

drying drops gave U-shaped deposits and fast drying drops gave W-shaped deposits. The relationship between h_{max} and evaporation rate did depend on geometry. In the oval wells (figure 4.11) faster evaporation rates were necessary to give dimple formation than in the square wells (1.4 µm s^{-1} as opposed to < 0.5 µm s^{-1}). Above this evaporation rate, h_{max} increased with evaporation rate up to 2.4 µm s^{-1}. For still faster evaporation the mode of evaporation changed to the M-shaped profile development seen in some o-xylene drops in the square wells, suggesting another mechanism was dominating profile development. There was a sharp transition between drying speeds which did not give dimple formation and those which did. The sudden switch from U-shaped to profile development to W-shaped development was different to the gradual appearance of W-shaped profile development in square wells (figure 4.7). Figures 4.12 and 4.13 show two film profiles for oval wells, one of which shows dimple formation and one which does not. As in the square wells the drops pin at the edges to give a constant contact area, though in the case of the oval wells the drops appeared to recede down the walls during drying as the curves do not all extrapolate back to the same point. Both figures 4.12b and 4.13b show flat topped film profiles for the earliest curves, in the case of the oval wells curvature was in the short dimension. In the oval wells, h_{max} was much smaller than in square wells (maximum value of 0.18 µm as opposed to > 0.6 µm) and the profile progression was different along the long and short dimensions of the pixel (figure 4.14b). No dimple was seen across the short dimension regardless of evaporation rate, most likely due to the small distance the fluid had to travel. Drainage due to the curvature in the film could come from the centre of the well in the short dimension where the distance the fluid had to travel was relatively short but could not come from the centre in the long dimension. It is also possible fluid which drained sideways out of the dimple could then drain along the long edge of the pixel through the meniscus. A second drainage pathway could provide an explanation as to why h_{max} values were smaller in oval than square wells as could the low level of curvature of the fluid in the oval wells compared to the square wells. It is important to note that the wall height in the oval wells was 2 µm as opposed to the 1.5 µm in square wells.

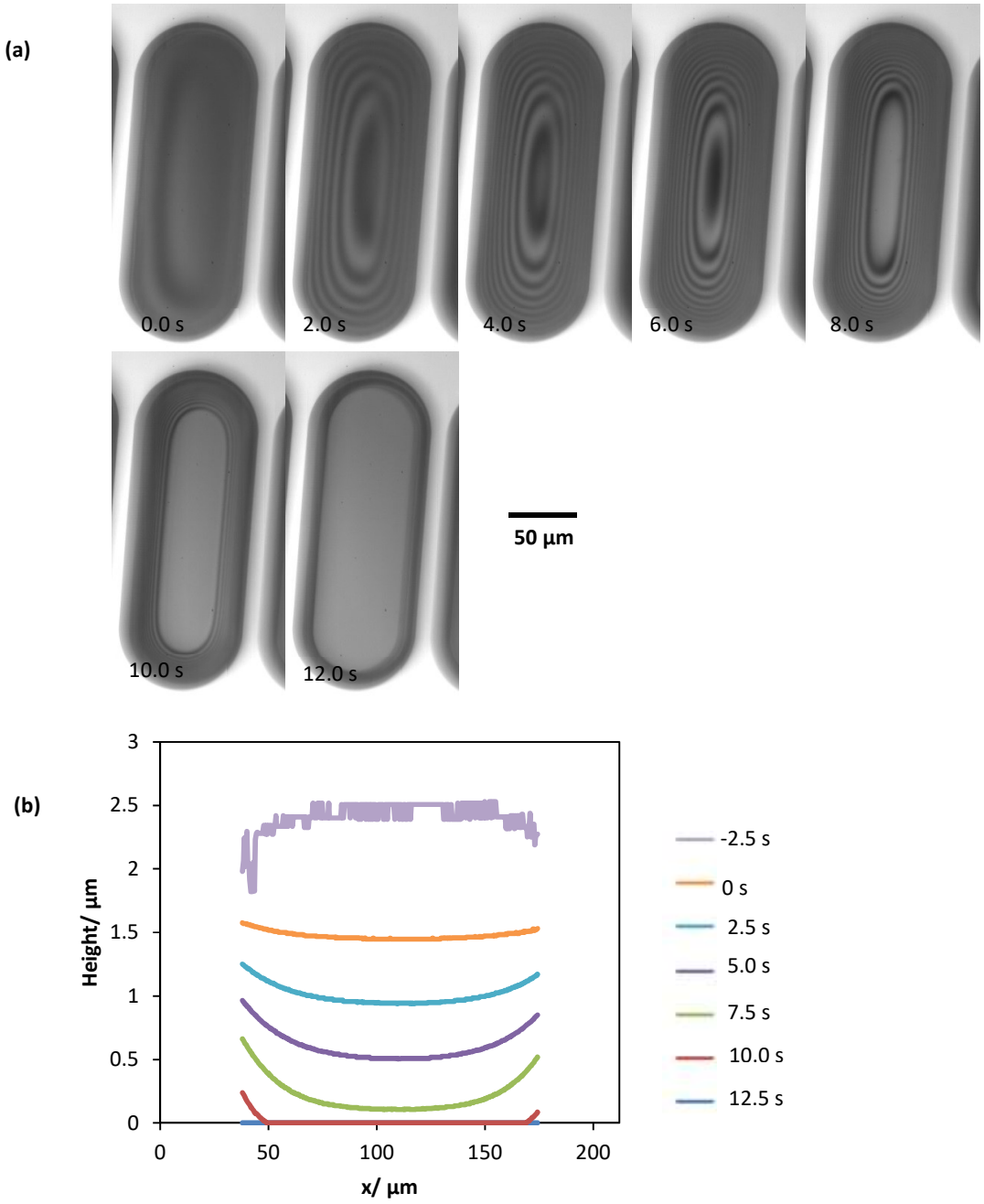

Figure 4.12: Images (a) and plots of profile progression (b) for dimethyl anisole in oval wells. Cross sections were taken vertically down the long dimension of the pixel. Total drying time for the drop was 16 s.

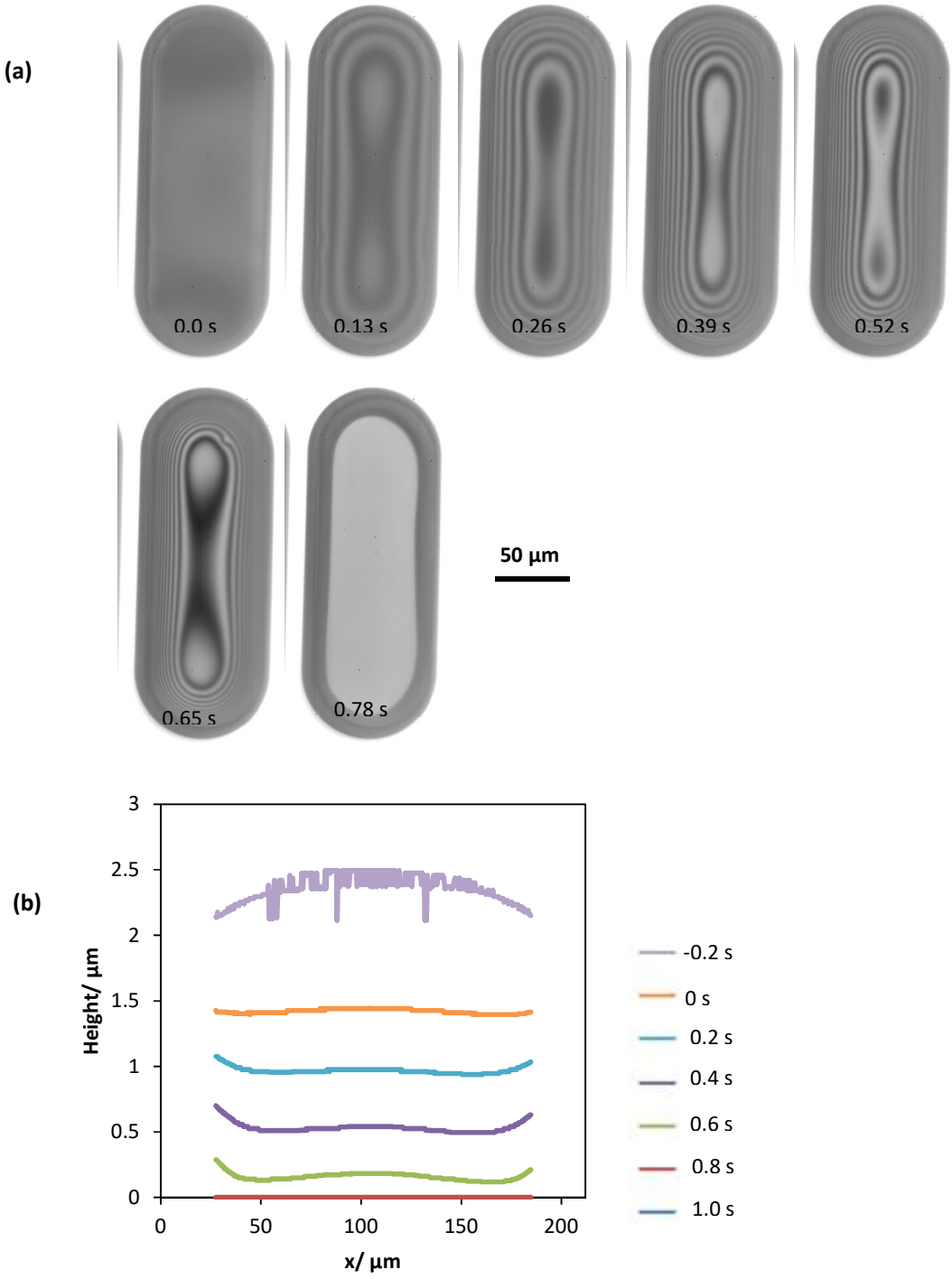

Figure 4.13: Images (a) and plots of profile progression (b) for anisole. Cross sections were taken vertically down the long dimension of the pixel. Total drying time for the drop was 5 s.

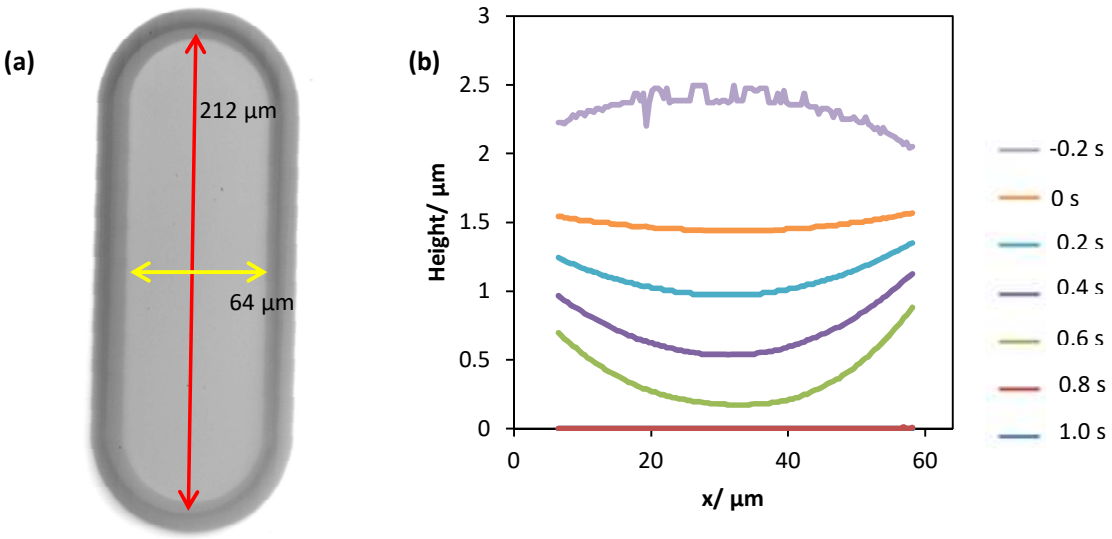

Figure 4.14: (a) An image of an oval pixel showing the long dimension (red arrow) and the short dimension (yellow arrow) and (b) a plot showing the profile progression along the short dimension of the anisole drop depicted in figure 4.12.

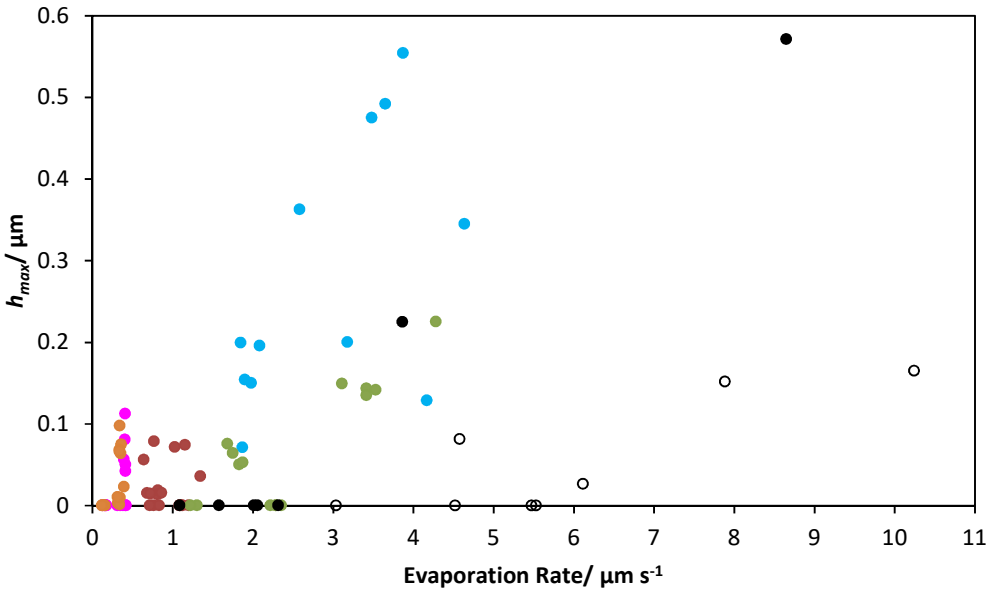

Figure 4.15: The relationship between h_{max} and evaporation rate for anisole (blue), methyl anisole (red), mesitylene (green), o-xylene (black), methyl benzoate (pink) and dimethyl anisole (orange) drying in circular wells. Each point represents a single drop, open symbols showed qualitative differences in the drop profile during drying.

Figure 4.15 shows the relationship between h_{max} and evaporation rate for the circular wells: h_{max} showed a gradual increase with evaporation rate rather than a sudden switch in behaviour from a U-shaped to a W-shaped profile. Examples of U- and W- shaped profiles from circular

wells are shown in figures 4.16 and 4.17. In circular wells the bank height was approximately 1.3 µm though it was not consistent from well to well. It appeared the drops drying in circular wells remained pinned at the bank tops throughout drying. The behaviour in the circular wells was more akin to the square wells than the oval wells. The axisymmetric nature of drops drying in circular wells could be used to confirm theoretical models and to compute behaviour in oval wells. Once again, qualitative differences were seen in the drying of some o-xylene drops in both oval and circular wells, highlighted by the open symbols in figures 4.11 and 4.15. The o-xylene drops highlighted gave M-shaped profile development as in the square wells. The M-shaped profile progression in all three geometries appeared to be governed by forces other than the pinning of the drops at the wall tops and the rate of evaporation. The mechanisms behind anomalous drying of o-xylene drops are explored further in the next section.

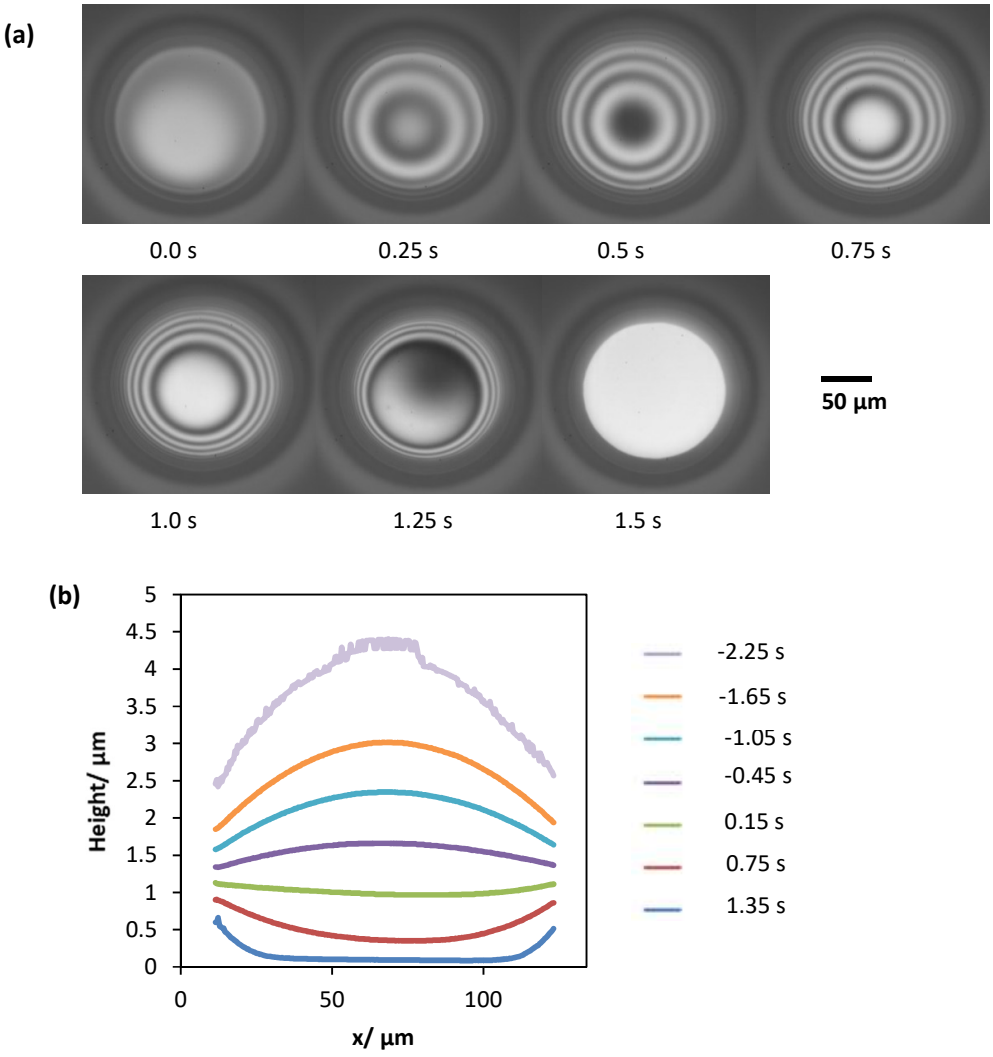

Figure 4.16: Images (a) and plots of profile progression (b) for methyl anisole in circular wells. Cross sections were taken horizontally across the centre of the wells. Total drying time for the drop was 2.5 s.

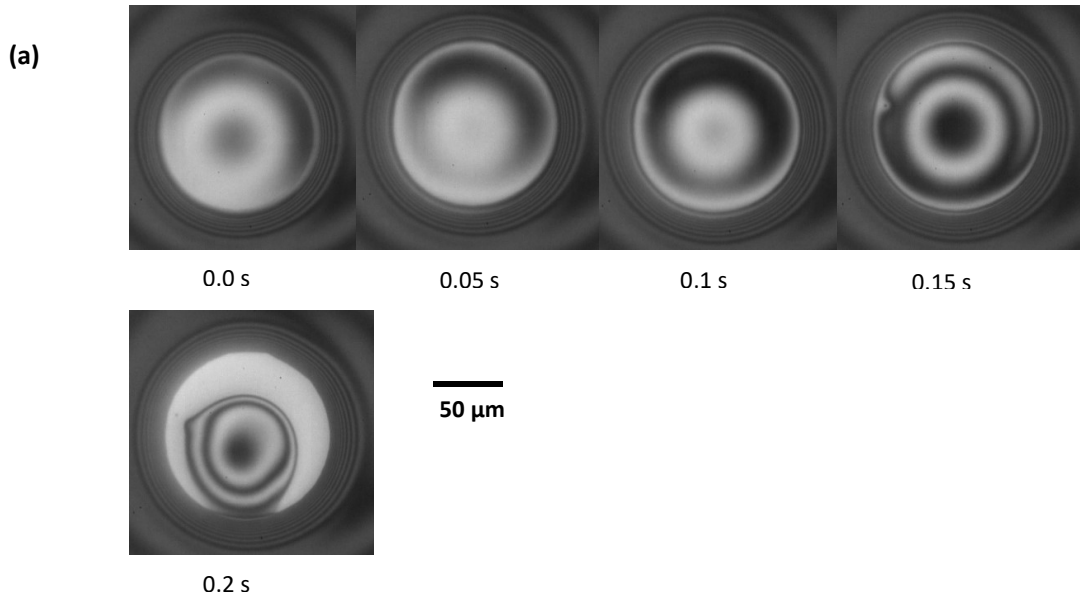

Figure 4.17: Images (a) and plots of profile progression (b) for anisole. Cross sections were taken horizontally across the centre of the wells. Total drying time for the drop was 0.6 s.

4.4 o-Xylene

Some of the o-xylene drops imaged in all of the three well geometries displayed drying behaviour that was not consistent with the h_{max} / evaporation rate relationship discussed thus far. This section investigates possible explanations. Drops were printed into the square wells and imaged as described in Chapter 2 section 2.1 and analysis of the images was carried out as described in section 2.5.

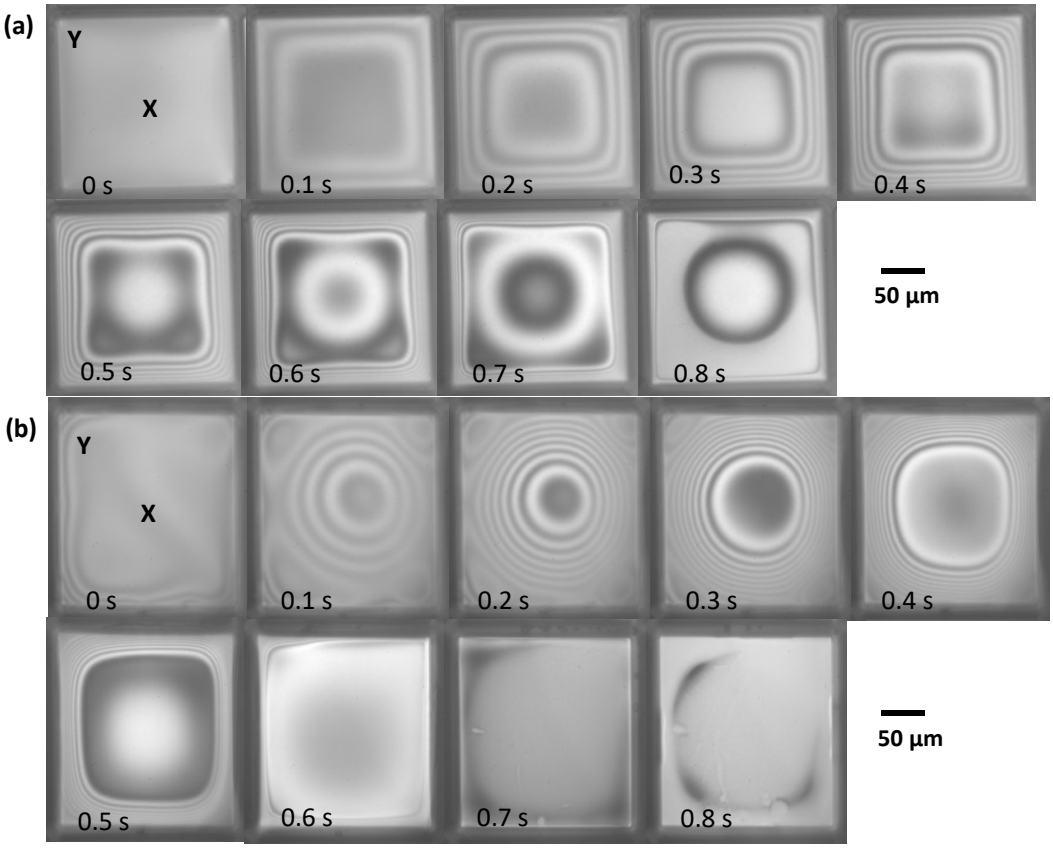

Figure 4.18: Images showing the profile progression of an o-xylene drop drying to give dimple formation (a) and one which dried to give enhanced drainage from the centre of the wells (b). Images were recorded at 1000 fps and a shutter speed of 1 ms. Total drying time of (a) was 3.7 s and for (b) was 1.2 s.

Figure 4.18 shows images from an o-xylene drop which dried to give a W-shaped profile alongside one that showed an M-shaped profile. The images in (b) show that the o-xylene drops were dipping below the level of the walls in the centre of the drop before the edges and corners of the drop had reached the wall tops; i.e. there is enhanced drainage from the centre of the drying drop. The video relating to figure 4.18b is video 8 on the attached disk. The negative curvature at the centre of the drop should result in a Laplace pressure that causes a flow from the edges of the drop towards the centre. However the images in 4.18b and the plot in 4.19b show the drop continues to thin faster in the centre than at the edges of the drop and as such the flow must be in the outward direction. Therefore there must be an additional

force that overcomes the Laplace pressure. The only plausible explanation is a surface stress arising from a surface tension gradient. The presence of surface tension driven flows alongside capillary driven flows from the curvature in the drop surface could overcome the relatively fast evaporation rate of the drop and prevent dimple formation, giving M-shaped profile progression. The plots in figure 4.20 show the central region of the fluid flattened out at thicker film heights than in drops which dried to give U-shaped deposits (figure 4.3). As OLED devices require flat films at thicknesses of the order of 10s of nm, surface-tension-driven flows could potentially be utilised to give flat films at the relevant thickness.

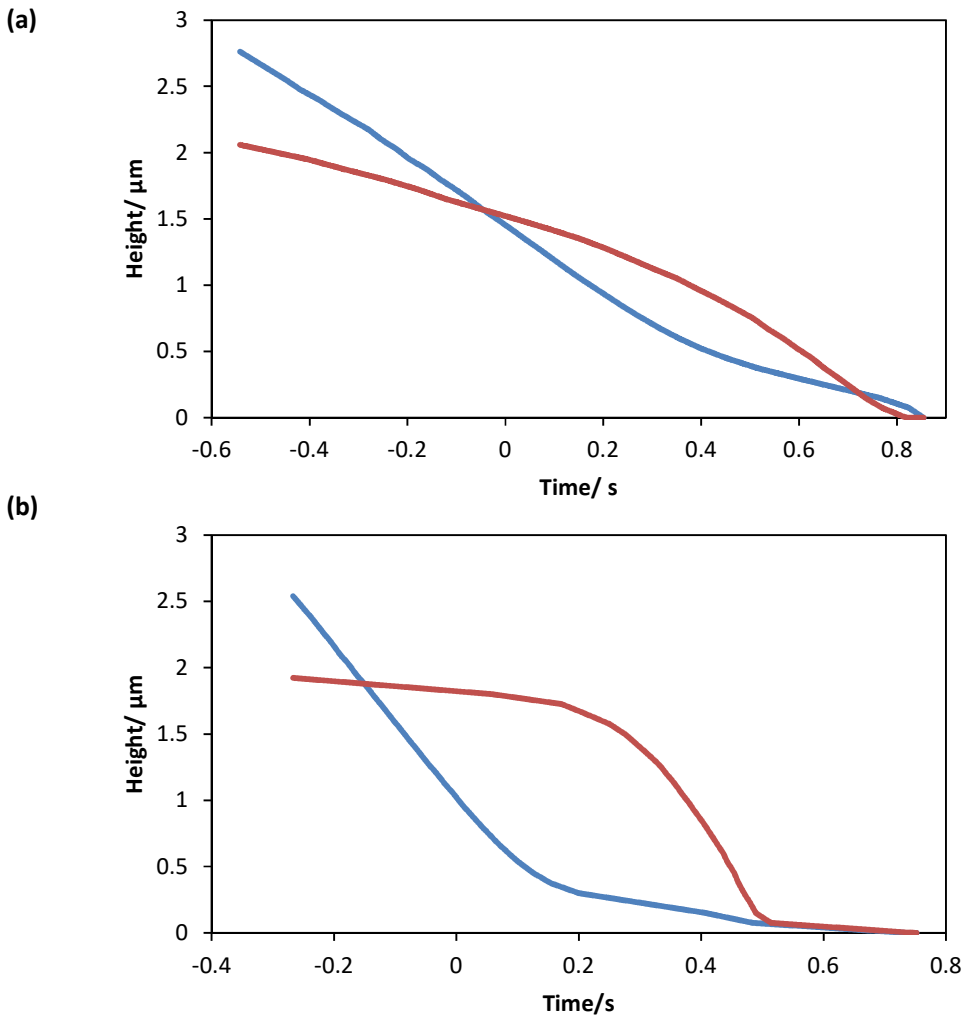

Figure 4.19: The relationship between drop height and time for the o-xylene drop imaged in figure 4.18a (a) and the o-xylene drop in figure 4.18b (b) in the centre (blue, labelled X in figure 4.18) and the top left intermediate region of the drop (red, labelled Y in figure 4.18).

Figure 4.19a shows that the centre (X in figure 4.18a) of the o-xylene drop which gave W-shaped profiles was higher than the intermediate region (Y in figure 4.18a) until the bank height of 1.5 µm where the intermediate region became higher. Thinning in the centre then

slowed relative to the intermediate region at $t \approx$ 0.4 s when a dimple started to form. At $t \approx$ 0.7 s the central region became higher than the intermediate region, this only happened so late in the drying process because of the choice of 'intermediate region'. The early stages of figure 4.19b are a more extreme version of the early stages of drying in figure 4.19a, (b) shows faster thinning in the centre of the well for the majority of the drying process and the centre (X in figure 4.18b) of the drop dipped below the intermediate region (Y in figure 4.18b) at $t \approx$ 0.16 s, before the bank height had been reached.

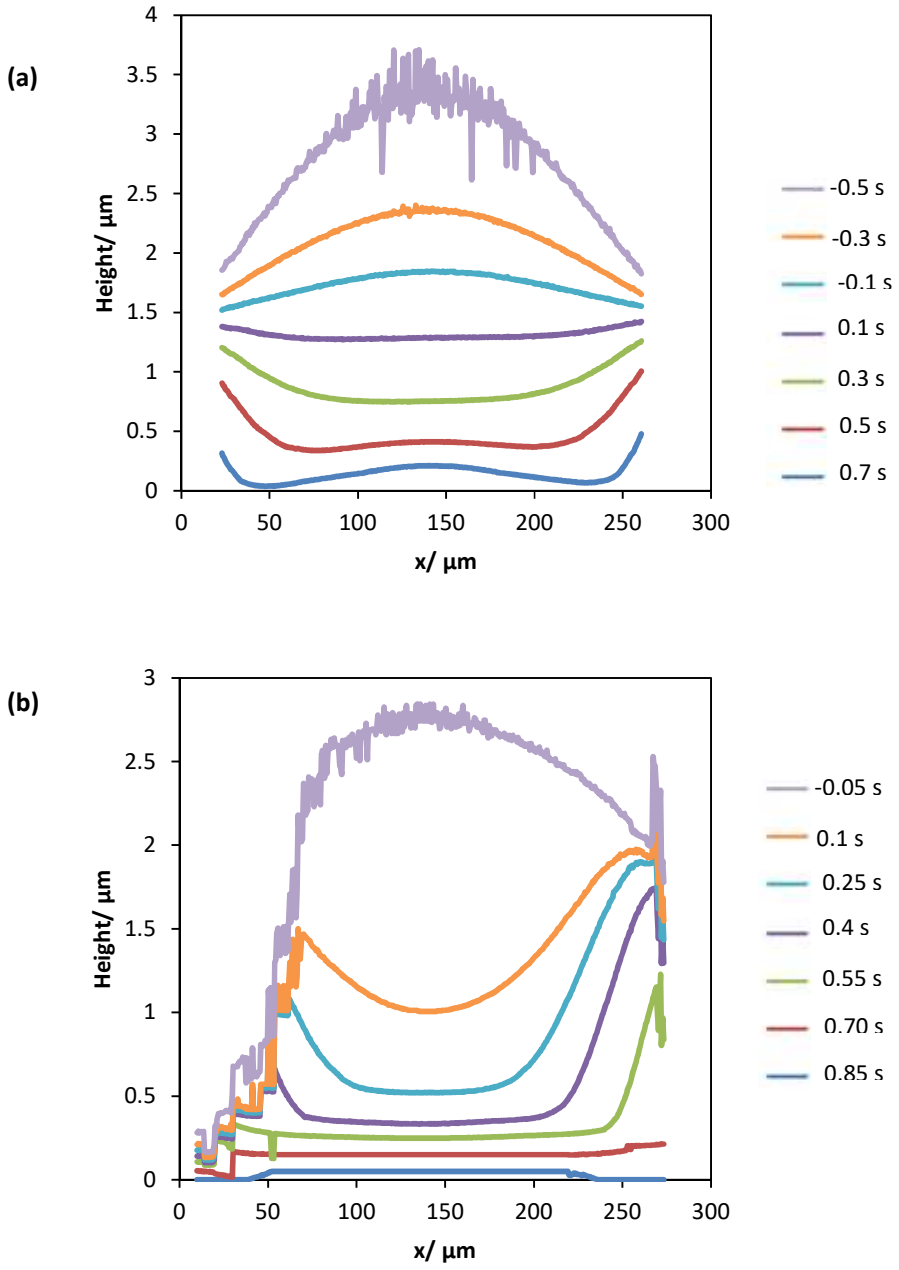

Figure 4.20: Plots showing the cross sectional profile of the o-xylene drops imaged in figure 4.13 representing dimple formation (a) and enhanced drainage from the centre of the wells (b). Cross sections were taken diagonally across the centre of the wells.

The left hand side of the plot in figure 4.20b would be expected to mirror the right hand side; however de-wetting of the fluid in this region during drying distorted the calculated profiles. The images in figure 4.18b show the left and right hand sides of the drop mirrored each other during drying. The left hand side of the plot in figure 4.20b can be reconstructed from the images in figure 4.18b to give the maximum height of the fluid and the fluid height at the walls. Reconstruction gives a maximum fluid height of 1.83 μm and a contact line height of 1.45 μm. The reconstruction suggests a slight asymmetry in the drying but does show the fluid reached a maximum in the corners of the wells before dropping down to the wall height at the contact line, akin to the right hand side of the plot. The code for full profile analysis could be improved in the future to calculate full profiles automatically, though care would be needed to locate local maxima and minima.

The far right hand side of the plot in figure 4.20b also shows some miscounting of the fringes, potentially due to some overlap with the bank in the analysis. The penultimate curve in figure 4.20b appears to show the drop was no longer pinned at the top of the banks, likely due to de-wetting of the fluid during drying. Whilst the presence of a surface tension gradient in some of the drying o-xylene drops was assumed, the reason for it was not clear. Not all drying o-xylene drops exhibited enhanced drainage from the centre of the well; some gave dimple formation as expected for a fast-drying solvent. It was important to determine which external factors had an impact on the drying to cause such different profile progression. As o-xylene was the most volatile of the six solvents investigated it is possible that thermal effects were causing surface tension gradients. Evaporation of a fluid cools down its surface,[78,152] as drops evaporate more quickly at the contact line than at the apex evaporative cooling gives a temperature gradient across the surface of the drop with the warmest fluid at the apex and the coldest fluid at the contact line.[78,152] Cooling down a fluid increases its surface tension; therefore a temperature gradient across the drop surface also induces a surface tension gradient with the lowest surface tension at the apex and the highest surface tension at the contact line (figure 4.21).[78,152] If the rate of heat gain within a drop occurs faster than evaporation, Marangoni flows due to thermal gradients can be negated; therefore the faster evaporating a drop is the more likely thermal gradients are to occur across the drop surface. Thermal gradients were present in all cases but only in o-xylene was the gradient high enough to give a Marangoni flow that changed the profile of drops during drying. In order to model other fast drying solvents such as anisole accurately, it is likely thermal effects would have to be included.

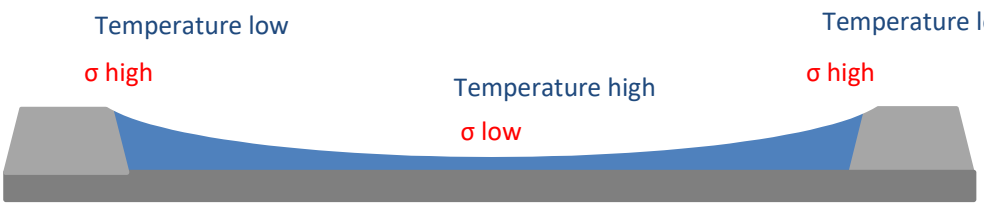

Figure 4.21: A schematic representation of the thermal and surface tension gradients present in drying o-xylene drops.

A previous study by Soltman and Subramanian[153] has shown that heating the substrate has a significant impact on the topology and morphology of inkjet printed drops and lines. Therefore to investigate the role of thermal gradients in determining whether W- or M-shaped profiles formed, a temperature-controlled stage was used to image the drying of o- xylene drops at temperatures between 15 and 34 ^{o}C. Other experimental conditions, including the distance between the nozzle and the substrate were kept constant. The data from the thermal measurements are shown in figure 4.22, dimple formation was observed for all drops with h_{max} independent of substrate temperature, suggesting thermal gradients were not the cause of the enhanced drainage seen in the drying of some o-xylene drops.

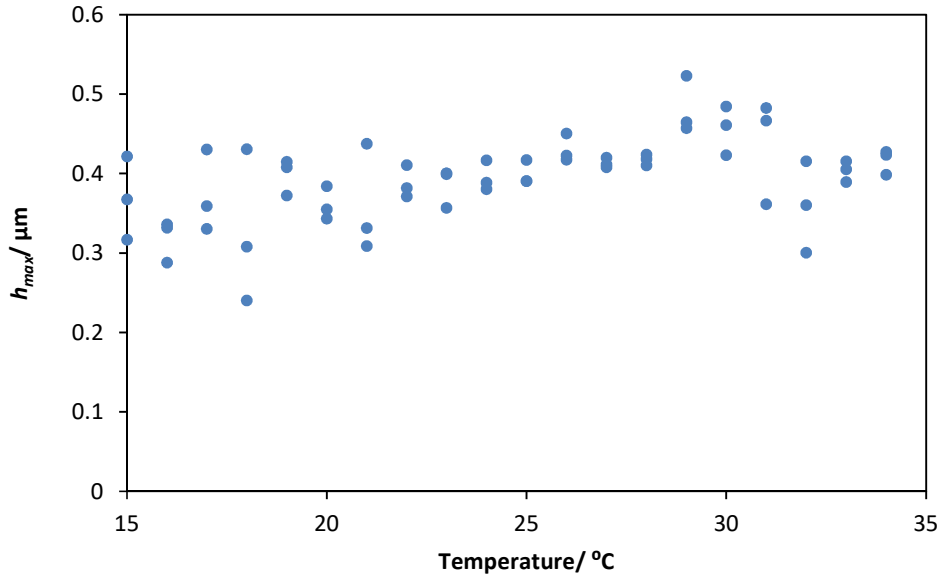

Figure 4.22: h_{max} as a function of substrate temperature for drying of o-xylene in square wells.

The evaporation rate increased with temperature (figure 4.23a) so when h_{max} is plotted against the evaporation rate (figure 4.23b), there is also no dependence of h_{max} on evaporation rate.

This result is at first surprising, given the earlier observation (figure 4.9) that h_{max} increased with increasing evaporation rate. However, figure 4.8 shows that h_{max} reaches a plateau at evaporation rates > 1.3 µm s^{-1}, and all the o-xylene data in figure 4.20 have evaporation rates above this threshold. It appears that there is an upper limit to h_{max}, which may be determined by the height of the banks (1.5 µm) and the geometry of the well.

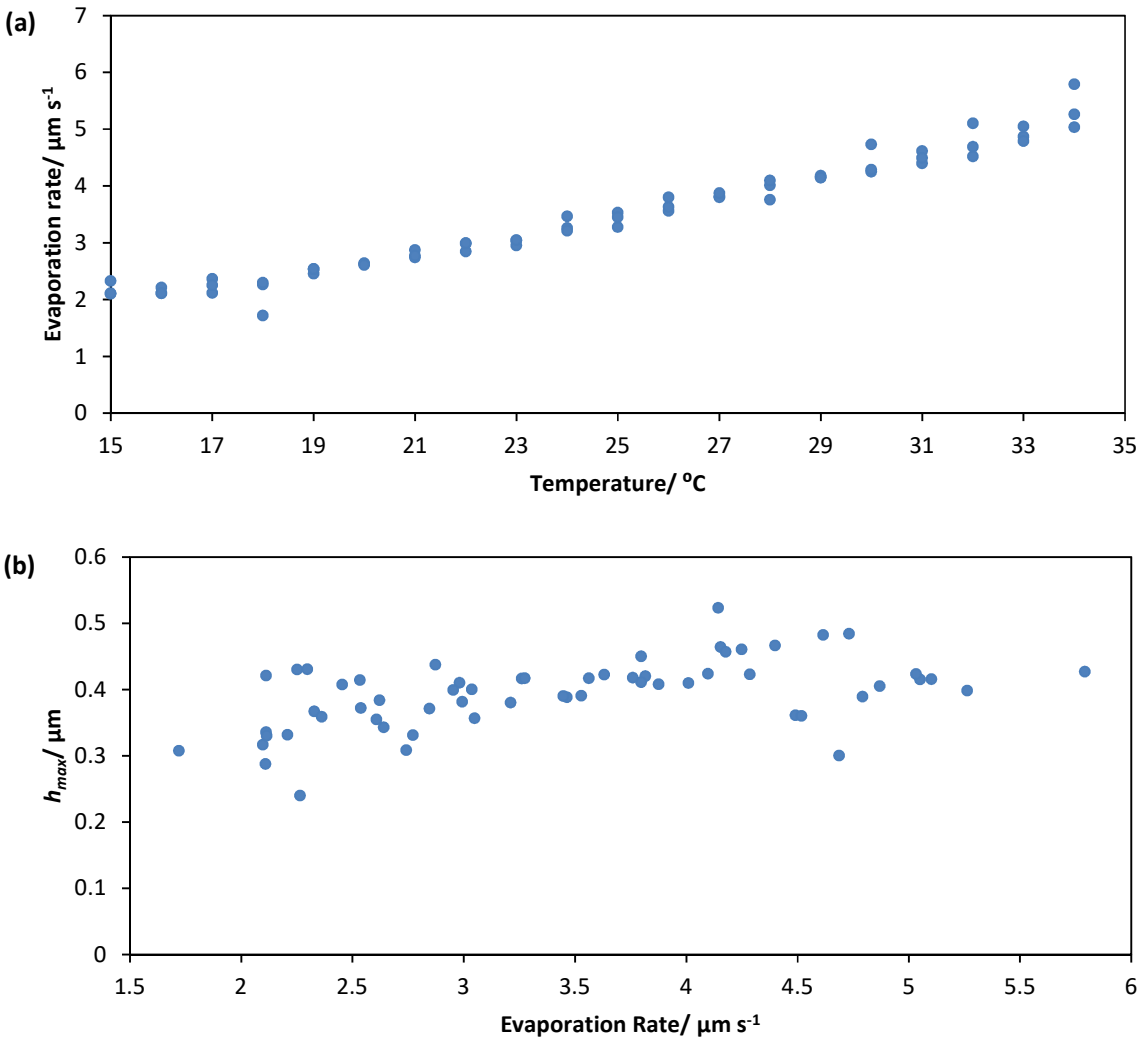

Figure 4.23: Dependence of evaporation rate on substrate temperature (a) and h_{max} on evaporation rate (b) for o-xylene drying in square wells.

A second factor that could affect the magnitude of surface tension gradients across the drop surface during drying is the proximity of the nozzle to the drying drop. The nozzle orifice was 50 µm in diameter, which was significantly smaller than the width of the drying drop (200 µm). Since the nozzle is placed over the centre of the well evaporation of the fluid in the nozzle increases the vapour pressure in the centre of the drop compared to the edges of the drop. Therefore evaporation from the centre of the drop would be reduced relative to the contact

line; the smaller the distance between the nozzle and the drop, the greater would be its influence. The effect of the nozzle is to enhance the difference in evaporative cooling between the contact line and the apex and thus to increase the thermal surface tension gradients across the drop surface. To determine the impact of the distance between the nozzle and the substrate on profile development, drying drops were imaged with different nozzle heights at a constant substrate temperature of 21.0 ^{o}C. No transition from dimple formation to enhanced drainage was seen as the nozzle was moved closer to the substrate (figure 4.24) and it appeared the distance between the nozzle and the fluid had no impact on drop profile development during drying.

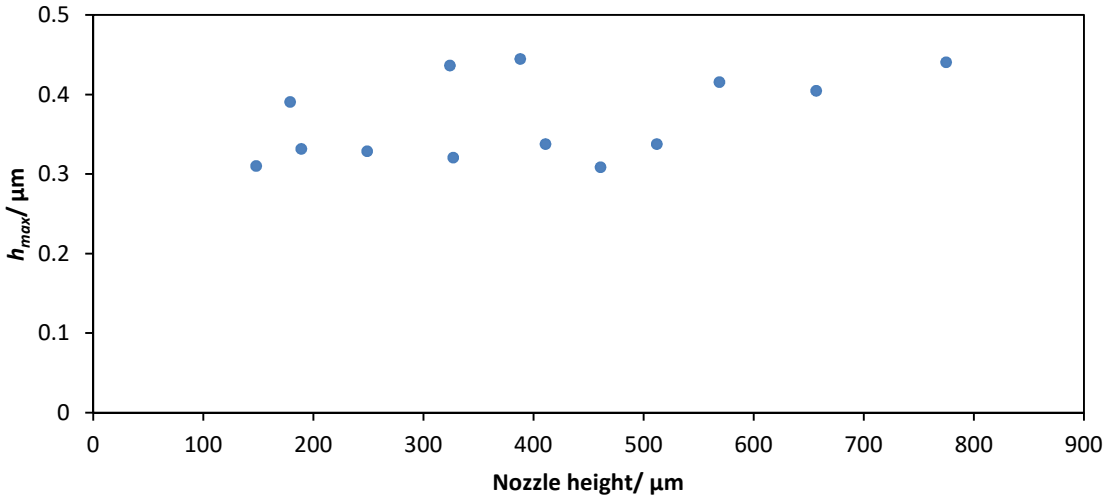

Figure 4.24: Relationship between h_{max} and the height of the nozzle above the substrate for o-xylene.

Other environmental factors in the laboratory were also considered. The RH was kept at 40 ± 5 % but should not have an impact on the drying of o-xylene as the humidity is only relevant to the evaporation rate of water. Important in the evaporation rate of o-xylene is the relative vapour pressure of o-xylene in the vicinity of the drop and this was shown to have no impact when investigating the influence of the distance between the nozzle and the substrate. Convective flow can also enhance evaporation, so the rig was surrounded by walls or curtains on all sides to eliminate drafts. The extract system was checked every day to ensure it was pulling evenly across the drop surface, which is evidenced in the symmetrical drying of the fluids in the wells. No other external factors were identified that could have caused the differences in drying witnessed.

It is plausible that the enhanced drainage seen from the centre of some o-xylene drops was caused by solutal Marangoni effects if the sample was contaminated by surface-active impurities; differential evaporation would lead to gradients in composition, and hence in

surface tension, across the surface. However as enhanced drainage of o-xylene was observed randomly in the initial experiments (roughly one third of the time in all three geometries) and the same solvent bottle and glassware was used for all experiments (with thorough washing in-between) contamination of the solvent was unlikely. Other factors which could influence drying include the chemical composition of the banks (which affects droplet pinning) and the geometry of the substrate (e.g. the height and shape of the banks). The geometry and chemistry of the substrates were outside of our control, so the impact of these factors could not be investigated. While it is frustrating that the origin of the enhanced drainage observed intermittently for o-xylene could not be identified, the subsequent experiments with careful control over external variables always showed dimple formation. It is therefore reasonable to conclude that pure o-xylene drying within wells with no external influences gives dimple formation, with the heights of the dimple that fit into the relationship between h_{max} and evaporation rate displayed in figures 4.9, 4.11 and 4.15.

4.6 Summary

Drops drying within wells of all geometries exhibited a pinned contact line at the wall tops throughout the drying process, though there was some recession down the banks in certain cases. The evaporation rate of the drying drop was then the determining factor in the morphology of the final film. The driving forces behind film progression in wells showed some similarities to those on flat substrates in that the pinning of the contact line and presence of enhanced evaporation rates at the contact line were key factors. Pinning of the contact line caused radial flows to maintain constant mean curvature across the drop surface and enhanced evaporation at the contact line is important in causing surface tension gradients across the drop surface. In contrast to flat substrates, the rate of evaporation was also key in the film profile development even in the absence of thermal effects. Slower evaporation (> 10 s) gave U-shaped final film profiles and faster evaporation (< 10 s) gave W-shaped final film profiles with the formation of a dimple in the centre of the well. There was a relationship between the evaporation rate of a drop and the level of dimple formation; square and circular wells showed a gradual increase in h_{max} with increasing evaporation rates whereas oval wells showed a sharp onset of dimple formation.

Some o-xylene drops showed M-shaped profiles rather than the W-shaped profiles expected from the high evaporation rates. The cause of enhanced drainage from the centre of the wells was investigated in depth and whilst the flow is assumed to originate from surface tension gradients across the drop surface, the cause of the gradients was not identified. As M-shaped development in o-xylene drops could not be reliably reproduced, the differences exhibited were assumed to be distinct from the evaporation rate/ h_{max} relationship explored here.

As the mechanisms governing film profile in drops drying within wells have shown some differences to those governing drops drying on flat substrates, strategies to give even deposits in wells will need to be different to those used on flat substrates. It is possible surface tension gradients could be used to counteract capillary drainage and give more even deposits than either the U- or W-shaped profiles described in this chapter.

5. The Effect of Temperature on Drop Profile During Drying

5.1 Introduction

Previous studies have shown thermal effects can have an impact on the flows present within drying drops on flat substrates.[102,154,155] Thermal gradients across a drop surface induce surface tension gradients which can cause recirculating flows, mitigating the formation of ring stains. Whilst studies have been reported for drops drying on flat substrates, thermal effects during drying have not been reported for drops drying within wells. We have already determined that the driving forces behind deposit morphology on flat substrates have some similarities to those within wells, though the presence of the walls increases the importance of evaporation rate. Ring stains on flat substrates are driven by the pinning of the contact line during drying and enhanced evaporation at the contact line relative to the apex of the drop; in wells drop profiles are driven by the pinning of the drop at the bank tops and the subsequent capillary flow due to negative curvature near the banks, combined with enhanced evaporation at the contact line. The rate of evaporation was key in determining the shape of the drop profile during the drying of drops within wells. It is therefore not certain the influence of thermal effects on drops drying within wells will be the same as on flat substrates. In chapter 4 we studied potential thermal effects in the drying of o-xylene drops within the square wells and saw no qualitative changes, this chapter will focus on systems where surface tension gradients are expected to be larger than in o-xylene to determine whether and when thermal Marangoni flows are important.

The prediction of thermal (and hence surface tension) gradients across the surface of drops drying within wells is a complicated process comprising four main effects:

1. The thermal conductivity of the substrate
2. The thickness and thermal conductivity of the fluid film
3. The cooling rate of the fluid surface
4. The presence of the banks

In all cases of drops drying within wells, we are working well within the limit of low contact angles. With a drop radius of 100 µm and average drop height at the beginning of drying of 5 µm, the maximum contact angle during drying is $\sim 3^{o}$. The thermal conductivities of the relevant materials are shown below in table 5.1.

Table 5.1: The thermal conductivities of the materials relevant to this chapter at 20 ^{o}C. The value denoted by ^ was taken at 25 ^{o}C and the value denoted by ˠ was taken at 23 ^{o}C

Material	**Thermal Conductivity/ W m^{-1} K^{-1}**
o-Xylene	0.142[156]
Glass	1.05^[157]
ITO	11-12[158]
Typical polymer resist material	0.17-0.19ˠ[159]

The thermal conductivity of the substrate is key in determining potential thermal gradients across the drop surface. If the substrate can be considered to be isothermal, the thickness of the fluid film determines relative thermal gradients across the drop surface. In 2012 Talbot et al[22] determined that evaporation rates on glass were what would be expected for an isothermal substrate. The substrates examined in this thesis can therefore be assumed to be isothermal for drops that do not evaporate faster than water.

The thickness of the evaporating film is also important. Since the film is much thinner than it is wide, the dominant heat transport will be in the vertical direction (except in the immediate vicinity of the periphery of the drop). Consequently the difference in temperature between the substrate and the fluid surface is directly proportional to the film thickness. If the substrate is a good thermal sink (a reasonable assumption as ${\kappa_s}/{\kappa_l} > 1$ where κ_s and κ_l are the thermal conductivities of the substrate and liquid respectively), then the temperature decrease of the drop surface can be treated as being proportional to the thickness of the film, for a fixed evaporative flux. In such a scenario the centre of the drop would be cooler than the contact line early in the drying process while the drop is sitting above the walls, while later in the drying process the centre of the drop would be warmer than the periphery (figure 5.1b).

Diffusion of heat from the substrate into the fluid is working in direct opposition to the cooling of the surface. Evaporation of a fluid cools down the surface of the drop and divergence of the evaporative flux at the contact line means the contact line of the drop would always be cooler than the centre if evaporation alone were considered. However, the same divergence at the contact line is present for the transfer of heat from the substrate to the drop and, without experimental evidence, it is uncertain which will control the surface temperature of drops drying within wells. Once the drop has dried past 'flat' the cooling effect and diffusion of heat through the liquid both lead to the centre being warmer than the periphery and the direction of the thermal gradient is easier to predict.

One factor which will influence thermal gradients across a drop surface in wells, which is not a consideration on flat substrates, is the presence of the banks. The thermal conductivity of the

banks is at least an order of magnitude lower than that of the glass/ITO base (table 5.1). It could be that the conduction of heat through the banks is limiting, giving finite thermal conductivity at the contact line of the drop. As the evaporative divergence is still present cooling may win out, making the contact line colder than the centre of the drop.

In sessile drops on flat substrates, the direction of thermal gradients is not important in determining deposit morphology as either direction causes re-circulation of fluid within the drops (figure 5.1a). We have observed that, in the case of drops containing active materials drying within wells, higher surface tensions at the contact line relative to the apex of a drop caused the development of M-shaped profiles. Marangoni flows will cause M-shaped profiles in the case where the contact line is cooler than the apex and are therefore unlikely to be of use in giving even deposits from drops drying within wells. However it is important to understand the impact of temperature on the drop profile during drying and the subsequent deposit morphology, as industrial processes can then be designed to give the appropriate level of temperature control. If the mechanisms behind drying at different temperatures are understood the temperature gradients across the drop surface can be controlled to optimise deposit morphology.

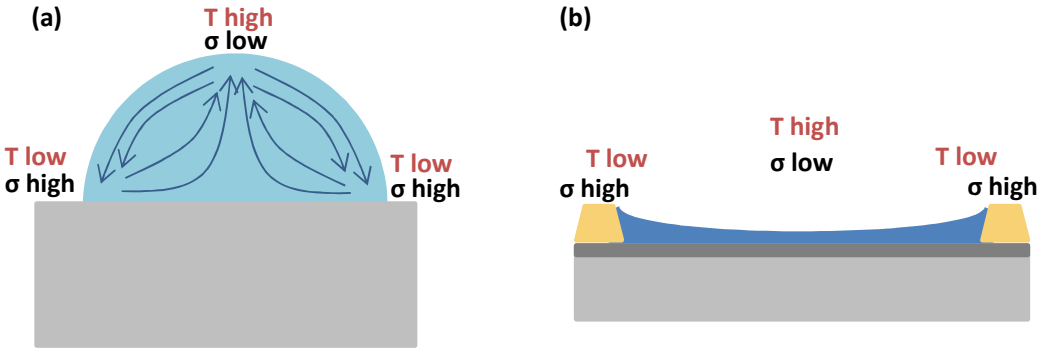

Figure 5.1: A schematic diagram showing the recirculation of flows caused by thermal gradients on flat substrates (a) and the expected thermal and surface tension gradients from drops drying within wells (b).

This chapter explores the effect of temperature on the drop profile during drying. The evaporation rate of a solvent under experimental conditions largely determines the formation of thermal gradients across the drop surface. For large drops (> 6 mm in diameter) the convection of vapour can affect the evaporation rate of the drop[160] but, in the picolitre sized drops discussed here, heat transfer due to internal flows is negligible compared to that through conduction as shown by the Peclet number for heat transfer

$$Pe_h = \frac{uR_c}{\alpha} \qquad (5.1)$$

where α is the thermal diffusivity of the fluid. For a droplet of o-xylene (α = 8.464 × 10^{-8} m^2 s^{-1})[161] with radius of 100 μm and internal velocities of the order of 20 μm s^{-1} (from the PTV data in chapter 3), Pe_h = 0.02 < 1, meaning conduction is dominant. Picolitre drops have Bond numbers much less than 1 and as such gravitational effects are negligible. In the case of very low Bond numbers and low contact angles, sessile drops take the form of a spherical cap with a mass approximated by[162]

$$M \approx \frac{\pi \rho_f R_c^3}{3\theta} \quad (5.2)$$

where ρ_f is the fluid density and θ is the apparent three-phase contact angle. In the case of a sessile drop sitting within a well the mass of fluid within the well must be added to equation 5.2 to give the overall mass of the drop (equation 5.3), once the drop dries below the level of the walls the mass is given by the volume of the well minus M (equation 5.4)

$$M = \frac{\pi \rho_f R_c^3}{3\theta} + \left(6 \times 10^{-14} \times \rho_f\right) \quad (5.3)$$

$$M = \left(6 \times 10^{-14} \times \rho_f\right) - \frac{\pi \rho_f R_c^3}{3\theta} \quad (5.4)$$

where M is in kg and ρ_f is in kg m^{-3}. In the systems considered here, evaporation is diffusion limited and diffusion is assumed to be quasi-steady. The full expressions for the evaporation rate are given by Popov.[82] Since the vertical height of the droplets in the wells is always much less than the diameter, $\frac{h}{R_c} \approx 0$, the limiting form of Popov's expressions as $\theta \rightarrow 0$ can be used:

$$J(r) = \frac{2}{\pi} \frac{D\,(n_s - n_\infty)}{\sqrt{R_c^2 - r^2}} \quad (5.5)$$

$$\frac{dM}{dt} = -4D(n_s - n_\infty)R_c \quad (5.6)$$

Where $J(r)$ is the mass flux, n_s is the saturation vapour density and n_∞ is the ambient vapour density.

For a droplet in a circular well with banks of height h and initial contact angle θ_i, the drying time is given by

$$t_{\rho,\theta_i} = \frac{\pi \rho R_c^2 \theta_i}{16\ (n_s - n_\infty)} + \frac{\pi \rho\ _c h}{4D(n_s - n_\infty)} \quad (5.7).$$

For non-aqueous solvents, n_∞ is equal to zero and n_s is determined by the vapour pressure of the solvent through the ideal gas equation.

The heat lost from the surface through evaporation of liquid must be equal to the heat gained by conduction from the substrate. The heat flux due to evaporation, $\gamma J(r)$, where γ is the latent heat of vapourisation is used to calculate the heat lost through evaporation and the heat flux due to conduction is given by

$$k_l \frac{(T_s - T_0)}{h} \qquad (5.8)$$

where k_l is the thermal conductivity of the liquid (SI units of W m^{-1} K^{-1}), T_s is the temperature of the surface and T_0 is the temperature of the substrate surface. The temperature difference across the fluid film, ΔT, is then given by

$$\Delta T = \frac{2\gamma h}{\pi \kappa_l} \frac{D(n_s - n_\infty)}{\sqrt{R_c^2 - r^2}} \qquad (5.9).$$

When vapour pressures are used considered in place of the ambient vapour density one obtains the following expression for ΔT:

$$\Delta T = \frac{2\gamma h}{\pi R T \kappa_l} \frac{D(p_s - p_\infty)}{\sqrt{R_c^2 - r^2}} \qquad (5.10)$$

where R is the gas constant (8.314 J K^{-1} mol^{-1}), p_s and p_∞ are the pressures of the solvent by the drop surface and at infinite distances respectively and p_s is equal to the vapour pressure, p_v, of the solvent. In equation 5.10 γ has units of J mol^{-1} (rather than J kg^{-1} as in equation 5.9). ΔT therefore depends on the material properties through the combination of constants $\frac{D p_v \gamma h}{T \kappa_l}$. The important factors to consider when comparing the solvents (ie. the material properties that will change from solvent to solvent) in this chapter are D, p_v, γ and $1/\kappa_l$.

Whilst surface cooling will give rise to thermal gradients across the surface of a drop, the presence of thermal gradients does not necessarily indicate the formation of surface tension gradients large enough to give Marangoni flows: the change in surface tension with temperature ($\frac{d\sigma}{dT}$) must also be significant. The in surface tension gradient is balanced by a viscous stress in the liquid:

$$\frac{d\sigma}{dR} = -\eta \frac{du_r}{dz} \qquad (5.11)$$

where u_r represents the radial velocity of flow within the drop and z is the direction normal to the surface. Equation 5.11 can be approximated by

$$\frac{\Delta\sigma}{R_c} \approx -\eta \frac{u_M}{h} \qquad (5.12)$$

where u_M is the velocity of flows due to Marangoni forces. The Marangoni number, Ma, gives the ratio of flow velocity due to Marangoni flows to the flow velocity due to convective flow from the evaporation and can be used to determine which flows are dominant in a drying drop.

$$Ma = \frac{u_M}{u_{cap}} \approx \frac{\Delta\sigma h}{u_{cap}\eta R_c} \quad (5.13)$$

If Ma > 1 Marangoni flows are dominant in the drying drop. Combined with the factors important in establishing thermal gradients across the surface, $\frac{d\sigma}{dT}$ is therefore also important in determining the strength of the driving forces behind Marangoni driven flows in the solvents discussed in this chapter.

In this chapter the impact of temperature on drop profile development for a number of solvents drying within square wells has been investigated. From the equations above, the material properties determining the surface tension gradient can be grouped into a single thermal constant, C_T, defined by

$$C_T = \left|\frac{p_v D\gamma\frac{d\sigma}{dT}}{\kappa_l}\right| \quad (5.14).$$

C_T has SI units of N^2 mol^{-1} and tells us how important Marangoni flows are in determining drop behaviour.

All of the constants used to calculate C_T are themselves dependent on temperature. However the exponential dependence of p_v on temperature (as determined by the Clausius-Clapeyron equation) makes it the most sensitive of the five components to changes in temperature. Therefore, when changes in temperature are made it is only really the change in vapour pressure that needs to be considered.

5.2 The Effect of Temperature on Dimple Formation

In this section, the drying of n-butyl acetate, 1-methoxy 2-propanol, 1-butanol and toluene is reported and compared with the data from o-xylene presented earlier in chapter 4. Drops were printed and imaged as described in chapter 2 section 2.1 and analysis of the images was as described in section 2.5. The substrates used were the square wells described in section 2.3. The temperature of the substrate was controlled between 10 °C and 45 °C by a Peltier device. The properties of the solvents are shown below in table 5.2.

Table 5.2: Physical properties of selected solvents. Values indicated by * were measured at 20 °C and those indicated by ^ were measured at 25 °C. Values in red for Methoxy Propanol have been estimated from the properties of other solvents and used to calculate C_T as the literature values were not available. Changes in surface tension with temperature were calculated from figure 5.2.

Solvent	p_v/ kPa	$D \times 10^5$/ $m^2 s^{-1}$	γ/ kJ mol^{-1}	κ_l/ W m^{-1} K^{-1}	$\frac{d\sigma}{dT}$/ mN m^{-1} K^{-1}	C_T/ N^2 mol^{-1}
n-Butyl acetate	1.52^[70]	0.672^[140]	43.86^[163]	0.137*[164]	-0.110^[70]	0.360
1-Methoxy 2-propanol	1.2*[129]	0.945^[165]	42.6^[129]	0.14	-0.12	0.414
Toluene	3.76^[70]	0.849^[140]	38.14^[166]	0.137*[167]	-0.122^[70]	1.08
1-Butanol	0.931^[70]	0.861^[140]	52.35^[168]	0.149*[169]	-0.124^[70]	0.349
o-Xylene	0.876^[70]	0.727^[140]	36.24^[170]	0.142*[156]	-0.110^[70]	0.179

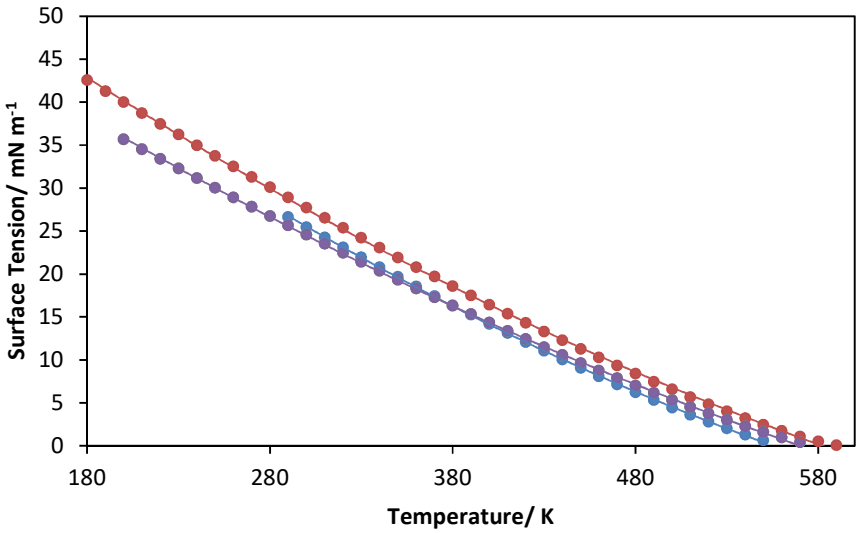

Figure 5.2: Change in surface tension with temperature for butyl acetate (green), toluene (red), butanol (blue) and o-xylene (purple).[70] No data are available for methoxy propanol. Polynomials were fitted to the data and $\frac{d\sigma}{dT}$ was calculated from the differential at 298 K. The equations for the curves were as follows:

toluene: $(\sigma/nM\ m^{-1}) = 7E\text{-}05(T/K)^2 - 0.1635(T/K) + 69.862$

butyl acetate: $(\sigma/\ mN\ m^{-1}) = 6E\text{-}05(T/K)^2 - 0.1457(T/K) + 62.466$

butanol: $(\sigma/\ mN\ m^{-1}) = 9E\text{-}05(T/K)^2 - 0.1774(T/K) + 70.586$

o-xylene: $(\sigma/\ mN\ m^{-1}) = 6E\text{-}05(T/K)^2 - 0.1457(T/K) + 62.466$.

Table 5.2 shows that the parameter that changes most among the solvents is p_v, so the vapour pressure has the largest influence on C_T.

In the droplet drying experiments, all four solvents behaved in a similar way to o-xylene (section 4.4): dimple formation was observed at all temperatures with no switch to enhanced drainage from the centre of the drops. Any thermal and surface tension gradients were too weak to alter the pattern of drying of the drops. Figure 5.3 shows the relationship between h_{max} and temperature for the four solvents investigated.

On one day only butanol showed M-shaped profile progression at all temperatures between 22 and 35 ^{o}C, as had been seen previously for some drying o-xylene drops; the cause is unknown but is explored further in section 5.3.

Methoxy propanol, toluene and o-xylene all showed no significant change in h_{max} with temperature, likely due to the high level of dimple formation present even at low temperatures. Methoxy propanol and toluene had higher levels of h_{max} than o-xylene, the likely reason for this is the larger values of C_T for methoxy propanol and toluene than o-xylene. The data presented in chapter 4 (figure 4.7) suggested there was an upper limit to h_{max} regardless of the evaporation rate. All evaporation rates of solvents which showed a plateau lay within the plateau region of figure 4.7 in chapter 4 at all temperatures. Butanol was the only solvent whose evaporation rate did not lie within the plateau region and was also the only solvent which showed a linear increase in h_{max} with temperature. The values of C_T for the solvents did not appear to correlate with the behaviour seen in figure 5.3; the lack of correlation is likely a result of maximum dimple sizes forming at low temperatures for all solvents except butanol.

Butyl acetate showed two distinct regions: h_{max} stayed fairly constant at $\sim$ 0.3 µm between 15 ^{o}C and 23 ^{o}C before stepping up to 0.7-0.8 µm between 24 ^{o}C and 34 ^{o}C. Excepting the step up in h_{max} butyl acetate did not appear to change behaviour much with the changes in temperature, consistent with its low value of C_T. A step up in h_{max} can only be explained by a step in one of the constants, the data in table 5.2 and figure 5.2 show no steps, consequently the sudden step in h_{max} is unexplained. It is possible the step was the result of a sudden increase in the evaporation rate due to poor thermal contact between the substrate and the Peltier element. Figure 5.4 shows the change in evaporation rate with temperature, it shows a linear increase in evaporation rate with temperature with no steps and as such poor thermal contact between the substrate and peltier element does not explain the step up in h_{max} at 24 ^{o}C. It would be useful if the butyl acetate data could be repeated at some point in the future.

When h_{max} is plotted against evaporation rate (which is proportional to Dp_v) instead of temperature (figure 5.5) the butyl acetate data fits the trend of the other solvents well and the step in h_{max} is within the range of the other solvents for the same evaporation rate, though this still does not explain the step in h_{max}. Butanol shows a steady increase in h_{max} with evaporation rate as it did with temperature. Methoxy propanol, toluene and o-xylene all show little dependence of h_{max} on evaporation rate, possibly due to the narrow range of evaporation rates studied. However, with more than a factor of 2 difference in the evaporation rate, you might expect some change in h_{max}. It is also odd that the o-xylene values are lower than methoxy propanol values at all evaporation rates. The data in this section need to be repeated to further clarify what is happening. Independent of solvent type figure 5.5 shows an initial sharp increase in h_{max} as the evaporation rate increases, followed by a small drop and then a plateau. The small drop in h_{max} before the plateau could be a function of the spread in the data, a function of toluene as a solvent or it could be that thermal effects are becoming important and a reduction in dimple size is becoming apparent as toluene has the highest value of C_T.

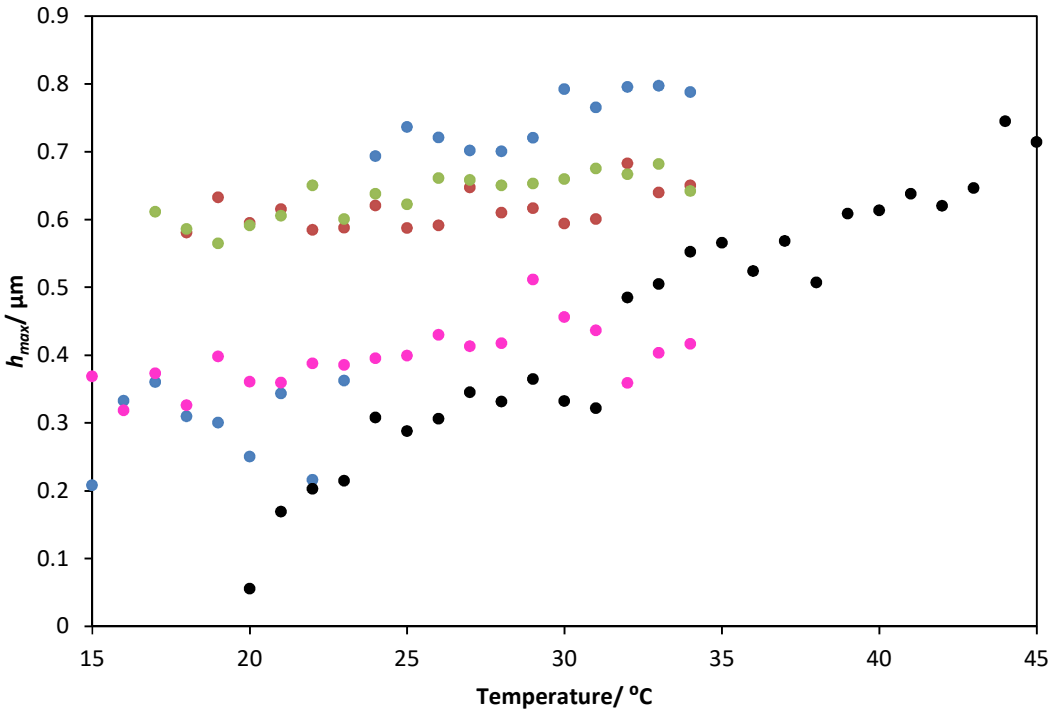

Figure 5.3: Relationship between h_{max} and temperature for butyl acetate (blue), methoxy propanol (red), toluene (green), butanol (black) and o-xylene (pink).

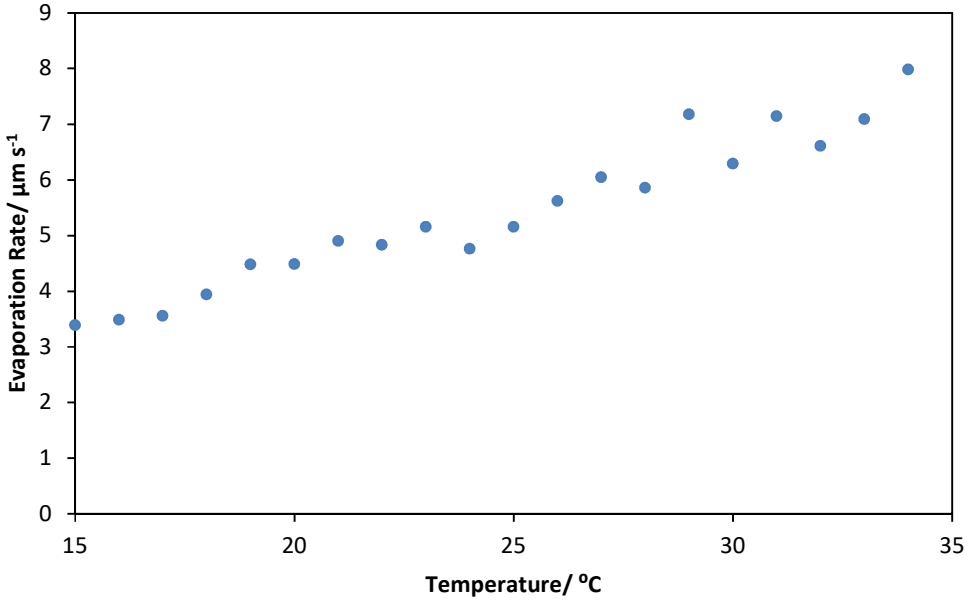

Figure 5.4: Relationship between evaporation rate and temperature for the butyl acetate.

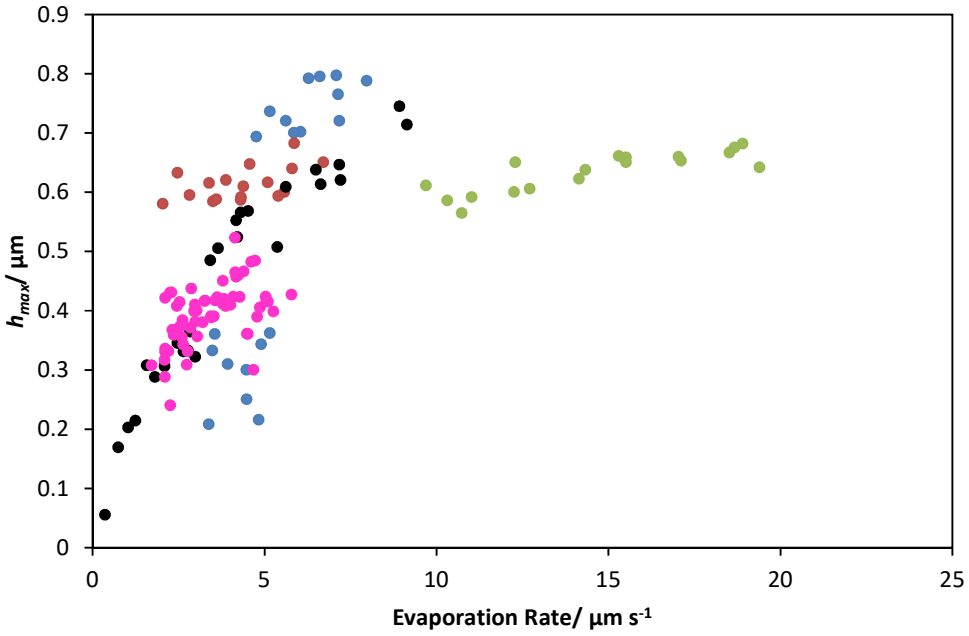

Figure 5.5: Relationship between h max and evaporation rate for butyl acetate (blue), methoxy propanol (red), toluene (green), butanol (black) and o-xylene (pink).

5.3 Thermal Marangoni Effects in Alcohols

In this section the drying of ethanol and IPA in square wells at different temperatures is discussed. Ethanol and IPA were selected to increase the value of C_T in the hope of seeing a thermal transition from W- shaped film profiles to thermally driven flows (table 5.3). Once again, the main influence on C_T was the vapour pressure of the solvent though D was also approximately twice as big for ethanol as all other solvents, likely due to its small size. Drops were printed and imaged as described in chapter 2 section 2.1 and analysis was as described in section 2.5. The temperature of the substrate was controlled using a Peltier device to between 12 °C and 35 °C.

Table 5.3: Physical properties of select solvents. Values indicated by * were taken at 20 °C and those indicated by ^ were taken at 25 °C. Changes in surface tension with temperature were calculated from figure 5.6.

Solvent	p_v/ kPa	$D \times 10^5$/ $m^2 s^{-1}$	γ/ kJ mol^{-1}	κ_l/ W m^{-1} K^{-1}	$\frac{d\sigma}{dT}$/ mN m^{-1} K^{-1}	C_T/ N^2 mol^{-1}
Ethanol	3.12^[70]	1.81^[140]	42.32^[171]	0.179*[172]	-0.149^[70]	1.99
IPA	6.05^[70]	1.01^[140]	45.39^[173]	0.135*[174]	-0.148^[70]	3.04

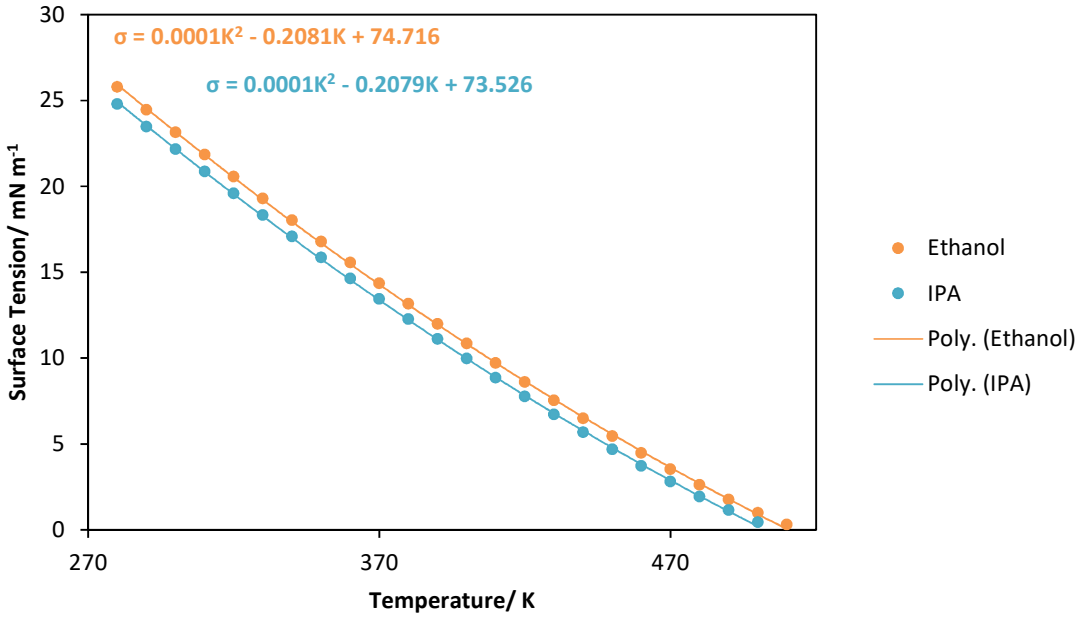

Figure 5.6: Change in surface tension with temperature for ethanol (orange) and IPA (blue).[70] Polynomials were fitted to the data and $\frac{d\sigma}{dT}$ was calculated from the differential at 298 K. The equations for the curves were as follows:
ethanol: $(\sigma/\ mN\ m^{-1}) = 0.0001(T/K)^2 - 0.2081(T/K) + 74.716$
IPA: $(\sigma/\ mN\ m^{-1}) = 0.0001(T/K)^2 - 0.2079(T/K) + 73.526$

It was not possible to plot complete drop profiles for ethanol at all temperatures due to de-wetting of the solvents during drying. It was possible to plot some of the curves however (figure 5.7b) and the profile could be inferred from images for the other temperatures. The video relating to figure 5.7 is video 9 on the attached disk. Ethanol showed M-shaped profiles at all temperatures between 15 and 35 ^{o}C (figure 5.7a), consistent with thermal Marangoni effects. It was possible to analyse the fringes all the way up to the banks in figure 5.7b but this caused miscounting of fringes at the edges as the fluid overlapped with the banks. IPA was only investigated at one temperature as it was evaporating too quickly from both the nozzle and the drop for the well to be filled; it showed an M-shaped profile at 12 ^{o}C though de-wetting of the drop during drying meant a complete drop profile could not be plotted. For ethanol and IPA C_T was an order of magnitude greater than all solvents investigated in section 5.2 with the exception of toluene which had a value of C_T approximately half the size of ethanol and a third the size of IPA .

The M-shaped profiles in the presence of thermal gradients suggest evaporative cooling is more important than diffusion of heat in determining the direction of thermal gradients initially. The contact line is therefore cooler than the apex of the drop and the contact line has a higher surface tension than the apex.

Whilst complete height profiles could not be plotted for the ethanol, counting of the fringes in the images could be used to determine the maximum difference between the top and bottom of the "M", termed d_{max} (figure 5.8). d_{max} is plotted against temperature in figure 5.9 for ethanol at temperatures between 24 and 35 ^{o}C (below 24 ^{o}C the fringes were not clear enough to determine d_{max} for ethanol) and for butanol at temperatures between 10 and 20 ^{o}C on the day it showed M-shaped profiles. d_{max} could not be determined from the imaged IPA drop as it did not fill the well completely.

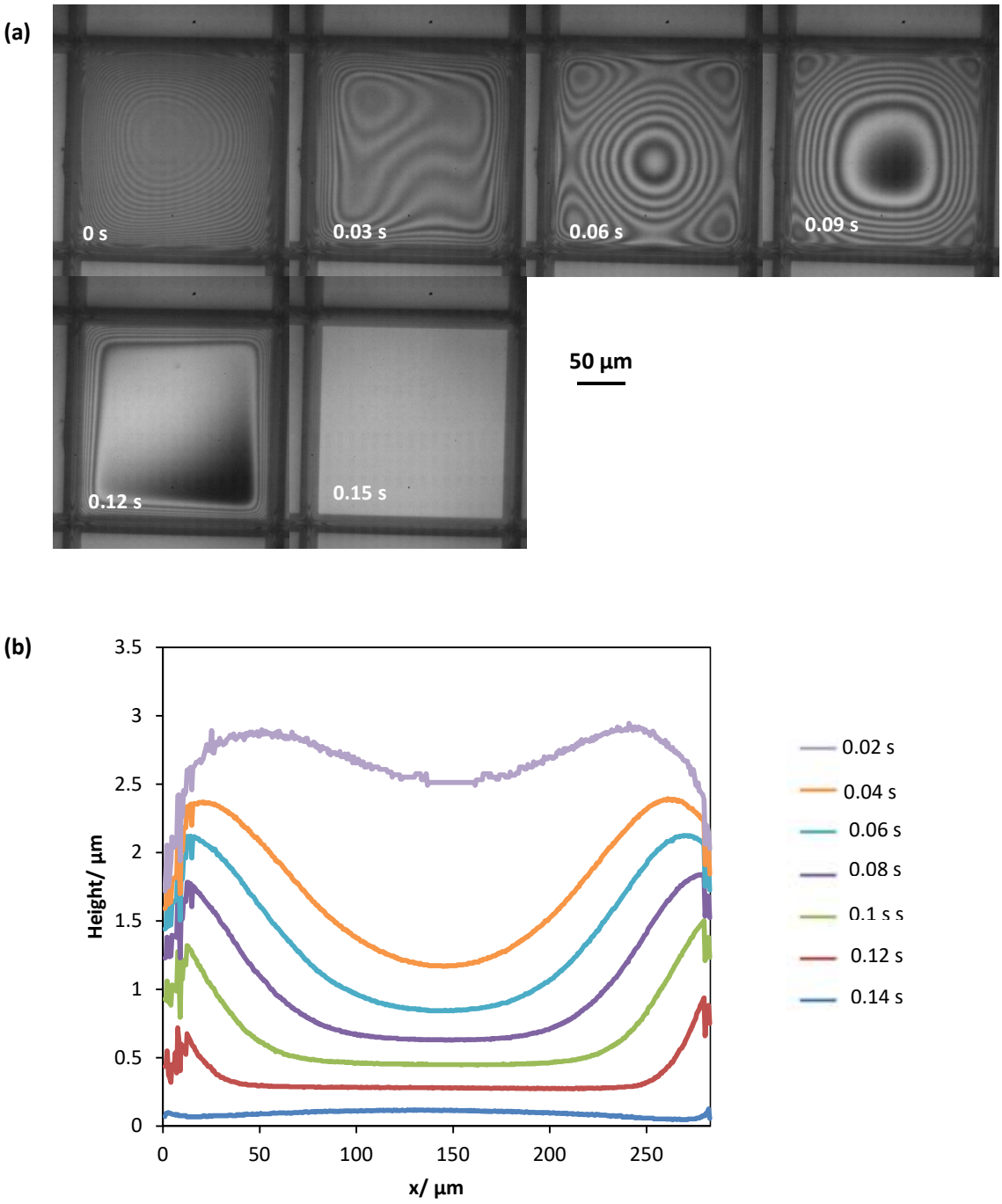

Figure 5.7: Images (a) and plots of profile progression (b) showing enhanced drainage from the centre of an ethanol drop at 32 ^{o}C. Images were taken at 3000 fps and a shutter speed of 0.33 ms.

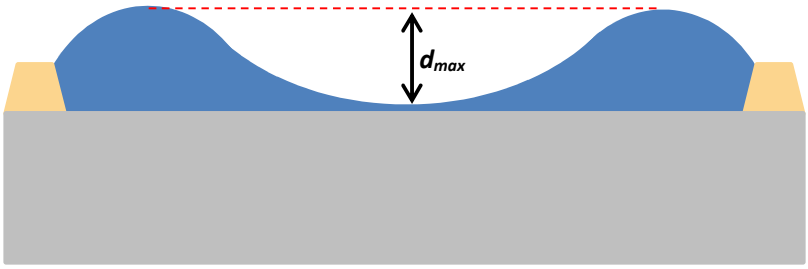

Figure 5.8: Schematic diagram showing the definition of d_{max} as the maximum difference between the top and the bottom of the drained region.

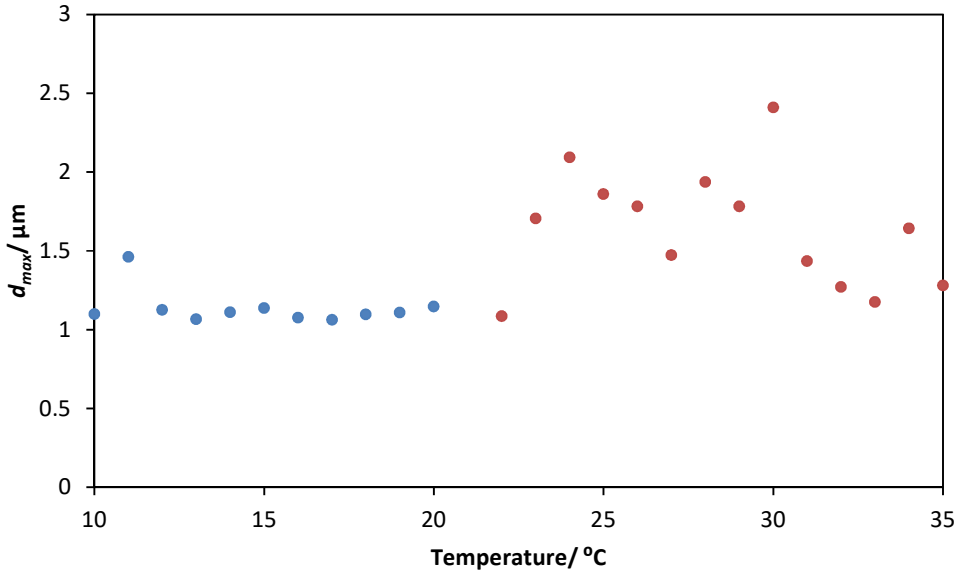

Figure 5.9: Relationship between d_{max} and temperature for ethanol (red) and butanol (blue) in cases where M-shaped profiles were seen.

Figure 5.9 shows no significant dependence of d_{max} on temperature for either ethanol or butanol, and whilst the spread in the data does increase as the temperature is increased this could be a function of either the solvent or the quality of the images. The data suggest the temperature is not overly important in determining the level of enhanced drainage. It was not possible to plot d_{max} against evaporation rate for the ethanol and butanol as the extreme M-shape of the profile made it difficult to determine the drying time precisely, though as the evaporation rate increased with temperature figure 5.9 suggests the value of d_{max} did not depend on evaporation rate.

Table 5.4 summarises the observed behaviour and values of C_T for all of the solvents discussed in this chapter. Three classes of behaviour were observed: butyl acetate, methoxy propanol and toluene showed W- shaped profiles at all temperatures studied, ethanol and IPA showed M- shaped profiles at all temperatures and butanol and o-xylene showed W- shaped profiles at all temperatures on some days and M-shaped profiles at all temperatures on other days. The values of C_T for ethanol and IPA were at least one order of magnitude larger than all other solvents except toluene. The values of C_T for butanol and o-xylene, which showed both behaviours, are of the same order as those which showed W-shaped profiles at all temperatures. Repeat measurements for all of the solvents studied should be taken to confirm behaviour as it is possible all solvents have the capability to show both W- and M-shaped profiles.

Table 5.4: Summary of behaviour and C_T values for all solvents at 298 K.

Solvent	Behaviour	C_T/ N^2 mol^{-1}
n-Butyl Acetate	W	0.360
1-Methoxy 2-Propanol	W	0.414
Toluene	W	1.08
1-Butanol	W/M	0.349
Ethanol	U/M	1.99
IPA	U	3.04
o-Xylene	W/M	0.179

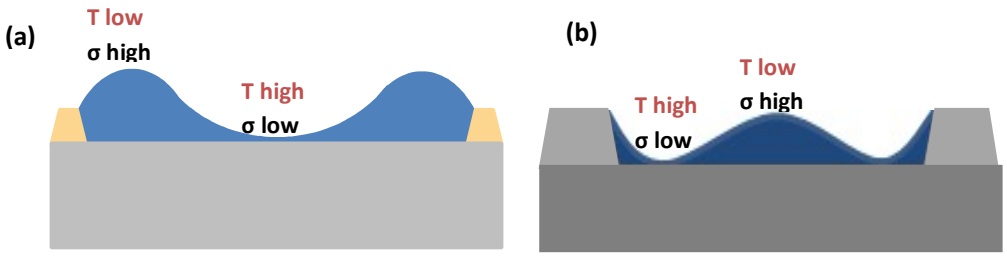

Figure 5.10: Schematic diagram showing the exaggeration of thermal gradients in M (a) and W (b) profiles.

The nature of thermal gradients gives positive feedback to both M-shaped profiles and W-shaped profiles once there is an initial deviation from a uniform profile. The surface temperature of a drop varies linearly with the fluid thickness and consequently, if there is a dip in the fluid, the temperature of the surface increases and the surface tension decreases. Therefore, in the case of M-shaped profiles, the dip in the middle will cause a Marangoni stress towards the walls (figure 5.10a) which makes the dip deeper and leads to the centre thinning

even further. Positive feedback explains why, in the case of M-shaped profiles, the dip grows even before there is any significant capillary curvature at the walls.

In the case of W-shaped profiles the dip in intermediate regions will cause an increased temperature and lower surface tension in the intermediate areas with cooler temperatures and higher surface tensions in the centre and at the contact line (figure 5.10b). Therefore Marangoni stresses act from the intermediate regions towards the centre and the walls, exaggerating dimple formation.

If the observed Marangoni effects are dominant the profile progression in drops may therefore be very sensitive to the initial behaviour, even before the film is flat, as feedback enhances the initial distortion of the drop surface. Positive feedback could therefore explain why both M- and W- shaped profiles are seen in the case of butanol and o-xylene. It is possible that butyl acetate, methoxy propanol and toluene all have the potential to show both W- and M- shaped profiles depending on the initial behaviour as their values of C_T are not very different to those of butanol and o-xylene. In the case of dominant Marangoni effects these systems are stable, what is not clear is the level of perturbation required for the effects to become stable. Some investigation into the level of perturbation required to stabilise Marangoni effects would therefore be useful.

5.4 Summary

A constant, C_T, was defined for all solvents and determined by the material properties of the solvents which were likely to influence thermal and surface tension gradients across the drop surface. It was found that the biggest influence on C_T for all solvents was the vapour pressure of the solvent and as such the vapour pressure is likely to be the key factor in determining the likelihood of thermal Marangoni flows within a drying drop.

The impact of changes in ambient temperature on the profile progression of drops during drying within wells was investigated and three behaviours were identified. Butyl acetate, toluene and methoxy propanol showed W-shaped profiles at all temperatures with no evidence of thermally-driven Marangoni flows. When considered independent of solvent type, h_{max} increased rapidly with evaporation rate until it reached a plateau. The plateau of h_{max} when plotted against evaporation rate showed a slight drop in h_{max} which could be associated with thermal effects becoming more important. The relationship between h_{max} and temperature was less clear and inconsistencies were present in the case of butyl acetate.

Ethanol and IPA showed M- shaped profiles at all temperatures, suggesting thermal gradients were important in driving surface tension flows towards the contact line. Ethanol and IPA have a value of C_T an order of magnitude higher than any of the other solvents with the exception of toluene.

Butanol and o-xylene showed M-shaped profiles at all temperatures on one day of measurement but then W-shaped profiles on another day. C_T values for butanol and o-xylene were of the same order as those for butyl acetate and methoxy propanol. The lack of consistent behaviour in o-xylene and butanol was likely due to the sensitivity of profile development to the initial behaviour. As such it is likely butyl acetate, toluene and methoxy propanol have the capability to show M-shaped profiles as well as W-shaped profiles and repeat measurements on all solvents are necessary. Small differences in printing conditions such as spilling over into an adjacent well could cause behaviour to switch from W- to M-shaped profiles.

The M-shaped profile development seen when thermal effects became important during drying showed evaporative cooling was dominant over diffusion of heat in determining the direction of thermal gradients. The contact line was apparently cooler than the apex of the drop and as such the surface tension of the fluid was higher at the contact line than the apex of the drop (inferred from M-shaped profile development).

6. The Effect of Binary Solvent Mixtures on Drop Profile During Drying.

6.1 Introduction

Previous printing studies on flat substrates have shown ring stains can be mitigated by introducing co-solvents into ink formulations.[93,97] Binary mixtures can cause recirculatory flows due to Marangoni stresses. If Marangoni forces are dominant over capillary forces and recirculatory flows dominate the drying process, even deposits can be gained on flat substrates. As it is important for printed OLED deposits to be flat and even across their entire area, it is necessary to determine whether binary solvent mixtures can be used to give flat deposits in wells. There are no studies into binary solvent mixtures drying within wells which look at the entire drying process in real time.

This chapter focuses on the influence of co-solvents on the profile development of drops drying within wells. Interferometry is used to determine the profile of the drop during drying. Flows present within the drops are inferred from the drop profiles. Solvent mixtures which should give Marangoni stresses in both possible directions are investigated in depth and compared with drop profiles from single solvents. The limitations associated with the measurements in this chapter are similar to those associated with the measurement of single solvents within wells; the coherence length of measurements is either 7 or 15 µm, depending on when the data was taken, and the region close to the banks cannot be analysed by the program. Extrapolation back to the bank tops has been performed in some key cases by counting of the fringes.

Three mixtures of industrially relevant solvents: anisole + methyl benzoate, anisole + mesitylene and anisole + o-xylene were studied and the profile of the drop throughout drying was determined. Drying was recorded in all three substrate geometries, though the majority of the investigation was carried out in the square substrates and most of the discussion will focus on these. The role of Marangoni stresses was inferred from differences in profile development during drying. As the differences in drying in the industrially relevant mixtures appeared to be inconsistent, some model solvent mixtures were identified and the drying imaged to confirm the effect Marangoni stresses had on the profile development of the drops during drying; all model solvent mixtures were imaged within the square wells alone.

6.2 Industrially Relevant Solvent Mixtures

Anisole + methyl benzoate, anisole + mesitylene and anisole + o-xylene were printed and imaged in square wells as described in chapter 2 section 2.1 and analysis of the images was as described in section 2.5. The properties of the solvents are shown in table 6.1. Anisole + mesitylene and anisole + o-xylene mixtures were used in 1:4, 2:3, 3:2 and 4:1 ratios and the anisole + methyl benzoate mixture was used in 1:1 and 3:2 ratios. The anisole + methyl benzoate data from chapter 3 showed it was a non-ideal mixture, though it also appeared anisole was evaporating more quickly than methyl benzoate at all compositions. The anisole + mesitylene data from chapter 3 showed ideal behaviour and anisole was evaporating more quickly relative to the bulk at all compositions. However the vapour pressures of anisole and mesitylene are close (table 6.1) so the evaporation rates may not be very different. The surface tension and density data for the anisole + o-xylene mixture is shown in figure 6.1: the density decreased smoothly with increasing amounts of o-xylene but the surface tension did not, suggesting non-ideal behaviour.

In the anisole + o-xylene and anisole + methyl benzoate mixtures, the expected surface tension gradient was from a high value at the contact line to a low value at the centre enhanced drainage from the centre of the drop towards the contact line. Anisole + o-xylene was originally selected to investigate surface tension flows towards the contact line and when no differences in the drying compared to single solvents were observed, anisole + methyl benzoate was selected to exaggerate the difference in volatility between the two solvents. The anisole + mesitylene mixture was selected to investigate the effect of surface tension gradients from a high value at the centre to a low value at the contact line; expected flows in this case would be from the contact line towards the centre. As it is likely the drop will remain pinned around the wall tops such flows may present as enhanced drainage from the corners of the wells towards the centre.

Table 6.1: Properties of solvents at 25 ^{o}C.

Solvent	Surface Tension/ mN m^{-1}	Density/ g cm^{-3}	Viscosity/ mPa s	Vapour Pressure/ kPa
Anisole	34.96[70]	0.990[70]	1.001[70]	0.477[70]
Methyl benzoate	37.27[70]	1.085[70]	1.958[70]	0.051[70]
o-Xylene	29.60[70]	0.876[70]	0.747[70]	0.876[70]
Mesitylene	28.05[70]	0.861[70]	0.916[70]	0.327[70]

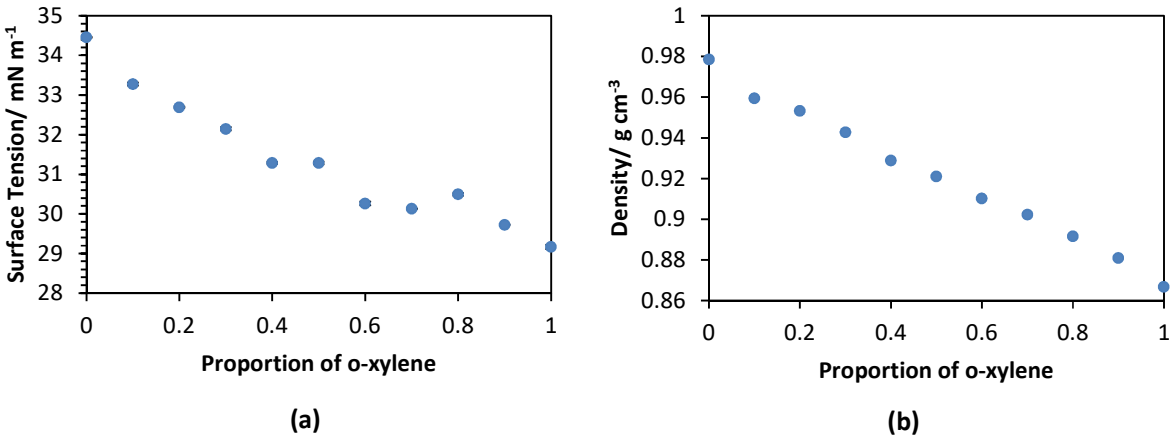

Figure 6.1: Surface tension (a) and density (b) values at changing compositions of the anisole + o-xylene mixture. Error bars show the standard deviation in surface tension measurements; if error bars are not visible they are smaller than the points. Systematic error associated with the density measurements was ± 0.001 g cm^{-3}.

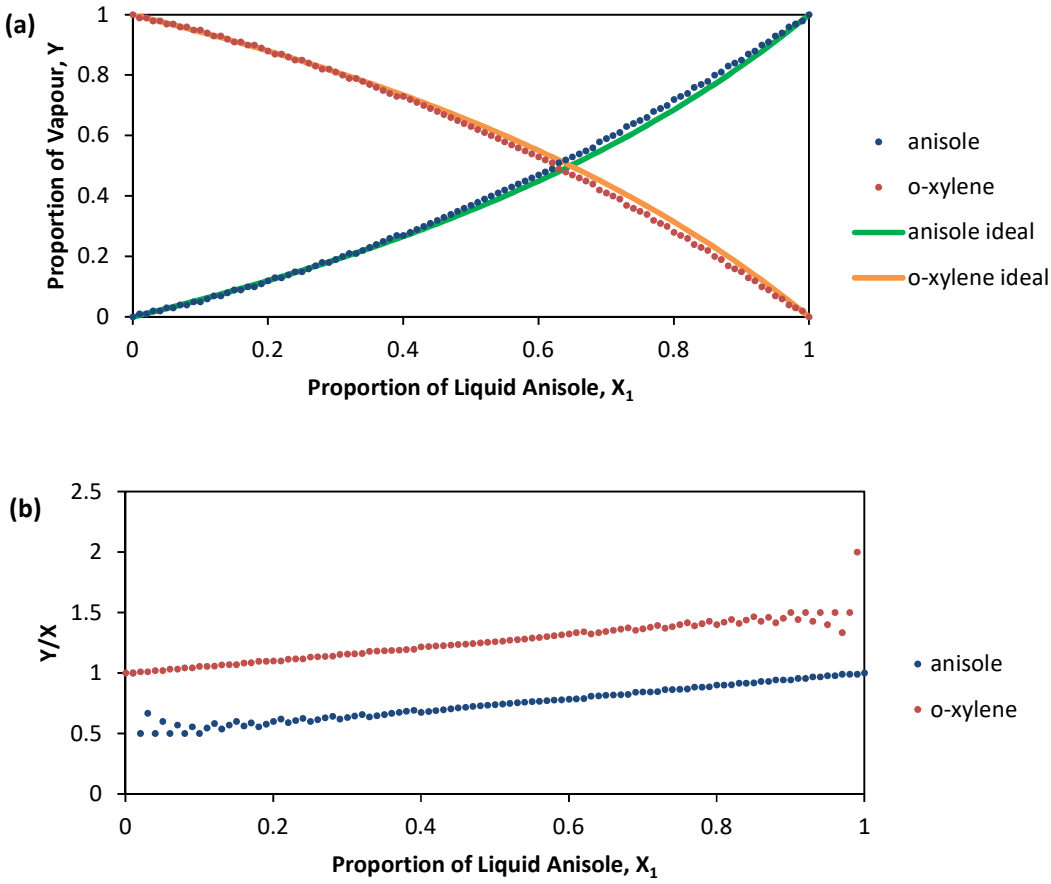

Figure 6.2: VLE curves for the anisole + o-xylene mixture (a) and the Y/X curve for the two solvents (b). VLE curves represent the mixtures at 25 °C.[141] Steps and divergence in the data are a result of numerical limitations in the computations.

VLE curves for the anisole + o-xylene mixture are shown in figure 6.2a. The mixture shows some deviation from ideal behaviour, though the deviations are not large. The $^{Y}/_{X}$ data for the mixture (figure 6.2b) shows o-xylene is always evaporating more quickly relative to what is in the bulk. As in chapter 3 there are steps and divergences in the VLE curves which are a result of numerical limitations in the computations, the creator of the software has been made aware of these issues.

In most cases the solvent mixture data appeared much like the single solvent data, slower drying drops gave U-shaped film profiles and faster drying drops gave W-shaped film profiles. Figure 6.3 shows example profile developments for all three solvent mixtures; the anisole + methyl benzoate mixture dried to give U-shaped film profiles while the anisole + mesitylene and anisole + o-xylene mixtures dried to give W-shaped film profiles. In figure 6.3a it was possible to analyse the profile right up to the banks as in the images the fringes on the banks were not clear and so did not interfere with the fluid fringes. The apparent noise on the right hand side of figure 6.3a was the result of the fluid overlapping with the banks. The step in figure 6.3c was due to an error in the analysis program. It was initially present in all of the time curves but was corrected in the earlier curves by an exact number of fringes. In the curve at 0.8 s the miscounting was not an exact number of fringes and as such could not be corrected. Figure 6.3c also appeared to de-pin from the walls during drying. Images corresponding to the curves in figure 6.3 are shown in appendix B.

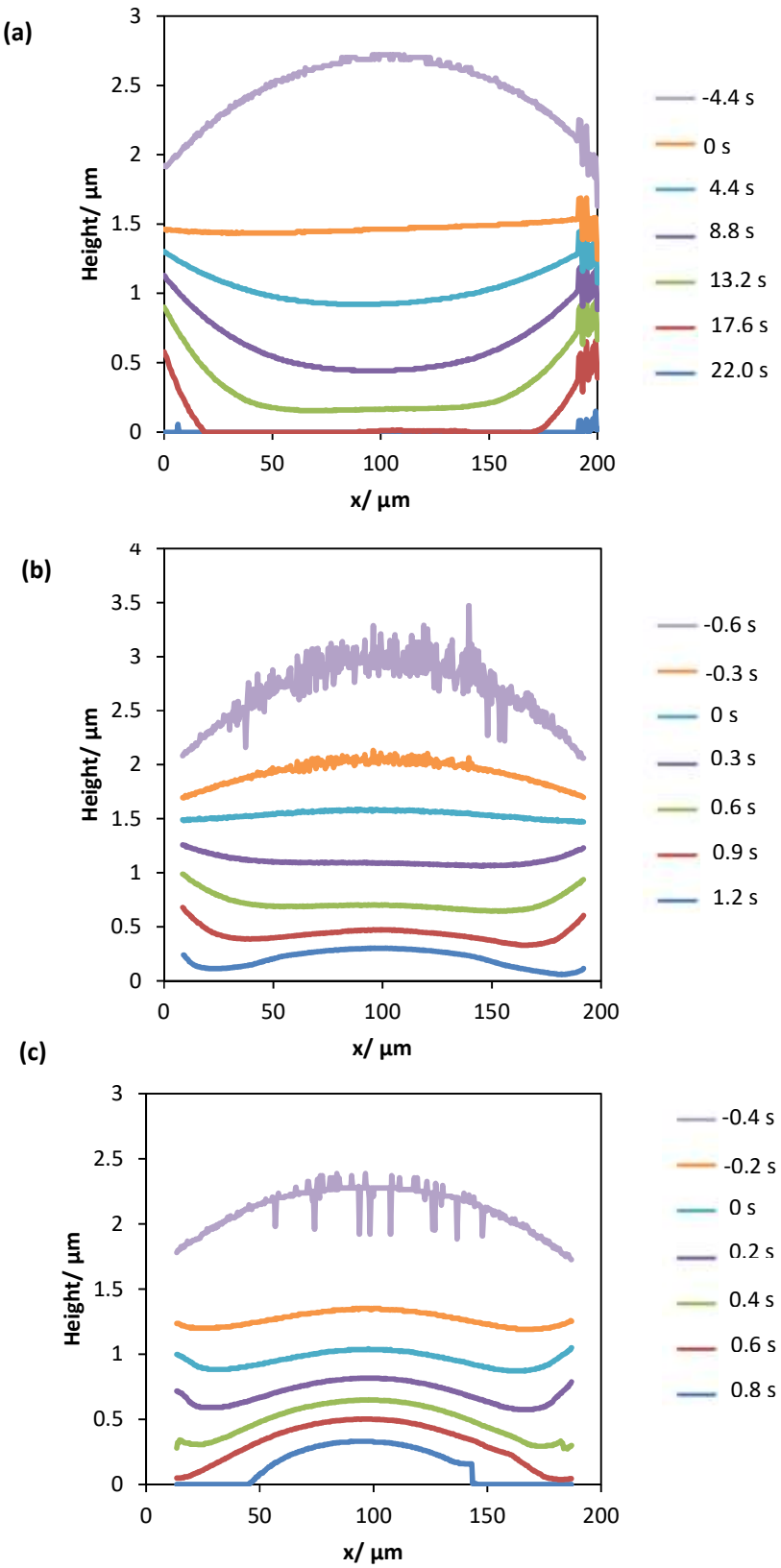

Figure 6.3: Examples of the profile progression in each of the three mixtures investigated; anisole + methyl benzoate in a 1:1 ratio (a), anisole + mesitylene in a 3:2 ratio (b) and anisole + o-xylene in a 2:3 ratio (c). Cross sections were taken horizontally across the centre of the wells.

To determine whether the presence of co-solvents had any impact on the level of dimple formation in drying drops the h_{max} and evaporation rate data for solvent mixture drops was plotted alongside the data for single solvents. Figure 6.4 shows that, for the most part, the solvent mixture data followed the same trend as the single solvent data, whereby h_{max} increased along with the evaporation rate. However, as with the single solvents, there were some drops (all for anisole + mesitylene) which did not give W-shaped profiles. Figure 6.5 shows images from the drying process and the corresponding plots of profile progression for one of the drops of anisole + mesitylene which did not give W-shaped profiles.

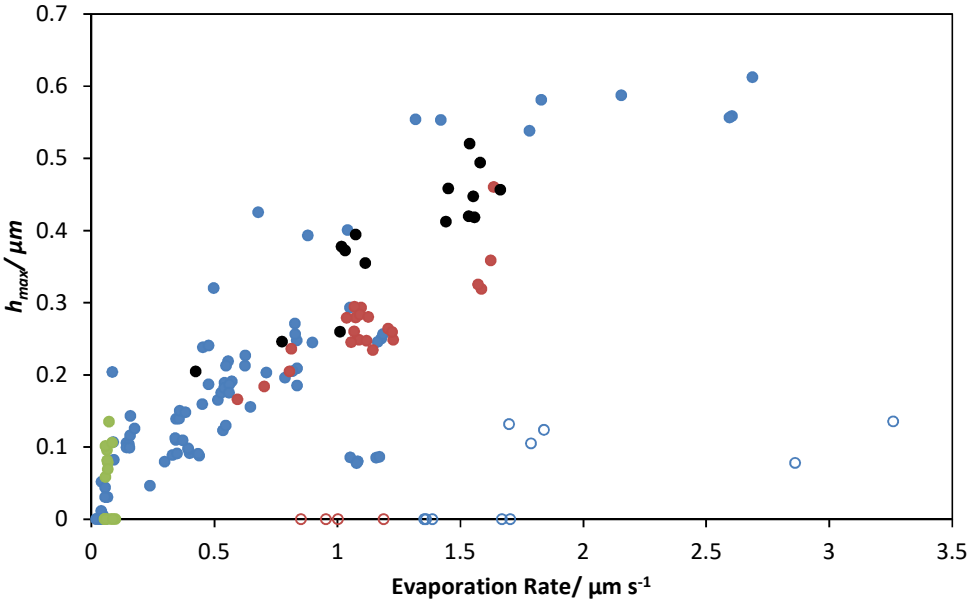

Figure 6.4: Relationship between h_{max} and evaporation rate for drops of single solvents (blue), anisole + mesitylene (red), anisole + methyl benzoate (green) and anisole + o-xylene (black) within the square wells. Open symbols represent drops which showed qualitative differences in the drying.

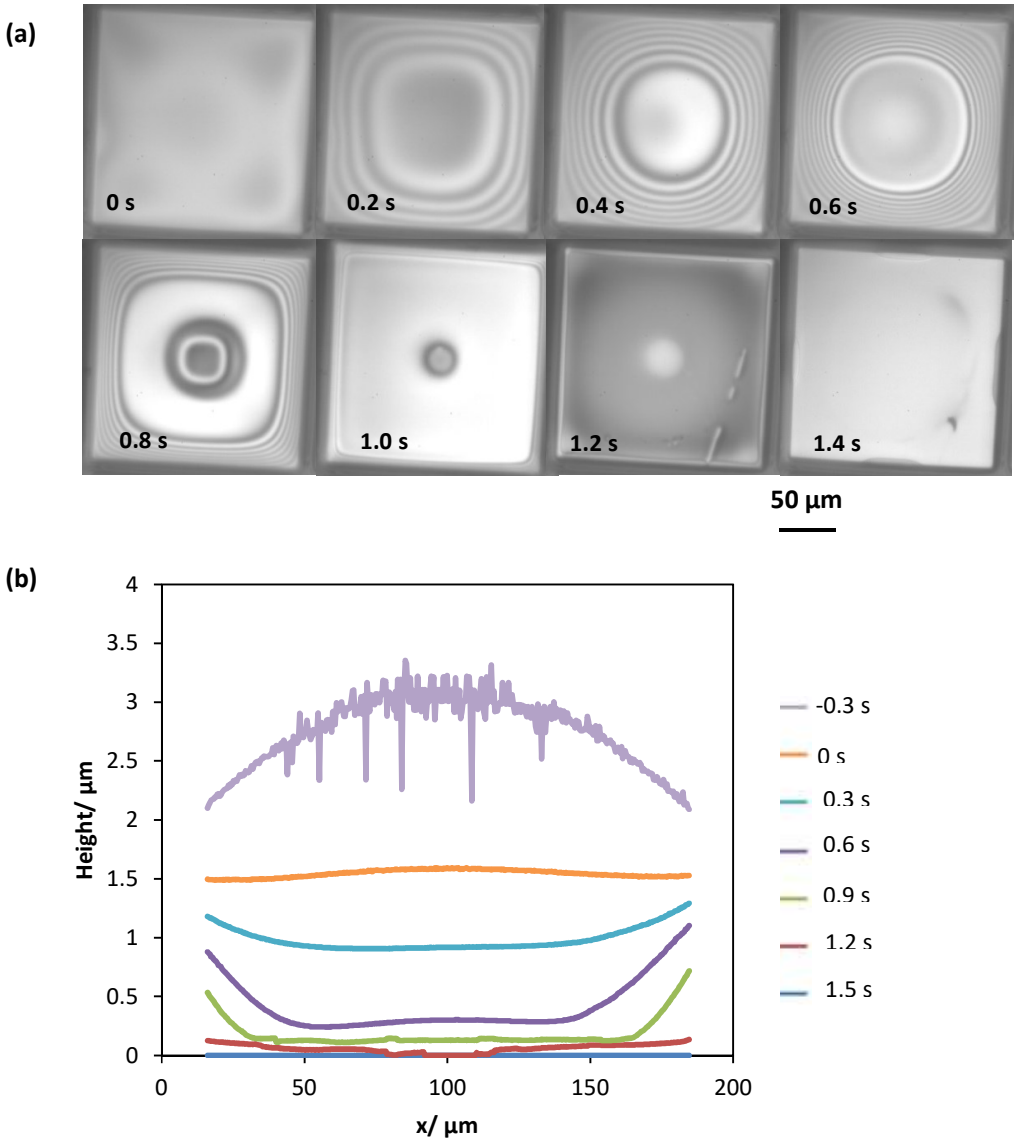

Figure 6.5: Images from drying (a) and the resulting plot of profile progression (b) for an anisole + mesitylene drop in a 3:2 ratio which showed differences in the drying. Images were recorded at 1000 fps and a shutter speed of 1ms. The cross section was taken horizontally across the centre of the well.

From the images and plot in figure 6.5 it was not entirely clear what had caused the differences in drying in some anisole + mesitylene drops. Anisole was more volatile than mesitylene and had a higher surface tension (table 6.1) so the expected surface tension gradients in this mixture would be a low surface tension at the contact line and a high surface tension at the centre of the drop, giving flows from the contact line towards the apex. The plot and images in figure 6.5 showed a largely U-shaped film profiles despite the relatively high drying speed, the drop was evaporating much faster than the anisole + mesitylene drop in figure 6.3b but did not give a dimple as expected. At the very end of drying there was a small build-up of fluid in the very centre of the well not seen in single solvents. The small raised

region in the centre of the well towards the end of drying was only a single fringe high. There were however some differences during the drying which separated the profile development from that of a standard U-shaped profile progression; the fluid flattened out earlier in the drying than with standard U-shaped progressions (figure 6.3a) so giving flatter films at thicker film heights, and the gradient of the fluid up to the wall tops was shallower. It is possible there was some form of Marangoni driven surface tension gradient acting towards the centre of the drop which counteracted capillary drainage from the centre of the drop and prevented dimple formation.

As the differences in drying for some anisole + mesitylene drops were not consistent, it would not be prudent to assign surface tension gradients as the cause of the imaged differences from these measurements alone. If surface tension gradients were the cause of the identified differences in drying you would expect the same pattern of drying in every drop, which was not the case. However the vapour pressures of anisole and mesitylene were similar (table 6.1) and it is possible the similarity of the vapour pressures meant the evaporation rates of the two solvents were not different enough to give surface tension driven flows that were dominant over capillary flows in all drops.

The anisole + methyl benzoate mixtures exhibited U-shaped profile progression consistently throughout drying (figure 6.3a) and the anisole and o-xylene mixture gave W-shaped profile progression in all cases (figure 6.3c), as would be expected from single solvents based on the evaporation rates. In both anisole + methyl benzoate and anisole + o-xylene mixtures, the higher volatility solvent had the lower surface tension, so expected flows were from the apex of the drop towards the contact line and you would expect to see M-shaped profiles. The relative vapour pressures of anisole and o-xylene were similar (table 6.1) and as such evaporation rates may not have been different enough to give surface tension driven flows that were dominant over capillary flows. In the case of anisole + methyl benzoate it is possible the large difference in vapour pressure meant anisole was evaporating much more quickly than methyl benzoate to leave essentially pure methyl benzoate for most of the drying and no surface tension driven flows.

In order for any firm conclusions on the impact of solutal surface tension gradients on drop profile progression during drying to be made, it was necessary to investigate some model solvent mixture systems. Model systems which exaggerate the differences in surface tension and volatility are necessary to determine the impact of solvent driven Marangoni stresses on the profile of drying drops in wells and thus to determine whether binary solvent mixtures could be useful in engineering flat deposits from drops printed into wells.

6.3 Other Substrate Geometries

The drying of solvent mixtures imaged within square wells showed some differences in profile development during drying for the anisole + mesitylene mixture, though not for the anisole + methyl benzoate or the anisole + o-xylene mixtures. Both anisole + methyl benzoate and anisole + o-xylene acted as would be expected of single solvents. In this section the drying of anisole + mesitylene and anisole + o-xylene mixtures in the oval and circular wells is discussed to determine how mixtures dried within more industrially relevant and axisymmetric systems. Drops were printed and imaged as described in chapter 2 section 2.1 and analysis of images was carried out as described in section 2.3. Solvent mixtures were made up in 1:4, 2:3, 3:2 and 4:1 ratios for each mixture.

The h_{max} and evaporation rate data for all solvent mixtures is plotted alongside the single solvent data for the oval wells in figure 6.6. As with the square wells, the majority of the solvent mixture measurements fitted within the general trend of the single solvent data. There were some data points which showed qualitative differences in drying behaviour, shown by the open symbols in figure 6.6. Drops which showed a difference in drying did not always sit outside the overall trend (figure 6.6); this was mostly due to de-wetting of the drop during drying giving a falsely high level of dimple formation.

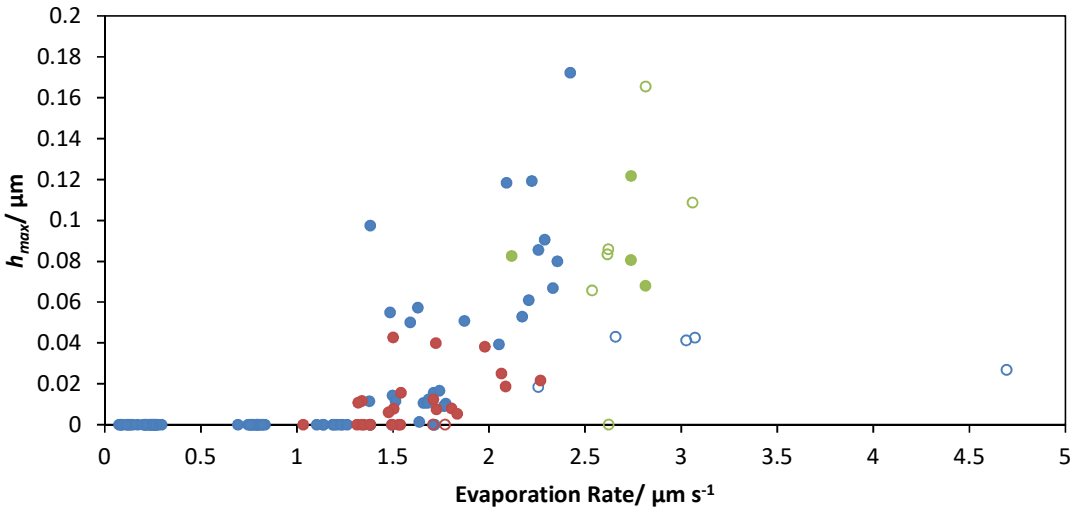

Figure 6.6: Relationship between h_{max} and evaporation rate for drops of single solvents (blue), anisole + mesitylene (red) and anisole + o-xylene (green) within the oval wells. Open symbols represent drops which showed qualitative differences in drying.

Some drops which showed qualitative differences in drying in the oval wells were for anisole + o-xylene drops. Images and plots of profile progression for the two behaviours of anisole + o-xylene are shown in figures 6.7 and 6.8. Some drops showed W-shaped profiles and others showed M-shaped profiles. The expected surface tension gradients in anisole + o-xylene

mixtures were high at the contact line and low at the apex, consistent with the M-shaped profiles seen in some cases. The similar vapour pressures of anisole + o-xylene could explain why enhanced drainage from the centre of the drop was not seen in each case (table 6.1). In the oval wells there is also another drainage pathway from the straight edges up to the curved ends, as seen by the lower values of h_{max} in chapter 4. The extra drainage pathway could reduce surface tension gradients and Marangoni stresses, so M-shaped profiles do not form in every case.

Some differences were also seen for the anisole + mesitylene mixture in the oval wells, similar to the differences seen in the square wells. Images and plots for the two behaviours are shown in figures 6.9 and 6.10. The profiles which showed qualitative differences displayed a slight build-up of fluid towards the centre of the wells at the end of drying. As previously discussed, expected surface tension gradients in the case of anisole and mesitylene were towards the centre of the drops, providing an explanation for the slight build-up of fluid towards the centre of the wells in the later stages of drying.

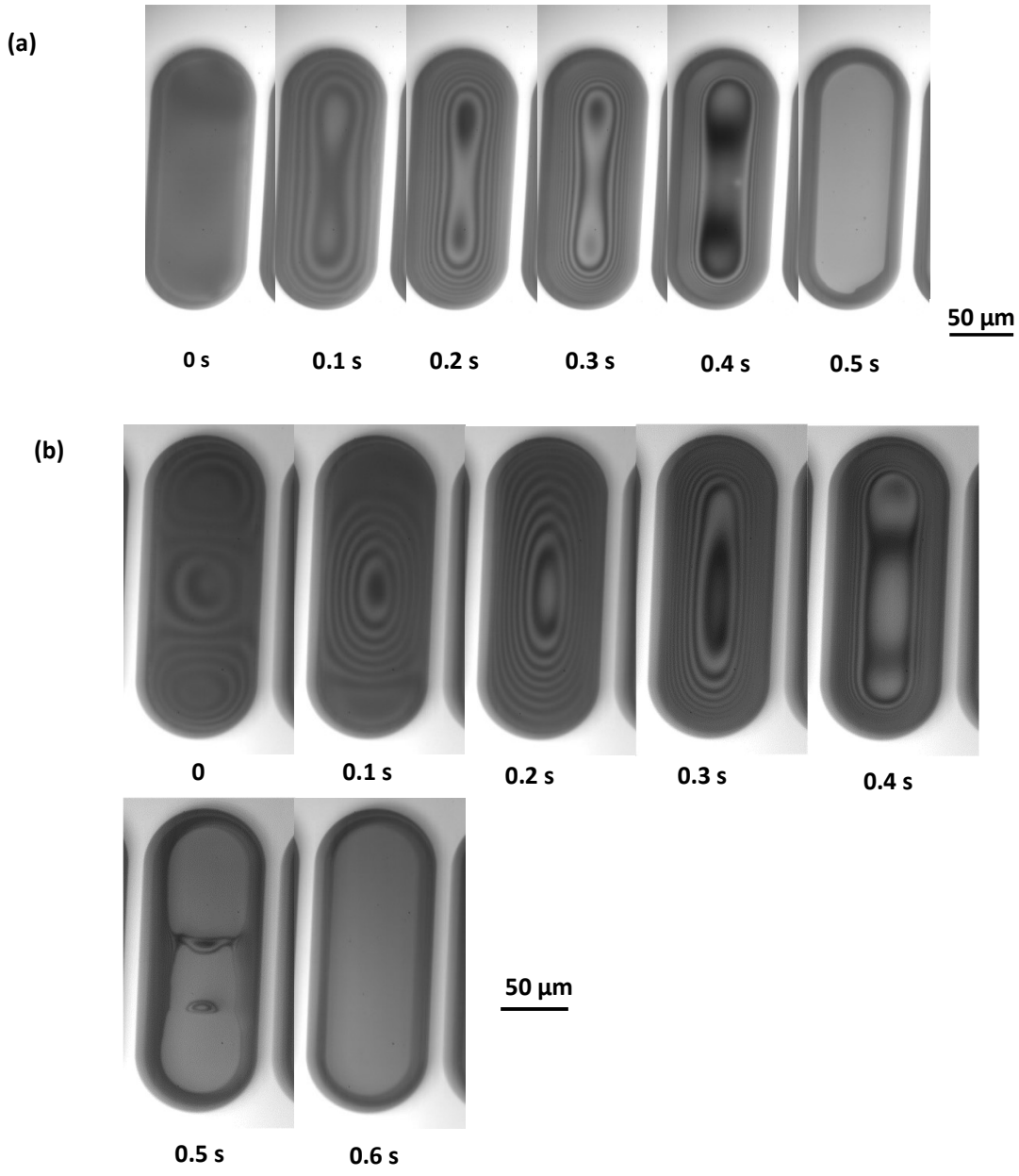

Figure 6.7: Images from the drying of anisole + o-xylene drops in a 2:3 ratio which dried to give W-shaped (a) and M- shaped (b) profiles in the oval wells. Images were recorded at 2000 fps and a shutter speed of 0.5 ms.

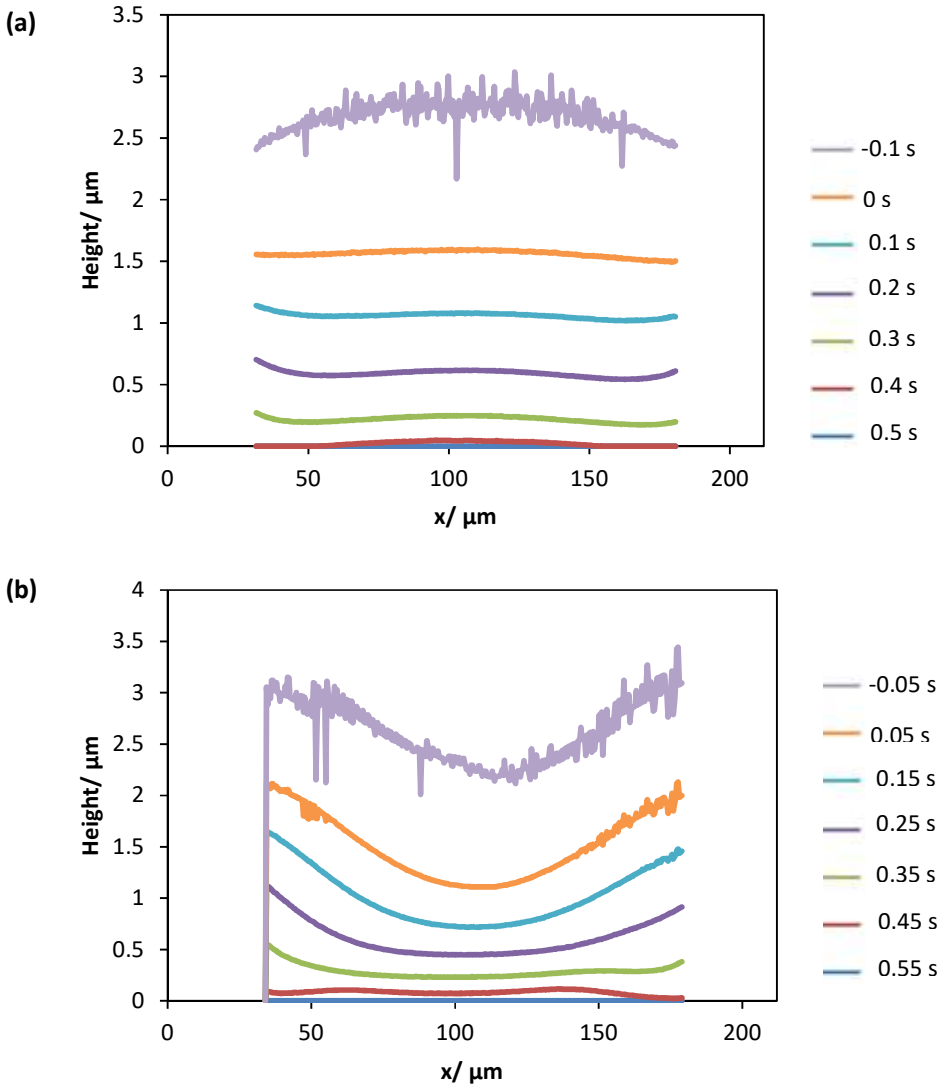

Figure 6.8: Plots of profile progression corresponding to the images in figure 6.7 for anisole and o-xylene drops in a 2:3 ratio which dried to give W- shaped (a) and M-shaped (b) profiles in the oval wells. Cross sections were taken along the long axis of the well.

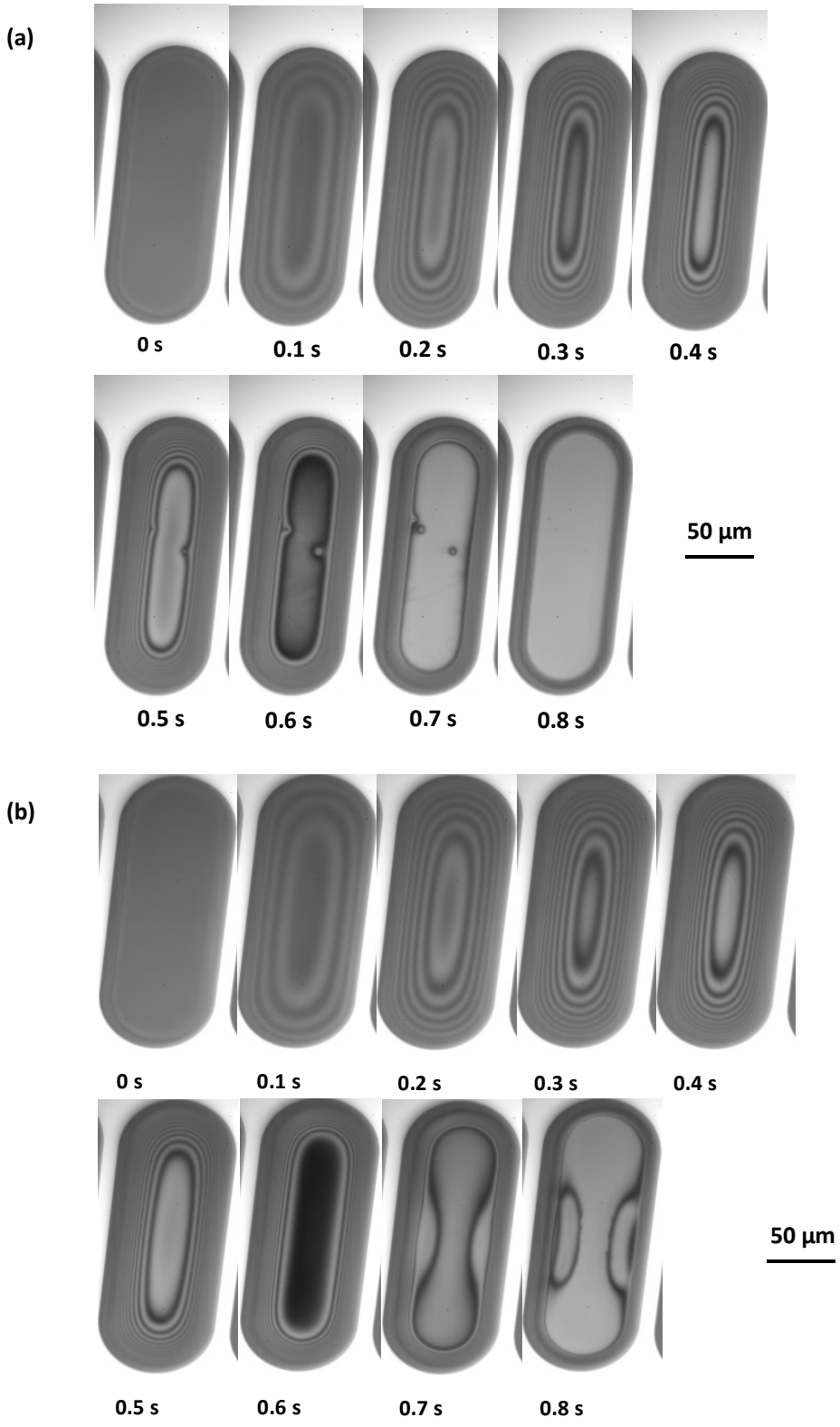

Figure 6.9: Images from the drying of anisole + mesitylene in a 3:2 ratio which dried to give U-shaped profiles (a) and a build-up of fluid towards the centre of the wells (b) in the oval wells. Images were recorded at 2000 fps and a shutter speed of 0.5 ms.

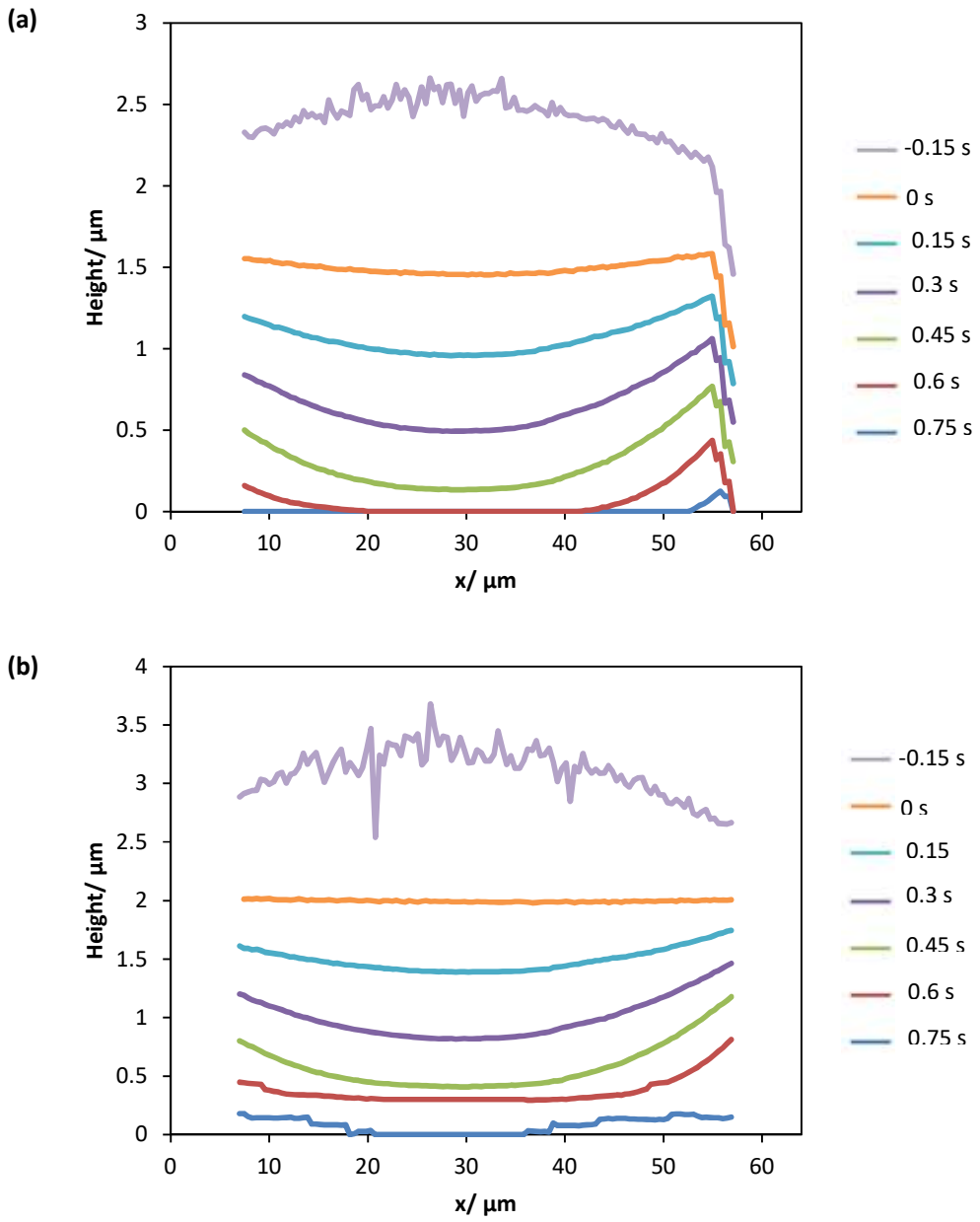

Figure 6.10: Plots of profile progression corresponding to the images in figure 6.9 for anisole and mesitylene in a 3:2 ratio which dried to give U- shaped profiles (a) and a build-up of fluid towards the centre of the wells (b) in the oval wells. Cross sections were taken along the short axis.

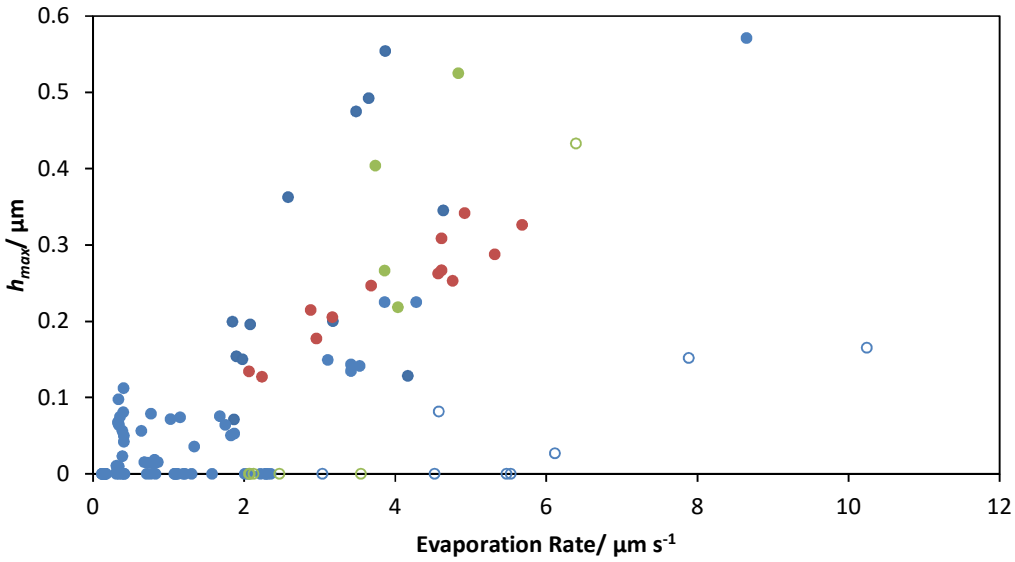

Figure 6.11: Relationship between h_{max} and evaporation rate for drops of single solvents (blue), anisole + mesitylene (red) and anisole + o-xylene (green) within the circular wells. Open symbols represent drops which showed qualitative differences during drying.

Figure 6.11 shows the h_{max} / evaporation rate data for the circular wells. As with the square wells most points fit within the single solvent data. Most anisole + o-xylene drops, shown by open symbols on the above plot, showed M-shaped profiles rather than W-shaped as would be expected from the evaporation rates. Images and plots from the two behaviours are shown in figures 6.12 and 6.13. The M-shaped profiles observed in most cases were consistent with the expected surface tension gradients. In the few anisole + o-xylene drops which did not show M-shaped profiles there was de-pinning of the drop down the walls during drying and W-shaped profiles formed. Figure 6.13a shows de-wetting of the fluid towards the end of drying to increase h_{max}, as well as de-pinning down the banks.

The absence of any solutal flows for the anisole + o-xylene mixture in the square wells (when they were present in both the oval and circular wells) could be explained by their relatively large size; if the surface tension gradients across the surface were weak, as indicated by enhanced drainage not being present in every case in oval and circular wells, then the larger surface area of the square wells could have prevented enhanced drainage from occurring.

In order to be certain what effect solvent mixtures had on the drying of drops within wells, more consistent data needed to be collected. The use of model solvent mixtures designed to exaggerate surface tension and volatility differences was necessary to gain more consistency from the data.

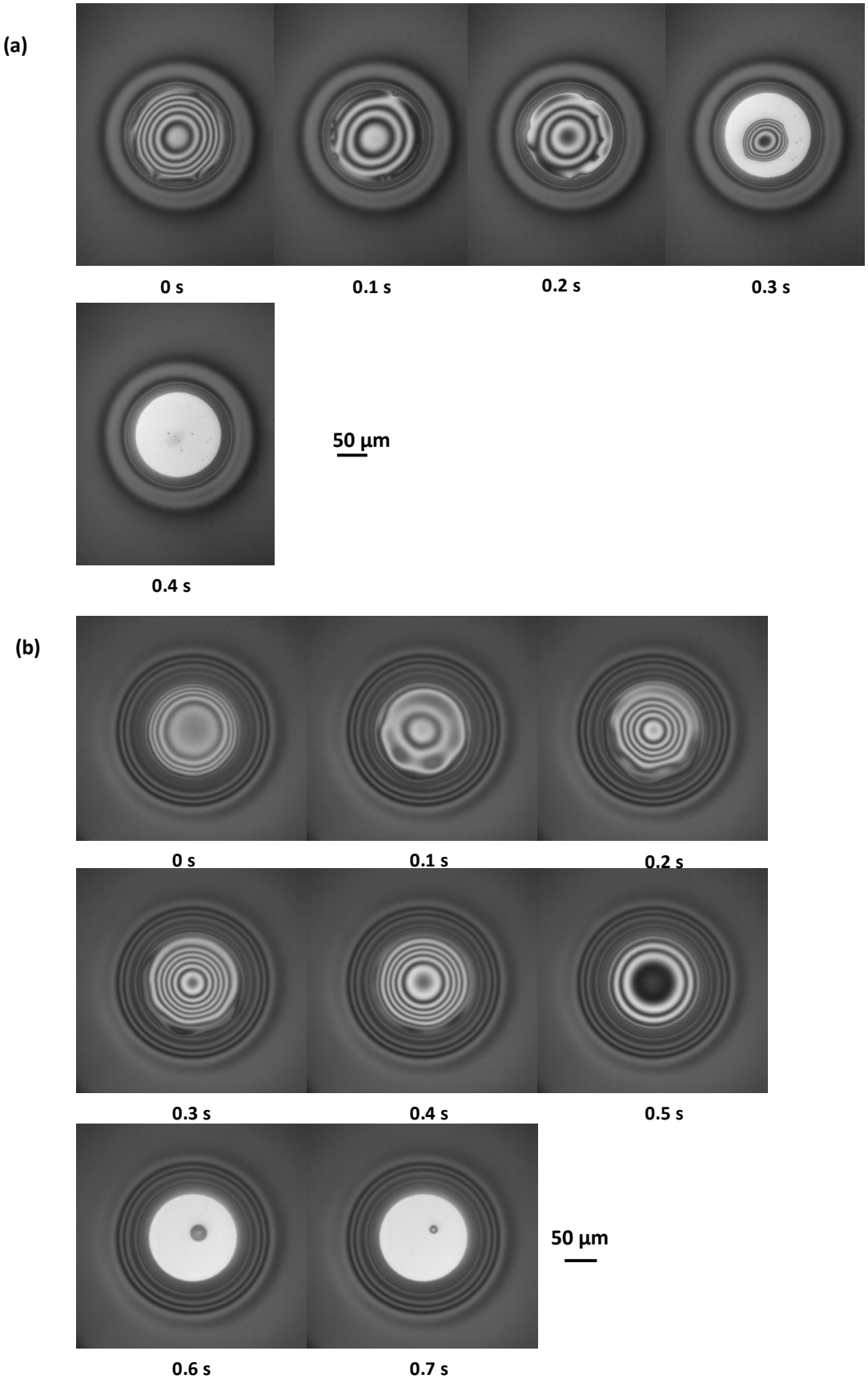

Figure 6.12: Images from the drying of anisole + o-xylene in a 2:3 ratio showing W-shaped (a) and W-shaped (b) profiles in the circular wells. Images were recorded at 2000 fps and a shutter speed of 0.5ms.

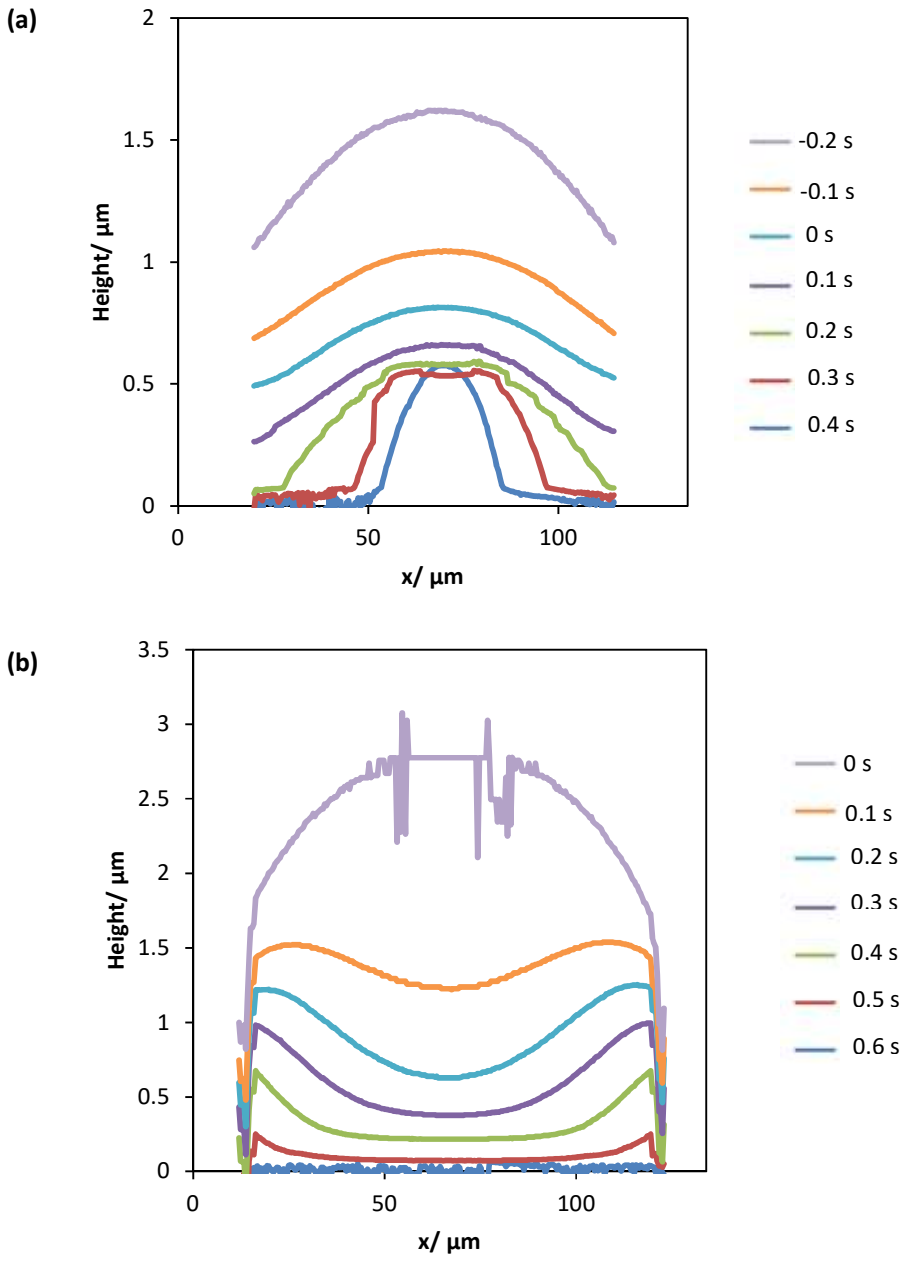

Figure 6.13: Plots of profile progression corresponding to the images in figure 6.12 for anisole + o-xylene in a 2:3 ratio drying to give W-shaped (a) and M-shaped (b) profiles in the circular wells. Cross sections were taken horizontally across the centre of the wells.

6.4 Model Solvent Mixtures

Images from the drying of industrially relevant mixtures in wells of all geometries showed the possible presence of solutal Marangoni gradients during drying, but without any consistency. Differences in drying and suspected Marangoni flows were not present in every case, most likely due to the similar volatilities of the solvents. To confirm the effect solutal Marangoni flows had on drop profiles during drying it was necessary to image the drying of model solvent mixtures designed to exaggerate differences in surface tension and volatility between the two solvents. Drying of three model mixtures has been imaged in the square wells and a picture of the changing drop profile during drying was built up. Drops were printed and imaged as described in chapter 2 section 2.1 and analysis of the images was as described in section 2.5. The solvent mixtures investigated were butyl acetate + ethanol, butyl acetate + methoxy propanol and butanol + toluene. The properties of the solvents are shown in table 6.2. All mixtures were imaged in a 1:1 ratio and butanol + toluene was also imaged in a 7:3 and 3:7 ratio. The surface tension and density data for all three mixtures are shown in figures 6.14 and 6.15. Each mixture was imaged on a minimum of three different days with a minimum of five drops of each mixture recorded on each day.

Table 6.2: Properties of all solvents, all values are quoted at 25 ^{o}C.

Solvent	**Surface Tension/ mN m^{-1}**	**Density/ g cm^{-3}**	**Viscosity/ mPa s**	**Vapour Pressure/ kPa**
Ethanol	23.39[70]	0.787[70]	1.057[70]	7.83[70]
Butyl acetate	24.78[70]	0.876[70]	0.677[70]	1.52[70]
Butanol	25.67[70]	0.806[70]	2.599[70]	0.931[70]
Toluene	27.93[70]	0.865[70]	0.548[70]	3.76[70]
Methoxy propanol	27.7[128]	0.916[128]	1.7[128]	1.2[129]

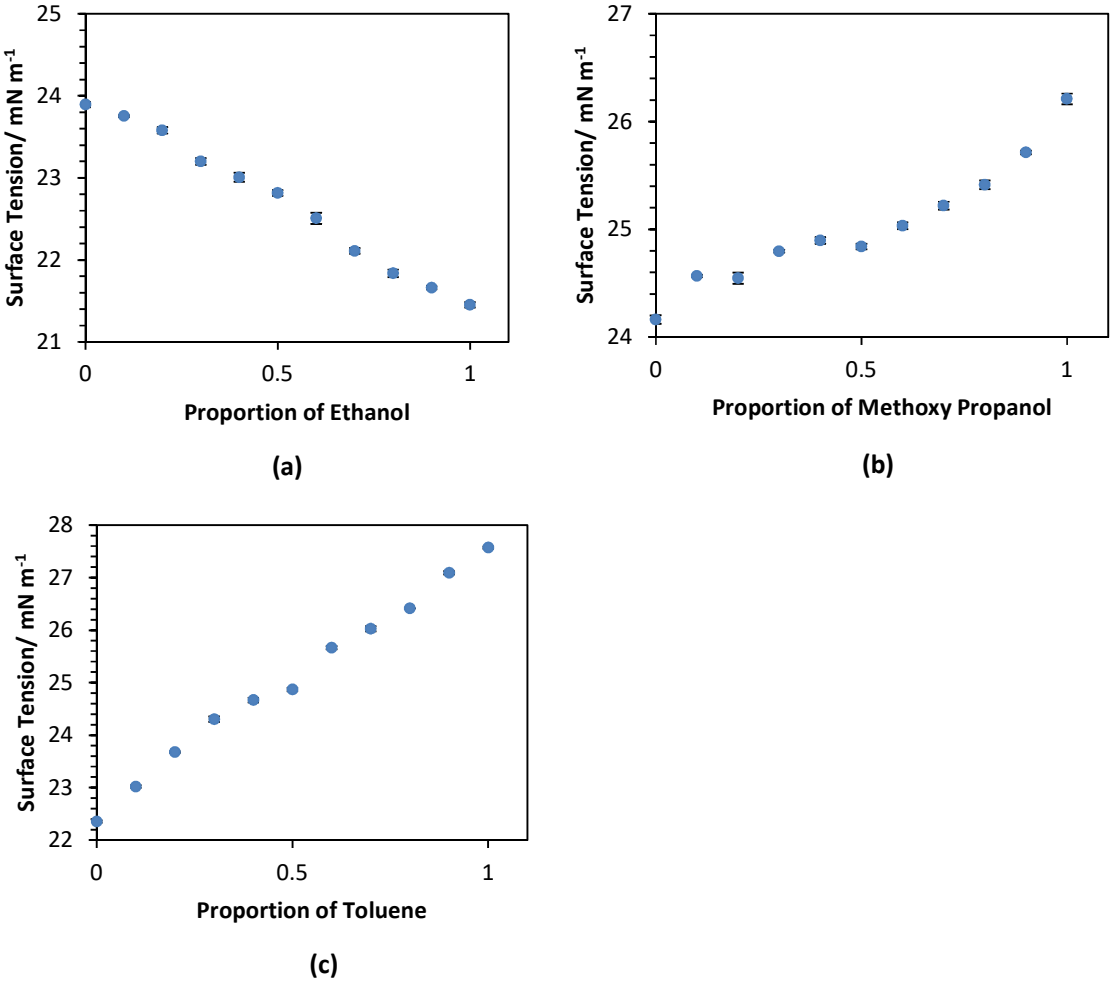

Figure 6.14: Surface tension data for mixtures of butyl acetate + ethanol (a), butyl acetate + methoxy propanol (b) and butanol + toluene (c) at differing compositions. Error bars show the standard deviation in the measurements; if error bars are not visible they are smaller than the points.

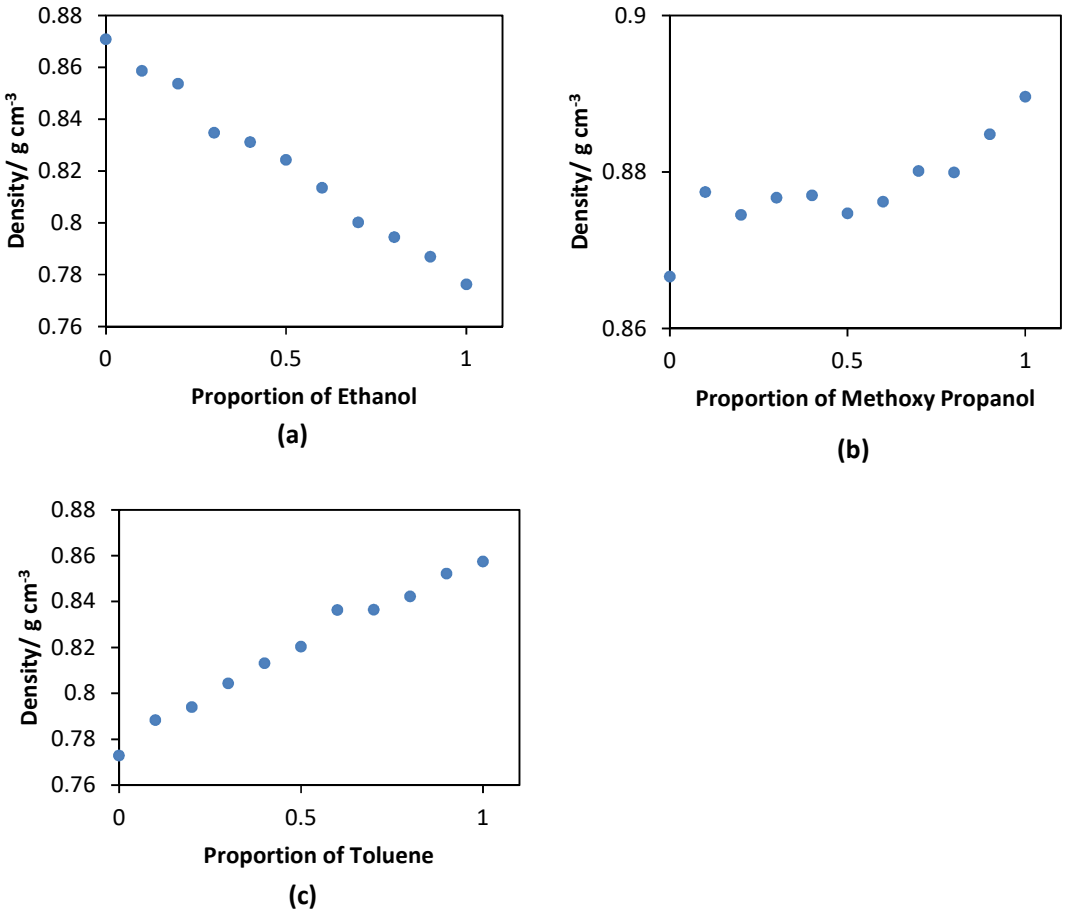

Figure 6.15: Density data for mixtures of butyl acetate + ethanol (a), butyl acetate + methoxy propanol (b) and butanol + toluene (c) at differing compositions. Systematic error associated with the density measurements was ± 0.001 g cm^{-3}.

The butyl acetate + ethanol mixture showed a steady decrease in surface tension and density with increasing proportions of ethanol. In the case of the butyl acetate + methoxy propanol mixture there appeared to be some non-ideal mixing as the surface tensions and densities of solutions did not increase smoothly with increasing proportions of methoxy propanol (figures 6.14b and 6.15b). The butanol + toluene data showed a linear increase in surface tension with increasing proportions of toluene.

VLE curves for the three mixtures are shown in figure 6.16, all three showed large deviations from ideal behaviour. The Y/X data for the mixtures is shown in figure 6.17. For all five solvents D was similar so the vapour pressures are the most important factor in determining which solvent evaporates fastest. For the butyl acetate + ethanol mixture, ethanol evaporation is enhanced relative to the bulk in all cases. As the vapour pressure of ethanol is higher than that of butyl acetate, the ethanol will evaporate more quickly at all compositions.

For the butyl acetate + methoxy propanol data (figure 6.17b) the evaporation of butyl acetate is enhanced relative to the bulk at all compositions, as such the butyl acetate should be evaporating more quickly throughout drying. The butanol + toluene data (figure 6.17c) shows an azeotrope at a butanol proportion of 0.07. However the lowest proportion of butanol investigated is 0.3 and as the toluene is evaporating more quickly relative to the bulk than butanol at this proportion, the mixture will never reach the azeotrope. Therefore toluene should be evaporating more quickly at all compositions.

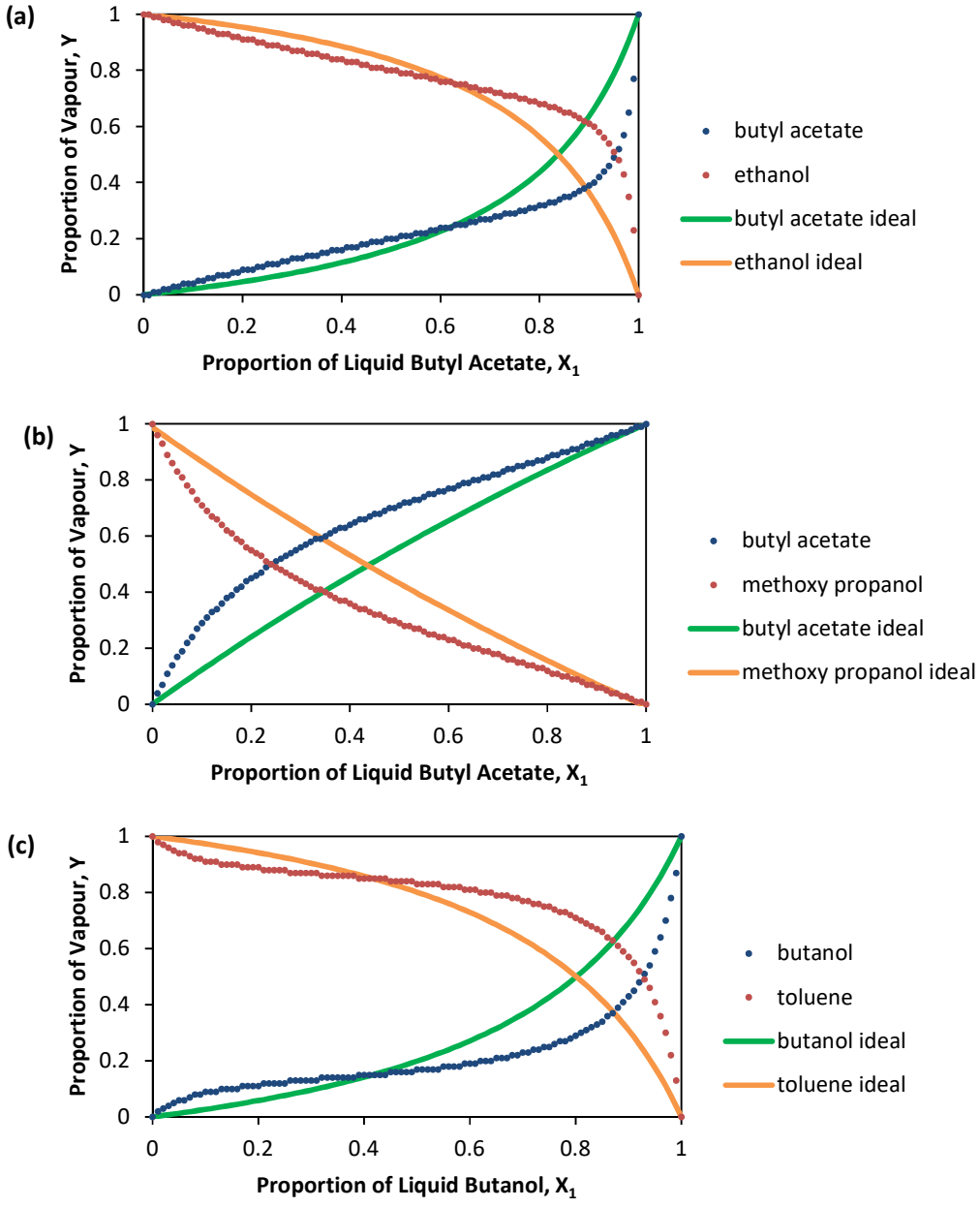

Figure 6.16: VLE curves for the butyl acetate + ethanol (a), butyl acetate + methoxy propanol (b) and butanol + toluene mixtures. VLE data was taken for all mixtures at 25 ^{o}C.[141] Apparent steps in the curves are the result of numerical limitations in the computations.

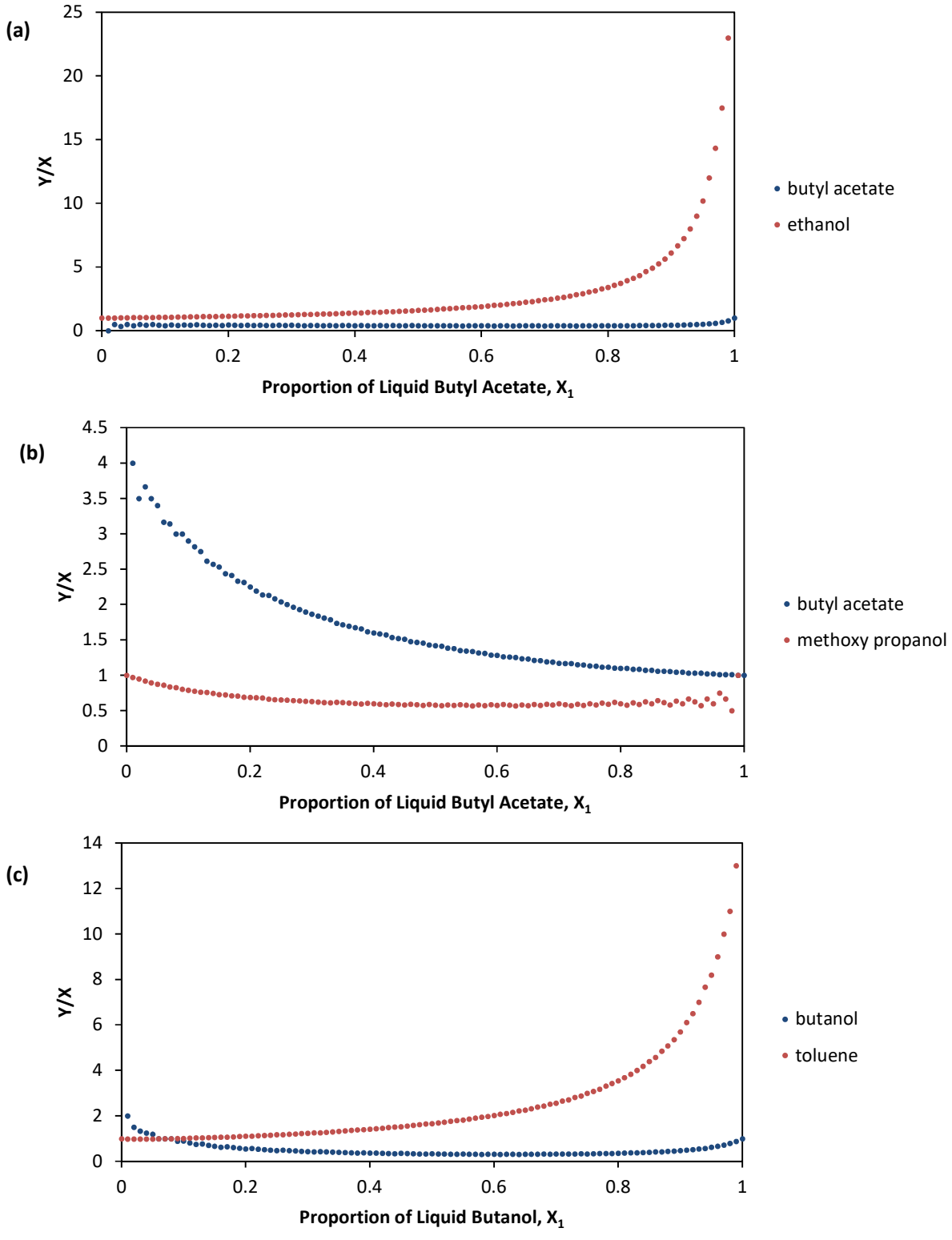

Figure 6.17: $^{Y}/_{X}$ curves calculated from figure 6.16 for the butyl acetate + ethanol (a), butyl acetate + methoxy propanol (b) and butanol + toluene mixtures. Apparent steps and divergence in the curves are the result of numerical limitations in the computations.

The images and plots of profile progression from the drying of one of the butyl acetate + ethanol drops are shown in figure 6.18. The video relating to figure 6.18 is video 10 on the attached disk. It showed M-shaped profile development in the early stages of drying before it switched back to give dimple formation. Ethanol has a lower surface tension than butyl acetate. As the more volatile solvent, ethanol was depleted at the contact line relative to the centre of the drying drops and there was a higher surface tension at the contact line of the drying drops than the centre. Expected solutal Marangoni flows were therefore from the apex towards the contact line, the M-shaped profiles seen in the early stages of drying were consistent with this. The switch to dimple formation in the later stages of drying confirmed the flows were solutal in nature as, once the ethanol had evaporated off, drying reverted to what would be expected from single drops evaporating at such rates.

Figure 6.19 shows the change in fluid height with time for the butyl acetate + ethanol drop shown in figure 6.18. The centre of the fluid (X in figure 6.18a) begins above the intermediate regions (Y in figure 6.18a) but quickly dips below the level of the fluid in the intermediate region (at $t \approx 0.02$ s) as the M-shaped profile forms. Once the M-shape has formed both regions then thin together from at $t \approx 0.2$ s until dimple formation occurs (at $t \approx 0.4$ s in figure 6.19 due to the chosen location of the intermediate region) and the intermediate region begins to thin more quickly than the centre. The data in figure 6.19 is consistent with the images and plots of profile progression in figure 6.18.

It was possible the enhanced drainage from the centre of the wells identified early on in the drying for butyl acetate + ethanol mixture was due to thermal effects from the rapid evaporation of ethanol, as ethanol has shown thermally driven surface tension gradients as a pure solvent. However images from the drying of the two drops appeared to suggest more pronounced enhanced drainage from the centre of the wells in the butyl acetate and ethanol mixture than in the pure ethanol (figure 6.18 compared to figure 6.20); indicating surface tension driven flows in figure 6.18 came from forces other than thermal gradients. Analysis of the images in figure 6.20 was not possible due to the de-wetting of the film during drying; evident from the pools of solvent left at 0.28 s. However qualitatively there appears to be a larger level of enhanced drainage in the images from the butyl acetate and ethanol mixture than the pure ethanol at 21 ^{o}C.

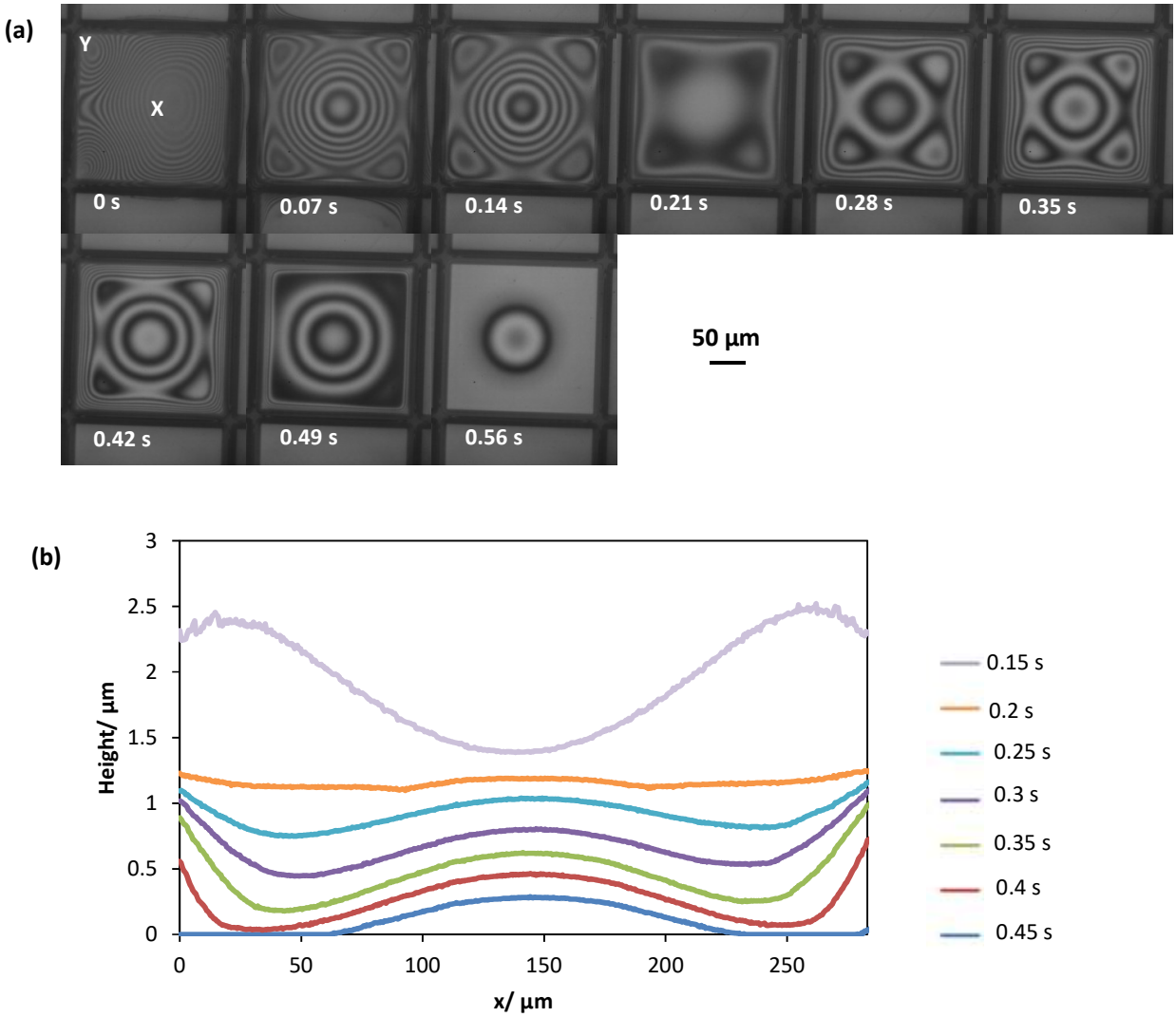

Figure 6.18: Images from the drying (a) and a plot of profile progression (b) for a drop of butyl acetate + ethanol in a 1:1 ratio drying within the square wells. Images were recorded at 2000 fps and a shutter speed of 0.5 ms Cross section was taken diagonally across the centre of the wells. In this case t = 0 has been defined as the time at which the drop finished spreading.

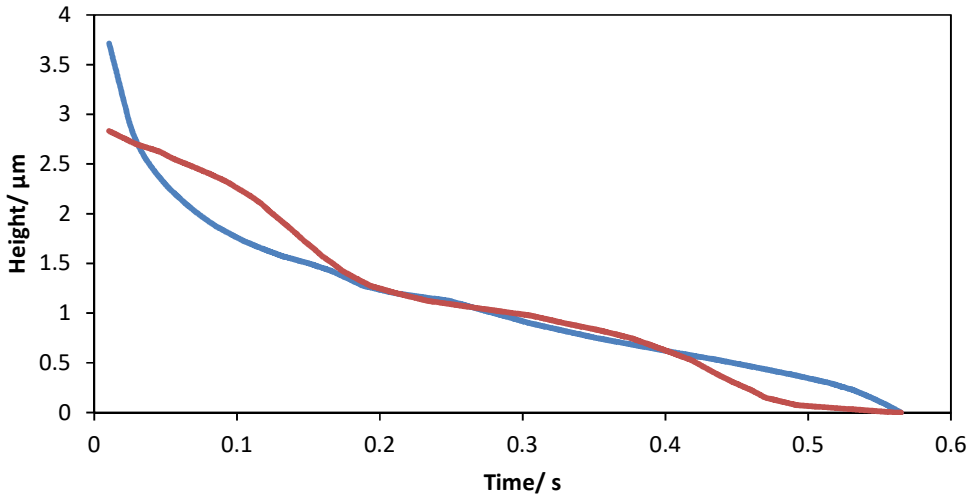

Figure 6.19: The relationship between fluid height and time in the centre of the well (blue, labelled X in figure 6.18a) and the intermediate region of the well (red, labelled Y in figure 6.18a) for the butyl acetate + ethanol drop shown in figure 6.18.

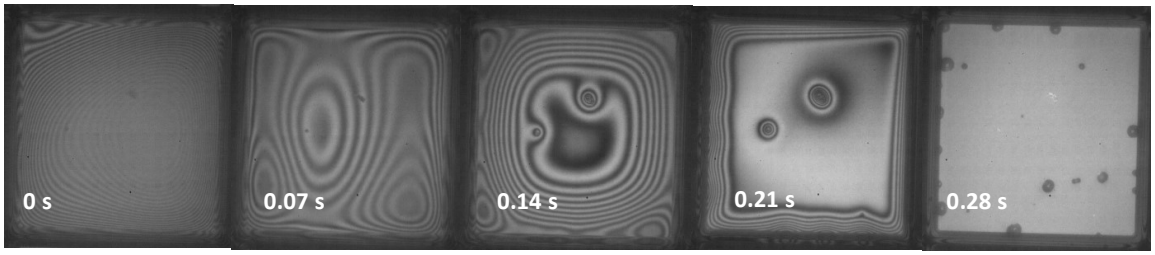

Figure 6.20: Images from the drying of pure ethanol at 21 ^{o}C in the square wells. Images were taken at 3000 fps and a shutter speed of 0.33 ms. Analysis of the images was not possible due to de-wetting of the film during drying (evident from the image at 0.28 s). There was also some dust present in the drying images (0.12 s onwards) though it did not impact on the film profile during drying.

In the case of the butyl acetate + methoxy propanol mixture, butyl acetate has a lower surface tension than methoxy propanol and was more volatile; giving the same direction for the surface tension gradients as in butyl acetate + ethanol. Images from the drying and plots of the drop profile are shown in figure 6.21: they show M-shaped profile progression. The video relating to figure 6.21 is video 11 on the attached disk. Profiles in the case of butyl acetate + methoxy propanol are consistent with the expected surface tension gradients. As neither butyl acetate nor methoxy propanol showed thermal effects in chapter 5, the Marangoni stresses are a result of compositional gradients.

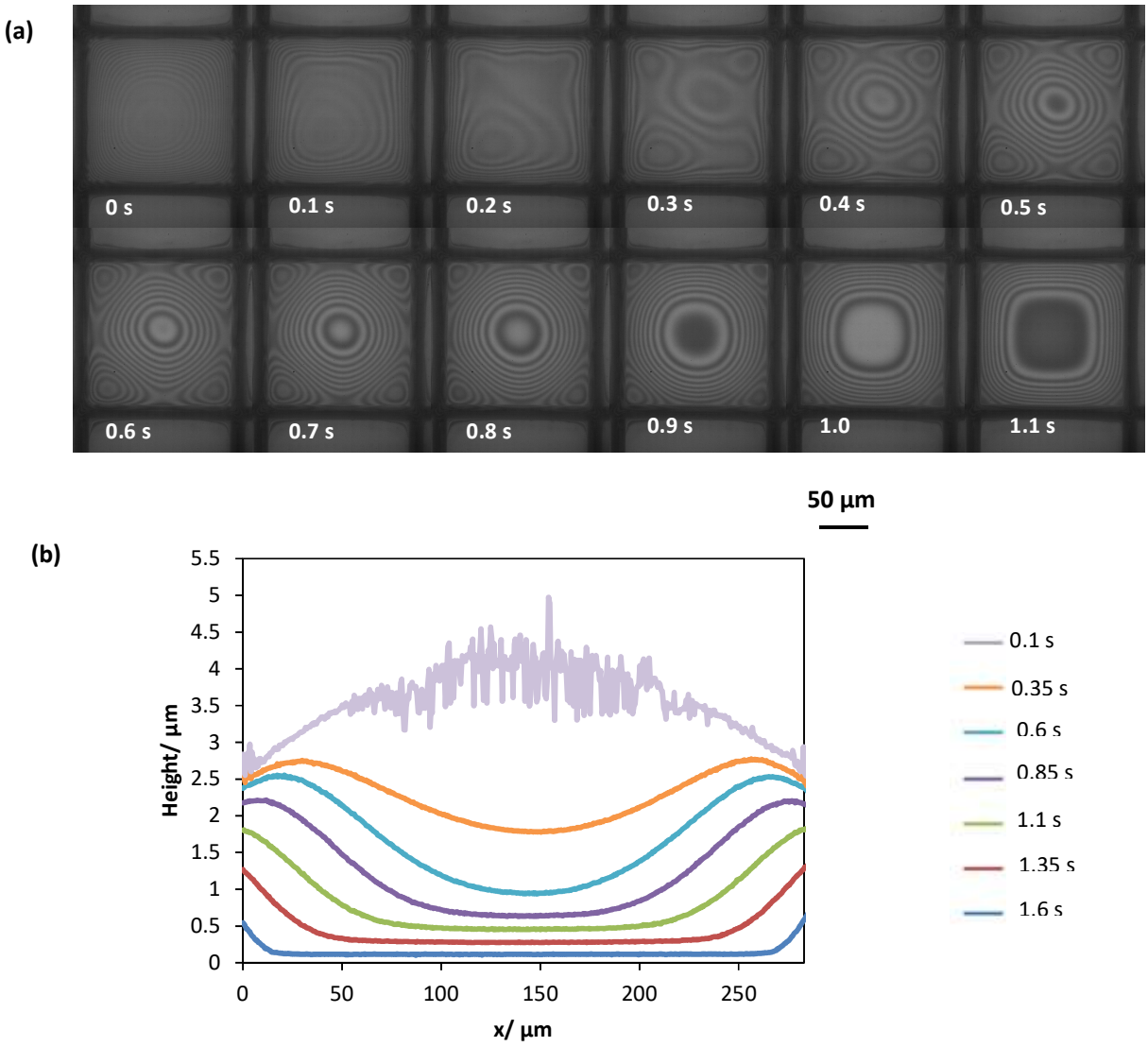

Figure 6.21: Images from the drying (a) and a plot of profile progression (b) for a drop of butyl acetate and methoxy propanol drying within the square wells. Images were recorded at 2000 fps and a shutter speed of 0.5 ms. The cross section was taken diagonally across the centre of the well.

The vapour pressure data in figure 6.17 show that toluene is more volatile than butanol at the ratios investigated, and as such the surface tension is expected to be lower at the contact line and higher in the centre. Images from the drying and plots of profile progression for the drying of a 1:1 drop of butanol + toluene are shown in figure 6.22. At first sight, the images do not appear to show any difference in drying from single solvents with dimple formation as drying progressed. However when the profile was taken diagonally across the wells (figure 6.22) there appeared to be a slight dipping of the fluid in the corners of the drops before they curved up towards the drop apex. The dipping of fluid in the corners of the wells and deviation from the constant mean curvature seen in single solvents (chapter 4) suggested possible solutal flows from the contact line towards the apex of the drop. The regions at both 0 and

300 µm in figure 6.22b which show apparent sharp drops in fluid height are the region of fluid on top of the slope of the banks.

To confirm the presence of solutal Marangoni flows from the contact line towards the apex of the drop, solutions at a ratio of 7:3 and 3:7 of butanol:toluene were made up and the drying was imaged. The 7:3 ratio showed deviations from constant mean curvature early in the drying ($t \approx$ -0.2 – 0 s in figure 6.23) but did not show enhanced drainage from the corners of the wells and gave dimple formation as expected from the evaporation rate, most likely due to the small proportion of toluene and its high vapour pressure relative to butanol. When the plot in figure 6.23b is compared to figure 4.19a (chapter 4, showing the diagonal profile of an o-xylene drop) the differences between the two become apparent. Figure 4.19a shows constant mean curvature across the drop in the early stages of drying whereas figure 6.23b does not.

Images from the drying and plots of the profile progression for the 3:7 mixture are shown in figure 6.24; there was now clear enhanced drainage from the corners of the well towards the apex of the drop. Dipping of the fluid in the corners of the wells and deviation from constant mean curvature early on in the drying appeared to confirm the presence of solutal Marangoni flows in the butanol + toluene mixture. Enhanced drainage from the corners of the wells was apparent in every case of printed butanol + toluene drops in a 3:7 ratio and was consistent with the expected solutal flows. The apparent noise early on in the profiles in figures 6.22 and 6.24 was due to the miscounting of fringes as the drop height approached the coherence limit of the light source. As the drop dipped in the corners very early on in the drying before reverting to give dimple formation, it was necessary to show these profiles but the apex of the drops at the relevant points in the drying was too high to show any clear interference fringes in the images. The regions close to 0 and 300 µm in figure 6.24b where there is a sudden drop in film height is where the fluid overlapped the slope of the banks.

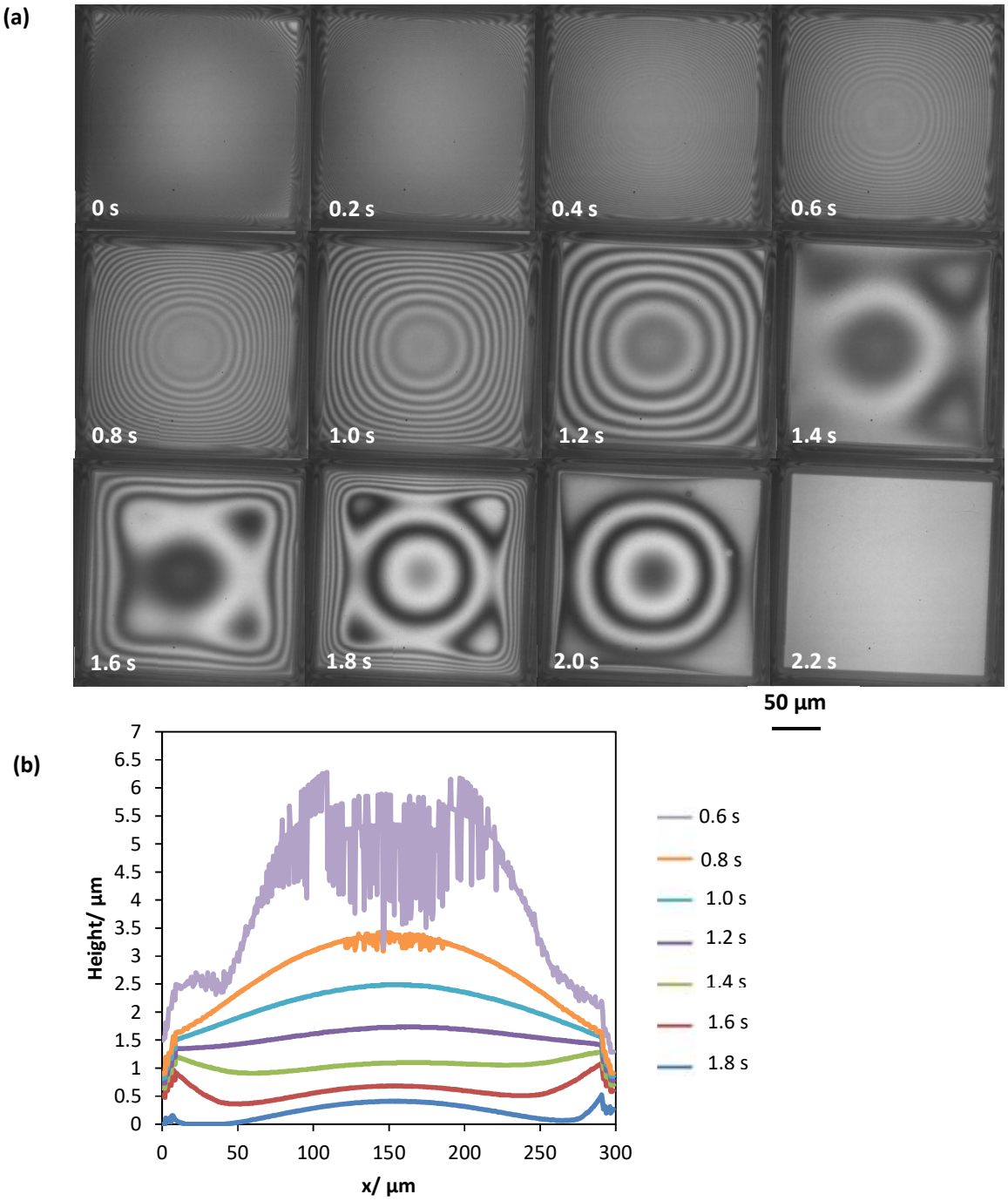

Figure 6.22: Images from the drying (a) and a plot of profile progression (b) for butanol + toluene in a 1:1 ratio. Images were recorded at 2000 fps and a shutter speed of 0.5 ms. The cross section was taken diagonally across the centre of the well.

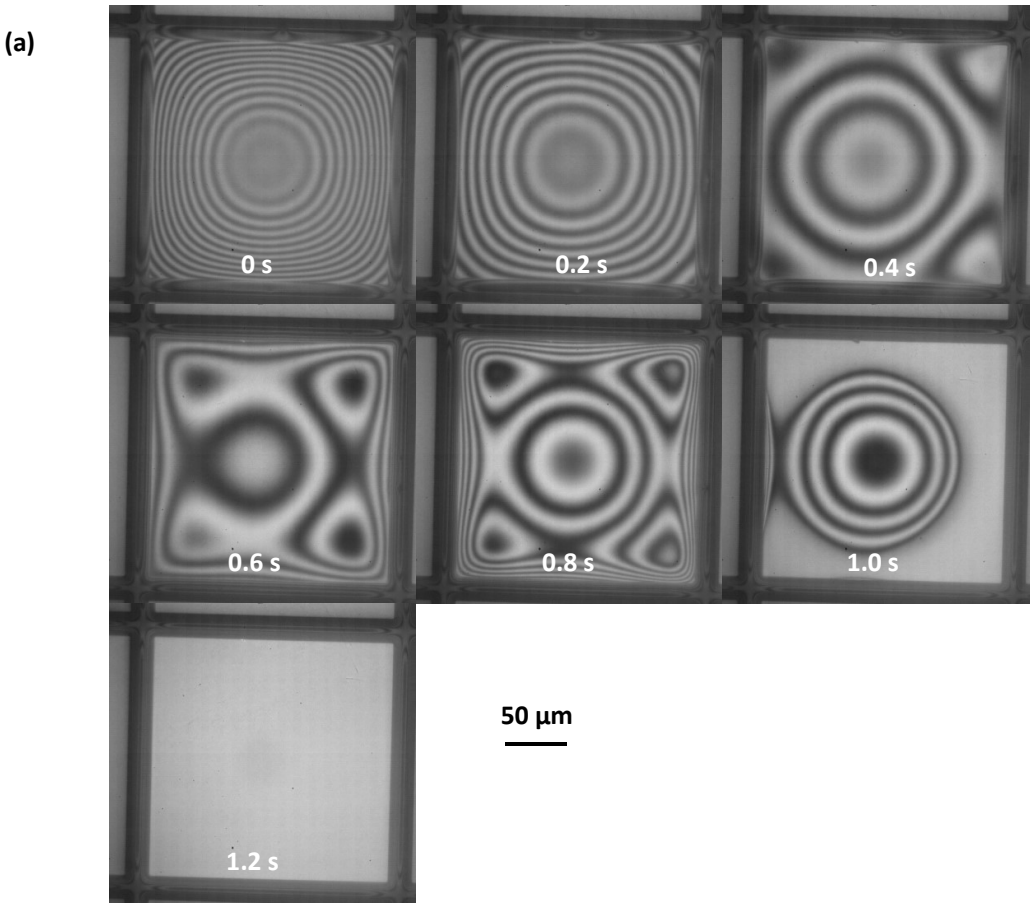

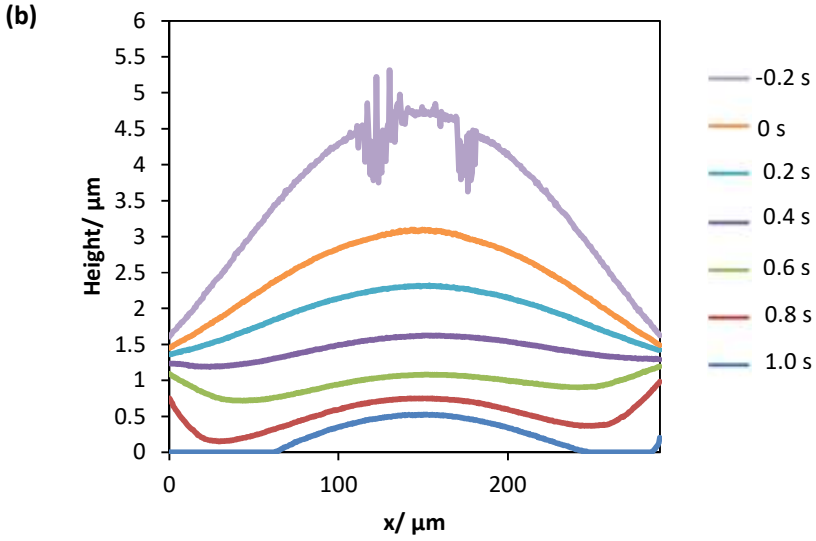

Figure 6.23: Images from the drying (a) and plots of profile progression (b) for butanol + toluene in a 7:3 ratio. Images were recorded at 2000 fps and a shutter speed of 0.5 ms. The cross section was taken diagonally across the centre of the well.

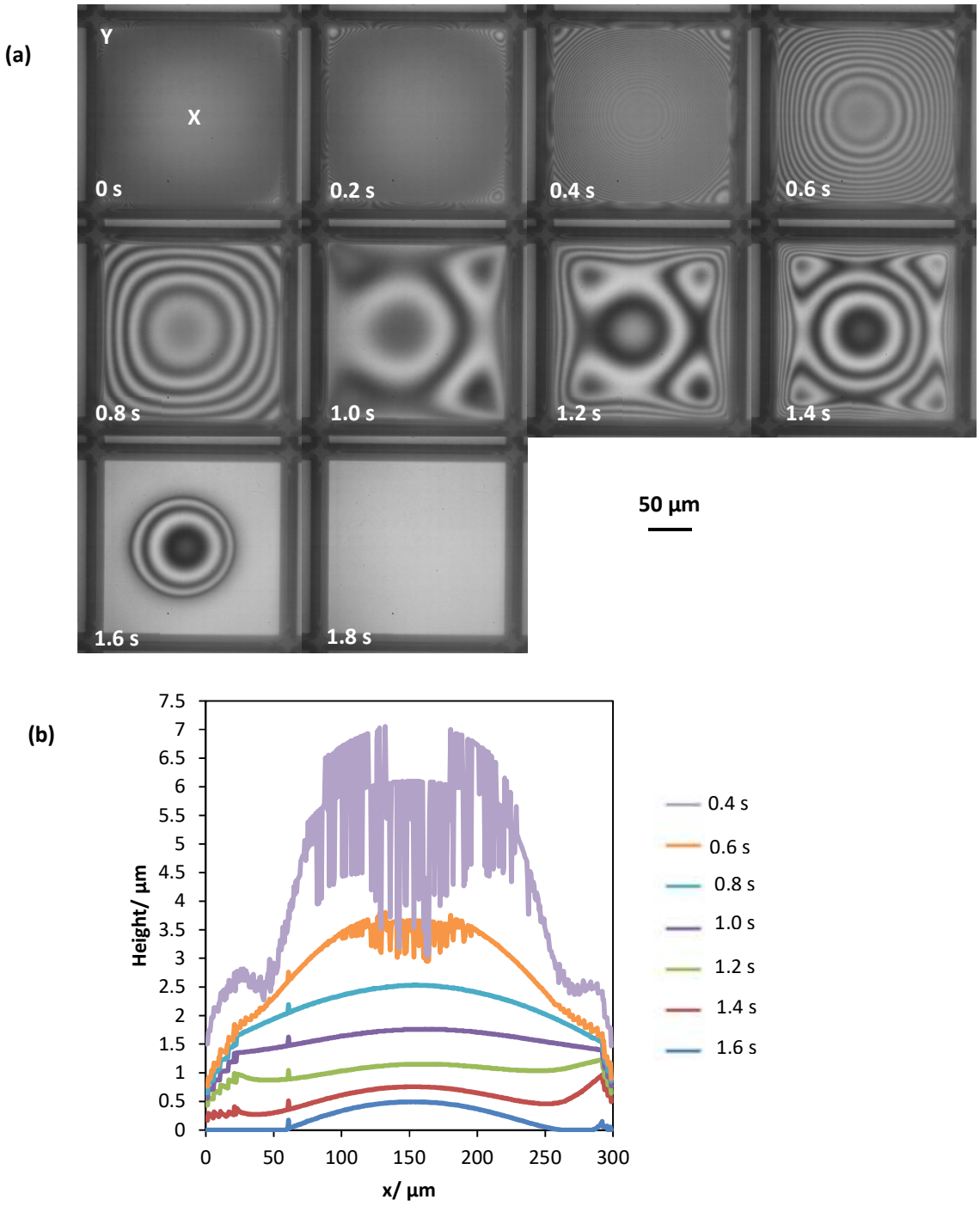

Figure 6.24: Images from the drying (a) and a plot of profile progression (b) for butanol + toluene in a 3:7 ratio Images were recorded at 2000 fps and a shutter speed of 0.5 ms. The cross section was taken diagonally across the centre of the well.

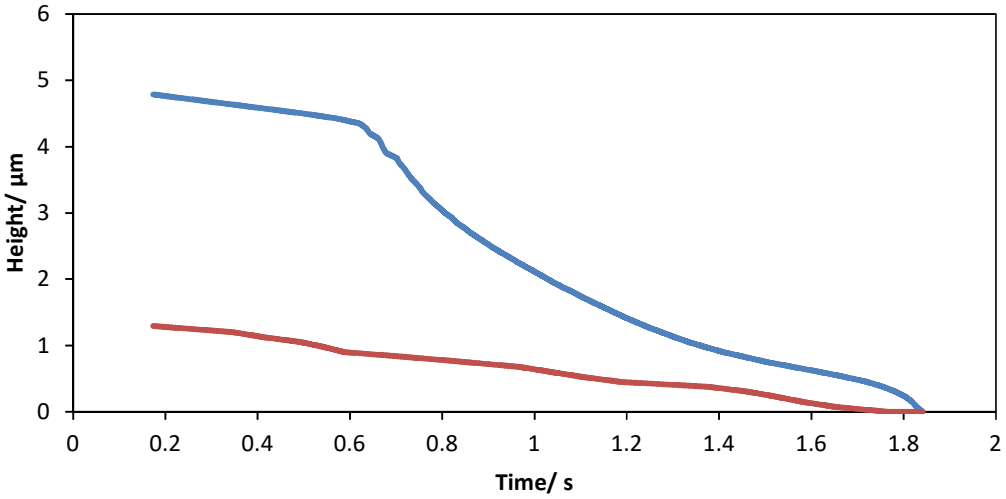

Figure 6.25: The relationship between fluid height and time in the centre of the well (blue, lableed X in figure 6.24a) and the intermediate region of the well (red, labelled Y in figure 6.24a) for the butanol + toluene drop shown in figure 6.24.

Figure 6.25 shows the change in fluid height with time for the butanol + toluene drop shown in figure 6.24. The centre of the fluid (X in figure 6.24a) remains higher than the intermediate regions (Y in figure 6.24a) for the entire drying process. Initially the intermediate and central regions thinned at roughly the same rate before the rate of thinning in the central region increased and became faster than the intermediate region. The increased rate of thinning in the centre after approximately 0.6 s is consistent with drainage from the corners to the centre stopping and evaporation progressing as a single solvent would. The data in figure 6.25 is consistent with the images seen in figure 6.24. The video relating to figure 6.24 is video 12 on the attached disk.

The imaging of model solvent mixtures has shown the influence of solutal Marangoni flows on drop profile progression during drying. It cannot be said for certain from these measurements that surface tension gradients were the cause of differences in drying for the anisole + o-xylene and anisole + mesitylene mixtures imaged in sections 6.2 and 6.3, though in the case of anisole + o-xylene profile development was as would be expected from solutal gradients. The differences seen in anisole + mesitylene mixtures looked different to the flows from surface tension gradients towards the apex of the drop and as such it is still unclear what caused those differences. Whilst the M-shaped profile development in the butyl acetate + ethanol mixture may not be useful in giving flat deposits of active materials from drops printed into wells, the enhanced drainage from the corners of the wells in the butanol + toluene mixture could.

6.5 Summary

Drops of industrially relevant solvent mixtures of anisole + methyl benzoate, anisole + mesitylene and anisole + o-xylene showed some differences in drying from the expected h_{max}/ evaporation rate relationship displayed by single solvents, though not consistently. The observed differences in drying were consistent with what would be expected from solutal surface tension gradients in each case. The likely reason for the inconsistency in measurements was the similar vapour pressures of the solvents involved. As the observed differences were not consistent it was not possible to assign them as solutal Marangoni effects, though the observed differences were consistent with the expected surface tension gradients in the case of each mixture.

To confirm the influence of solutal Marangoni flows on drops drying within wells, a number of model solvent mixtures were identified and the drying was imaged. Butyl acetate + ethanol and butyl acetate + methoxy propanol mixtures showed M-shaped profiles due to solutal Marangoni gradients in all cases. Butyl acetate + ethanol then reverted to give the expected dimple formation from fast drying drops once all of the ethanol had evaporated. The measurements of butyl acetate + ethanol and butyl acetate + methoxy propanol confirmed solutal Marangoni flows towards the contact line give M-shaped profiles. Enhanced drainage from the centre of the drop is not likely to be useful in gaining flat deposits from OLED drops printed into wells.

Butanol + toluene mixtures showed enhanced drainage from the contact line towards the apex of the drop due to solutal Marangoni gradients before reverting to the expected dimple formation once all of the toluene had evaporated. The measurements of butanol and toluene mixtures confirmed the impact solutal Marangoni flows towards the apex of the drop have on profile progression during drying. Enhanced drainage from the contact line of the drops is potentially useful in counteracting the enhanced drainage from the centre of the drop caused by the presence of active materials.

7. The Impact of Active Materials

7.1 Introduction

Thus far only pure solvent systems have been considered, in the absence of active OLED materials. It cannot be assumed the drying profiles will be the same in the presence of active materials as they are in pure solvents as the surface tension of the solution will depend on composition, even for non-surface active materials, and changing compositions may affect evaporation rates. Precipitation of solids from the solution may also change the bulk or interfacial rheology of the fluid. To understand the mechanisms behind active material transport and deposit morphology in drops containing active materials (necessary for industry to understand what they are printing) imaging of drying drops containing such materials is necessary.

Typical active material concentrations printed industrially are 12 – 40 mg cm^{-3} and the solubility limit of active materials is generally 60 – 80 mg cm^{-3}. The solubility limit of active materials suggests the material will not precipitate out of solution until at least halfway through the drying process, with it more likely to occur in the last quarter of drying.

In this chapter the drying of drops containing active material at a concentration of 5 mg cm^{-3} is discussed, this concentration is lower than those used industrially due to low availability of the material. At a concentration of 5 mg cm^{-3}, precipitation of the active material will not happen until the very end of the drying process. Solutions of Livilux TH-123 in anisole, methyl anisole, dimethyl anisole, methyl benzoate, mesitylene and o-xylene were imaged after they were identified as industrially relevant solvents. The presence of active materials meant it was not possible to use the same interferometry method to determine height profiles quantitatively as material present at the end of drying prevented the determination of the zero of height. The precipitation of active materials also caused scattering of the illumination light which destroyed the presence of fringes before the drop was fully evaporated. However the profile development during drying could be inferred from the images.

Alongside the imaging of Livilux TH-123 in single solvents, the drying of butanol + toluene drops in a 3:7 ratio containing Livilux TH-123 at a concentration of 5 mg cm^{-3} is considered. In chapter 6, butanol + toluene was identified as a potentially useful mixture in giving even deposits from drops printed into wells. The Livilux TH-123 is a host material used in active OLED films though the exact compound was unknown to us. As the compound was unknown to us it was unclear what impact it would have on the surface tension of the solvents, this had to be determined from measurements on the solutions.

7.2 Single Solvents

In this section the drying of single solvent drops containing active materials is considered. Solutions of 5 % by weight Livilux TH-123 in anisole, methyl anisole, dimethyl anisole, methyl benzoate and mesitylene were prepared and printed into square wells as described in chapter 2 section 2.2.

Images of drying anisole and dimethyl anisole drops are shown in figure 7.1. The anisole drop in figure 7.1a shows pronounced M-shaped profile progression during drying whereas the dimethyl anisole drop (figure 7.1b) shows mainly U- shaped profiles. There is a slight dip in the centre of the wells before the corners have reached that level in figure 7.1b, suggesting there may have been some very muted enhanced drainage from the centre of the dimethyl anisole drop. Images from the drying of all other solvents in the presence of active materials are shown in appendix C. The videos relating to figure 7.1 are videos 13 and 14 on the attached disk. In all cases the presence of active materials caused some form of M-shaped profile progression akin to the flows seen in drops with surface tension gradients which are high at the contact line and low at the apex. It was likely the surface tension gradient was a function of a compositional gradient in the drying drops. The slower evaporating solvents such as methyl benzoate and dimethyl anisole showed muted enhanced drainage whereas the faster evaporating solvents such as anisole, methyl anisole and mesitylene showed pronounced M-shaped profiles.

To determine the effect active materials had on surface tension, solutions of Livilux TH-123 were made up at concentrations between 2 and 8 % by weight of active and the surface tensions of all solutions were measured and compared to the pure solvents. Surface tension values were measured for each sample until all three consecutive measurements within 0.1 mM m^{-1} of one another were obtained. All solvents showed a general increase in surface tension with increasing concentration of active material (figure 7.2) though the increase was not smooth. All changes in surface tension were larger than the standard deviations associated with the measurements (shown as error bars on the plots in figure 7.2). The quoted errors arise only from the fitting errors of the pendant drop profiles: the same density is used for all measurements on the same sample. Errors in the density measurement lead to variability between the surface tensions measured on different samples. The precision in the density measurement is 0.1 %, leading to an error of 0.15 % in the surface tension (approximately 0.05 mN m^{-1}). This error does not account for the variation in figure 7.2.

If errors in density measurements outside the systematic errors accounted for were the reason for the inconsistencies in surface tension values, a plot of measured density against the

measured surface tension should give a straight line. A plot of surface tension against density for methyl benzoate is shown in figure 7.3 and does not show a straight line. The inconsistency in surface tension was therefore not solely due to an error in density measurement though, as a linear increase in density with concentration is expected for dilute solutions, an error in density measurement was clearly a factor. Inconsistencies in the surface tension measurement could also have been made worse by errors in the measurement of surface tension itself. Due to the limited availability of active materials it was not possible to repeat these measurements.

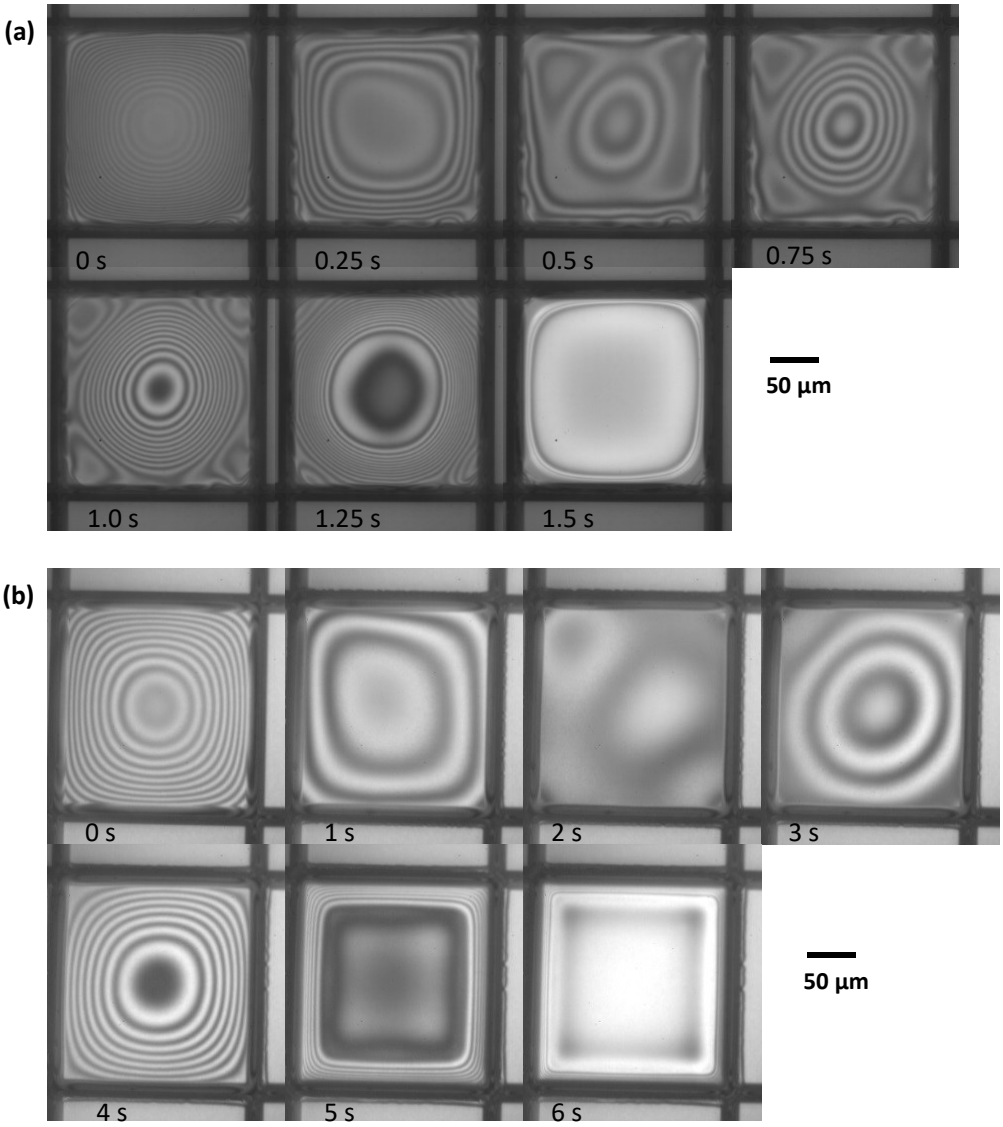

Figure 7.1: Images showing profile progression in an anisole drop which showed pronounced enhanced drainage from the centre of the wells (a) and from a dimethyl anisole drop which showed muted drainage from the centre of the wells (b). In the case of anisole images were recorded at 1000 fps and 1 ms exposure whereas in dimethyl anisole images were recorded at 50 fps and 1 ms exposure.

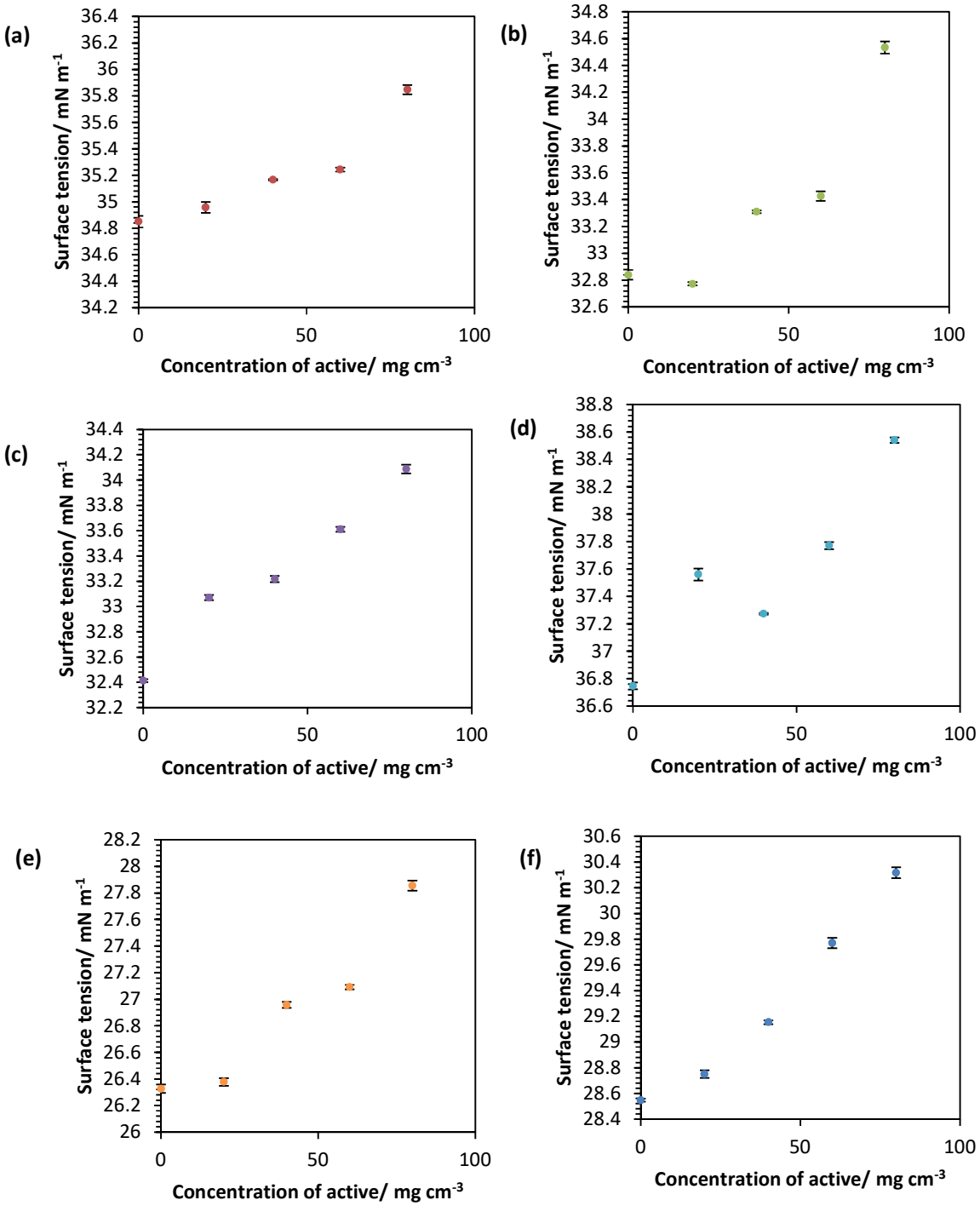

Figure 7.2: Variation in surface tension with concentration of Livilux TH-123 in anisole (a), methyl anisole (b), dimethyl anisole (c), methyl benzoate (d), mesitylene (e) and o-xylene (f). Points are the mean of three measurements and error bars show the standard deviation in the measurements.

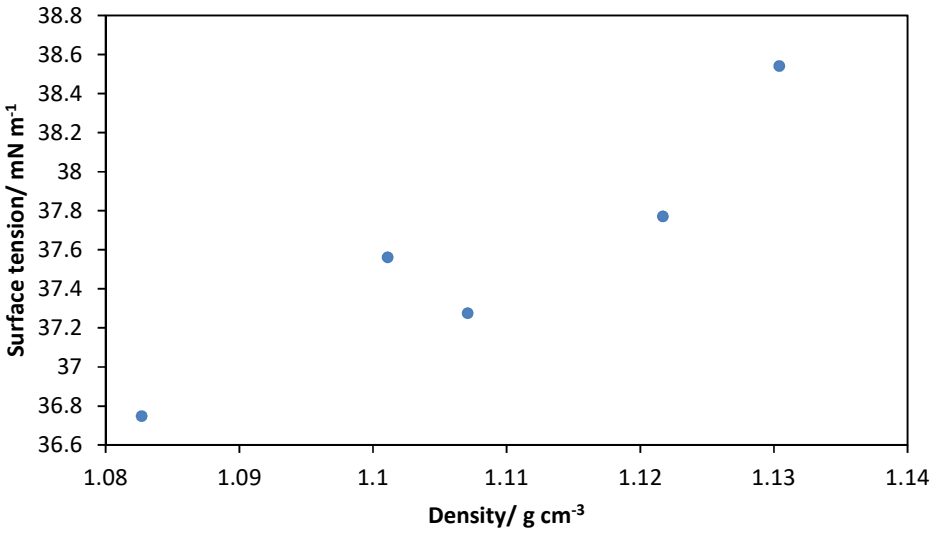

Figure 7.3: Correlation of surface tension and density for the methyl benzoate measurements in figure 4.19d.

The surface tension of all solutions increased with increasing concentration of active material. In an evaporating drop enhanced evaporation at the contact line gives a higher concentration of active material at the contact line than at the apex of the drop. The higher concentration of active leads to a higher surface tension at the contact line than at the apex, consistent with the observed M-shaped profiles. The disparity between slower and faster evaporating drops in terms of level of enhanced drainage could be explained by the amount of time the active material has to diffuse through the drop during the drying process. The Peclet number in the vertical direction ($Pe = 0.08$, $t_{diff} = 10^{-3}$ s) is small so diffusion averages concentration vertically. In the horizontal direction the Peclet number is larger than in the vertical direction ($Pe = 5$, $t_{diff} = 25$ s) and as such concentration in the horizontal direction will not always be averaged by diffusion.

For faster drying solvents such as anisole, methyl anisole and mesitylene where $t_{dry} << 25$ s the concentration does not average horizontally in the drying time and there is a higher concentration of active material at the contact line than at the apex; giving Marangoni driven flows. For slower drying solvents such as dimethyl anisole and methyl benzoate where $t_{dry} >> 25$ s diffusion averages the concentration horizontally in the drying time and there are no concentration gradients to drive Marangoni flow.

The morphology of some printed deposits was measured by epifluorescence microscopy (now including o-xylene). The images in figure 7.4 and plots in figures 7.5 and 7.6 showed that, in most cases, luminescence intensity was enhanced at the contact line relative to the centre of the deposit and in the corners relative to the straight edges. The exception was o-xylene

which appeared to have non-uniform deposition of material along the edges of the drops. In o-xylene the material had been deposited on the banks rather than in the wells most likely due to the material overflowing the wells in the printing process. Non-uniformity of the deposit from o-xylene most likely arose from de-wetting of the fluid during drying; so giving a wavy intensity profile along the straight edges of the wells. In general the deposit profiles were similar to a coffee ring, though the driving mechanisms behind particle transport were different as has already been described. The data presented in this section suggests that the driving force behind deposit morphology in the presence of active materials was surface tension gradients due to compositional gradients in the fast drying solvents. Capillary flow into the meniscus was probably more important than Marangoni effects in slow drying solvents such as dimethyl anisole. Both Marangoni effects and capillary flow to the contact line would give a build-up of deposit around the contact line.

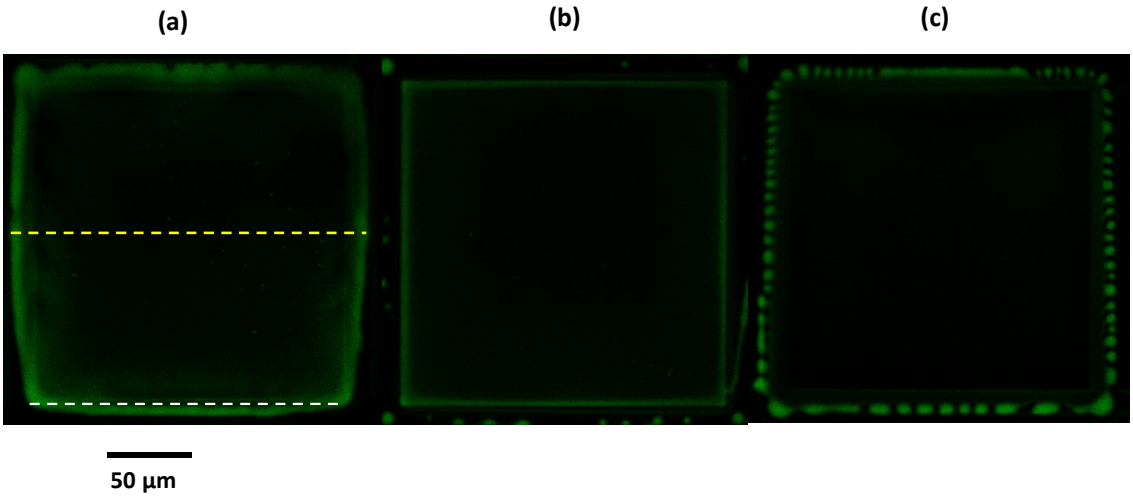

Figure 7.4: Epifluorescence images of active material deposits printed from anisole (a), dimethyl anisole (b) and o-xylene (c). The dotted lines show the cross sections taken for the plots of luminescence intensity in figures 7.5 (yellow) and 7.6 (white). The cross sections were taken in the same positions for each of the three deposits.

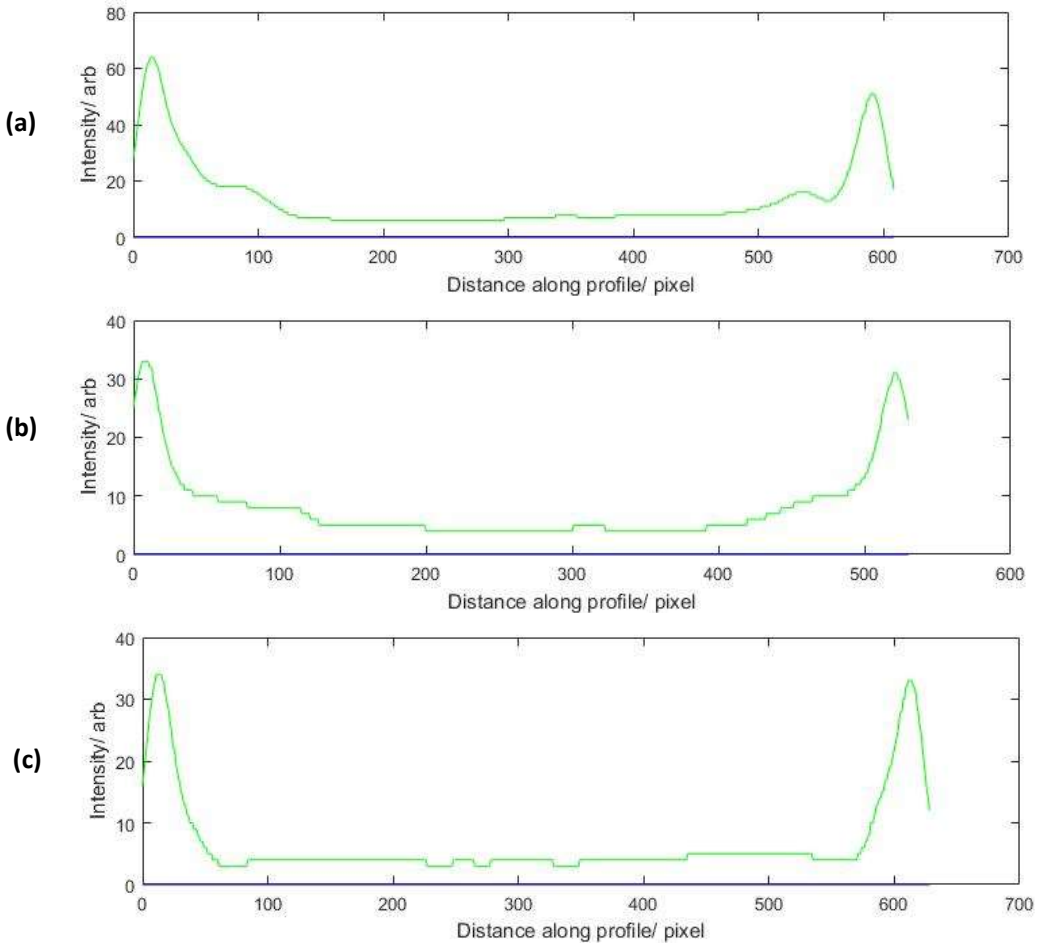

Figure 7.5: Luminescence intensity from the images in figure 7.4 across the centre of the wells. The drops were printed from anisole (a), dimethyl anisole (b) and o-xylene (c).

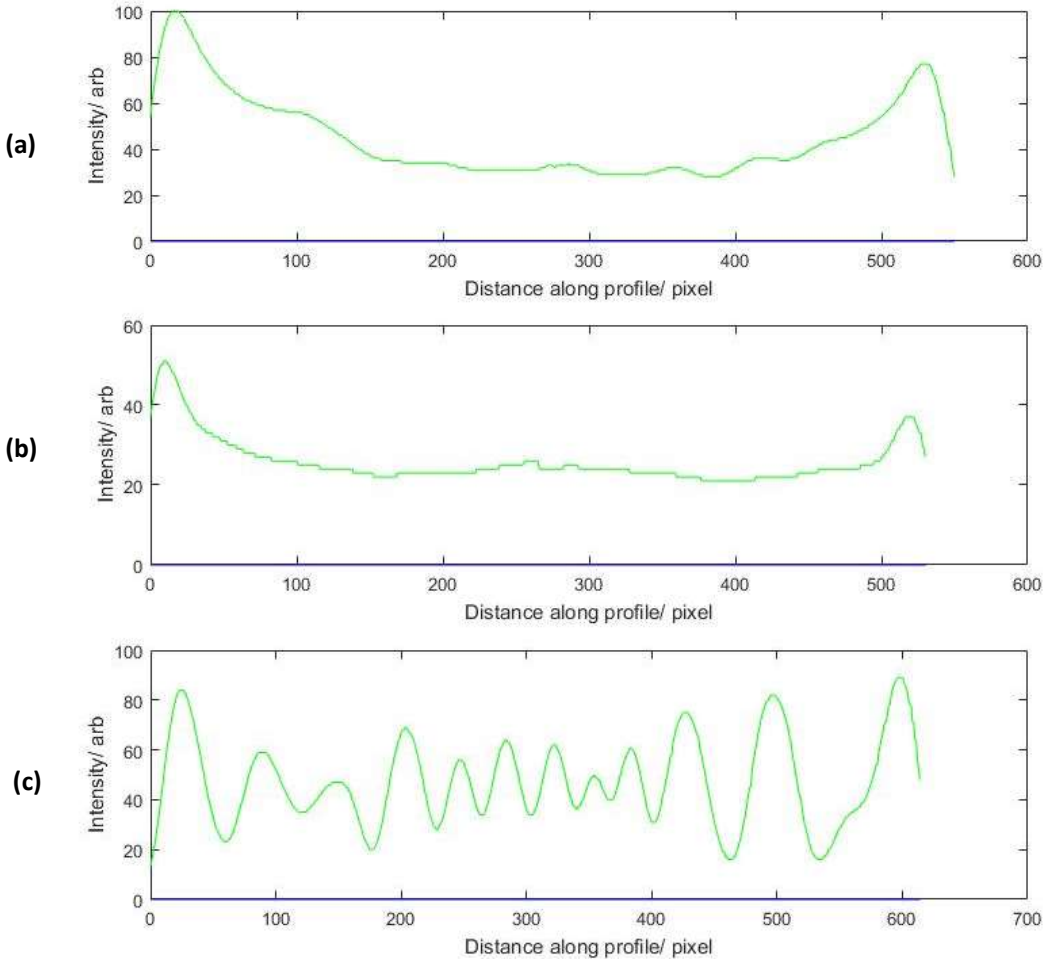

Figure 7.6: Luminescence intensity from the images in figure 7.4 along the edges of the wells. The drops were printed from anisole (a), dimethyl anisole (b) and o-xylene (c).

All experiments in this thesis were conducted under ambient conditions in the lab whereas in industrial printing of OLED devices drying is usually done in a vacuum. In a vacuum chamber, drying switches from diffusion control to ballistic control[175,176] as the pressure drops. Once the mean free path exceeds the length scale of the drop, any vapour immediately moves away from the drop surface and evaporation is no longer enhanced at the contact line. Compositional gradients are reduced compared to the case where enhanced evaporation is present. Smaller compositional gradients reduce the strength of Marangoni surface stresses so enhanced drainage from the centre of the drop is less likely to occur and the processes controlling deposit morphology revert to the pinning of the drop at the wall tops and the speed of evaporation.

The images shown in figure 7.7 were taken from deposits dried in a vacuum chamber at Merck Chemicals Ltd. at different speeds where the speed of drying was controlled by the pressure in the vacuum chamber. They appear to show that in a vacuum, the speed of drying once again determined deposit morphology with slow drying drops giving U-shaped deposits and fast drying drops giving W-shaped deposits. Therefore in a vacuum the pinning of drops at the wall tops and speed of drying of the solvent were the key factors in determining the final deposit morphology (as in the case of single solvents drying in the absence of any active materials). It is possible the apparent U-shaped deposit in figures 7.6a and 7.7a was a result of M-shaped profile development as the build-up of fluid around the contact line could be a result of either U- shaped or M-shaped profile development. The W-shaped deposit however could not be a result of M-shaped profile development.

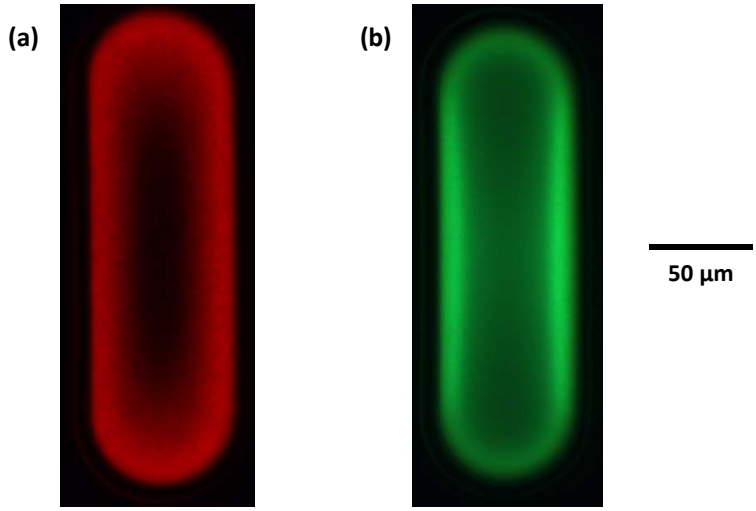

Figure 7.7: Epifluorescence images of active material deposits in oval wells which had been dried in a vacuum at different speeds; the slow drying gave a U-shaped deposit (a) and the fast drying gave a W-shaped deposit (b). The images were provided by Merck Chemical Ltd.

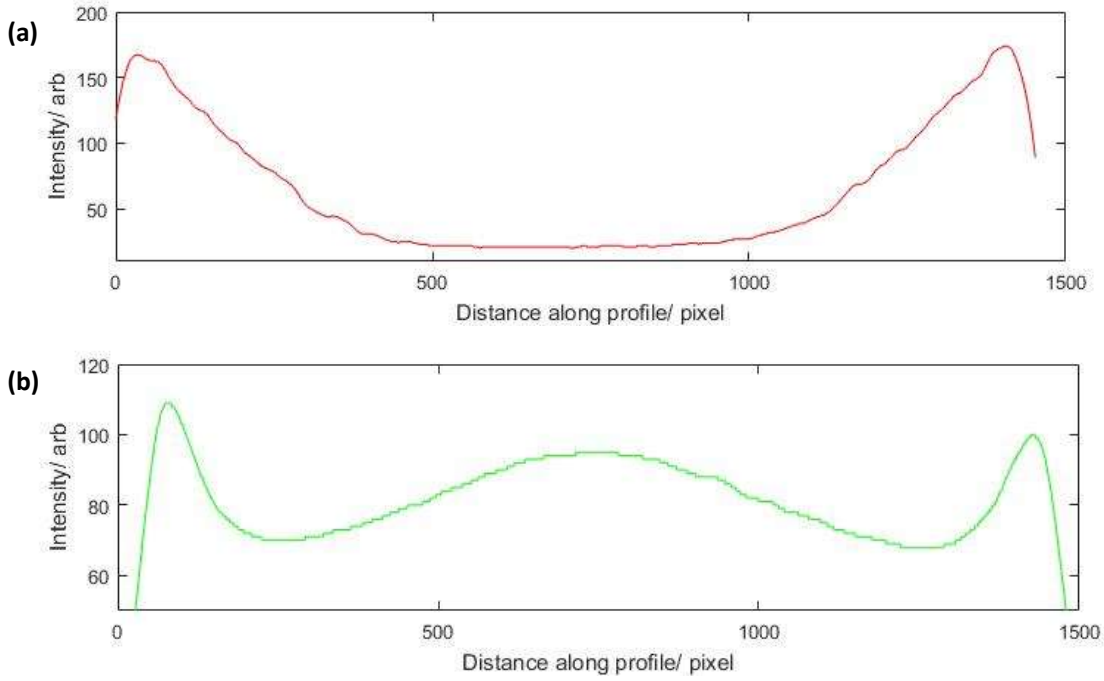

Figure 7.8: Plots showing luminescence intensity from the images in figure 4.24 down the centre of the long dimension of the pixels; the slow drying gave a U-shaped deposit (a) and the fast drying gave a W-shaped deposit (b).

In summary, the surface active properties of Livilux TH-123 cause M-shaped profiles under ambient conditions due to compositional surface tension gradients. When printed drops are dried within a vacuum chamber they are no longer drying within the diffusive regime and as the pressure drops drying becomes ballistic. Once drying is ballistic, compositional surface tension gradients due to Livilux TH-123 are no longer large enough to give M-shaped profiles and U- or W-shaped profiles form depending on evaporation rate.

7.3 Binary Solvent Mixtures

The model solvent mixtures imaged in section 6.4 showed the impact solutal Marangoni flows had on the drop profile during drying. Single solvent drops containing active materials showed M-shaped profile progression. It is possible solutal Marangoni flows from the contact line towards the centre of the drop could be used to mitigate the enhanced drainage from the centre of the drop caused by the presence of active materials. In this section the drying of drops of butanol + toluene in a 3:7 ratio containing Livilux TH-123 at a concentration of 5 mg cm^{-3} in square wells is reported. Solutions were made up and printed as described in chapter 2 sections 2.1 and 2.2.

The drying of single solvent drops containing active materials showed M- shaped profiles as the presence of active materials increased the surface tension of the solvents. Images of profile progression during drying of a butanol + toluene drop containing Livilux TH-123 are shown in figure 7.9. From the images it is clear the fluid in the corners of the wells is dipping below the level of the banks before the centre of the drop reached that level, as was the case in this mixture when no active material was present. The data suggest solvent driven surface tension gradients were dominant over the impact of active materials during drying.

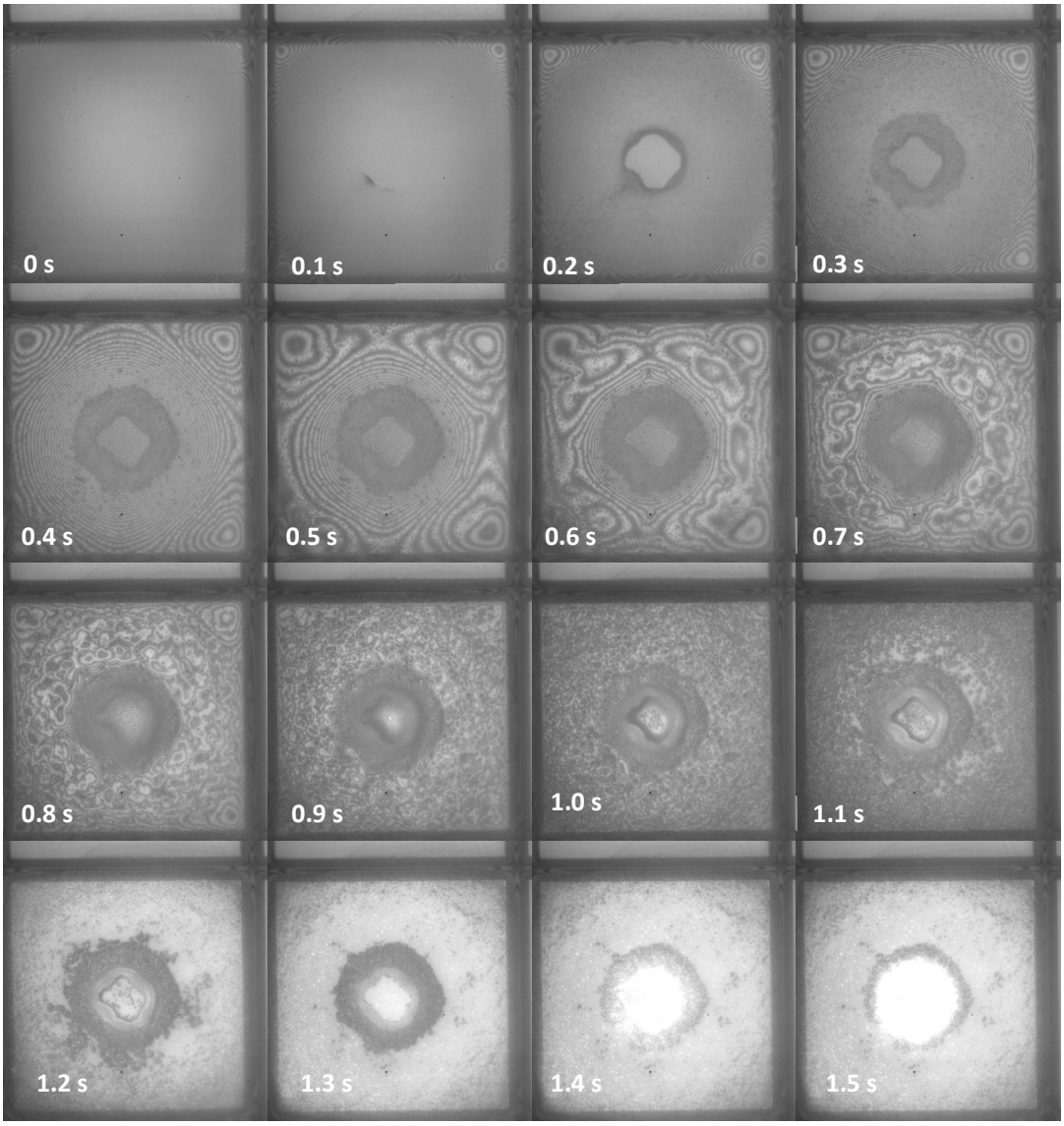

Figure 7.9: Images from the drying of a drop containing butanol and toluene in a 3:7 ratio in the presence of active materials. Images were recorded at 2000 fps and a shutter speed of 0.5 ms.

The disruption to the regular interference fringes in figure 7.9 is indicative of active material crystallising out of solution very early on in the drying process, first seen by the dark specks appearing in the corners of the wells (figure 7.11a). The active material is soluble toluene but not in butanol. As the toluene evaporates, the mixture becomes richer in butanol and the active ingredient reaches its solubility limit. Crystallisation began in the corners of the wells where evaporation is fastest. In pure solvents, active materials did not crystallise but gave amorphous films. The crystallisation of active materials during drying is not desirable when printing OLED films; the presence of crystals did however have some unexpected benefits in terms of understanding the mechanisms behind drying in the butanol and toluene mixture. The video relating to figure 7.9 is video 15 on the attached disk.

As drying progressed the crystals of active material began to follow the flows within the drying drops, acting as tracer particles. It was not possible to analyse particle tracks from the drying but from the videos it was clear there were recirculating flows within the drying drop, confirming the presence of solutal Marangoni flows. As the drying film was thin relative to the depth of focus of the objective, the entire depth of the drop was in focus throughout drying and it was not possible to determine the z position of the moving crystals. It is likely the crystals were moving into the centre of the drop along the liquid-air interface, as this was the direction of the solutal surface tension gradients, then moving out towards the contact line along the base of the wells (figure 7.10).

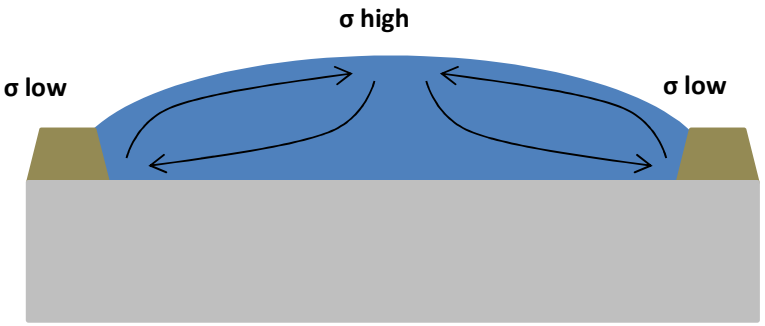

Figure 7.10: A schematic showing the likely direction of travel of the active material crystals.

Just after crystals began to appear in the corners, a circular region formed in the very centre of the butanol + toluene drop which did not appear to contain any crystals (figure 7.11b). As drying progressed active material crystals appeared in the central circular region (figure 7.11c), suggesting the active material had been present throughout drying but was still in solution and not visible in the images. The active material crystals may have remained in solution for longer at the apex of the drop as it was enriched in toluene relative to the contact line and as such it took longer for the solubility limit to be reached. Whilst butanol and toluene are fully miscible, it is possible that a toluene + active ingredient-rich phase could separate from a butanol-rich phase. Just before the drops were completely dry, the images appeared to show 3 different regions of crystals in a circle in the centre of the well (figure 7.11d). The central region contained a dark grey outer ring of large crystals, a light grey ring of apparently smaller crystals and a central circular region apparently devoid of any crystals. However, as can be seen from figure 7.12 the final images from drying showed the region that appeared to be devoid of active material in figure 7.11d did contain active material after all, perhaps due to a crystal size too small to be seen or an amorphous film region. The different crystal sizes seen in figure 7.11d were likely due to the length of time they had been in solution; those which crystallised

out later in the drying had less time to grow and so were smaller than those which precipitated out early on in the drying.

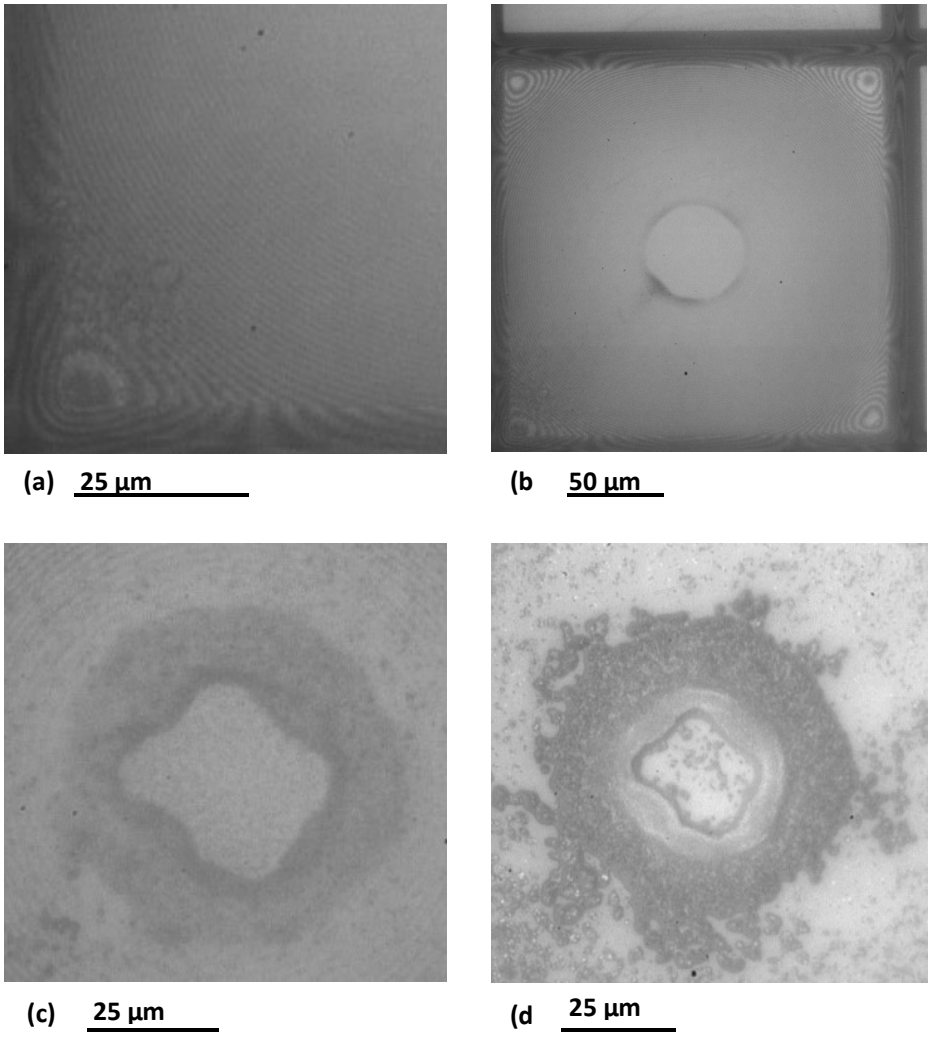

Figure 7.11: Stills from the drying of the drop of butanol and toluene in a 3:7 ratio containing active material. Images show the initial formation of crystals in the corners of the wells (a) the formation of a circular region in the centre of the drop which appeared to be devoid of any crystals (b), crystals appearing within that central region (c) and rings of different sized crystals (d).

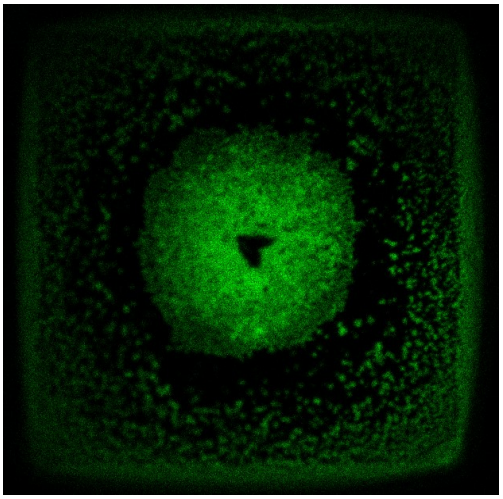

Figure 7.12: An epifluorescence image of a deposit of active material printed from butanol and toluene in a 3:7 ratio.

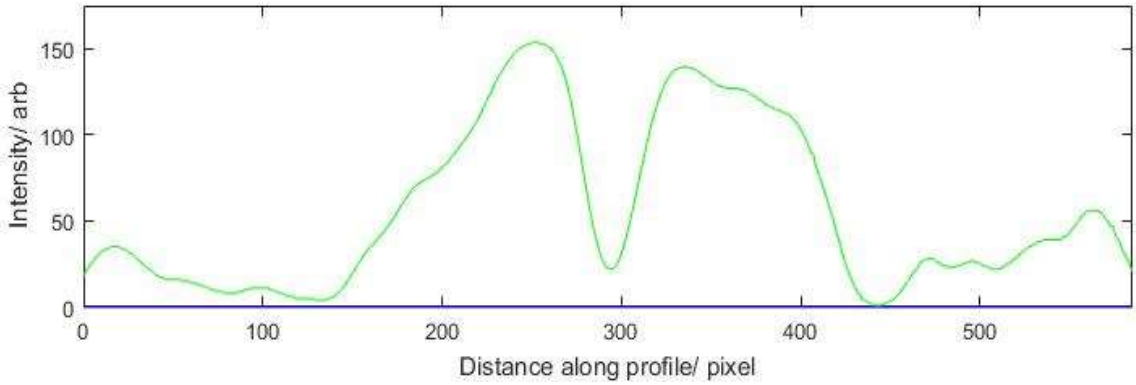

Figure 7.13: A plot of luminescence intensity across the pixel for the deposit imaged in figure 7.12.

Epifluorescence images and the resulting luminescence profiles of active material deposits (figures 7.12 and 7.13) printed from the 3:7 butanol + toluene mixture confirmed the presence of active material in the apparently devoid central region in figure 7.11d. Images showed a bright circular region of deposit in the centre of the wells with a pinprick sized hole in the very centre. The size of the hole in the epifluorescence images was much smaller than the region apparently devoid of particles in the centre of figure 7.11d (approximately 15 µm as opposed to approximately 50 µm); suggesting the apparently devoid region did contain active material that could not be seen in the drying images as discussed above. However the image in figure 7.12 was not from the same deposit as in figure 7.11, it is likely the size of the hole varies from sample to sample. The pinprick sized hole in the centre of deposits has been reported for systems which show recirculatory flows with migrations across streamlines towards the centre of drops;[24] it is possible migration across streamlines was occurring in these systems though more experiments need to be carried out to confirm this.

The imaging of drops containing a mixture of butanol + toluene along with active materials has created a lot of interesting questions. In terms of printing deposits of active materials for use in OLED systems, for the system investigated we have shown solvent driven Marangoni flows were dominant over surface tension flows from the presence of active materials. The use of solvent driven Marangoni gradients to counteract active material driven drainage from the centre of the drop could potentially be useful in the printing of OLED materials. Crystallisation of the active material during drying meant the butanol and toluene mixture imaged here would not be useful for printing OLED materials where amorphous films are desirable. The area of the printed deposit was much smaller than the area of the original drop (approximately one third the well size) again not desirable in the printing of OLED deposits; but the small circular deposit could be useful in some applications where small deposits are wanted from large drops. In the printing of OLED materials the deposit needs to be level across the entire area of the pixel so printing small dots as imaged here would not be useful.

Aside from the printing of OLED materials, the images from drying in the butanol and toluene mixture have created a number of questions about the presence of recirculatory flows and driving mechanisms behind the deposits imaged here. More investigations need to be carried out before any firm conclusions can be drawn. The experiments reported in this section show it should be possible to carry out PTV successfully within banked structures.

7.4 Summary

The impact of active materials on drying mechanisms was considered to relate the drying behaviour of pure solvents to more industrially relevant systems. Active materials increased the surface tension of the solvents. Enhanced evaporation at the edges of the wells caused gradients in composition and hence in surface tension, leading to a flow from the centre of the drop towards the contact line. Under ambient conditions, surface tension gradients in the presence of active materials became the main driving force behind final deposit morphology.

In industry, inkjet-printed OLED devices are dried within a vacuum chamber; and as such drying switches from diffusion control to ballistic control. Images of final deposits from drops dried within a vacuum showed U-shaped and W-shaped deposit morphologies, suggesting ballistic drying may have prevented surface tension driven flows due to active materials. Drying under ballistic conditions would cause the evaporation rate of the solvent to determine whether U-or W- shaped profiles form as with single solvents.

Data from drops containing a mixture of butanol + toluene in the presence of active materials showed surface tension gradients caused by solutal gradients were dominant over surface tension gradients caused by the presence of active materials. Deposits consisted of small, circular deposits in the centre of the wells; smaller than the total well size. Deposits were crystalline in nature due to the low solubility of the active material in the mixture. Crystalline deposits which are smaller than the well size are not useful in the printing of OLED materials where flat, amorphous deposits across the entire well are desired. However the deposits imaged in section 7.3 could be useful in other applications. More investigation into the impact of active materials on the drying of solvent mixtures is necessary before any firm conclusions can be made, though the dominance of solvent over active material driven flows could be useful in gaining flat deposits.

8. Conclusions and Future Work

The major contribution of this thesis has been the determination of the key factors behind the profile development of drops drying within wells. The mechanisms behind the drying of drops within wells show some similarities to those on flat substrates, though there are some differences. Now the mechanisms behind the drying of drops within wells have been largely identified it should be possible to begin to formulate strategies to give even deposits from printed drops.

This chapter discusses the main findings of this thesis and proposes a method for obtaining even deposits from drops drying within wells, along with a few preliminary results towards that goal. Some suggestions are given for future work.

8.1 Key Factors Determining Drop Profiles During Drying

The results in chapter 4 on single solvents drying within wells suggest that the key factors in determining final film morphology under ambient conditions are the pinning of drops at the bank tops, enhanced evaporation at the contact line and the evaporation rate of the solvent. Single solvents dried to give either U- or W- shaped profiles depending on the evaporation rate of the solvent in all three well geometries, though the exact relationship between evaporation rate and level of dimple formation differed between geometries. Square and circular wells showed a steady increase in h_{max} with increasing evaporation rates whereas in the oval wells there was a definitive switch between evaporation rates which gave U-shaped profiles and those which gave W-shaped profiles.

Some o-xylene drops in all geometries showed qualitative differences in drying, where they dried to give M-shaped profiles. Causes of the differences were investigated, though M-shaped profiles could not be consistently replicated. A probable cause of the M-shaped profiles in some o-xylene drops was a surface tension gradient across the drop as a result of thermal gradients. A number of solvents chosen to exaggerate thermal gradients were investigated and three main behaviours were identified. Butyl acetate, methoxy propanol and toluene showed W-shaped profiles at all temperatures, as would be expected from their evaporation rates. Ethanol and IPA showed M-shaped profiles at all temperatures due to thermal surface tension gradients across the drop. Butanol, like o-xylene, showed W-shaped profiles on one day of measurement and M-shaped profiles on another. Inconsistencies in profile development from day to day may be due to the sensitivity of the drop profile to its initial behaviour, since positive feedback enhances both M- and W-shaped profiles.

Drop profiles of binary solvent mixtures were imaged in the square wells to identify the impact of co-solvents on drying. Industrially relevant mixtures showed inconsistent behaviour due to differences in volatility that were either too small or too large to give surface tension driven flows. Model mixtures chosen to exaggerate differences in surface tension and volatility were identified and the drying imaged. Butyl acetate + ethanol drops and butyl acetate + methoxy propanol drops showed M-shaped profiles in all cases, consistent with expected surface tension gradients. Butanol + toluene in a 1:1 and 3:7 ratio showed enhanced drainage from the corners towards the centre of the wells in all cases, once again consistent with expected surface tension gradients. Butanol + toluene in a 7:3 ratio showed W-shaped profiles in all cases as the toluene evaporated too early on in the drying to give surface tension driven flows.

Once the key factors driving profile development during the drying of single and mixed solvent drops within wells had been identified, active materials were introduced to the formulation. Livilux TH-123 is an OLED host material and was used to determine the influence of active OLED materials on drop profile during drying and subsequent deposit morphology. In the case of single solvents Livilux caused M-shaped profiles in every case, though to differing levels in different solvents. M-shaped profiles were a result of compositional surface tension gradients across the drop and the level of enhanced drainage from the centre of the drop was a function of the drying time of the solvent. In slower drying solvents, diffusion in the lateral direction reduced compositional gradients and the resulting surface tension driven flows. In fast drying drops there was no time for diffusion to even out compositional gradients in the lateral direction and pronounced M-shaped profiles formed. Epifluorescence images of Livilux deposits showed ring stains in all cases, which is likely to be a result of M-shaped profiles during drying.

Drops of butanol + toluene in a 3:7 ratio containing active materials showed circular deposits in the centre of the wells, which were smaller than the well diameter. Small deposits in the centre of the wells would not be of any use in the printing of OLED displays but may potentially be useful in other applications. Overall it did not appear that solvent mixtures were beneficial in giving flat deposits from drops drying within wells. Crystallisation of the active material during drying showed re-circulating flows in the drying drop. Many of the mechanisms behind the drying of butanol + toluene drops containing active material remain unclear.

When OLEDs are manufactured industrially drying is done in a vacuum and evaporation switches from diffusion control to ballistic control as the pressure drops. Images of drops dried within a vacuum showed U- and W-shaped deposits dependent on evaporation rates.

The removal of enhanced evaporation at the contact line reduces compositional surface tension gradients in the drying drops.

All in all, the data presented in this thesis has identified the key factors driving drop profiles and deposit morphology of drops drying within wells. The understanding of which factors are important in controlling drop morphology can now be used to determine how the drying can be controlled in order to give even deposits from drops printed into wells.

8.2 Proposal for Obtaining Even Deposits in Wells

This section proposes a method for obtaining flat deposits from drops drying within wells along with some preliminary experiments.

The proposed method is as follows:

1) Select a solvent pair of similar, low volatility that provides optimum solubility of the active material.
2) Dissolve the active material to a concentration such that when the fluid just fills the wells it dries to give a final deposit of the required thickness.
3) Dilute the optimised solution with a third, volatile solvent.
4) Design banks such that the receding contact angle of the low volatility solvent pair is equal to the bank angle.
5) Print the solution into the banks such that once the volatile solvent has evaporated entirely it leaves the less volatile solvent mixture behind so it just fills the wells and is flat and level with the tops of the banks.
6) Transfer to a vacuum drier and allow the fluid to dry down so it remains flat and level.

If the above steps could be achieved no curvature would be introduced into the drying film and there would be no capillary drainage from the centre of the drops to give U- or W-shaped deposits. If devices were dried in a vacuum under ballistic control, there would not be the problem of capillary flows due to enhanced evaporation at the contact line, mitigating any ring stains and giving flat deposits.

Steps 1 and 2 in the above proposal would be fairly simple to achieve; the identity of the solvents is not overly important and they can be chosen to optimise the formulation in terms of solubility and printing properties. The third and fifth steps are necessary as the fluid must be flat and level with the wall tops before it is transferred to the vacuum chamber for drying. If only enough fluid was used to just fill the wells, a spherical cap would form in the base of the wells due to the surface tension of the solvents, shown in figure 8.1a. Instead the wells need to be overfilled to ensure that the base and walls are fully wetted. The volatile solvent allows time before transfer to a vacuum chamber for any compositional gradients to even out by diffusion (figure 8.1b). Under ballistic conditions drops should then dry down maintaining a flat surface if the fourth step is carried out; if active material is dispersed evenly throughout the drop that should then give a flat deposit which fills the entire area of the wells.

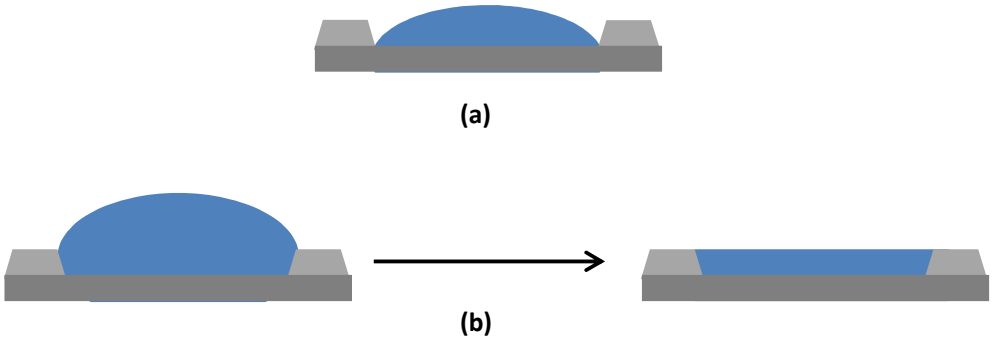

Figure 8.1: Schematic diagrams showing the spherical cap that would form if only enough fluid to fill it was printed into a well (a) and the process by which overfilled wells dry down to give fluid flat and level with the wall tops (b).

Matching the receding contact angle of the fluid to the angle of the bank walls requires treatment of the substrates in order to maximise contact angles. Aromatic solvents such as those used in the printing of OLEDs industrially often give very low (≤10^{o}) contact angles on the polymer surfaces used to fabricate the banks. Angles less than approximately 40^{o} are not feasible for bank walls as too much of the device area would become dominated by wall material (this value was suggested by Merck Chemicals Ltd.). The receding contact angles of organic solvents on the polymer walls need to be increased until it reaches a feasible wall angle.

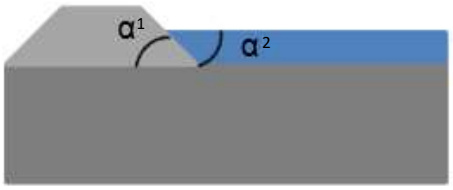

Figure 8.2: A schematic diagram showing the matching of the receding contact angle of the fluid (α^2) to the angle of the bank wall (α^1).

To identify the maximum receding contact angle that could be achieved on the banks, flat substrates of treated bank material were provided by Merck and advancing and receding contact angles were measured. Measurements of butyl benzoate on three treated substrates were taken as described in chapter 2 section 2.4.The substrates were referred to as D139_1, D139_2 and D139_3; all were prepared and treated in the same way. Five drops were measured on each substrate, table 8.1 summarises the advancing contact angle data and

figure 8.3 shows the plots for D139_3 used to determine the angles in table 8.1. The average advancing contact angle over the three substrates was 72° with the range of measurements covering 66–74°. Variations between measurements were assumed to be due to slight variations in treatment across the substrate surfaces. The advancing contact angles should be larger than the respective receding contact angles on all surfaces so the data in table 8.1 can be used to verify the receding contact angle measurements.

Table 8.1: Showing a summary of the advancing contact angle data from measurements across the three substrates. Measurements were all taken at 21 °C and 40 % humidity.

Substrate	**Advancing Contact Angle/ °**					**Average**
	1	**2**	**3**	**4**	**5**	**Angle/ °**
D139_1	70	71	73	72	73	71.8
D139_2	73	72	71	66	70	70.4
D139_3	74	74	74	74	74	74

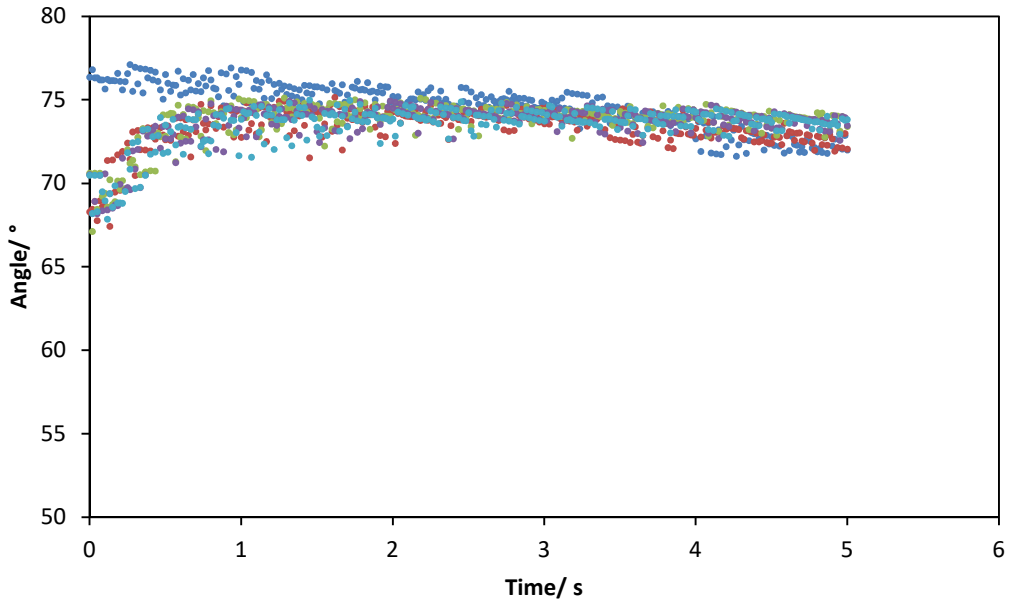

Figure 8.3: A Plot showing the advancing contact angle measurement data taken from the D139_3 substrate; each of the five drops measured showed an increasing angle initially before it settled out at an equilibrium angle. The equilibrium angle was taken to be the advancing contact angle of the fluid.

Data from receding contact angle measurements are shown in table 8.2 with example measurements from D139_3 shown in figure 8.4. The average receding contact angle across the three substrates was approximately 68° with a range of angles between 65 and 71°. Average advancing contact angles on each substrate were larger than their respective average receding contact angles as expected.

Table 8.2: Showing a summary of the receding contact angle data from measurements across the three substrates. Measurements were all taken at 21 ^{o}C and 40 % humidity.

Substrate	Receding Contact Angle/ °					Average
	1	2	3	4	5	Angle/ °
D139_1	71	71	71	70	70	70.6
D139_2	66	66	65	65	65	65.4
D139_3	67	68	68	67	67	67.4

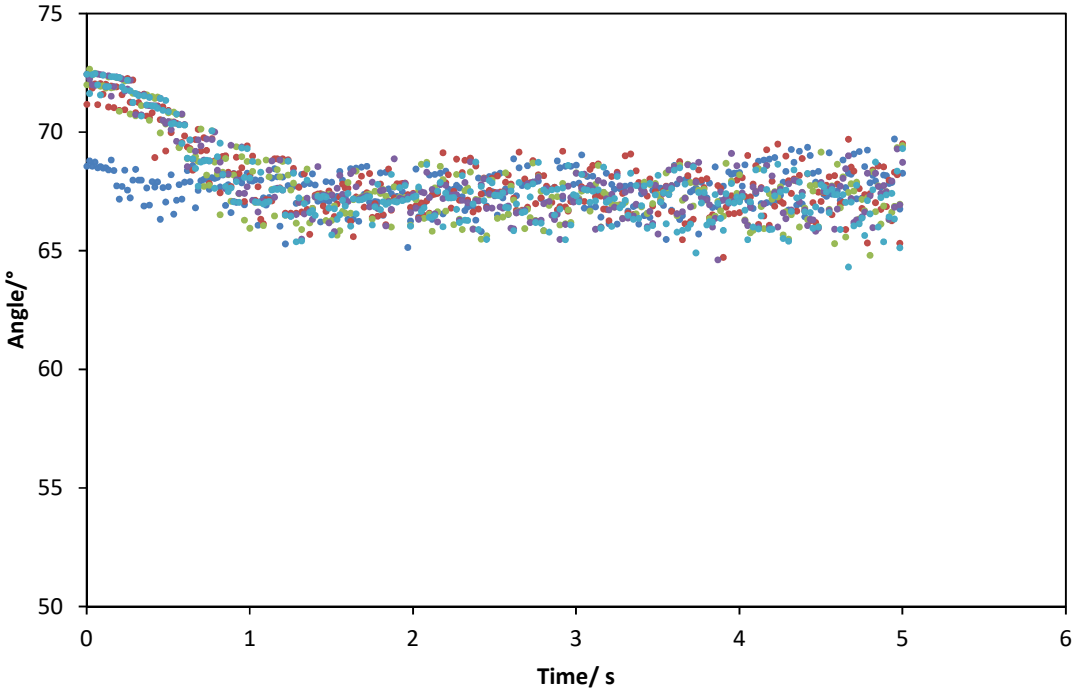

Figure 8.4: A Plot showing the receding contact angle measurement data taken from the D139_3 substrate; each of the five drops measured showed a decreasing angle initially before it settled out at an equilibrium angle. The equilibrium angle was taken to be the receding contact angle of the fluid.

When using the substrates investigated here as the bank wall material, angles somewhere between 65 and 70^{o} should be used to allow films to dry down and remain flat. More experiments into the tolerance of the receding contact angle would need to be carried out to determine whether the angles would have to match exactly or whether there would be some leeway. The data here is encouraging as it suggests receding contact angles of organic solvents on the bank wall material can be increased far beyond the required minimum of 40^{o} (suggested by Merck) and as such can be increased to levels required to match commercially viable bank wall angles.

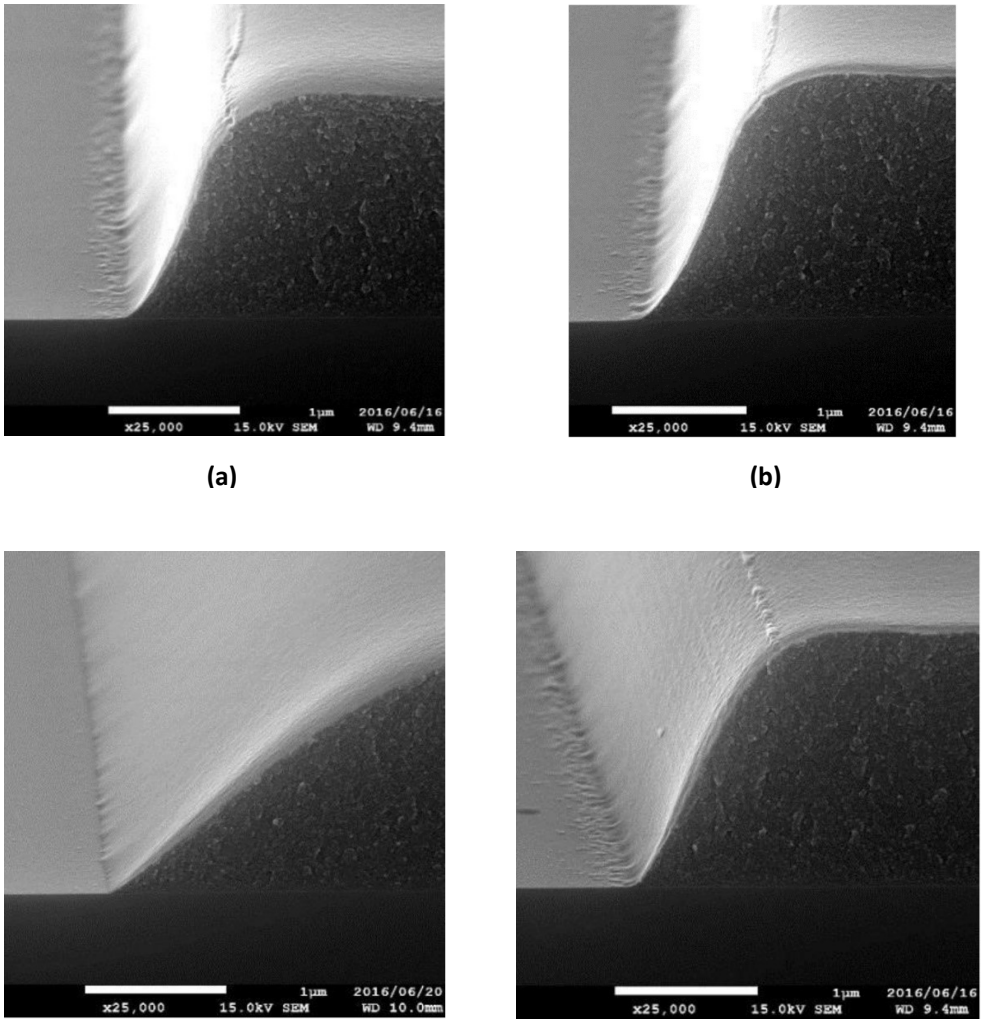

Figure 8.5: Images showing the varying bank wall angles of substrates containing wells. Angles are as follows (a) is 72^{o} along the entire length, (b) is 70^{o} along most of the length but reduces to 60^{o} near to its base, (c) is approximately 40^{o} along the entire length and (d) is approximately 65^{o} along the entire length. The images were provided by Merck Chemicals and were of substrates they had used in house.

Some substrates were provided by Merck Chemicals which had varying bank angles (figure 8.5) but they were not treated and as such the receding contact angles were too low to measure accurately; they were also too low to match to any of the bank wall angles, the lowest of which was 40^{o}. If the walls imaged in figure 8.5 could be treated in a way such that the receding contact angle of the fluid on the walls was increased to the values measured in the treated substrates (table 8.2) they would be ideal to determine whether the proposed method for flat deposits from drops printed into wells is feasible.

8.3 Next Steps for This Project

To investigate further the proposed method for obtaining flat deposits from drops printed into wells, it is necessary to have complete control over the substrates and the well geometry. The angle and height of the banks needs to be controlled in order for them to be matched to the receding contact angle of the fluid. For complete control of bank geometry and properties they need to be manufactured and treated in house or to strict specifications. Substrates could be manufactured in house using photolithography and fluorinated using plasma treatment.

All of the measurements reported in this thesis were performed under ambient conditions in the laboratory. In an industrial setting, however, OLEDs are printed under ambient conditions before being dried in a vacuum chamber at reduced pressures, which qualitatively changes the drying. Depending on the pressures being used to dry printed drops, they could be drying in either the diffusive (as under ambient conditions) or the ballistic regime. In order to relate the findings of this thesis more closely to industrially relevant OLED systems, the drying of drops within a vacuum chamber at varying pressures needs to be imaged. If data on profile progression of drops drying within wells at different pressures can be obtained, comparisons can be made with the data presented here. Measurements within a vacuum should be taken for single solvents and binary solvent mixtures, both in the presence and absence of active materials, at a range of temperatures. The entire drying process should be recorded, as has been done for the measurements discussed in this thesis.

Another consideration that will become important when printing OLED devices industrially is that more than one pixel will be drying at any one time, rather than isolated pixels as explored in this thesis. In the diffusive regime, the presence of liquid in one pixel affects the drying of neighbouring pixels as the diffusion fields of the pixels overlap. In the ballistic regime neighbouring pixels may dry independently. To determine the impact of filling neighbouring pixels on the drying, experiments in both ambient conditions and under vacuum will need to be performed for single solvents and binary solvent mixtures at all temperatures in the presence and absence of active materials.

Much experimental data has been discussed in this thesis and whilst some comparisons to reported models has been done, a model designed to work specifically for the relevant systems does not exist and any comparisons include assumptions which may not be sound. The presence of banks introduces many complexities into the drying process, all of which must be carefully considered. A model developed specifically for systems relevant to this thesis would be very useful in determining the most important factors in profile development and

provide further information for the theoretical and physical basis for the observed results. The development of quantitative convection-diffusion models for circular wells would also be useful.

In summary, this thesis considers a highly interesting area of research which could be of benefit to a number of fields alongside the inkjet printing of OLED films. Any application which requires patterned products and printed drops could benefit from this research. This thesis demonstrates the importance of understanding what drives drop profiles and deposit morphology from drops printed into wells. This understanding allows us to devise strategies for giving even deposit morphologies and suggests ways in which the research can be expanded to benefit the area.

References

1. Gorter, H. *et al.* Toward inkjet printing of small molecule organic light emitting diodes. *Thin Solid Films* **532,** 11–15 (2013).

2. Burrows, P. E. *et al.* Achieving full-color organic light-emitting devices for lightweight, flat-panel displays. *IEEE Trans. Electron Devices* **44,** 1188–1203 (1997).

3. Hung, L. . & Chen, C. . Recent progress of molecular organic electroluminescent materials and devices. *Mater. Sci. Eng. R Reports* **39,** 143–222 (2002).

4. Shirota, Y. & Hiroshi, K. Charge Carrier Transporting Molecular Materials and Their Applications in Devices. *Chem. Rev.* **107,** 953–1010 (2007).

5. Thejo Kalyani, N. & Dhoble, S. J. Organic light emitting diodes: Energy saving lighting technology—A review. *Renew. Sustain. Energy Rev.* **16,** 2696–2723 (2012).

6. Wei, M.-K. *et al.* Emission Characteristics of Organic Light-Emitting Diodes and Organic Thin-Films with Planar and Corrugated Structures. *Int. J. Mol. Sci.* **11,** 1527–1545 (2010).

7. Chaskar, A., Chen, H.-F. & Wong, K.-T. Bipolar Host Materials: A Chemical Approach for Highly Efficient Electrophosphorescent Devices. *Adv. Mater.* **23,** 3876–3895 (2011).

8. Laquai, F., Park, Y.-S., Kim, J.-J. & Basché, T. Excitation Energy Transfer in Organic Materials: From Fundamentals to Optoelectronic Devices. *Macromol. Rapid Commun.* **30,** 1203–1231 (2009).

9. Tao, Y. *et al.* Organic host materials for phosphorescent organic light-emitting diodes. *Chem. Soc. Rev.* **40,** 2943 (2011).

10. Chen, Y.-M. *et al.* Carbazole–benzimidazole hybrid bipolar host materials for highly efficient green and blue phosphorescent OLEDs. *J. Mater. Chem.* **21,** 14971 (2011).

11. Abhishek P. Kulkarni, Christopher J. Tonzola, Amit Babel, A. & Jenekhe*, S. A. Electron Transport Materials for Organic Light-Emitting Diodes. *Chem. Mater.* **16,** 4556–4573 (2004).

12. Teichler, A. *et al.* Inkjet printing of chemically tailored light-emitting polymers. *Eur. Polym. J.* **49,** 2186–2195 (2013).

13. Patel, N., Cina, S. & Burroughes, J. High-efficiency organic light-emitting diodes. *IEEE J. Sel.* **8,** 346–361 (2002).

14. Xiao, L. *et al.* Recent Progresses on Materials for Electrophosphorescent Organic Light-Emitting Devices. *Adv. Mater.* **23,** 926–952 (2011).

15. Mertens, R. *The OLED handbook a guide to OLED technology, industry & market*. (Ron Mertens, 2015).

16. Jung, S.-H., Kim, J.-J. & Kim, H.-J. High performance inkjet printed phosphorescent organic light emitting diodes based on small molecules commonly used in vacuum processes. *Thin Solid Films* **520,** 6954–6958 (2012).

17. Teichler, A. *et al.* Inkjet printing of chemically tailored light-emitting polymers. *Eur. Polym. J.* **49,** 2186–2195 (2013).

18. Deegan, R. D. *et al.* Contact line deposits in an evaporating drop. *Phys. Rev. E* **62,** 756–

765 (2000).

19. Deegan, R. D. *et al.* Capillary flow as the cause of ring stains from dried liquid drops. *Nature* **389,** 827–829 (1997).

20. Deegan, R. Pattern formation in drying drops. *Phys. Rev. E* **61,** 465–485 (2000).

21. Hu, H. & Larson, R. G. Evaporation of a Sessile Droplet on a Substrate. *J. Phys. Chem. B* **106,** 1334–1344 (2002).

22. Talbot, E. L., Berson, A., Brown, P. S. & Bain, C. D. Evaporation of picoliter droplets on surfaces with a range of wettabilities and thermal conductivities. *Phys. Rev. E* **85,** 061604 (2012).

23. Talbot, E. L., Yang, L., Berson, A. & Bain, C. D. Control of the Particle Distribution in Inkjet Printing through an Evaporation-Driven Sol?Gel Transition. *ACS Appl. Mater. Interfaces* **6,** 9572–9583 (2014).

24. Talbot, E. L., Berson, A., Yang, L. & Bain, C. D. Internal Flows and Particle Transport Inside Picoliter Droplets of Binary Solvent Mixtures. in *2013 International Conference on Digital Printing Technologies* 307–312 (Society for Imaging Science and Technology, 2013).

25. Talbot, E. L., Berson, A., Brown, P. S. & Bain, C. D. Drying and Deposition of Picolitre Droplets of Colloidal Suspensions in Binary Solvent Mixtures. *NIP28 28th Int. Conf. Digit. Print. Technol. Digit. Fabr. 2012, Soc. Imaging Sci. Technol.* 420–423 (2012).

26. Saenz, P. J. *et al.* Dynamics and universal scaling law in geometrically-controlled sessile drop evaporation. *Nat. Commun.* **8,** 14783 (2017).

27. UBI Research. OLEDNET. Available at: www.olednet.com. (Accessed: 1st September 2017)

28. Sze, S. M. & Ng, K. K. *Physics of semiconductor devices*. (Wiley-Interscience, 2007).

29. Žutić, I., Fabian, J. & Das Sarma, S. Spintronics: Fundamentals and applications. *Rev. Mod. Phys.* **76,** 323–410 (2004).

30. Brus, L. E. Electron–electron and electron-hole interactions in small semiconductor crystallites: The size dependence of the lowest excited electronic state. *J. Chem. Phys.* **80,** 4403–4409 (1984).

31. Köhler, A. & Bässler, H. Triplet states in organic semiconductors. *Mater. Sci. Eng. R Reports* **66,** 71–109 (2009).

32. Köhler, A., Wilson, J. & Friend, R. Fluorescence and phosphorescence in organic materials. *Adv. Eng. Mater.* **14,** 701–707 (2002).

33. Derby, B. Inkjet printing ceramics: From drops to solid. *J. Eur. Ceram. Soc.* **31,** 2543–2550 (2011).

34. Singh, M., Haverinen, H. M., Dhagat, P. & Jabbour, G. E. Inkjet Printing-Process and Its Applications. *Adv. Mater.* **22,** 673–685 (2010).

35. Paul, C. Inkjet Printing for Materials and Devices. *Chem. Mater.* **13,** 3299–3305 (2001).

36. Hoath, S. D. *Fundamentals of Inkjet Printing*. (Wiley-VCH Verlag GmbH & Co. KGaA, 2016). doi:10.1002/9783527684724

37. Le, H. P. Progress and Trends in Ink-jet Printing Technology. *J. Imaging Sci. Technol.* **42,** 49–62 (1998).

38. Wijshoff, H. The dynamics of the piezo inkjet printhead operation. *Phys. Rep.* **491,** 77–177 (2010).

39. Bush, J. Interfacial Phenomena. *MIT OpenCourseWare* **18.357,** 41–43 (2010).

40. Yang, L., Adamson, L. J. & Bain, C. D. Study of liquid jet instability by confocal microscopy. *Rev. Sci. Instrum.* **83,** 073104 (2012).

41. Vaught, J. L. *et al.* Thermal ink jet printer. (1982).

42. Endo, I., Sato, Y., Saito, S., Nakagiri, T. & Ohno, S. Bubble jet recording method and apparatus in which a heating element generates bubbles in a liquid flow path to project droplets. (1986).

43. Tekin, E., Smith, P. & Schubert, U. Inkjet printing as a deposition and patterning tool for polymers and inorganic particles. *Soft Matter* **4,** 703–713 (2008).

44. Steven I Zoltan. Pulsed droplet ejecting system. (1970).

45. Kyser, E. L. & Sears, S. B. Method and apparatus for recording with writing fluids and drop projection means therefor. (1970).

46. Hutchings, I. M., Martin, G. D. & Hoath, S. D. High Speed Imaging and Analysis of Jet and Drop Formation. *J. Imaging Sci. Technol.* **51,** 438 (2007).

47. Morrison, N. F. & Harlen, O. G. Viscoelasticity in inkjet printing. *Rheol. Acta* **49,** 619–632 (2010).

48. Gargir, E., Lifshitz, L. & Tirosh, L. A method and system for compensating for banding defects in inkjet printers. (2002).

49. Childers, W. D., Ronald, A. & Li, A. G. Misfiring print nozzle compensation. (2006).

50. Kwon, K.-S. Methods for detecting air bubble in piezo inkjet dispensers. *Sensors Actuators A Phys.* **153,** 50–56 (2009).

51. Kim, B.-H. *et al.* Effects of trapped air bubbles on frequency responses of the piezo-driven inkjet printheads and visualization of the bubbles using synchrotron X-ray. *Sensors Actuators A Phys.* **154,** 132–139 (2009).

52. Kwon & Kye-Si. Experimental analysis of waveform effects on satellite and ligament behavior via in situ measurement of the drop-on-demand drop formation curve and the instantaneous jetting speed curve. *J. Micromechanics Microengineering* **20,** 115005 (2010).

53. Robert G. Capurso. Method and apparatus for cleaning and capping a print head in an ink jet printer. (1998).

54. Paul Wouters. Method and apparatus for removing excess ink from inkjet nozzle plates. (2003).

55. de Jong, J. *et al.* Marangoni flow on an inkjet nozzle plate. *Appl. Phys. Lett.* **91,** 204102 (2007).

56. Jang, D., Kim, D. & Moon, J. Influence of Fluid Physical Properties on Ink-Jet Printability.

Langmuir **25,** 2629–2635 (2009).

57. Derby, B. Inkjet Printing of Functional and Structural Materials: Fluid Property Requirements, Feature Stability, and Resolution. *Annu. Rev. Mater. Res.* **40,** 395–414 (2010).

58. Xiang, Q. F., Evans, J. R. G., Edirisinghe, M. J. & Blazdell, P. F. Solid freeforming of ceramics using a drop-on-demand jet printer. *Proc. Inst. Mech. Eng. Part B J. Eng. Manuf.* **211,** 211–214 (1997).

59. Mott, M., Song, J.-H. & Evans, J. R. G. Microengineering of Ceramics by Direct Ink-Jet Printing. *J. Am. Ceram. Soc.* **82,** 1653–1658 (1999).

60. Noguera, R., Lejeune, M. & Chartier, T. 3D fine scale ceramic components formed by ink-jet prototyping process. *J. Eur. Ceram. Soc.* **25,** 2055–2059 (2005).

61. Chen, L. & Evans, J. R. G. Arched Structures Created by Colloidal Droplets as They Dry. *Langmuir* **25,** 11299–11301 (2009).

62. Ebert, J. *et al.* Direct Inkjet Printing of Dental Prostheses Made of Zirconia. *J. Dent. Res.* **88,** 673–676 (2009).

63. Hebner, T. R., Wu, C. C., Marcy, D., Lu, M. H. & Sturm, J. C. Ink-jet printing of doped polymers for organic light emitting devices. *Appl. Phys. Lett.* **72,** 519 (1998).

64. Chang, S.-C. *et al.* Multicolor Organic Light-Emitting Diodes Processed by Hybrid Inkjet Printing. *Adv. Mater.* **11,** 734–737 (1999).

65. Bruner, S., Xu, D. & Phillips, C. 54.3: Drop Landing Accuracy Improvements in Inkjet Printed OLED Displays. *SID Symp. Dig. Tech. Pap.* **38,** 1611–1612 (2007).

66. Ding, Z., Xing, R., Fu, Q., Ma, D. & Han, Y. Patterning of pinhole free small molecular organic light-emitting films by ink-jet printing. *Org. Electron.* **12,** 703–709 (2011).

67. Müller, C. D. *et al.* Multi-colour organic light-emitting displays by solution processing. *Nature* **421,** 829–833 (2003).

68. Lee, S.-H., Hwang, J. Y., Kang, K. & Kang, H. Fabrication of organic light emitting display using inkjet printing technology. in *2009 International Symposium on Optomechatronic Technologies* 71–76 (IEEE, 2009). doi:10.1109/ISOT.2009.5326101

69. Schiaffino, S. & Sonin, A. A. Molten droplet deposition and solidification at low Weber numbers. *Phys. Fluids* **9,** 3172–3187 (1997).

70. Carl L. Yaws. *Chemical Properties Handbook: physical, thermodynamic, environmental, transport, safety, and health related properties for organic and inorganic chemicals.* (McGraw-Hill, 1999).

71. Reis, N., Fabrication-2000, B. D.-S. F. and A. & 2000, undefined. Ink jet deposition of ceramic suspensions: modelling and experiments of droplet formation. *researchgate.net*

72. Duineveld, P. C. *et al.* Ink-jet printing of polymer light-emitting devices. in (ed. Kafafi, Z. H.) **4464,** 59 (International Society for Optics and Photonics, 2002).

73. Tanner, L. H. The spreading of silicone oil drops on horizontal surfaces. *J. Phys. D. Appl. Phys.* **12,** 1473–1484 (1979).

74. Ely, F. *et al.* Patterning quality control of inkjet printed PEDOT:PSS films by wetting properties. *Synth. Met.* **161,** 2129–2134 (2011).

75. Rowan, S. M., Newton, M. I. & McHale, G. Evaporation of Microdroplets and the Wetting of Solid Surfaces. *J. Phys. Chem.* **99,** 13268–13271 (1995).

76. Cazabat, A.-M. *et al.* Evaporation of macroscopic sessile droplets. *Soft Matter* **6,** 2591 (2010).

77. Shanahan, M. E. R., Sefiane, K. & Moffat, J. R. Dependence of Volatile Droplet Lifetime on the Hydrophobicity of the Substrate. *Langmuir* **27,** 4572–4577 (2011).

78. Murisic, N., Kondic, L. & Velarde, M. G. On evaporation of sessile drops with moving contact lines. *J. Fluid Mech.* **679,** 219–246 (2011).

79. Stauber, J. M., Wilson, S. K., Duffy, B. R. & Sefiane, K. Comment on "Increased Evaporation Kinetics of Sessile Droplets by Using Nanoparticles". *Langmuir* **29,** 12328–12329 (2013).

80. Erbil, H. Y. & Muzeyyen, D. Determination of Diffusion Coefficient−Vapor Pressure Product of Some Liquids from Hanging Drop Evaporation. *Langmuir* **16,** 9267–9273 (2000).

81. David, S., Sefiane, K. & Tadrist, L. Experimental investigation of the effect of thermal properties of the substrate in the wetting and evaporation of sessile drops. *Colloids Surfaces A Physicochem. Eng. Asp.* **298,** 108–114 (2007).

82. Popov, Y. O. Evaporative deposition patterns: Spatial dimensions of the deposit. *Phys. Rev. E* **71,** 036313 (2005).

83. Smith, J. D., Cappa, C. D., Drisdell, W. S., Cohen, R. C. & Saykally, R. J. Raman Thermometry Measurements of Free Evaporation from Liquid Water Droplets. *J. Am. Chem. Soc.* **128,** 12892–12898 (2006).

84. Poulard, C., Guéna, G. & Cazabat, A. M. Diffusion-driven evaporation of sessile drops. *J. Phys. Condens. Matter* **17,** S4213–S4227 (2005).

85. Picknett, R. . & Bexon, R. The evaporation of sessile or pendant drops in still air. *J. Colloid Interface Sci.* **61,** 336–350 (1977).

86. Birdi, K. S., Vu, D. T. & Winter, A. A study of the evaporation rates of small water drops placed on a solid surface. *J. Phys. Chem.* **93,** 3702–3703 (1989).

87. Bourges-Monnier, C. & Shanahan, M. E. R. Influence of evaporation on contact angle. *Langmuir* **11,** 2820–2829 (1995).

88. Masoud, H. & Felske, J. D. Analytical solution for inviscid flow inside an evaporating sessile drop. *Phys. Rev. E* **79,** 016301 (2009).

89. Sefiane, K., Wilson, S. K., David, S., Dunn, G. J. & Duffy, B. R. On the effect of the atmosphere on the evaporation of sessile droplets of water. *Phys. Fluids* **21,** 062101 (2009).

90. Sefiane, K. & Bennacer, R. An expression for droplet evaporation incorporating thermal effects. *J. Fluid Mech.* **667,** 260–271 (2011).

91. Sefiane, K., Tadrist, L. & Douglas, M. Experimental study of evaporating water–ethanol mixture sessile drop: influence of concentration. *Int. J. Heat Mass Transf.* **46,** 4527–

4534 (2003).

92. Hamamoto, Y., Christy, J. R. E. & Sefiane, K. The Flow Characteristics of an Evaporating Ethanol Water Mixture Droplet on a Glass Substrate. *J. Therm. Sci. Technol.* **7,** 425–436 (2012).

93. Park, J. & Jooho, M. Control of Colloidal Particle Deposit Patterns within Picoliter Droplets Ejected by Ink-Jet Printing. *Langmuir* **22,** 3506–3513 (2006).

94. Lim, J. A. *et al.* Self-Organization of Ink-jet-Printed Triisopropylsilylethynyl Pentacene via Evaporation-Induced Flows in a Drying Droplet. *Adv. Funct. Mater.* **18,** 229–234 (2008).

95. Christy, J. R. E., Hamamoto, Y. & Sefiane, K. Flow Transition within an Evaporating Binary Mixture Sessile Drop. *Phys. Rev. Lett.* **106,** 205701 (2011).

96. Thomson, J. On certain curious motions observable at the surfaces of wine and other alcoholic liquors. *Philosphical Mag.* **10,** (1855).

97. Hu, H. & Larson, R. G. Marangoni Effect Reverses Coffee-Ring Depositions. *J. Phys. Chem. B* **110,** 7090–7094 (2006).

98. Still, T., Yunker, P. J. & Yodh, A. G. Surfactant-Induced Marangoni Eddies Alter the Coffee-Rings of Evaporating Colloidal Drops. *Langmuir* **28,** 4984–4988 (2012).

99. Truskett, V. N. & Stebe, K. J. Influence of Surfactants on an Evaporating Drop: Fluorescence Images and Particle Deposition Patterns. *Langmuir* **19,** 8271–8279 (2003).

100. Kajiya, T., Nishitani, E., Yamaue, T. & Doi, M. Piling-to-buckling transition in the drying process of polymer solution drop on substrate having a large contact angle. *Phys. Rev. E* **73,** 011601 (2006).

101. Hu, H. & Larson, R. G. Analysis of the Effects of Marangoni Stresses on the Microflow in an Evaporating Sessile Droplet. *Langmuir* **21,** 3972–3980 (2005).

102. Ristenpart, W. D., Kim, P. G., Domingues, C., Wan, J. & Stone, H. A. Influence of Substrate Conductivity on Circulation Reversal in Evaporating Drops. *Phys. Rev. Lett.* **99,** 234502 (2007).

103. Ristenpart, W. D., Kim, P. G., Domingues, C., Wan, J. & Stone, H. A. Influence of Substrate Conductivity on Circulation Reversal in Evaporating Drops. *Phys. Rev. Lett.* **99,** 234502 (2007).

104. Girard, F., Antoni, M., Faure, S. & Steinchen, A. Evaporation and Marangoni Driven Convection in Small Heated Water Droplets. *Langmuir* **22,** 11085–11091 (2006).

105. Sefiane, K., Fukatani, Y., Takata, Y. & Kim, J. Thermal Patterns and Hydrothermal Waves (HTWs) in Volatile Drops. *Langmuir* **29,** 9750–9760 (2013).

106. Hu, H. & Larson, R. G. Analysis of the Microfluid Flow in an Evaporating Sessile Droplet. *Langmuir* **21,** 3963–3971 (2005).

107. Fischer Benjamin J. Particle Convection in an Evaporating Colloidal Droplet. *Langmuir* **18,** 60–67 (2001).

108. Wong, T.-S., Chen, T.-H., Shen, X. & Ho, C.-M. Nanochromatography Driven by the Coffee Ring Effect. *Anal. Chem.* **83,** 1871–1873 (2011).

109. Kruglova, O., Demeyer, P.-J., Zhong, K., Zhou, Y. & Clays, K. Wonders of colloidal

assembly. *Soft Matter* **9,** 9072 (2013).

110. Bigioni, T. P. *et al.* Kinetically driven self assembly of highly ordered nanoparticle monolayers. *Nat. Mater.* **5,** 265–270 (2006).

111. Kaya, D., Belyi, V. A. & Muthukumar, M. Pattern formation in drying droplets of polyelectrolyte and salt. *J. Chem. Phys.* **133,** 114905 (2010).

112. Sempels, W., Dier, R. De, H. Mizuno, J. H. & Vermant, J. Auto-production of biosurfactants reverses the coffee ring effect in a bacterial system - Biolin Scientific. *Nat. Commun.* **4,** 1757 (2013).

113. Good, R. J. A Thermodynamic Derivation of Wenzel's Modification of Young's Equation for Contact Angles; Together with a Theory of Hysteresis [1]. *J. Am. Chem. Soc.* **74,** 5041–5042 (1952).

114. Sefiane, K. Effect of nonionic surfactant on wetting behavior of an evaporating drop under a reduced pressure environment. *J. Colloid Interface Sci.* **272,** 411–419 (2004).

115. Innocenzi, P., Malfatti, L. & Falcaro, P. *Water Droplets to Nanotechnology : a Journey Through Self-Assembly*. (2013).

116. Xu, W. & Choi, C.-H. From Sticky to Slippery Droplets: Dynamics of Contact Line Depinning on Superhydrophobic Surfaces. *Phys. Rev. Lett.* **109,** 024504 (2012).

117. Shen, X., Ho, C.-M. & Wong, T.-S. Minimal Size of Coffee Ring Structure. *J. Phys. Chem. B* **114,** 5269–5274 (2010).

118. Vancauwenberghe, V., Di Marco, P. & Brutin, D. Wetting and evaporation of a sessile drop under an external electrical field: A review. *Colloids Surfaces A Physicochem. Eng. Asp.* **432,** 50–56 (2013).

119. Eral, H. B. *et al.* Suppressing the coffee stain effect: how to control colloidal self-assembly in evaporating drops using electrowetting. *Soft Matter* **7,** 4954 (2011).

120. Tamaddon, A. H. *et al.* Role of Ambient Composition on the Formation and Shape of Watermarks on a Bare Silicon Substrate. *ECS J. Solid State Sci. Technol.* **3,** N3081–N3086 (2014).

121. Chen, L. & Evans, J. R. G. Drying of colloidal droplets on superhydrophobic surfaces. *J. Colloid Interface Sci.* **351,** 283–287 (2010).

122. Kajiya, T., Kobayashi, W., Okuzono, T. & Doi, M. Controlling the Drying and Film Formation Processes of Polymer Solution Droplets with Addition of Small Amount of Surfactants. *J. Phys. Chem. B* **113,** 15460–15466 (2009).

123. Stigloher, J. *et al.* Snell's Law for Spin Waves. *Phys. Rev. Lett.* **117,** 037204 (2016).

124. Creath, K. Calibration of numerical aperture effects in interferometric microscope objectives. *Appl. Opt.* **28,** 3333 (1989).

125. Boddeke, F., Young, I. & Zagers, R. Depth-of-focus in microscopy. in *Proc. of the 8th Scandanavian Conference on Image Analysis* 493–498 (1993).

126. Eugene Hecht. Optics. in 385–442 (Addison Wesley, 2002).

127. Akcay, C., Parrein, P. & Rolland, J. Estimation of longitudinal resolution in optical coherence imaging. *Appl. Opt.* **41,** 5256–5262 (2002).

128. Glycol, P. & Ether, M. DOWANOL ™ PM Propylene Glycol Methyl Ether. **3,**

129. PubChem. 1-Methoxy 2-propanol. Available at: https://pubchem.ncbi.nlm.nih.gov/compound/1-Methoxy-2-propanol#section=Top. (Accessed: 1st September 2017)

130. Hoorfar, M. & W. Neumann, A. Recent progress in Axisymmetric Drop Shape Analysis (ADSA). *Adv. Colloid Interface Sci.* **121,** 25–49 (2006).

131. Roura, P. & P. Thermodynamic derivations of the mechanical equilibrium conditions for fluid surfaces: Young's and Laplace's equations. *Am. J. Phys.* **73,** 1139–1147 (2005).

132. University, G. Department of Physics | Georgetown University. Available at: https://physics.georgetown.edu/matlab/tutorial.html. (Accessed: 9th June 2015)

133. Derby, B. Inkjet printing ceramics: From drops to solid. *J. Eur. Ceram. Soc.* **31,** 2543–2550 (2011).

134. Coenen, M. J. J., Slaats, T. M. W. L., Eggenhuisen, T. M. & Groen, P. Inkjet printing the three organic functional layers of two-colored organic light emitting diodes. *Thin Solid Films* **583,** 194–200 (2015).

135. Ely, F. *et al.* Patterning quality control of inkjet printed PEDOT:PSS films by wetting properties. *Synth. Met.* **161,** 2129–2134 (2011).

136. Adrian, R. J. Particle-Imaging Techniques for Experimental Fluid Mechanics. *Annu. Rev. Fluid Mech.* **23,** 261–304 (1991).

137. Westerweel, J. & J. Fundamentals of digital particle image velocimetry. *Meas. Sci. Technol.* **8,** 1379–1392 (1997).

138. Grant, I. Particle image velocimetry: A review. *Proc. Inst. Mech. Eng. Part C J. Mech. Eng. Sci.* **211,** 55–76 (1997).

139. Meinhart, C. D., Wereley, S. T. & Santiago, J. G. PIV measurements of a microchannel flow. *Exp. Fluids* **27,** 414–419 (1999).

140. Lugg, G. A. Diffusion coefficients of some organic and other vapors in air. *Anal. Chem.* **40,** 1072–1077 (1968).

141. Hansen, S. Hansen Solubility Parameters in Practice. (2017).

142. Jain, P. K., Lee, K. S., El-Sayed, I. H. & El-Sayed, M. A. Calculated Absorption and Scattering Properties of Gold Nanoparticles of Different Size, Shape, and Composition: Applications in Biological Imaging and Biomedicine. *J. Phys. Chem. B* **110,** 7238–7248 (2006).

143. Eustis, S. & El-Sayed, M. A. Why gold nanoparticles are more precious than pretty gold: Noble metal surface plasmon resonance and its enhancement of the radiative and nonradiative properties of nanocrystals of different shapes. *Chem. Soc. Rev.* **35,** 209–217 (2006).

144. Willets, K. A. & Van Duyne, R. P. Localized Surface Plasmon Resonance Spectroscopy and Sensing. *Annu. Rev. Phys. Chem.* **58,** 267–297 (2007).

145. Reynolds, O. On the Theory of Lubrication and Its Application to Mr. Beauchamp Tower's Experiments, Including an Experimental Determination of the Viscosity of Olive Oil. *Philos. Trans.* **177,** 157–234 (1886).

146. Mackay, G. D. M. & Mason, S. G. The gravity approach and coalescence of fluid drops at liquid interfaces. *Can. J. Chem. Eng.* **41,** 203–212 (1963).

147. Allan, R. S., Charles, G. E. & Mason, S. G. The approach of gas bubbles to a gas/liquid interface. *J. Colloid Sci.* **16,** 150–165 (1961).

148. Frankel, S. P. & Myseis, K. J. ON THE "DIMPLING" DURING THE APPROACH OF TWO INTERFACES [1]. *J. Phys. Chem.* **66,** 190–191 (1962).

149. Platikanov, D. Experimental investigation on the "dimpling" of thin liquid films. *J. Phys. Chem.* **68,** 3619–3624 (1964).

150. Joye, J., Hirasaki, G. & Miller, C. Dimple formation and behavior during axisymmetrical foam film drainage. *Langmuir* **8,** 3083–3092 (1992).

151. Sheludko, A. Thin liquid films. *Adv. Colloid Interface Sci.* **1,** 391–464 (1967).

152. Cazabat, A.-M. & Guna, G. Evaporation of macroscopic sessile droplets. *Soft Matter* **6,** 2591 (2010).

153. and, D. S. & Subramanian, V. Inkjet-Printed Line Morphologies and Temperature Control of the Coffee Ring Effect. (2008). doi:10.1021/LA7026847

154. Girard, F., Antoni, M., Faure, S. & Steinchen, A. Evaporation and Marangoni Driven Convection in Small Heated Water Droplets. *Langmuir* **22,** 11085–11091 (2006).

155. Sefiane, K., Fukatani, Y., Takata, Y. & Kim, J. Thermal Patterns and Hydrothermal Waves (HTWs) in Volatile Drops. *Langmuir* **29,** 9750–9760 (2013).

156. Chemicals, C. o-Xylene. Available at: https://cameochemicals.noaa.gov/chris/XLO.pdf. (Accessed: 1st September 2017)

157. Thermal Conductivity for Some Common Materials. Available at: http://www.postdiluvian.org/~mason/materials/thermal_conductivity.html. (Accessed: 1st September 2017)

158. Umicore. High Density Ceramic TCO Sputtering Targets: Indium Tin Oxide (ITO). Available at: http://www.thinfilmproducts.umicore.com/Products/TechnicalData/show_datenblatt_ito.pdf. (Accessed: 1st September 2017)

159. Goodfellow. Polymethylmethacrylate - online catalogue source - supplier of research materials in small quantities - Goodfellow. Available at: http://www.goodfellow.com/E/Polymethylmethacrylate.html. (Accessed: 7th September 2017)

160. P.L. Kelly-Zion, Pursell, C. J., Vaidya, S. & Batra, J. Evaporation of sessile drops under combined diffusion and natural convection. *Colloids Surfaces A Physicochem. Eng. Asp.* **381,** 31–36 (2011).

161. Watanabe, H. & Kato, H. Thermal Conductivity and Thermal Diffusivity of Twenty-Nine Liquids: Alkenes, Cyclic (Alkanes, Alkenes, Alkadienes, Aromatics), and Deuterated Hydrocarbons. *J. Chem. Eng. Data* 809–825 (2004). doi:10.1021/JE034162X

162. Talbot, E. L. Drying Inkjet Droplets - Internal Flows and Deposit Structure. (University of Durham, 2014).

163. PubChem. Butyl Acetate. Available at:

https://pubchem.ncbi.nlm.nih.gov/compound/Butyl_acetate#section=Top. (Accessed: 1st October 2017)

164. Chemicals, C. n-Butyl Acetate. Available at: https://cameochemicals.noaa.gov/chris/BCN.pdf. (Accessed: 1st September 2017)

165. GSI environmental. GSI Chemical Database. (2016). Available at: http://www.gsi-net.com/en/publications/gsi-chemical-database/single/470-CAS-107982.html. (Accessed: 1st July 2017)

166. Chemeo. Chemical Properties of Toluene. Available at: https://www.chemeo.com/cid/17-837-4/Toluene. (Accessed: 1st October 2017)

167. Chemicals, C. Toluene. Available at: https://cameochemicals.noaa.gov/chris/TOL.pdf. (Accessed: 1st September 2017)

168. PubChem. 1-Butanol. Available at: https://pubchem.ncbi.nlm.nih.gov/compound/1-butanol#section=Decomposition. (Accessed: 1st October 2017)

169. Chemicals, C. n-Butyl Alcohol. Available at: https://cameochemicals.noaa.gov/chris/BAN.pdf. (Accessed: 1st September 2017)

170. Chemeo. Chemical Properties of o-Xylene. Available at: https://www.chemeo.com/cid/62-853-6/o-Xylene. (Accessed: 1st October 2017)

171. PubChem. Ethanol. Available at: https://pubchem.ncbi.nlm.nih.gov/compound/702#section=Auto-Ignition. (Accessed: 1st October 2017)

172. Fluids, T. Thermal Fluids Database. Available at: https://www.thermalfluidscentral.org/encyclopedia/index.php/Thermophysical_Properties:_Ethanol. (Accessed: 1st July 2017)

173. PubChem. Isopropanol. Available at: https://pubchem.ncbi.nlm.nih.gov/compound/isopropanol#section=Viscosity. (Accessed: 1st October 2017)

174. Chemicals, C. Isopropyl Alcohol. Available at: https://cameochemicals.noaa.gov/chris/IPA.pdf. (Accessed: 1st September 2017)

175. Hołyst, R., Litniewski, M. & Jakubczyk, D. A molecular dynamics test of the Hertz-Knudsen equation for evaporating liquids. *Soft Matter* **11,** 7201–6 (2015).

176. Mokeba, M. L., Salt, D. W., Lee, B. E. & Ford, M. G. Simulating the dynamics of spray droplets in the atmosphere using ballistic and random-walk models combined. *J. Wind Eng. Ind. Aerodyn.* **67–68,** 923–933 (1997).

Appendix A: Images and Curves of Profile Progression for All Single Solvents

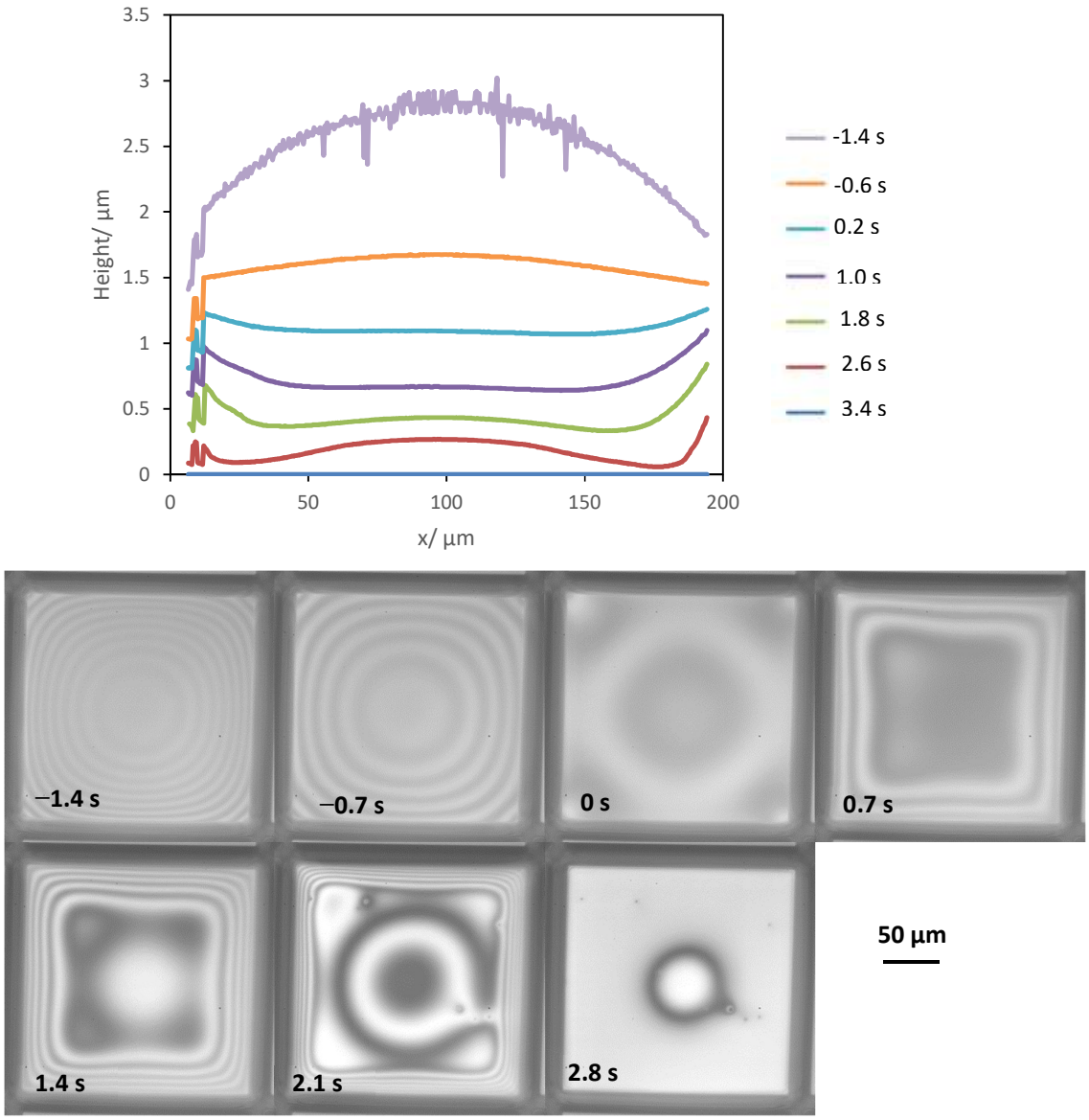

Figure A1: Plots (a) and images (b) from the drying of a methyl anisole drop in the square wells. Images were recorded at 125 fps and a shutter speed of 1.1 ms. The plot cross section was taken horizontally across the centre of the well. Zero time is defined at the time at which the average height of the fluid is equal to the average height of the banks.

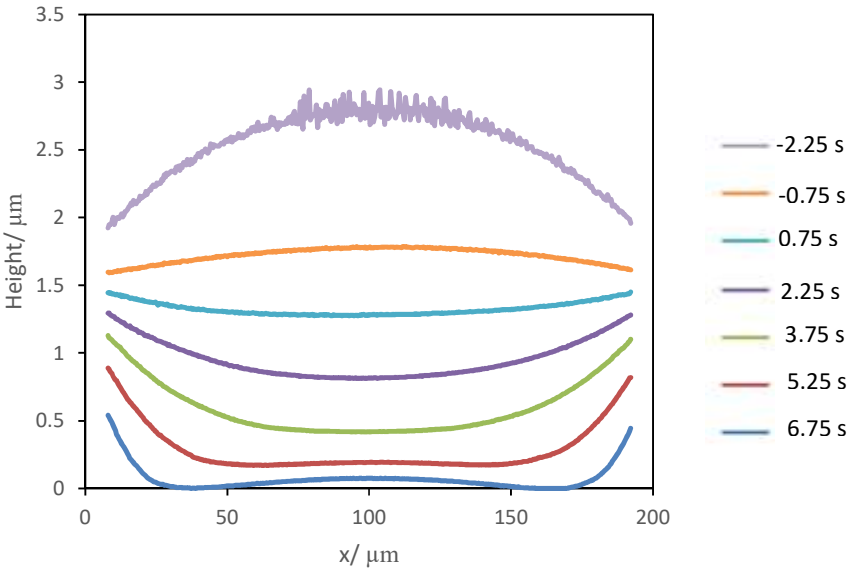

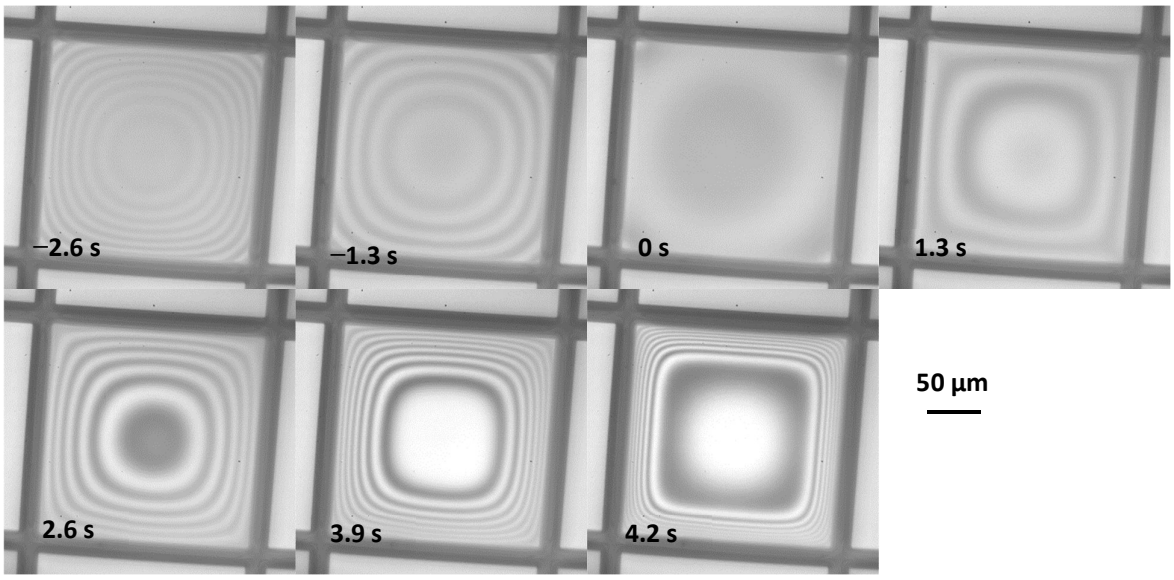

Figure A2: Plots (a) and images (b) from the drying of a mesitylene drop in the square wells. Images were recorded at 125 fps and a shutter speed of 1.1 ms. The plot cross section was taken horizontally across the centre of the well. Zero time is defined at the time at which the average height of the fluid is equal to the average height of the banks.

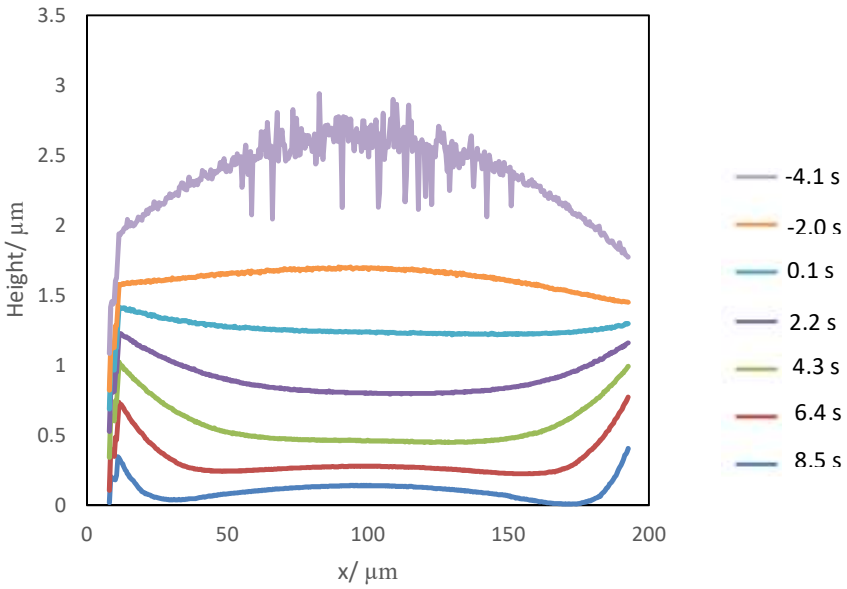

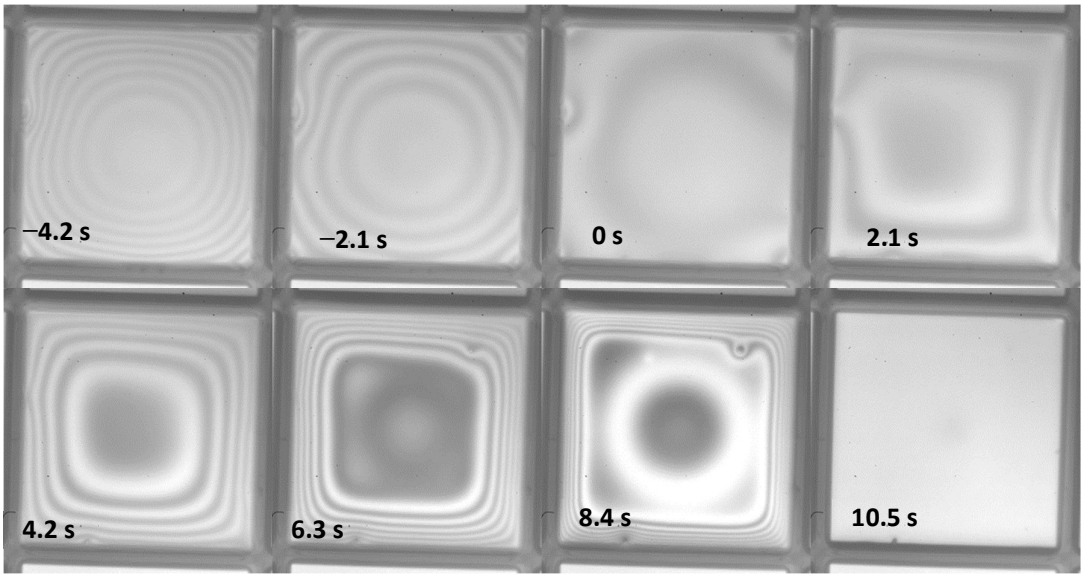

Figure A3: Plots (a) and images (b) from the drying of a methyl benzoate drop in the square wells. Images were recorded at 50 fps and a shutter speed of 1.1 ms. The plot cross section was taken horizontally across the centre of the well. Zero time is defined at the time at which the average height of the fluid is equal to the average height of the banks.

Appendix B: Images Corresponding to Figure 6.3

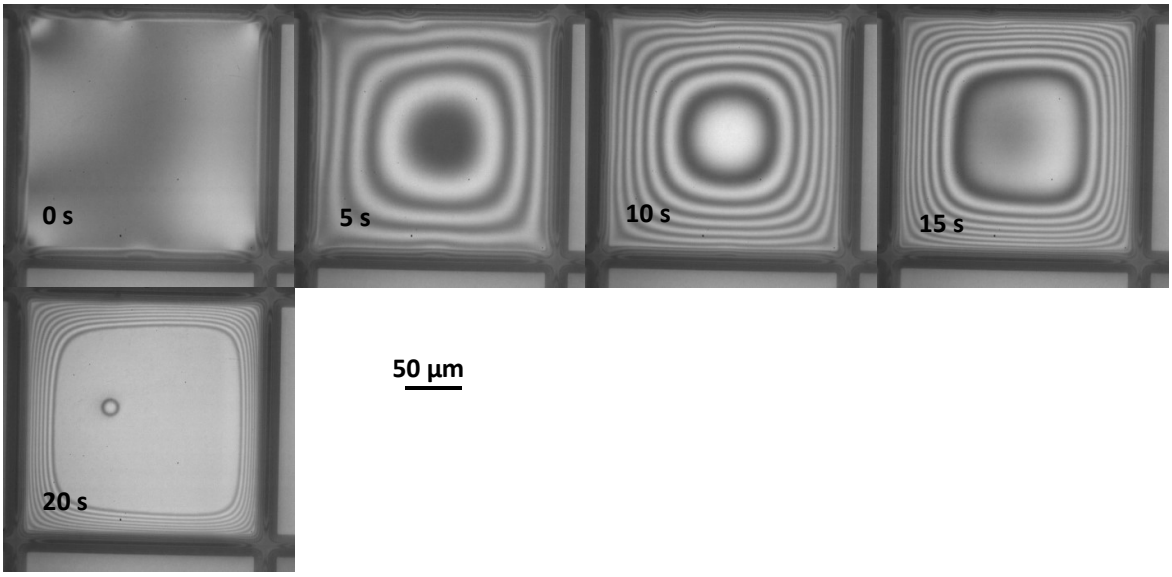

Figure B1: Images from the drying of the anisole + methyl benzoate plot from figure 6.3a. Images were recorded at 125 fps and a shutter speed of 1.1 ms. The plot cross section was taken horizontally across the centre of the well. Zero time is defined at the time at which the average height of the fluid is equal to the average height of the banks.

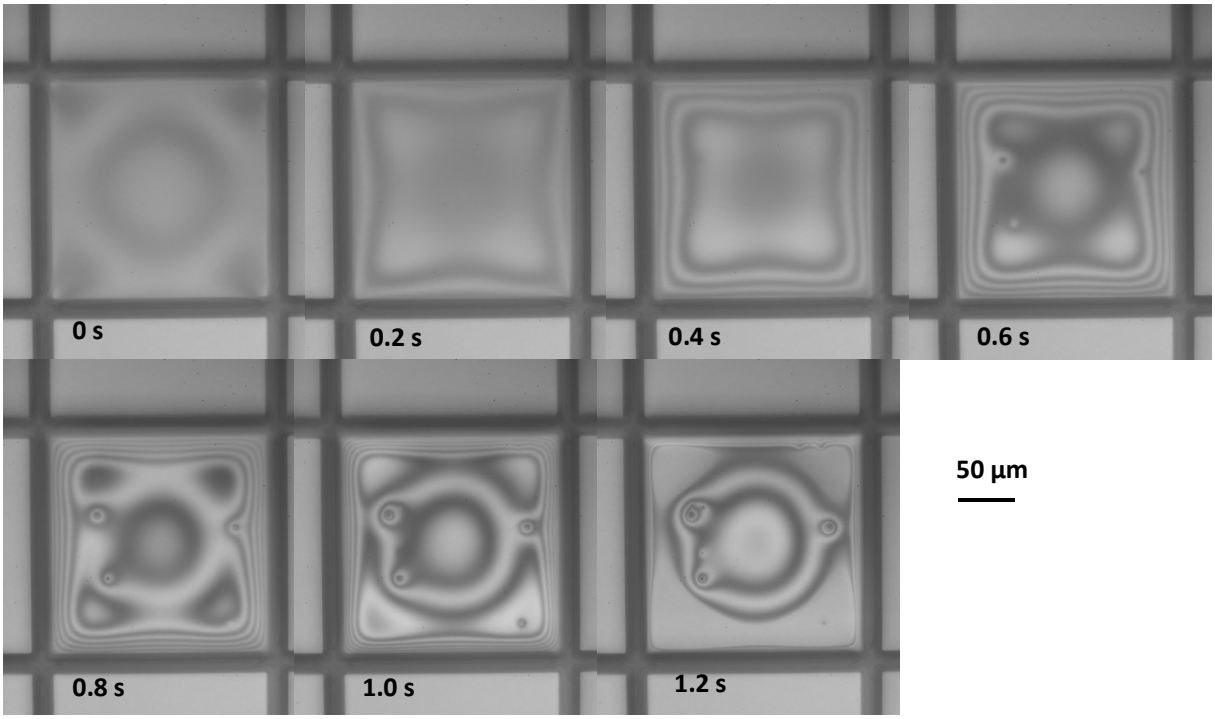

Figure B2: Images from the drying of the anisole + mesitylene plot from figure 6.3b. Images were recorded at 1000 fps and a shutter speed of 1 ms. The plot cross section was taken horizontally across the centre of the well. Zero time is defined at the time at which the average height of the fluid is equal to the average height of the banks.

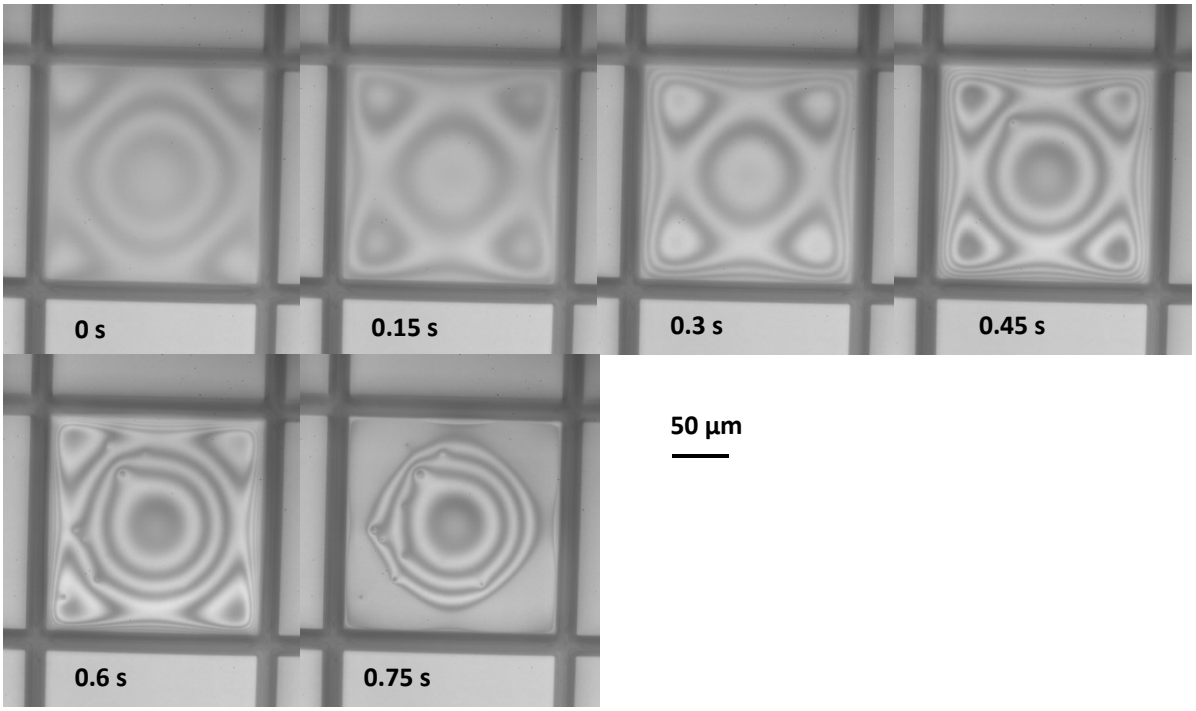

Figure B3: Images from the drying of the anisole + o-xylene plot from figure 6.3c. Images were recorded at 2000 fps and a shutter speed of 0.5 ms. The plot cross section was taken horizontally across the centre of the well. Zero time is defined at the time at which the average height of the fluid is equal to the average height of the banks.

Appendix C: Images of Profile Progression of All Single Solvents in the Presence of Active Materials

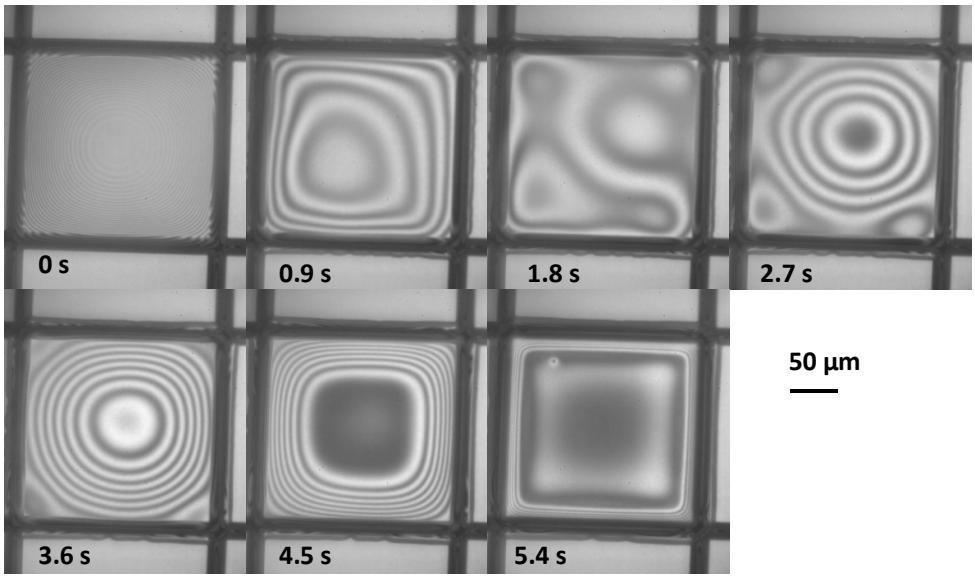

Figure C1: Images from the drying of methyl anisole in the presence of active material. Images were recorded at 500 fps and a shutter speed of 1 ms. The drop shows M-shaped profile progression. Zero time is defined as the time at which the drop stopped spreading.

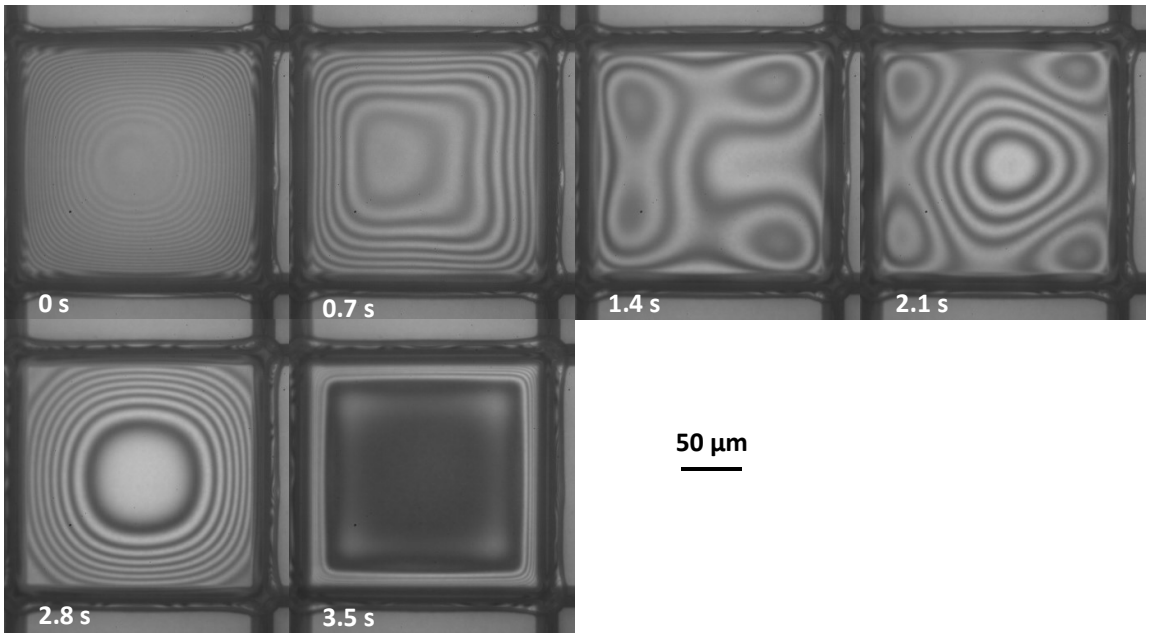

Figure C2: Images from the drying of mesitylene in the presence of active material. Images were recorded at 500 fps and a shutter speed of 1 ms. The drop shows M-shaped profile progression. Zero time is defined as the time at which the drop stopped spreading.

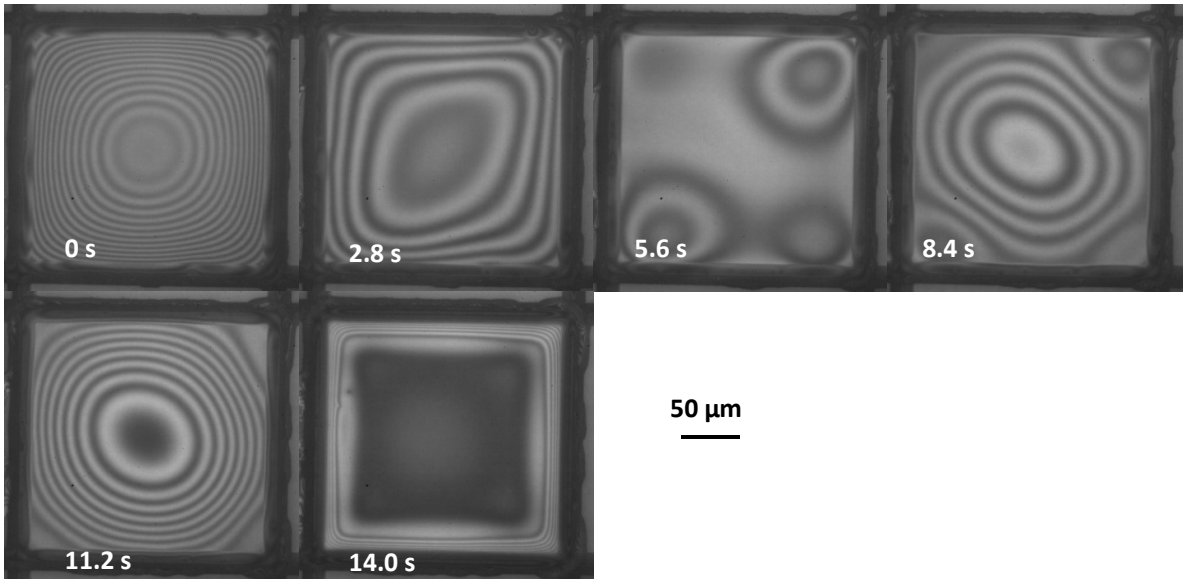

Figure C2: Images from the drying of methyl benzoate in the presence of active material. Images were recorded at 125 fps and a shutter speed of 1.1 ms. The drop shows some muted enhanced drainage from the centre of the well but a less prominent M-shaped profile than anisole, methyl anisole or mesitylene. Zero time is defined as the time at which the drop stopped spreading.

Appendix D: Matlab Code Used for Particle Tracking Velocimetry

D.1 Save Contact Centre and Radius

```
%%  PART ONE
% initiating parameters and variables

clear all;
PTV_2D_file % load file information

%%%%%%%%% some parameters need to be adjusted for particle
identification
%%%%%%%%% and tracking

% intensity and particle movement threshold
intensity_threshold_particle=5;% for particle identification
intensity_threshold_contact=60; % for contact line
particle_enhance=2; % background smooth. case 0: no, case 1:; case 2:
particle_move_threshold=3; %pixel, above which movement particle
counts

%%%%%%%%%%%%%%%%%%%%% Variable initiation


%%%%%%%%%%%%%%%%% locate contact line
        cd(folder)

        filename =
[filetitle,num2str(background_file),'.',fileformat];
        background = imread(filename);

        if contact_line_fixed
            frame_start_contact=deposit_file;
            frame_end_contact=deposit_file;
        else
            frame_start_contact=frame_start;
            frame_end_contact=frame_end;
        end

        for i=frame_start_contact:skip_frames+1:frame_end_contact
%               if i > 999
              filename = [filetitle2,num2str(i),'.',fileformat];
%               elseif i>99
%                     filename =
[filetitle2,'0',num2str(i),'.',fileformat];
%               elseif i>9
%                           filename =
[filetitle2,'00',num2str(i),'.',fileformat];
%               else
%                           filename =
[filetitle2,'000',num2str(i),'.',fileformat];
%             end


%             filename = [filetitle,num2str(i),'.',fileformat];
            b = imread(filename);

             I=double(background-b)+double(b-background);
             I=I(:,:,1);
             I = imrotate(I,rotation_angle,'crop');
```

```
            cla;
            figure(1);
            imagesc(I);
            size_I=size(I);
            colormap gray;
            axis equal;
            axis([0 size_I(2) 0 size_I(1)]);
            xlabel('x /pixel');
            ylabel('y /pixel');

            hold on;

            [n m]=find(I>intensity_threshold_contact); % in matrix
row 'n' is coordinates' y and column 'm' is x
            plot(m,n,'yo','Markersize',2)

          %%%%%%%%%%%%%%%%%%%%%%%%%%%%%% Automatic determine the
contact line
          pklist=[m n];
          indCL=convhull(pklist(:,1),pklist(:,2));
          CL=pklist(indCL,:);

          %%Plot the convex hull of each frame
           plot(CL(:,1),CL(:,2),'go-','Markersize',2,'Linewidth',1);

            if contact_circle
               if contact_line_auto
                  text(1,20,'Contact line
auto','color','yellow','Fontsize',10);
               else
                   text(1,20,'Evenly select 6 points near
contact','color','yellow','Fontsize',10);
                   CL=ginput(6);
               end
                %%%%Circular fitting (comment if you want ellipsoidal
fit)
                %Fit a circle and extract the centre
                 circ_fit=[CL ones(length(CL),1)]\[-
(CL(:,1).^2+CL(:,2).^2)];
                 xc_c = -.5*circ_fit(1);
                 yc_c = -.5*circ_fit(2);
                 R_c  =  sqrt((circ_fit(1)^2+circ_fit(2)^2)/4-
circ_fit(3));
                 th=0:0.01:2*pi; %%%%Angle
                 xy_c=[xc_c+R_c*cos(th) ; yc_c+R_c*sin(th)]';
                 plot(xy_c(:,1),xy_c(:,2),'-g','LineWidth',2)
                 plot(xc_c,yc_c,'xg','Markersize',10,'Linewidth',2)

                 contact=[xc_c yc_c R_c];

                 %%%%%%%%%%%%% Define region of interest for cropping
                 %%%%%%%%%%%%% square if needed

%
leftx_min=floor(min(min(xy_c(:,1)),min(CL(:,1))));
%
lefty_min=floor(min(min(xy_c(:,2)),min(CL(:,2))));
%
rightx_max=floor(max(max(xy_c(:,1)),max(CL(:,1))));
%
righty_max=floor(max(max(xy_c(:,2)),max(CL(:,2))));
%
```

```
            else
               if contact_line_auto
                  text(1,20,'Contact line
auto','color','yellow','Fontsize',10);
                  leftx_min=floor(min(CL(:,1)));
                  lefty_min=floor(min(CL(:,2)));
                  rightx_max=floor(max(CL(:,1)));
                  righty_max=floor(max(CL(:,2)));
               else
                   text(1,20,'Contact line manual: top-left and
bottom-right','color','yellow','Fontsize',10);
                   selection=ginput(2);
                   leftx_min=floor(selection(1,1));
                   lefty_min=floor(selection(1,2));
                   rightx_max=floor(selection(2,1));
                   righty_max=floor(selection(2,2));
               end
               corner=[leftx_min lefty_min; rightx_max lefty_min;
rightx_max righty_max;...
               leftx_min righty_max; leftx_min lefty_min];
               line(corner(:,1),corner(:,2),'Color','y');
         end

%               disp(['processing frame....',num2str(i)]);
%               pause;
%
        end

     cd ..

%%%%%%% identification of particles for each frame

particles=[];

for drop_frame=frame_start:skip_frames+1:frame_end;
    cd(folder)
    filename = [filetitle,num2str(drop_frame),'.',fileformat];
%       if drop_frame > 999
%               filename =
[filetitle2,num2str(drop_frame),'.',fileformat];
%               elseif drop_frame>99
%                     filename =
[filetitle2,'0',num2str(drop_frame),'.',fileformat];
%               elseif drop_frame>9
%                         filename =
[filetitle2,'00',num2str(drop_frame),'.',fileformat];
%               else
%                         filename =
[filetitle2,'000',num2str(drop_frame),'.',fileformat];
%             end
    b = imread(filename);

    I=double(b);
    I=I(:,:,1);
    size_I=size(I);
%     figure(2)
%     cla
%     imagesc(I);
%     colormap gray;

%     axis equal;
%     axis([0 size_I(2) 0 size_I(1)]);
```

```
%       line(corner(:,1),corner(:,2),'Color','y');
%     text(10,20,'Orginal image','color','yellow');
%
    switch particle_enhance
        case 0,
            background=0;
        case 1,
            background = imopen(I,strel('disk',4));%%%%%%%%%%%%%%%%%%
Background smooth
        case 2,
            backApprox = blkproc(I,[15 15],'min(x(:))');
            background = imresize(backApprox, size_I,
'bilinear');%%%%%%%%%%%%%%%%%% Background smooth
    end

    I = I - background;%%%%%%%%%%%%%%%%%% Background subtract

    if contact_circle~=1
        I = imrotate(I,rotation_angle,'crop'); %%% rotation
        I=I(lefty_min:righty_max,leftx_min:rightx_max); %%% cropping
    end

    size_I=size(I);

%     figure(3)
%     cla
%     imagesc(I);
%     colormap gray;
%     axis equal;
%     axis([0 size_I(2) 0 size_I(1)]);
%     text(10,20,'Particles intensity enhanced','color','yellow');
%
     cd ..
     cd PTVtracking_prog\
     I = bpass(I,1,5); % filter
     pk=pkfnd(I,intensity_threshold_particle,7);  % second argument:
intensity level-threshold, the third: the size of average blobs

     if isempty(pk)
        particles=particles;
     else
        cnt=cntrd(I,pk,7); %%%%Find peaks with sub-pixel accuracy
RECCOMMENDED  size is the long lengthscale used in bpass plus 2.
        particles=[particles; cnt(:,1:2)
ones(length(cnt(:,1)),1).*drop_frame]; %%%%store peaks in a matrix
suitable for the following
     end
     cd ..

    %%%Plot results
    figure(4)
    cla
    imagesc(I);
    colormap gray;
    axis equal;
    axis([0 size_I(2) 0 size_I(1)]);
    hold on;
     message=sprintf('Particle identified in
frames:%4.0f',drop_frame);
     text(10,20,message,'color','yellow');
     plot(cnt(:,1),cnt(:,2),'rx','Markersize',4,'Linewidth',1)
     xlabel('x /pixel');
```

```
     ylabel('y /pixel');

    % M(drop_frame-frame_start+1)=getframe;

     %pause(1);
end
% movie2avi(M,'test.avi','FPS',5);

%%%%%%tracking and seperating non-moving and moving particles

traj_0=[];
traj_v=[];

    cd PTVtracking_prog\

    param.mem=4;% How long a particle can disappear
    param.good=3;%The minimum number of hits in a track
    param.dim=2;%  The dimensions of the answer
    param.quiet=1;% Useful text on or off

    %%%%Compute trajectories
    traj=tracking(particles,5,param); %%%%%%%traj= [x y t id]
                                % second parameter an estimate of the
maximum
                                %distance that a particle would move in
a single time interval.(see Restrictions)

    cd ..


%%%%%%%%%%%%%%%%%%%%%%%%%%%%%%%%%%%%%%%%%%%%%%%%%%%%%%%%%%%%%%%%%%%%%%%%
    %%%% tracking the movement less than particle_move_threshold pixel
in particle lifetime

%%%%%%%%%%%%%%%%%%%%%%%%%%%%%%%%%%%%%%%%%%%%%%%%%%%%%%%%%%%%%%%%%%%%%%%%
    count_0=0;
    count_v=0;

    for i_part=1:max(traj(:,4))  %%%loop on particles for all frames

    ind=find(traj(:,4)==i_part); %%%indices of the i_part particle
       if
(sum(sqrt(diff(traj(ind,1)).^2+diff(traj(ind,2)).^2))<particle_move_th
reshold) |...
               (sqrt((traj(ind(end),1)-
traj(ind(1),1))^2+(traj(ind(end),2)-
traj(ind(1),2))^2)<particle_move_threshold)
           count_0=count_0+1;
          for j=1:size(ind)
               traj_0=vertcat(traj_0, [traj(ind(j),1) traj(ind(j),2)
traj(ind(j),3) count_0]);
          end
       else
           count_v=count_v+1;
          for j=1:size(ind)
               traj_v=vertcat(traj_v, [traj(ind(j),1) traj(ind(j),2)
traj(ind(j),3) count_v]);
          end
       end

%%%%%%%%%%%%%%%%%%%%%%%%%%%%%%%%%%%%%%%%%%%%%%%%%%%%%%%%%%%%%%%%%%%%%%%%
```

```
    end

    track_frame_start=min(traj_v(:,3));
    track_frame_end=max(traj_v(:,3));

    figure(5)
    cla
    imagesc(I);
    colormap(gray);
    axis equal;
    hold on;
    axis normal; box on;
    set(gca,'YDir','reverse');

    if contact_circle
        plot(xy_c(:,1),xy_c(:,2),'-g','LineWidth',2)
        plot(xc_c,yc_c,'xg','Markersize',10,'Linewidth',2)
    end

    plot(traj_0(:,1),traj_0(:,2),'bo','Markersize',2)

    message=sprintf('Tracked: %4.2f - %4.2f
t_{f}',track_frame_start/drying_end_frame,track_frame_end/drying_end_f
rame);
    text(1,20,message,'color','y');

    for id = 1:max(traj_v(:,4))
        ontrack = traj_v(:,4) == id;
        st = find(ontrack,1,'first');
        en = find(ontrack,1,'last');

         plot(traj_v(ontrack,1),traj_v(ontrack,2),'-y','markersize',4)
      %   plot(traj(st,1),traj(st,2),'.g','markersize',2)
         plot(traj_v(en,1),traj_v(en,2),'>r','markersize',4)
    end
                xlabel('x /pixel');
                ylabel('y /pixel');
                axis([0 size_I(2) 0 size_I(1)]);

%%%%% Compute velocities v=[x y t id vx vy] unit: pixel, frame, m/s
%%%%% Save files

%%%%velocity is at t(1) is given by x(2)-x(1)/t(2)-t(1)
v=[];

    for i_part=1:max(traj_v(:,4))   %%%loop on particles
        ind=find(traj_v(:,4)==i_part); %%% indices of the i_part
particle


v_x=diff(traj_v(ind,1))*resolution./(diff(traj_v(ind,3))*frame_dt);
%%%x component of velocity

v_y=diff(traj_v(ind,2))*resolution./(diff(traj_v(ind,3))*frame_dt);
%%%y component of velocity

        v=vertcat(v, [traj_v(ind(1:end-1),1:2) traj_v(ind(1:end-1),3)
traj_v(ind(1:end-1),4) v_x v_y]);
    end
```

```
%%%%% Convert to polar coordinate for circular deposit (consider
moving
%%%%% contact line in circular deposit)
   if contact_circle
            v=[v(:,1:6) zeros(length(v(:,1)),4)]; %%%initialize
velocity matrix
            for frame_part=min(v(:,3)):skip_frames+1:max(v(:,3))
              ind=find(v(:,3)==frame_part); %%% indices of each frame
               %%%%Convert particle position in polar coordinates
              for j=1:length(ind)
                  %%%%convert position into polar cordinates
                     xr=sqrt((v(ind(j),1)-xc_c)^2 + (v(ind(j),2)-
yc_c)^2 ); %%compute radius
                     xth=atan2((v(ind(j),2)-yc_c),(v(ind(j),1)-xc_c));
%%compute angle

                   %%%%Convert velocities into polar coordinates
                     vrth=[cos(xth), -sin(xth) ; sin(xth),
cos(xth)]\[v(ind(j),5); v(ind(j),6)];
                     v(ind(j),7:10)=[xr xth vrth'];
              end
            end
   end

   %% save contact centre and radius
   % save non-moving particles
   % save moving particles
   if contact_circle
       contact=[xc_c yc_c R_c];
       save contact.mat contact
   end
   save traj_0.mat traj_0
   save v.mat v
```

D.2 Particle Tracking

```
%% PART TWO

clear all;

PTV_2D_file % load file information

% traj_0 = [x y t id] particle that doesn't move
% v=[x y t id vx vy] and in case of circular deposit v=[x y t id vx vy
r theta vr vtheta] moving partiles, units: pixel, frame, m/s

if contact_circle
    load p-test5_v.mat
    load p-test5_traj_0.mat
    load p-test5_contact.mat

    xc_c=contact(1);
    yc_c=contact(2);
    R_c=contact(3);
    %%%%%%%%%%%%%%%% Bin space window (divisions)
    window_div=10; % for radial binning
    %%%%%%%%%%%%%%%%%%%%%%%%%%%%
    R0=max(v(:,7)); % in pixel
    dr=R0/window_div; %pixels for spatial-binned, polar coordinator
else
    load v.mat
    load traj_0.mat

    window_divm=8; % x-division
    window_divn=8; % y-division

    dx=max(v(:,1))/window_divm;
    dy=max(v(:,2))/window_divn;
end

%%%%%%%%%%%%%%%% Bin time window (divisions)
t_div=10; % division of time

% velocity scale
scale_factor=0.5;
scale_velocity=1; %micron/s

%%%%%%%%%%%%%%%%%%%%%%%%%%%
dt=drying_end_frame/t_div; %frames for temporal-binned

%%%% Plot general traj over the tracked particles (results from
Part.1)

    track_frame_start=min(v(:,3));
    track_frame_end=max(v(:,3));

    figure(1)
    cla
    axis equal;
    hold on;
    box on;
    set(gca,'YDir','reverse');

    plot(traj_0(:,1),traj_0(:,2),'ro','Markersize',2)
```

```
    message=sprintf('Tracked: %4.1f - %4.1f
t_{f}',track_frame_start/drying_end_frame,track_frame_end/drying_end_f
rame);
    text(5,20,message,'color','b','FontSize',8);

    for id = 1:max(v(:,4))
        ontrack = v(:,4) == id;
        st = find(ontrack,1,'first');
        en = find(ontrack,1,'last');

         plot(v(ontrack,1),v(ontrack,2),'-b','markersize',4)
      %   plot(v(st,1),v(st,2),'.g','markersize',2)
         plot(v(en,1),v(en,2),'>b','markersize',4)
    end

    if contact_circle
         for rings=1:window_div
            th=0:0.01:2*pi; %%%%Angle
            r=rings*dr;
            xy_c=[xc_c+r*cos(th) ; yc_c+r*sin(th)]';
            plot(xy_c(:,1),xy_c(:,2),'-.y','LineWidth',2)
         end
         th=0:0.01:2*pi; %%%%Angle
         xy_c=[xc_c+R_c*cos(th) ; yc_c+R_c*sin(th)]';
         plot(xy_c(:,1),xy_c(:,2),'-.g','Linewidth',1)
         plot(xc_c,yc_c,'xg','Markersize',10,'Linewidth',2)
    else
         %%% plot y-binning lines
        for i=1:window_divn-1
            lines_y=[0 dy*i; max(v(:,1)) dy*i];
            line(lines_y(:,1),lines_y(:,2),'color','y','linestyle','-
.','linewidth',2);
        end

         %%% plot x-binning lines
        for i=1:window_divm-1
            lines_x=[dx*i 0; dx*i max(v(:,2))];
            line(lines_x(:,1),lines_x(:,2),'color','y','linestyle','-
.','linewidth',2);
        end
    end
        xlabel('x /pixel');
        ylabel('y /pixel');
        axis tight;

%%
% Locate the particles in the bin

    % Bin in dr and dt
if contact_circle
    vrt_m=[];
    vtht_m=[];

             for count_t=1:t_div
               t=count_t*dt;
                id_t=find(v(:,3)>=t-dt & v(:,3)<t) ; %%find particles
within the time bin
                xrt=v(id_t,7);
                xtht=v(id_t,8);
                vrt=v(id_t,9);
                vtht=v(id_t,10);
                 for count_r=1:window_div
```

```
                    r=count_r*dr;
                     vrt_m(count_t,count_r)=mean(vrt(find(xrt >=r-dr &
xrt <= r)));%%find particles within the space bin
                     vtht_m(count_t,count_r)=mean(vtht(find(xrt >=r-dr
& xrt <= r)));

                end
             end

    % from now on, unit in plot: micron and seconds

        r=((1:window_div)*dr-dr/2)*resolution;
        t=((1:t_div)*dt-dt/2)*frame_dt;

        figure(2)
            axis equal;
            hold on;
            box on;
            set(gca,'YDir','reverse');
            xlabel('x /\mum');
            ylabel('y /\mum');

              for count_t=1:t_div
                 cla;
                 for rings=1:window_div
                    th=0:0.01:2*pi; %%%%Angle
                    r_ring=rings*dr;
                    xy_c=[xc_c+r_ring*cos(th) ;
yc_c+r_ring*sin(th)]'*resolution;
                    plot(xy_c(:,1),xy_c(:,2),'-.y','LineWidth',2)
                    axis tight;
                 end
                  for th=0:0.3:2*pi
                      x=r*cos(th)+xc_c*resolution;
                      y=r*sin(th)+yc_c*resolution;
                      %%%%Convert velocities into cardesian coordinate
                      vxyt_m=[cos(th), -sin(th) ; sin(th),
cos(th)]*[vrt_m(count_t,1:window_div); vtht_m(count_t,1:window_div)];


quiver(x,y,vxyt_m(1,:)*scale_factor,vxyt_m(2,:)*scale_factor,0,'b'); %
auto-scale off
                  end
                  message=sprintf('%3.2f - %3.2f t_{f}',(count_t-
1)*dt/drying_end_frame,count_t*dt/drying_end_frame);
                     text(0,10,message,'color','b');

                     %%% plot scale

quiver(10,20,scale_velocity*scale_factor,0,0,'b','MaxHeadSize',0.9)
                     message=sprintf('%3.0f',scale_velocity);
                     text(0,25,[message '\mum s^{-1}'],'color','b');

                     pause(1);
              end
             % Normalisation and plot
             r=r/max(r);
             t=t/max(t);

              figure(3)
              hold on
              colormark=['b';'r';'g';'k';'m';'c'];
```

```
            message=[];

            lines_t=5; % how many lines in r-vr plot
            lines_r=5; % how many lines in t-vr plot
            line_dr=floor(window_div/lines_r);
            line_dt=floor(t_div/lines_t);

            for i=1:lines_t
                line=i*line_dt;
                  plot(r,vrt_m(line,:),['o--' colormark(mod(i-
1,length(colormark))+1)],'Markersize',2,'Linewidth',1)
                  message=[message; sprintf('%3.2f - %3.2f
t_{f}',(line-1)*dt/drying_end_frame,line*dt/drying_end_frame)];
            end
                  legend(message)
                  set(gca,'Fontsize',8)
                  legend('boxoff')
                  xlabel('r/R_{0}','Fontsize',12)
                  ylabel('v_{r} /\mum.s^{-1}','Fontsize',12)
                  axis([0 1 0 40]);
                  box on

              % check v_th component
        %       for i=1:lines_t
        %           line=i*line_dt;
        %           plot(r,vtht_m(line,:),['+:' colormark(mod(i-
1,length(colormark))+1)],'Markersize',2,'Linewidth',1)
        %       end

                  figure(4);
                  hold on;
                  message=[];

                  for i=1:lines_t
                            line=i*line_dr;
                            plot(t,vrt_m(:,line),['o--'
colormark(mod(i-1,length(colormark))+1)],'Markersize',2,'Linewidth',1)
                            message=[message; sprintf('%3.2f - %3.2f
R_{0}',(line-1)*dr/R0,line*dr/R0)];
                  end

                  legend(message,'Location','NorthWest')
                  set(gca,'Fontsize',8)
                  legend('boxoff')
                  xlabel('t/t_{f}','Fontsize',12)
                  ylabel('v_{r} /\mum.s^{-1}','Fontsize',12)
                  axis([0 1 0 40]);
                  box on;

  else

        %%%%% Bin rectangurally
            x=((1:window_divm)*dx-dx/2);
            y=((1:window_divn)*dy-dy/2);
            t=((1:t_div)*dt-dt/2)*frame_dt;

            xbins=unique(0:window_divm-1);
            ybins=unique(0:window_divn-1);

            grid_id = bsxfun(@plus,xbins,(max(xbins)+1)*ybins.');   %
And this is a list of
```

```
                                                                % all of the
possible unique identifiers.
                                                                % bsxfun is
very useful function to
                                                                % generate
special matrix
            for count_t=1:t_div
                 figure(2)
                 cla
                 hold on;
                    %%% plot x-binning lines
                    for i=1:window_divm-1
                        lines_x=[dx*i 0; dx*i max(v(:,2))]*resolution;

line(lines_x(:,1),lines_x(:,2),'color','y','linestyle','-
.','linewidth',2);
                    end
                    for i=1:window_divn-1
                        lines_y=[0 dy*i; max(v(:,1)) dy*i]*resolution;

line(lines_y(:,1),lines_y(:,2),'color','y','linestyle','-
.','linewidth',2);
                    end
                     axis equal;
                     xlabel('x /\mum');
                     ylabel('y /\mum');
                     set(gca,'YDir','reverse');
                     axis tight;
                     box on;

                t=count_t*dt;
                id_t=find(v(:,3)>=t-dt & v(:,3)<t) ; %%find particles
within the time bin
                new_v=v(id_t,:);

                pops = zeros(size(grid_id));    % Blank array to store
the populations
                vx_m=zeros(size(grid_id)); %blank array to store the
averaged velocity within bin
                vy_m=zeros(size(grid_id));

                inxbin = floor(new_v(:,1)/dx);  % Bin the particle
coordinates appropraitely in x and y
                inybin = floor(new_v(:,2)/dy);
                combined = inxbin+(max(xbins)+1)*inybin;  % Locate
particle in the bin of a unique number

                 message=sprintf('%3.2f - %3.2f t_{f}',(count_t-
1)*dt/drying_end_frame,count_t*dt/drying_end_frame);
                 text(0,5,message,'color','b');

                    % Loop through all the unique identifiers
                   for j = 1:numel(grid_id)
                      pops(j) = sum(combined==grid_id(j));
                      valid = find(combined == grid_id(j));
                      vx_m(j)=mean(new_v(valid,5));
                      vy_m(j)=mean(new_v(valid,6));
                   end
                  vxt_m(:,:,count_t)=vx_m; %
                  vyt_m(:,:,count_t)=vy_m;
                  vxyt_m(:,:,count_t)=sqrt(vx_m.^2+vy_m.^2);
```

```
%quiver(new_v(:,1),new_v(:,2),new_v(:,5),new_v(:,6));
                    for i=1:window_divn
                        yp(1:window_divm)=y(i);

quiver(x(:)*resolution,yp(:)*resolution,vxt_m(i,:,count_t)'*scale_fact
or,vyt_m(i,:,count_t)'*scale_factor,0,'b');
                    end

                      %%% plot scale

quiver(10,20,scale_velocity*scale_factor,0,0,'b','MaxHeadSize',0.9)
                      message=sprintf('%3.0f',scale_velocity);
                      text(0,25,[message '\mum s^{-1}'],'color','b');

                      pause;
            end
  end
```

Appendix E: Matlab Code Used for Interferometry Measurements

E.1 Fringe Analysis Square Wells

```
%%  PART ONE
% initiating parameters and variables

clear all;
drop_fringes_file % load file information

%%%%%%%%% some parameters need to be adjusted for particle
identification
%%%%%%%%% and tracking

% intensity threshold
background_sub=1;
fringe_enhance=0; % background smooth. case 0: no, case 1:; case 2:
intensity_threshold_contact=34; % for contact line

bright_ring_threshold=1;% identifying bright rings
dark_ring_threshold=1; % identifying dark rings

% region of interest
ROI_auto=0;
contact_fixed=1;

%%%%%%%%%%%%%%%%%%%%%% Variable initiation
    cd(folder)

%%%%%%% identification of ROI manually or automatically
    switch background_sub
        case 0,
            background=0;
        case 1,
             filename =
[filetitle,num2str(background_file),'.',fileformat];
             background = imread(filename);
    end

    filename = [filetitle,num2str(deposit_file),'.',fileformat];
    deposit = imread(filename);

    % I=double(background-deposit)+double(deposit-
background);%%%%%%%%%%%%%%%%%% Background subtract
    I=abs(double(background-deposit));%%%%%%%%%%%%%%%%%% Background
subtract

            I=I(:,:,1);
            background=background(:,:,1);
            I = imrotate(I,rotation_angle,'crop');

             cla;
             figure(1);
             imagesc(I);
             size_I=size(I);
             colormap gray;
             axis equal;
             axis([0 size_I(2) 0 size_I(1)]);
             xlabel('x /pixel');
             ylabel('y /pixel');
```

```
            hold on;


    if ROI_auto
        if contact_fixed
                    leftx_min=68;
                    lefty_min=58;
                    rightx_max=498;
                    righty_max=496;
      else
              [n m]=find(I>intensity_threshold_contact); % in matrix
row 'n' is coordinates' y and column 'm' is x
             plot(m,n,'yo','Markersize',2)

           %%%%%%%%%%%%%%%%%%%%%%%%%%%%%% Automatic determine the
contact line
           pklist=[m n];
           indCL=convhull(pklist(:,1),pklist(:,2));
           CL=pklist(indCL,:);

           %%Plot the convex hull of each frame
            plot(CL(:,1),CL(:,2),'go-','Markersize',2,'Linewidth',1);
                   text(1,20,'Contact line
auto','color','yellow','Fontsize',10);
                   leftx_min=floor(min(CL(:,1)));
                   lefty_min=floor(min(CL(:,2)));
                   rightx_max=floor(max(CL(:,1)));
                   righty_max=floor(max(CL(:,2)));
        end
      else
                    text(1,20,'Contact line manual: top-left and
bottom-right','color','yellow','Fontsize',10);
                   selection=ginput(2)
                   leftx_min=floor(selection(1,1));
                   lefty_min=floor(selection(1,2));
                   rightx_max=floor(selection(2,1));
                   righty_max=floor(selection(2,2));
       end
                corner=[leftx_min lefty_min; rightx_max lefty_min;
rightx_max righty_max;...
                leftx_min righty_max; leftx_min lefty_min];
                line(corner(:,1),corner(:,2),'Color','y');

                I=I(lefty_min:righty_max,leftx_min:rightx_max); %%%
cropping
                size_I=size(I);


%% cross section frames pixel by pixel

frame_i=0;
frames=floor((frame_start-frame_end)/(skip_frames+1))+1;
I_3D=zeros(size_I(1),size_I(2),frames);

    for drop_frame=frame_start:-(skip_frames+1):frame_end
    filename = [filetitle,num2str(drop_frame),'.',fileformat];
    frame_i=frame_i+1;
    I = imread(filename);
    I=I(:,:,1);
   % I=double(background-I)+double(I-background);%%%%%%%%%%%%%%%%%%
Background subtract
    I=abs(double(background-I));%%%%%%%%%%%%%%%%%% Background subtract
```

```
    % rotation and crop
    I = imrotate(I,rotation_angle,'crop'); %%% rotation
    I=I(lefty_min:righty_max,leftx_min:rightx_max); %%% cropping
    % size_I=size(I);

    I_3D(:,:,frame_i)=I;

    figure(2)
    cla
      imagesc(I_3D(:,:,frame_i));
    colormap gray;
    axis equal;
    axis([0 size_I(2) 0 size_I(1)]);

     message=sprintf('Frames:%4.0f; Frame after
skip:%4.0f',drop_frame,frame_i);
     text(10,20,message,'color','blue');

    if background_sub
        text(10,40,'Orginal image background off','color','blue');
    else
        text(10,40,'Orginal image','color','blue');
    end

    end


%% test codes for intensity variation
%
%      button=1;
%
%      while button==1
%           L=[];
%           figure(2)
%            [px,py,button]=ginput(1)
%          for k=1:frames
%               L=[L;I_3D(round(py),round(px),k)];
%          end
%          figure(3)
%          cla;
%          hold on
%                message=sprintf('x=%4.0f; y=%4.0f',px,py);
%                text(10,220,message,'color','blue');
%
%               % for fringe changing rate varies
%               %
L1=[smooth(L(1:390),30,'lowess');smooth(L(391:frames),1,'lowess')];
%
%                  L1=smooth(L,8,'lowess');
%
%               plot(L,'b');
%                 plot(L1,'r');
%                 xlabel('t /Frame');
%                 ylabel('y /Intensity');
%                 axis tight;
%
%       end
%
%
% % %
%%   % slice plot
```

```
%  [x y z]=meshgrid(1:size_I(2),1:size_I(1),1:frames);
%     figure(3)
%     slice(x,y,z,I_3D,Inf,Inf,[plotframes])
%     colormap gray
%     shading interp
%     xlabel('x /Pixel');
%      ylabel('y /Pixel');
%        zlabel('t /Frame');
%     axis tight
%
% plotframes = zeros(4,1);
%         plotstep = floor(size(I_3D,3) / 5);
%         plotframes(4) = size(I_3D,3);
%         plotframes(1) = plotstep;
%
%         for i=2:3
%             plotframes(i) = plotframes(i-1) + plotstep;
%         end
% %
%% covert fringes' number to height

%%%%%%%%%%%%%%%%%%%%% Variable initiation

cd ..
centre_fixed=0;
cross_section_fixed=0;
peak_width=15;

lambda=0.455; %um
n_index=1.516; % Anisole

size_I=size(I_3D);
frames=size_I(3);

H_3D=zeros(size_I(1),size_I(2),frames);

t=1:frames;
centre=round([size_I(2)/2 size_I(1)/2]);
mask_half_width=100; % inside the mask the fringes evolve faster

for i=1:size_I(1) % row, y
         for j=1:size_I(2) % column, x
             L=[];
%              bright_p=0;
%              dark_p=0;

            for k=1:frames
                L=[L;I_3D(i,j,k)];
            end

              % for \IOP data
%           if (i>centre(2)-mask_half_width) &
(i<centre(2)+mask_half_width) & (j>centre(1)-mask_half_width) &
(j<centre(1)+mask_half_width)
%
L1=[smooth(L(1:500),30,'lowess');smooth(L(501:frames),1,'lowess')];
%                 [maxtab, mintab] = peakdet(L1, 4, t);
%           else
%
L1=[smooth(L(1:540),30,'lowess');smooth(L(541:frames),1,'lowess')];
%                 [maxtab, mintab] = peakdet(L1, 12, t);
%           end
```

```
                L1=smooth(L,8,'lowess');
                if max(L1)<10
                [maxtab, mintab] = peakdet(L1, 1, t);
                else
                 [maxtab, mintab] = peakdet(L1, 6, t);
                end

%               figure(4);
%               cla;
%               hold on
%               plot(t,L,'b');
%               plot(t,L1,'r');
%
%                   message=sprintf('x=%4.0f; y=%4.0f',j,i);
%                   text(10,180,message,'color','blue');
%
%                   xlabel('x /Frame');
%                   ylabel('y /Intensity');
%                   axis tight;
%
            if ~isempty(mintab) & ~isempty(maxtab)
              bright_p=maxtab(:,1);
  %            plot(mintab(:,1), mintab(:,2), 'g*');

              dark_p=mintab(:,1);
   %           plot(maxtab(:,1), maxtab(:,2), 'r*');
            end
%                legend('raw data', 'lowess fit-
30','Location','SouthWest');
%               legend boxoff;
%
%               pause(0.01);
%
%               figure(5)
%               cla;
%               hold on
              height_bright=zeros(length(bright_p),2);
              for m=1:length(bright_p)
                 height_bright(m,:)=[maxtab(m,1) (m-
1)*lambda/2/n_index];
              end
              height_dark=zeros(length(dark_p),2);
              for m=1:length(dark_p)
                 height_dark(m,:)=[mintab(m,1);((m-
1)*lambda+lambda/2)/2/n_index];
              end
            height=[height_bright; height_dark];
            height=sort(height);

            % interpolate linearly, outside height(:1) region use
'extrap'

height_p=interp1(height(:,1),height(:,2),t,'linear','extrap');
            height_p(find(height_p<0))=0;

%             plot(height(:,1),height(:,2),'or',t,height_p,'b');
%             axis tight

            % save to H_3D
            H_3D(i,j,:)=height_p;
            %pause;
```

```
        end

         message=sprintf('processing =%5.3f',100*i/size_I(1));
         disp(message);
end
%  %% slice plot
%  [x y z]=meshgrid(1:size_I(2),1:size_I(1),1:round(frames/2));
%     figure(3)
%     start_frame=10;
%     step=round(frames/6);
%    %
slice(x,y,z,I_3D,Inf,Inf,[start_frame,start_frame+step,start_frame+ste
p*2])
%      slice(x,y,z,I_3D,Inf,Inf,[10,50,90])
%     colormap gray
%     shading interp
%     xlabel('x /Pixel');
%      ylabel('y /Pixel');
%        zlabel('t /Frame');
%     axis tight

%% save file
  cd(folder)

    save I_3D.mat I_3D
    save H_3D.mat H_3D
    cd ..

  Get improfiles along radial lines (Method1: using improfile)
  N_line=4; % the number to divide the circle
  theta =(0:2*pi/N_line:(N_line-1)*2*pi/N_line)';
  rho = R_basin*ones (N_line,1);
  r=(0:R_basin)'.*resolution;
  Endpoint_x=Centroid_X+rho.*cos(theta);
  Endpoint_y=Centroid_Y+rho.*sin(theta);
  hline1=zeros(R_basin+1,N_line);
  hline_ave=zeros(R_basin+1,frames);
  fn=10;
 for f=frames:-1:1
   for p=1:N_line
    [cx, cy,
hline]=improfile(H_3D(:,:,f),[Centroid_X;Endpoint_x(p)],[Centroid_Y;En
dpoint_y(p)],R_basin+1);
    hline1(:,p)=hline;
    legendInfo{p} = ['\theta = ', num2str((p-1)*2/N_line),' \pi'];
    hold on
   end
   hline_ave(:,(frames-f+1))=mean(hline1,2);


%%%* Plot the height profiles along lines for cetain time steps
%* comment this to save time

 if mod(f,400)==0
     oldFolder=cd(folder);
     legendInfo=legendInfo';
     figure (fn)
     clear title
     plot (r,hline1,'-o')
     legend(legendInfo)
     legend('Location','best')
```

```
     title(strcat('Frame No. ',num2str(frame_IndexInverse(f)),',',' t
= ',num2str(timeInverse(f)),' s'));
     hold on
     plot(r,hline_ave (:,(frames-f+1)),'-
o','DisplayName','Averaged','color',[0 0 0],'LineWidth',1)%* the
legend for the mean cannot be shown,??
     legend show
     axis([0 R_basin_real 0 6])
     xlabel('r, \mum')
     ylabel('h, \mum')
     % save the figure
     FigureName=strcat('Film height profile along radial lines at',' t
= ',num2str(timeInverse(f)),' s.png');
     print(gcf,FigureName,'-dpng');% gcf, returns the current figure
handle
     fn=fn+1;
     cd(oldFolder);
 end
 close all;
 %%%%* comment above to save time
 end

 %%
%* Get improfiles along radial lines (Method2: using pinned radius)
%%%%convert position into polar cordinates
[row_Y,col_X] = find(I) ; % indexes of I
PixelNum = numel(row_Y);
xr=zeros(PixelNum,1);
xth=zeros(PixelNum,1);
for j=1:PixelNum % columns, x     %* this saves time comparing looping
through row frist
 xr(j)=sqrt((col_X(j)-Centroid_X)^2 + (row_Y(j)-Centroid_Y)^2 );
%%compute radius
 xth(j)=atan2((row_Y(j)-Centroid_Y),(col_X(j)-Centroid_X)); %%compute
angle
end
[xr,Index]=sort(xr);
R_section=16; % the sections to devide the radius
R_delta=R_basin/R_section; % the delta in pixels
radialDelta=R_delta*resolution;%the delta in um
xr2=(0:R_delta:R_basin)';
r2=xr2*resolution;
H_xr2=zeros(R_section+1,frames);
fn=20;
figure (fn)
legend_text=[];
for f=frames:-1:1
H_xr=H_3D(:,:,f);
H_xr=H_xr(:);
H_xr=H_xr(Index);% the height profile corresponding to xr

for rn=1:R_section+1
ind= find(xr<=(xr2(rn)+2)& xr>=(xr2(rn)-2));
H_xr2(rn,(frames-f+1))=mean(H_xr(ind));
end

%%%* Plot the height profiles r-h
%* comment this to save time

if mod(f,400)==0
     clear title
     axis([0 R_basin_real 0 6])
     xlabel('r, \mum')
```

```
     ylabel('h, \mum')
     title=strcat('Frame No. ',num2str(frame_IndexInverse(f)),',',' t
= ',num2str(timeInverse(f)),' s');
     legend_text=strvcat(legend_text,title);
     legend('Location','best')
     plot (r2,H_xr2(:,frames-f+1),'-o')
     hold on
 end
end
legend(legend_text,'Location','best');
 % save the figure
 oldFolder=cd(folder);
 FigureName=strcat('Film height profile along radial
lines_polar','.png');
 print(gcf,FigureName,'-dpng');% gcf, returns the current figure
handle
 cd(oldFolder);
%  close all;
%% Profiles of height with time at paticular points
cd(folder)
figure(1)
imagesc(I_3D(:,:,end));
axis equal
axis tight

colormap gray;
text(1,20,'Select five points:','color','yellow','Fontsize',10);
hold on
Points=ginput(5);
close all;

figure(1)
imagesc(I_3D(:,:,end));
axis equal
axis tight

colormap gray;
hold on
for k = 1:5

    plot(round(Points(k,1)),round(Points(k,2)),'black+'); % plot
centroids
    text(round(Points(k,1)+4),round(Points(k,2)),sprintf('%d',
k),'Color','black');% text

end
fig = gcf;
fig.Color = 'white'; % set the background figure color
fig.InvertHardcopy = 'off';
iptsetpref('ImshowBorder','tight'); % Figures without any borders

print(fig,'Points_Selection','-dtiff','-r100','-r0' );
close all;
 H_points=zeros(frames,5);
 for j=1:5
 for i=frames:-1:1
   H_points(frames-
i+1,j)=H_3D(round(Points(j,1)),round(Points(j,2)),i);
 end
 end

   figure(2)
```

```
   legend_text=[];
    axis tight;
for k=1:5

    plot(time_real(:),H_points(:,k));
    xlabel('Time,s')
    ylabel('Height, \mum')
    title=strcat('Point ',num2str(k));
    legend_text=strvcat(legend_text,title);
    legend('Location','best')
    hold on;
end
legend(legend_text,'Location','best');
fig = gcf;
fig.Color = 'white'; % set the background figure color
fig.InvertHardcopy = 'off';
iptsetpref('ImshowBorder','tight'); % Figures without any borders
print(fig,'Height_time','-dtiff','-r100','-r0' );% gcf, returns the
current figure handle, change the resolution if needed...
cd ..
%% save file
  cd(folder)
%     save hline_ave.mat hline_ave %* the height profile along radical
line for different frames (frame index from low to high/time
increases)
%     save r.mat r
    save frame_realIndex.mat frame_realIndex %* the exact frame index
corresponding hline_ave
    save time_real.mat time_real %* the time information corresponding
hline_ave
    save H_points.mat H_points;
    save xr2.mat xr2 % the radial distance in pixel
    save r2.mat r2 % the radial distance in um
    save H_xr2.mat H_xr2 % the height corresponding xr2
    save radialDelta.mat radialDelta % the radial discretized cell
length
%     save I_3D.mat I_3D
%     save H_3D.mat H_3D % the 3_d height profile for different frames
(real frame index from high to low/inverse direction of the droplet
drying )

    save
    cd ..
```

E.2 Plot Profile Dynamics Square Wells

```
%%  PART Two Ploting profile dynamics

% initiating parameters and variables

% Clear all and load file info only needed when not running Dyn2
immediately after Dyn1

% clear all;
% drop_fringes_file % load file information
%
% cd(folder)
% load I_3D.mat
% load H_3D.mat
% cd ..

size_I=size(I_3D);
frames=size_I(3);

   %%
% % %
%    [x y z]=meshgrid(1:size_I(2),1:size_I(1),1:frames);
%
%     figure(3)
%      slice(x,y,z,H_3D,Inf,Inf,[62])
%     colormap gray
%     shading interp
%     xlabel('x /Pixel');
%      ylabel('y /Pixel');
%        zlabel('Height /microns');
%     axis tight

%     figure(3)
%      slice(x,y,z,H_3D,Inf,Inf,[frames2])
%     colormap gray
%     shading interp
%     xlabel('x /Pixel');
%      ylabel('y /Pixel');
%        zlabel('Height /microns');
%     axis tight%

% frames2 = zeros(7,1);
%         plotstep = floor(size(I_3D,3) / 8);
%         plotframes(7) = size(I_3D,3);
%         plotframes(1) = plotstep;
%
%         for i=2:6
%             plotframes(i) = plotframes(i-1) + plotstep;
%         end


    %%
    figure(4)
    imagesc(I_3D(:,:,frames));
    colormap gray;
    axis equal tight
    leg=[];

    plotframes = zeros(7,1);
        plotstep = floor(size(I_3D,3) / 8);
        plotframes(7) = size(I_3D,3);
```

```
        plotframes(1) = plotstep;

        for i=2:6
            plotframes(i) = plotframes(i-1) + plotstep;
        end


    [x y]=ginput(2)
%       x=[0;453];
%       y=[230;230];
    colormark=['b';'r';'g';'k';'m';'c'];
    figure(5)
    hold on
%     for i=1:7
%        [cx cy I]=improfile(H_3D(:,:,520-(i-1)*75),x,y);
%         d=((cx-x(2)).^2+(cy-y(2)).^2).^(1/2);
%         %I=smooth(I,50,'lowess');
%         plot(d, I,['.-' colormark(mod(i-1,length(colormark))+1)])
%         leg= strvcat(leg,num2str(520-(i-1)*75));
%     end

    for i=1:7
       [cx cy I]=improfile(H_3D(:,:,plotframes(i)),x,y);
        d=((cx-x(2)).^2+(cy-y(2)).^2).^(1/2);
        %I=smooth(I,50,'lowess');
        plot(d, I,['.-' colormark(mod(i-1,length(colormark))+1)])
        leg= strvcat(leg,num2str(plotframes(i)));

        filename = ['plot-',num2str(i),'.txt'];
         fp=fopen(filename,'w');
         profile=[d I]';
         fprintf(fp,'%12.8f  %12.8f\n',profile); % save file
         fclose(fp);
    end

xlabel('x /Pixel');
ylabel('Height /micron');
legend([leg],'Location','NorthEastOutside');
legend boxoff
axis tight
```

E.3 Fringe Analysis Circular Wells

```
%%  PART ONE
% initiating parameters and variables

clear all;
drop_fringes_file % load file information

%%%%%%%%% some parameters need to be adjusted for particle
identification
%%%%%%%%% and tracking

% intensity threshold
background_sub=0;
fringe_enhance=0; % background smooth. case 0: no, case 1:; case 2:
intensity_threshold_contact=34; % for contact line

bright_ring_threshold=1;% identifying bright rings
dark_ring_threshold=1; % identifying dark rings

% region of interest
ROI_auto=0;
contact_fixed=1;

%%%%%%%%%%%%%%%%%%%%%% Variable initiation
    cd(folder)

%%%%%%% identification of ROI manually or automatically
    switch background_sub
        case 0,
            background=0;
        case 1,
             filename =
[filetitle,num2str(background_file),'.',fileformat];
             background = imread(filename);
    end

    filename = [filetitle,num2str(deposit_file),'.',fileformat];
    deposit = imread(filename);

    % I=double(background-deposit)+double(deposit-
background);%%%%%%%%%%%%%%%%%% Background subtract
    I=abs(double(deposit-background));%%%%%%%%%%%%%%%%%% Background
subtract

            I=I(:,:,1);
            background=background(:,:,1);
            I = imrotate(I,rotation_angle,'crop');

             cla;
             figure(1);
             imagesc(I);
             size_I=size(I);
             colormap gray;
             axis equal;
             axis([0 size_I(2) 0 size_I(1)]);
             xlabel('x /pixel');
             ylabel('y /pixel');

             hold on;
```

```
    if ROI_auto
        if contact_fixed
                    leftx_min=68;
                    lefty_min=58;
                    rightx_max=498;
                    righty_max=496;
        else
             [n m]=find(I>intensity_threshold_contact); % in matrix
row 'n' is coordinates' y and column 'm' is x
             plot(m,n,'yo','Markersize',2)

           %%%%%%%%%%%%%%%%%%%%%%%%%%%%%% Automatic determine the
contact line
           pklist=[m n];
           indCL=convhull(pklist(:,1),pklist(:,2));
           CL=pklist(indCL,:);

           %%Plot the convex hull of each frame
            plot(CL(:,1),CL(:,2),'go-','Markersize',2,'Linewidth',1);
                   text(1,20,'Contact line
auto','color','yellow','Fontsize',10);
                   leftx_min=floor(min(CL(:,1)));
                   lefty_min=floor(min(CL(:,2)));
                   rightx_max=floor(max(CL(:,1)));
                   righty_max=floor(max(CL(:,2)));
        end
      else
                    text(1,20,'Contact line manual: top-left and
bottom-right','color','yellow','Fontsize',10);
                   selection=ginput(2)
                   leftx_min=floor(selection(1,1));
                   lefty_min=floor(selection(1,2));
                   rightx_max=floor(selection(2,1));
                   righty_max=floor(selection(2,2));
       end
               corner=[leftx_min lefty_min; rightx_max lefty_min;
rightx_max righty_max;...
               leftx_min righty_max; leftx_min lefty_min];
               line(corner(:,1),corner(:,2),'Color','y');

               I=I(lefty_min:righty_max,leftx_min:rightx_max); %%%
cropping
               size_I=size(I);


%% cross section frames pixel by pixel

frame_i=0;
frames=floor((frame_start-frame_end)/(skip_frames+1))+1;
I_3D=zeros(size_I(1),size_I(2),frames);

    for drop_frame=frame_start:-(skip_frames+1):frame_end
    filename = [filetitle,num2str(drop_frame),'.',fileformat];
    frame_i=frame_i+1;
    I = imread(filename);
    I=I(:,:,1);
   % I=double(background-I)+double(I-background);%%%%%%%%%%%%%%%%%%
Background subtract
    I=abs(double(I-background));%%%%%%%%%%%%%%%%%% Background subtract

    % rotation and crop
```

```
    I = imrotate(I,rotation_angle,'crop'); %%% rotation
    I=I(lefty_min:righty_max,leftx_min:rightx_max); %%% cropping
    % size_I=size(I);

    I_3D(:,:,frame_i)=I;

    figure(2)
    cla
      imagesc(I_3D(:,:,frame_i));
    colormap gray;
    axis equal;
    axis([0 size_I(2) 0 size_I(1)]);

     message=sprintf('Frames:%4.0f; Frame after
skip:%4.0f',drop_frame,frame_i);
     text(10,20,message,'color','blue');

    if background_sub
        text(10,40,'Orginal image background off','color','blue');
    else
        text(10,40,'Orginal image','color','blue');
    end

    end


%% test codes for intensity variation

     button=1;

     while button==1
          L=[];
          figure(2)
           [px,py,button]=ginput(1);
         for k=1:frames
               L=[L;I_3D(round(py),round(px),k)];
         end
         figure(3)
         cla;
         hold on
                message=sprintf('x=%4.0f; y=%4.0f',px,py);
                text(10,220,message,'color','blue');

               % for fringe changing rate varies
               %
L1=[smooth(L(1:390),30,'lowess');smooth(L(391:frames),1,'lowess')];

                  L1=smooth(L,8,'lowess');

               plot(L,'b');
                 plot(L1,'r');
                 xlabel('t /Frame');
                 ylabel('y /Intensity');
                 axis tight;

     end

     %%
cd ..
%% covert fringes' number to height
```

```
%%%%%%%%%%%%%%%%%%%%% Variable initiation

centre_fixed=0;
cross_section_fixed=0;
peak_width=15;

lambda=0.455; %um
n_index=1.516; % Anisole

size_I=size(I_3D);
frames=size_I(3);

H_3D=zeros(size_I(1),size_I(2),frames);

t=1:frames;
centre=round([size_I(2)/2 size_I(1)/2]);
mask_half_width=100; % inside the mask the fringes evolve faster

for i=1:size_I(1) % row, y
         for j=1:size_I(2) % column, x
             L=[];

           for k=1:frames
               L=[L;I_3D(i,j,k)];
           end

             % for \IOP data
%           if (i>centre(2)-mask_half_width) &
(i<centre(2)+mask_half_width) & (j>centre(1)-mask_half_width) &
(j<centre(1)+mask_half_width)
%
L1=[smooth(L(1:500),30,'lowess');smooth(L(501:frames),1,'lowess')];
%                 [maxtab, mintab] = peakdet(L1, 4, t);
%           else
%
L1=[smooth(L(1:540),30,'lowess');smooth(L(541:frames),1,'lowess')];
%                 [maxtab, mintab] = peakdet(L1, 12, t);
%           end

               L1=smooth(L,8,'lowess');
               if max(L1)<10
               [maxtab, mintab] = peakdet(L1, 20, t);
               else
                [maxtab, mintab] = peakdet(L1, 40, t);
               end

%              figure(4);
%              cla;
%              hold on
%              plot(t,L,'b');
%              plot(t,L1,'r');
%
%                  message=sprintf('x=%4.0f; y=%4.0f',j,i);
%                  text(10,180,message,'color','blue');
%
%                  xlabel('x /Frame');
%                  ylabel('y /Intensity');
%                  axis tight;
%
           if ~isempty(mintab) & ~isempty(maxtab)
```

```
            bright_p=maxtab(:,1);
 %            plot(mintab(:,1), mintab(:,2), 'g*');

            dark_p=mintab(:,1);
%             plot(maxtab(:,1), maxtab(:,2), 'r*');
          end
%             legend('raw data', 'lowess fit-
30','Location','SouthWest');
%              legend boxoff;
%
%             pause;

%              figure(5)
%              cla;
%              hold on
%
            if ~isempty(mintab) & ~isempty(maxtab)
               height_bright=zeros(length(bright_p),2);
               height_dark=zeros(length(dark_p),2);

               for m=1:length(bright_p)
                  height_bright(m,:)=[maxtab(m,1) (m-
1)*lambda/2/n_index];
               end

               for m=1:length(dark_p)
                  height_dark(m,:)=[mintab(m,1);((m-
1)*lambda+lambda/2)/2/n_index];
               end

               height=[height_bright; height_dark];
               height=sort(height);

              % interpolate linearly, outside height(:1) region use
'extrap'

height_p=interp1(height(:,1),height(:,2),t,'linear','extrap');
%                height_p(find(height_p<0))=0;

%             plot(height(:,1),height(:,2),'or',t,height_p,'*b');
%             axis tight
%
%             pause;

               % save to H_3D
               H_3D(i,j,:)=height_p;
            else
                H_3D(i,j,:)=0;
            end

         end

          message=sprintf('processing =%5.3f',100*i/size_I(1));
          disp(message);
end
 %% slice plot
%  [x y z]=meshgrid(1:size_I(2),1:size_I(1),1:frames);
%     figure(3)
%     start_frame=50;
%     step=round(frames/3);
```

```
%
slice(x,y,z,I_3D,Inf,Inf,[start_frame,start_frame+step,start_frame+ste
p*2])
%     colormap gray
%     shading interp
%     xlabel('x /Pixel');
%      ylabel('y /Pixel');
%        zlabel('t /Frame');
%     axis tight

%% save file
  cd(folder)

    save I_3D.mat I_3D
    save H_3D.mat H_3D
    cd ..
```

E.4 Plotting Profile Dynamics Circular Wells

```
%%  PART Two Ploting profile dynamics

% initiating parameters and variables

% Clear all and load file info only needed when not running Dyn2
immediately after Dyn1

% clear all;
% drop_fringes_file % load file information
%
% cd(folder)
% load I_3D.mat
% load H_3D.mat
% cd ..

size_I=size(I_3D);
frames=size_I(3);

   %%
% % %
%    [x y z]=meshgrid(1:size_I(2),1:size_I(1),1:frames);
%
%     figure(3)
%      slice(x,y,z,H_3D,Inf,Inf,[62])
%     colormap gray
%     shading interp
%     xlabel('x /Pixel');
%      ylabel('y /Pixel');
%        zlabel('Height /microns');
%     axis tight

%     figure(3)
%      slice(x,y,z,H_3D,Inf,Inf,[frames2])
%     colormap gray
%     shading interp
%     xlabel('x /Pixel');
%      ylabel('y /Pixel');
%        zlabel('Height /microns');
%     axis tight%

% frames2 = zeros(7,1);
%         plotstep = floor(size(I_3D,3) / 8);
%         plotframes(7) = size(I_3D,3);
%         plotframes(1) = plotstep;
%
%         for i=2:6
%             plotframes(i) = plotframes(i-1) + plotstep;
%         end


    %%
    figure(4)
    imagesc(I_3D(:,:,frames));
    colormap gray;
    axis equal tight
    leg=[];

    plotframes = zeros(7,1);
        plotstep = floor(size(I_3D,3) / 8);
        plotframes(7) = size(I_3D,3);
```

```
        plotframes(1) = plotstep;

        for i=2:6
            plotframes(i) = plotframes(i-1) + plotstep;
        end


    [x y]=ginput(2)
%       x=[0;453];
%       y=[230;230];
    colormark=['b';'r';'g';'k';'m';'c'];
    figure(5)
    hold on
%     for i=1:7
%        [cx cy I]=improfile(H_3D(:,:,520-(i-1)*75),x,y);
%         d=((cx-x(2)).^2+(cy-y(2)).^2).^(1/2);
%         %I=smooth(I,50,'lowess');
%         plot(d, I,['.-' colormark(mod(i-1,length(colormark))+1)])
%         leg= strvcat(leg,num2str(520-(i-1)*75));
%     end

    for i=1:7
       [cx cy I]=improfile(H_3D(:,:,plotframes(i)),x,y);
        d=((cx-x(2)).^2+(cy-y(2)).^2).^(1/2);
        %I=smooth(I,50,'lowess');
        plot(d, I,['.-' colormark(mod(i-1,length(colormark))+1)])
        leg= strvcat(leg,num2str(plotframes(i)));

        filename = ['plot-',num2str(i),'.txt'];
         fp=fopen(filename,'w');
         profile=[d I]';
         fprintf(fp,'%12.8f  %12.8f\n',profile); % save file
         fclose(fp);
    end

xlabel('x /Pixel');
ylabel('Height /micron');
legend([leg],'Location','NorthEastOutside');
legend boxoff
```